EINDHOVEN
UNIVERSITY OF
TECHNOLOGY

Voltage-dependent scanning tunneling microscopy on the {110}-surfaces of GaAs, AlGaAs, and their heterostructures

Citation for published version (APA):
Raad, de, G. J. (2001). *Voltage-dependent scanning tunneling microscopy on the {110}-surfaces of GaAs, AlGaAs, and their heterostructures*. [Phd Thesis 1 (Research TU/e / Graduation TU/e), Applied Physics and Science Education]. Technische Universiteit Eindhoven. https://doi.org/10.6100/IR543694

DOI:
10.6100/IR543694

Document status and date:
Published: 01/01/2001

Document Version:
Publisher's PDF, also known as Version of Record (includes final page, issue and volume numbers)

Please check the document version of this publication:

• A submitted manuscript is the version of the article upon submission and before peer-review. There can be important differences between the submitted version and the official published version of record. People interested in the research are advised to contact the author for the final version of the publication, or visit the DOI to the publisher's website.
• The final author version and the galley proof are versions of the publication after peer review.
• The final published version features the final layout of the paper including the volume, issue and page numbers.

Link to publication

General rights
Copyright and moral rights for the publications made accessible in the public portal are retained by the authors and/or other copyright owners and it is a condition of accessing publications that users recognise and abide by the legal requirements associated with these rights.

• Users may download and print one copy of any publication from the public portal for the purpose of private study or research.
• You may not further distribute the material or use it for any profit-making activity or commercial gain
• You may freely distribute the URL identifying the publication in the public portal.

If the publication is distributed under the terms of Article 25fa of the Dutch Copyright Act, indicated by the "Taverne" license above, please follow below link for the End User Agreement:

www.tue.nl/taverne

Take down policy
If you believe that this document breaches copyright please contact us at:

openaccess@tue.nl

providing details and we will investigate your claim.

Download date: 16. Nov. 2023

Voltage-dependent Scanning Tunneling Microscopy on the {110}-surfaces of GaAs, AlGaAs and their heterostructures

PROEFSCHRIFT

ter verkrijging van de graad van doctor aan de Technische Universiteit Eindhoven, op gezag van de Rector Magnificus, prof.dr. M. Rem, voor een commissie aangewezen door het College voor Promoties in het openbaar te verdedigen op maandag 22 januari 2001 om 16.00 uur

door

Gijs Jan de Raad

geboren te Ede.

Dit proefschrift is goedgekeurd door de promotoren:

prof.dr. J.H. Wolter
en
prof.dr. H. van Kempen

en de Copromotor:
dr. P.M. Koenraad.

CIP-DATA LIBRARY TECHNISCHE UNIVERSITEIT EINDHOVEN

Raad, de, Gijs Jan

Voltage-dependent Scanning Tunneling Microscopy on the {110}-surfaces of GaAs, AlGaAs and their heterostructures / by Gijs Jan de Raad. - Eindhoven : Technische Universiteit Eindhoven, 2001. -
Proefschrift.
ISBN 90-386-1709-7
NUGI 812
Trefw.: Scanning Tunneling Mikroscopie; III-V halfgeleiders; oppervlaktetoestanden; doteringen; tip; wolfraam.
Subject headings: Scanning Tunneling Microscopy; III-V semiconductors; surface states; dopants; tip; tungsten.

The work described in this thesis was carried out at the COBRA Inter-University Research Institute on Communication Technology of the Department of Physics of the Eindhoven University of Technology and was part of the research program of the Dutch Foundation for Fundamental Research on Matter (FOM), which is financially supported by the Dutch Organization for the Advancement of Research (NWO).

Aan tante Cock

"Een relatie kan alleen dán goed zijn,
als ze goed is voor beide partijen."

Speijk de Raad, mijn vader.

Contents

INTRODUCTION **i**

The STM and how we use it i
Bias-voltage dependent effects in STM iii
The spatial distribution of dopants in STM v
The experimental setup and methods vi
References viii

1: THEORY **1**

1.1 Introduction 1
1.2 The tunneling current 2
1.3 Some properties of the tunneling current 4
1.4 Atomically resolved STM-images 6
1.5 Lateral motion of electrons and sample density of states 8
1.6 Tunneling for a tungsten tip: non-s tip states 9
1.7 Tip-sample interaction 11
1.8 Effects of the tip-sample interaction 13
1.9 Tip-induced band bending 15
1.10 Summary 17
References 18

2: STM-SETUP AND SAMPLE PREPARATION **21**

2.1 Introduction 21
2.2 Outline of measurement procedure 21
2.3 The UHV-system and STM 22
2.4 Sample preparation 25
2.5 The measurement 28
2.6 Typical morphology of cleaved surfaces 30
2.7 Discussion on the cleavage process 34
2.8 Summary 39
References 40

3: PREPARATION OF STM-TIPS AND RELATED EXPERIMENTS 41

3.1 Introduction 41
3.2 Tip preparation method 42
3.2.1 *Tip etching* 44
3.2.2 *Heating* 45
3.2.3 *Self-sputtering* 46
3.2.4 *Argon ion bombardment* 46
3.2.5 *Tip characterization* 47
3.2.6 *Regeneration of tips* 47
3.3 Description of the self-sputtering behaviour 49
3.4 Characterization of STM-tips by field emission 50
3.5 Discussion on self-sputtering behaviour and field emission characterization 56
3.6 The occurrence and prevention of vacuum-arcs 59
3.7 Comments on the argon-ion bombardment 62
3.8 Summary 63
References 64

4: TUNEABILITY OF THE SURFACE-CORRUGATION ON GaAs (110) SURFACES: THE PRECISE ROLE OF TIP-INDUCED BAND BENDING 67

4.1 Introduction 67
4.2 Experimental 70
4.3 STM: Corrugation-change on n-GaAs and p-GaAs-(110) 74
4.4 Model results: Different scenarios of band bending 78
4.5 Discussion 90
4.5.1 *p-GaAs, empty states* 90
4.5.2 *n-GaAs, filled states* 91
4.5.3 *n-GaAs, empty states* 91
4.5.4 *p-GaAs, filled states* 93
4.5.5 *The reliable use of the model* 98
4.5.6 *Atomic resolution on GaAs (110) in type I depletion* 99
4.6 Some other examples of corrugation-change on GaAs (110) 103
4.7 Summary 107
References 108

5: OBSERVATION OF A NEW IMAGE-FORM OF GaAs-(110) SHOWING THE TOP- AND BOTTOM ZIG-ZAG ROWS OF THE SURFACE 113

5.1 Introduction 113
5.2 Experimental 115
5.3 True lattice resemblant corrugation 115
5.4 Discussion 119
5.5 Summary and conclusion 123
References 124

6: VOLTAGE-DEPENDENT CHANGES IN THE FILLED- AND EMPTY-STATES IMAGES OF AlGaAs AND OF GaAs/AlGaAs THIN LAYERS 127

6.1 Introduction 127
6.2 Experiment 130
6.3 Results 131
6.4 Expected tip-induced band bending 145
6.4.1 *The thick AlGaAs layer* 145
6.4.2 *The GaAs/AlGaAs superlattice* 148
6.5 Discussion on the thick AlGaAs layer 151
6.5.1 *Filled-states images* 151
6.5.2 *Empty-states images* 153
6.5.3 *Comparison between the filled- and empty-states of the same area of AlGaAs* 156
6.6 Discussion on the GaAs/AlGaAs superlattice 158
6.6.1 *Filled states images* 158
6.6.2 *Empty states images* 161
6.7 Summary, conclusions, outlook 167
References 165

7: NANO-SCALE CHARACTERIZATION OF Si δDOPED LAYERS IN GaAs 169

7.1 Introduction 169
7.2 Identification of dopants in filled-states STM-images of n-GaAs 171
7.3 Sample structure and STM-results 179
7.4 Individual features occurring in Si δ-doped layers 181
7.5 Spatial distribution of Si-dopants within a δ-doped layer 189
7.6 Discussion on the spatial distribution of Si-dopants within a δ-doped layer 193
7.6.1 *Ordering effects during growth of delta-doped layers* 193
7.6.2 *Detecting short-range order in δlayers using X-STM.* 196
7.7 Summary 198
References 199

SUMMARY 203

NEDERLANDSE SAMENVATTING 207

VOOR NIET-NATUURKUNDIGEN 212

Wat is een STM? 212
Wat kunnen we in een STM-beeld zien? 217
Waarover gaat dit proefschrift? 218

LIST OF ABBREVIATIONS 223

DANKWOORD 224

LIST OF PUBLICATIONS 226

CURRICULUM VITAE 227

Introduction

The STM and how we use it

Ever since the days of Galileo Galilei (1564 - 1642) and van Leeuwenhoek (1632 - 1723), telescopes and microscopes have played a vital role in the advancement of science. The importance of these instruments comes from the fact that they enable us to see what the physical universe looks like at a different characteristic length-scale than the one we know from our daily lives. And when we observe the universe at another length-scale than our own, it looks so different that it seems as if we enter an entirely new world. But do we really? In fact, we do not. Because regardless of the length-scale at which we choose to observe the universe, the physical laws that govern it remain the same. This means that what we observe at one length-scale, must have implications for the physical reality as we observe it at other length-scales. Herein lies the scientific value of microscopes and telescopes, whether we look at living cells and try to understand their chemistry, whether we gaze at stars and wonder about the physical processes that make them hot enough to emit vast amounts of light, or whether we study a crystal surface and ask ourselves what determines the distribution of its electronic states.

A more recent addition to the different types of microscope available to scientists is the Scanning Tunneling Microscope (STM). The STM was invented by Binnig and Rohrer at the IBM research-laboratory near Zürich, Switzerland, in 1981. Over the last 20 years, it has evolved from a new and interesting gadget to the fully-fledged experimental technique it is today. The first major success of the STM as an experimental tool has been the real-space imaging of the 7x7-reconstruction of the Si-(111) surface [1 (page 10), 2]. Nowadays, the STM and the other Scanning Probe techniques that have spun off are used to investigate a very wide range of scientific topics: Ordering effects in epitaxially grown ternary compound semiconductors, the appearance of dopant atoms in STM, the spatial distribution of dopants in epitaxially grown semiconductor devices, friction at the atomic scale, and the dynamics of mono-atomic steps on metal surfaces at elevated temperature are but a few examples.

The research-group at the University of Eindhoven that I was part of during this PdD-project uses Molecular Beam Epitaxy (MBE) and Chemical Beam Epitaxy (CBE) to grow III-V semiconductor materials and heterostructures. These materials and heterostructures can then be characterized and studied by a variety of methods, including magneto-transport measurements, Photo-Luminescence (PL) and Photo-Luminescence Exitation (PLE), and X-ray diffraction. A setup for Cross-sectional STM in Ultra-High Vacuum (UHV) was added to the set of tools available for the study of the grown materials and structures at the start of this PhD-project. At a later stage, a

setup for in-plane STM at low temperature and in magnetic fields has been added, as well as an ambient Atomic Force Microscope (AFM). The setup for Cross-sectional STM (X-STM) in UHV, which is the main experimental tool used for this thesis, has been aquired for the specific purpose of studying the atomic-scale properties of III-V semiconductor materials and structures. We use it to address topics like atomic-scale roughening of interfaces between GaAs and $Al_xGa_{(1-x)}As$ layers, the spatial distribution of dopants in epitaxially grown layers, or the shape and local In content of self-assembled InAs quantum dots in GaAs.

X-STM has several advantages over competing techniques such as High-Resolution Transmission Electron Microscopy (HR-TEM) [30 (p. 6-8)] or in-plane STM [14]: In HR-TEM, the beam of electrons that probes the sample always passes through a thin layer of material, which has a thickness of up to 100 nm [29 (p. 31)]. This means that the representation of the sample structure as obtained by HR-TEM is always an average over many atomic layers. X-STM, on the other hand, images only the surface layer. This makes the technique ideal for the study of interface roughness in heterostructures or alloy fluctuations in ternary materials like $Al_xGa_{(1-x)}As$. Another advantage of STM is that this technique can image individual dopant atoms.

An advantage of X-STM over in-plane STM is that it images hetero-structures of different semiconducting materials or dopant-structures such as a δ-doped layer, after growth of the entire sample including the cap layer: After a semiconductor structure has been grown by epitaxial techniques such as MBE or CBE, it is buried by a cap layer in order to isolate the structure from the ambient. This means that the newly grown structure remains at growth temperature for some time. During this time, redistribution of atoms can occur due to diffusion or segregation effects [28]. Such redistribution can cause broadening of δ-doped layer, or roughening of interfaces between the different materials that make up a heterostructure. The technique of in-plane STM has been used very successfully by Däweritz *et al.* [14] to study the dynamics of dopant atoms as they reside on the sample surface during epitaxial growth of the sample. In this thesis, however, we are interested mainly in the final form of dopant- or heterostructures. This makes the technique of X-STM more suitable for our purposes than in-plane STM.

The research in this thesis focuses two topics, apart from the research that was carried out in relation to the experimental methods: The first topic consists of the changes in the atomic-scale morphology of the {110}-surface of GaAs, $Al_xGa_{(1-x)}As$ and that of a GaAs/AlGaAs superlattice. The second one is the spatial distribution of Si dopant atoms which make up a Si δ-doped layer in GaAs. The rest of this introduction is organized as follows: We first reflect on bias-voltage dependent effects in STM, in particular the ones that are observed on the {110}-surfaces of III-V semiconductors. This part explains the relations between chapters four, five and six, and also the relation that each of these chapters has with existing literature. The second part explains why we are interested in the spatial distribution of dopants in δ-doped layers in GaAs, which is the topic of chapter 7. The last part of this introduction briefly considers our methods of sample- and tip preparation, and the experimental work that has been spent on making the methods work as they should (chapters 2 and 3). Chapter one is not discussed in this introduction: This chapter qualitatively explains some basic aspects of tunneling between a metal tip and a semiconducting sample.

Bias-voltage dependent effects in STM

Any textbook on scanning tunneling microscopy (STM) explains that atomically resolved images are in reality maps of the local electronic surface density of states (surface-DOS or LDOS), and do not show the atoms themselves. Within the STM-community this fact is so well-known that it seems trivial to even mention it here. And yet, it is important: if an STM were to show the atomic surface lattice of a sample directly, the voltage-dependent effects that are one of the main subjects of this thesis, would not exist.

If the STM images the surface-DOS rather than the atoms of the surface, then why is it said that we "see atoms" in STM, and why should the appearance of the "atoms" depend on the tunneling voltage that is applied? The reason is that the atomic structure of a crystal surface and its electronic surface-DOS are very closely related: In the bulk of the crystal, the motion and spatial distribution of the electrons are described by Bloch-states. The amplitude of these Bloch-wavefunctions is modulated with the same periodicity as that of the atomic lattice [30 (p. 194, 195)]. This should hardly be surprising as the Bloch-states are the solutions to a Schrödinger equation of which the potential-term is determined by the atomic lattice.

The surface of a crystal is build up of a two dimensional *surface lattice* of atoms. As a consequence, the spatial distribution of the electrons at and near the surface is described by similar Bloch-states. However, in this case the electronic states are solutions to a Schrödinger equation of which the potential-term is defined by the first few crystal-planes at the surface of the crystal. Depending on their localization in the direction perpendicular to the surface, such near-surface states are known as (terminated) bulk states, surface states, or surface resonances. Surface states can be divided further into dangling bond states and back-bond states [4,31]. The sum of these states makes up the surface-DOS. As the surface-DOS consists of the solutions to a Schrödinger equation of which the potential-term is determined by the atomic lattice near the surface, the surface-DOS must reflect the periodicity of the atomic surface lattice. This is why we "see atoms" in STM.

The spatial distribution of the solutions to a given Schrödinger equation in general depends on the energy associated with that solution. We can see that from the difference in spatial distribution between the cosine wavefunction and the sine wavefunction, which describe the two energetically lowest states of a square potential well. For the electronic states that make up the surface-DOS, this applies as well. That is why the spatial distribution of the surface-DOS varies with the electron-energy [3,4,7]. When we apply a different voltage to the tunneling junction formed between our tip and sample, electronic states with a different energy and a possibly different spatial distribution become involved in the tunneling process (see sections 1.2 and 1.3). This is why the appearance of the "atoms" in STM-images can change as a function of applied bias voltage.

Voltage-dependent changes in the morphology of atomically resolved STM-images have been reported before [3,4,5,6]. Of particular importance to this thesis is the work performed by Ebert *et al.* [3] and Engels *et al.* [4], who report voltage-dependent changes in the atomic morphology of several III-V semiconductor {110}-surfaces.

These authors also show the relation between the voltage-dependent changes and the local surface-DOS of these surfaces. The {110}-surfaces of GaAs, InP and GaP have several surface states. Four of these states are located on either side of the bulk band gap of the semiconductor and are the only surface states relevant for STM [3,4,7]. The states are designated as A5, A4, C3, and C4. The voltage-dependent changes in the atomic morphology of GaAs {110}, InP {110} and GaP {110} are caused by these surface states contributing in varying relative amounts to the total tunneling current.

When imaging a semiconducting sample in STM using a metal tip, the electrostatic field between the tip and sample penetrates into the semiconducting sample, thereby shifting the energetic location of the surface states relative to the sample Fermi level (see section 1.9 and chapter 4). The effect is known as Tip-Induced Band Bending (TIBB). From I(V) spectroscopy it is evident that TIBB has a profound influence on the tunneling process between a metal tip and a semiconducting sample [8]. It is also known that the amount of TIBB, or local changes in the amount of TIBB, can influence the atomic morphology of a given STM-image by changing the contribution to the total tunneling current of one surface state relative to the other surface states [9]. In order to understand voltage-dependent effects in STM-images of semiconducting surfaces, the effects of TIBB have to be taken into account. In refs. 3 and 4, however, the effects of TIBB are only considered qualitatively.

In chapter 4 of this thesis, voltage-dependent changes in the atomic morphology of GaAs {110} are compared to the results of a one-dimensional model which calculates the amount of TIBB. The purpose of the model is to provide a general description of TIBB. It is very helpful in showing for which circumstances the amount of TIBB becomes strongly dependent on the applied bias voltage. A main result shown in chapter 4 is that certain voltage regions exist for which none of the four relevant surface states (A5, A4, C3, C4) can contribute to the tunneling current. For these voltages, tunneling occurs between the tip and bulk states of the sample through a depletion zone at the semiconductor surface. In spite of that atomic, surface-like corrugation is observed under these circumstances. The effect is observed for both p-type GaAs and n-type GaAs. In chapter 4, several possible explanations for this effect are discussed. In any case, the way in which atomic resolution on semiconductor surfaces is usually understood, cannot be regarded as complete.

In chapter 5, we present an unusual image-form of GaAs-{110} which we occasionally observe when imaging the surface at small, positive sample voltage. We assume that the image-mode involves a tip-sample distance which is significantly smaller than usual: When the bias voltage in a given STM-experiment is varied while the set-point for the tunneling current is kept constant, the tip-sample distance will vary as a function of bias voltage (see figure 4.8 b,e). For normal imaging conditions, we expect that the tip-sample distance is about 6 or 7 Ångstrøm (1 Å = 0.1 nm), as explained in section 1.7. When a small absolute value for the bias voltage is chosen, the tip will approach the sample surface more closely. When the tip comes within a few Ångstrøm of the sample surface, tip-sample interaction effects will start to determine the appearance of the resulting STM-image. Images of GaAs {110} obtained at significantly reduced tip-sample distance have been reported by Heinrich [10] and Jäger [11]. At the same time, tip-sample interaction effects between a GaAs {110}-surface and a Si tip have been described theoretically by Ke *et al* [12]. Their calculations predict that

as the tip apex atom approaches the GaAs {110} surface to within some 3 Å, a chemical bond is likely form between the tip apex and a Ga atom in the top row of the surface. In chapter 5, we present an unusual image-form of n-doped GaAs {110} imaged in the empty-states tunneling mode. The morphology of this image clearly shows the top zig-zag rows of the surface, while it also shows traces of the bottom zig-zag rows that lie in between. The image thereby closely resembles the atomic lattice of the surface as it is shown by the ball-and-stick drawings in many textbooks. We attribute the occurrence of this image-form to the formation of a chemical bond between the tip and sample as described by Ke *et al.* [12].

As is shown in chapter 6, the voltage-dependent changes in the atomic morphology of the STM-images of GaAs-{110} are also observed for $Al_xGa_{(1-x)}As$-{110}, and for the {110}-surface of a crystal consisting of a GaAs/$Al_xGa_{(1-x)}As$ superlattice. However, since $Al_xGa_{(1-x)}As$ is a heterogeneous material, many other effects are seen as well [13]. The essence of a series of voltage-dependent images is that it combines spectroscopic information with atomic lateral resolution. As a result, much can be learned about the electronic structure of the sample surface from a series of voltage-dependent images.

One very important result shown in chapter 6 is based on two STM-images of the same patch of AlGaAs-surface obtained at positive and negative bias voltage, respectively: The shapes and positions of the alloy-related minima are voltage-dependent. The effect can be understood from the fact that a given surface atom in an AlGaAs-crystal can have many different bonding configurations: It can have only Ga atoms as next-nearest neighbors, it can have one other Al atom occupying a next-nearest neighbor site, and so on. A common "rule of thumb" in the interpretation of STM-images of AlGaAs is that the dark portions of the image represent areas with a high local content of Al. The dissimilarity of the empty states and filled states images of AlGaAs casts doubt over the validity of this assumption. Another result shown in chapter 6 is that the images of a GaAs/AlGaAs superlattice obtained at intermediate positive sample voltage ($+0.59\ V < V < +0.71\ V$) show an apparent broadening of the GaAs-layers in the superlattice. For these voltages, we expect to be sensitive to the confined electron-levels that are present in the GaAs-layers of the superlattice. Since the spatial distribution of these levels extends into the AlGaAs barriers, we think that the observed broadening of the GaAs-layers reflects the spatial distribution of the confined electron-level in the GaAs quantum-wells of the superlattice.

The spatial distribution of dopants in δ-doped layers

The last chapter deals with the spatial distribution of Si dopants in δ-doped layers in GaAs. It has been shown by several authors that considerable redistribution of dopants in a δ-doped layer can occur, both as the dopants are adsorbed onto the growth surface prior to incorporation [14], as well as during the growth of the cap layer that covers the δ-doped layer. A major factor that determines the final distribution of dopants in a δ-doped layer is Coulomb-repulsion which occurs between dopants when the screened

Coulomb-potentials associated with these dopants overlap (see figure 7.9). As a consequence, a maximum local concentration of dopants in GaAs exists [15]. For the same reason it is also suspected that a minimum distance between any two given dopant atoms in a δ-doped layer layer exists [16]. Such a minimum distance between dopants is expected to enhance the mobility of electrons in the potential well formed by the δ-doped layer [17,18,19]. For these reasons, the spatial distribution of dopants within a δ-doped layer becomes a scientifically interesting topic.

Our own images of Si δ-doped layers in GaAs indicate that there is indeed an apparent minimum distance of about 2 nm between any two given dopants within the δ-layer. However, the observed spatial distribution of the dopants can also be explained from the fact that a dopant appears as a fairly large feature in STM. When two dopant atoms lie close enough to each other for their screened Coulomb potential-fields to overlap, it becomes difficult to observe the dopant atoms separately, as is shown in figure 7.7 of this thesis. It is thus possible that closely separated dopant-pairs are not clearly resolved in the STM-image and are instead interpreted as one single dopant. This may cause an artificial minimum distance between dopants to appear in the STM-images. Since the apparent size of a dopant in STM depends on the spatial extent of the screened Coulomb potential [39], such an artificial minimum distance between two dopants would be related to the spatial extent of the screened Coulomb-potential associated with a dopant as well (see figures 7.7, 7.8 and 7.9).

The redistribution of impurities during the epitaxial growth of the sample and the apparent feature-size of a dopant in STM are both related to the spatial extent of the screened Coulomb potential associated with a dopant embedded in the semiconductor. This leads to a problematic situation: The real minimum distance between dopants caused by redistribution of dopants during the epitaxial growth of the crystal is expected to have about the same value as the minimum distance between dopants that might appear artificially due to the fact that closely separated dopants are possibly not resolved in STM. Therefore, we cannot decide from the value of the observed minimum distance between the dopants whether it is real or artificial. The last part of chapter 7 discusses ways in which the STM-measurement might be adapted to overcome this problem.

The experimental setup and methods

The first part of this project has been spent on the assembly of the experimental setup and on getting the methods for tip- and sample preparation right. These are the topics of chapters 2 and 3.

Cross-sectional STM on III-V semiconductor (110)-surfaces in UHV has been pioneered by Salemink and Albrektsen *et al.* [32]. They used the technique to study interfaces between layers of different materials (mainly GaAs/AlGaAs) which occur in epitaxially grown heterostructures [32,33,34,35]. Salemink *et al.* were also the first to apply the technique to study alloy-fluctuations in the ternary compound semiconductor AlGaAs, and to image electrically active dopants that lie inside or just beneath the

surface of the sample crystal [36,37,38]. The work presented in these papers quite clearly demonstrates that the technique of Cross-Sectional STM can be used very effectively to analize (epitaxially grown) semiconductor devices and heterostructures.

Preparation of sample surfaces by cleavage sounds deceptively simple: You make your sample, bring it into the vacuum, push something against it, and it breaks. However, one of the major issues in the field of cross-sectional STM on semiconductor surfaces is, and has been for some time, how to cleave the sample in such a way that the density of (mono-atomic) steps on the surface is minimized [20,21,22]. Our experimental setup and method of sample preparation are described in chapter 2. The chapter ends with a discussion on cleavage, which we hope will make a meaningful contribution to the ongoing effort to produce smooth sample surfaces by cleavage in a controlled and reproducible way.

In high-resolution STM, the ability to prepare high-quality tips is crucial. This project was no exception. We use electro-chemically etched tungsten (W) tips. These tips are then heated and self-sputtered by Ne^+-ions in the way that is described by Albrektsen *et al.* [23]. At a later stage, an Ar^+-ion gun was added for head-on sputtering of tips. It is has been shown that during the Ne^+ self-sputter process which we apply to our tips, a “head and neck” structure can form on the tip [24]. As the sputtering process continues, the head is at some point torn off by the electrostatic force present between the tip and the counterelectrode. In chapter 3 it is shown that occurrence of this “decapitation” process can be recognized from a change in the signal to noise ratio of the applied sputter voltage when the sputtering process is carried out in the constant current mode. This allows us to choose the moment to terminate the sputtering process appropriately, which is immediately after the decapitation of the tip has occurred. The last part of chapter 3 describes a theoretical model that we use to characterize STM-tips from field emission measurements.

REFERENCES

1: C.J. Chen: *Introduction to Scanning Tunneling Microscopy.* Oxford University Press, New York (1993).

2: G. Binnig, H. Rohrer, Ch. Gerber, E. Weibel: *7x7 reconstruction on Si (111) resolved in real space.* Phys. Rev. Lett, Vol. 50, pp. 120 – 123 (1983).

3: Ph. Ebert, B. Engels, P. Richard, K. Schroeder, S. Blügel, C. Domke, M. Heinrich, K. Urban: *Contribution of surface resonances to Scanning Tunneling Microscopy images: (110) surfaces of III-V semiconductors.* Phys. Rev. Lett, Vol. 77, No. 14, pp. 2997-3000 (1996).

4: B. Engels, P. Richard, K. Schroeder, S. Blügel, Ph. Ebert, K. Urban: *Comparison between ab initio theory and Scanning Tunneling Microscopy for (110)-surfaces of III-V semiconductors.* Phys. Rev. B, Vol. 58, No. 12, pp. 7799 – 7814 (1998).

5: J.F. Zheng, X. Liu, E.R. Weber, D.F. Ogletree, M. Salmeron: *Si donors (Si_{Ga}) observed by Scanning Tunneling Microscopy.* Journal of Vac. Sci. and Tech. B, Vol. , pp. 2104 – 2106 (1994).

6: J.A. Stroscio, R.M. Feenstra, A.P. Fein: *Local state density and long-range screening of adsorbed oxygen atoms on the GaAs (110) surface.* Phys. Rev. Lett, Vol. 58, No. 16, pp. 1668 – 1671 (1987).

7: J.R. Chelikowski, M.L. Cohen: *Self-consistent pseudopotential calculation for the relaxed (110) surface of GaAs.* Phys. Rev. B, Vol. 20, pp. 4150-4159 (1979).

8: R.M. Feenstra, J.A. Stroscio: *Tunneling Spectroscopy of the GaAs (110) surface.* JVST-B, Vol. 5, No. 4, page 923 (1987).

9: C.S. Jiang,T. Nakayama, M. Aono: *Tip-induced occupation of an unoccupied surface state in Scanning Tunneling Microscopy imaging of a GaAs (110) surface with Ag clusters.* Japn. Journal of Appl. Phys, Vol. 36, pp. L1336-L1339 (1997).

10: A.J. Heinrich, M. Wenderoth, M.A. Rosentreter, M.A. Schneider, R.G. Ulrich: *Scanning Tunneling Microscopy of the atomic structure of the GaAs (110) surface at reduced tip sample separation.* Appl. Phys. Lett, Vol. 70, No. 4, pp 449 – 451 (1996).

11: N.D. Jäger, X. Liu, J.F. Zheng, N Newman, D.F. Olgletree, E.R. Weber, M. Salmeron*: Scanning Tunneling Microscoy of the GaAs (110) surface at low bias*. 23rd International Conference on the Physics of Semiconductors (World Scientific, Berlin), pp. 847 – 850.

12: S.H. Ke, T. Uda, R. Perez, I. Stich, K. Terakura: *First-principles investigation on GaAs (110) surface: Implications for atomic force and scanning tunneling microscopies.* To be published in Phys. Rev. B, issue of oct. 15, 1999.

13: Our experiments on AlGaAs and on the GaAs/AlGaAs superlattice involve n-type material only.

14: L. Däweritz, K. Hagenstein, P. Schützendübe: *Self-organization during Si incorporation in MBE-grown vicinalGaAs (001) surfaces*. Journ. of Cryst. growth, Vol. 127, pp. 1051 – 1055 (1993).

15: E.F. Schubert, G.H. Gilmer, R.F. Kopf, H.S. Luftman: *Maximum concentration of impurities in semiconductors.* Phys. Rev. B, Vol. 46, No. 23, pp. 15078 – 15084 (1992).

16: M.B. Johnson, P.M. Koenraad, W.C. v.d. Vleuten, H.W.M. Salemink, J.H. Wolter: *Be delta-doped layers in GaAs imaged with atomic resolution using STM.* Phys. Rev. Lett, Vol. 75, No. 8, pp. 1606 – 1609 (1995).

17: A.F.J. Levi, S.L. Mc Call, P.M. Platzman: *Nonrandom doping and elastic scattering of carriers in semiconductors.* Appl. Phys. Lett, Vol. 54, No. 10, pp. 940 – 942 (1989)

18: R.L. Headrick, L.C. Feldman, B.E. Weir: *Ordered delta-doping,* in: Delta-doping of semiconductors, ed. by E.F. Schubert, Cambridge Univ. Press, Cambridge, pp. 461 - 484 (1996). The paper discusses ordered δ-doping in Si.

19: P.M. Koenraad: *Electron mobility in ddoped layers,* in: Delta-doping of semiconductors, ed. by E.F. Schubert, Cambridge Univ. Press, Cambridge, pp. 407 – 443 (1996).

20: O. Albrektsen: *Scanning Tunneling Microscopy and Spectroscopy on III-V Semiconductor compounds and their interfaces.* PhD-thesis by O. Albrektsen, Technical University of Denmark, page 71 (1990).

21: M.A. Rosentreter, M. Wenderoth, N.H. Theuerkrauf, A.J. Heinrich, M.A. Schneider, R.G. Ulbrich: *Non-equilibrium configurations of mono-atomic steps on cleaved GaAs (110) surfaces.* Phys. Rev. B, Vol. 56, No. 16, pp 10538 – 10543.

22: K. Sauthoff, M. Wenderoth, M.A. Rosentreter, K.J. Engel, T.C.G. Reusch, R.G. Ulbrich: *Non-linear dinamic instability in brittle fracture of GaAs.* Phys. Rev. B, Vol. 60, No. 7, pp. 4789 – 4795 (1999).

23: O. Albrektsen: *Reliable tip preparation for high-resolution STM.* Journ. of Vac. Sci and Technology B12 (6) Nov/Dec 1994 page 3187.

24: Christoph Schiller, Arie Koomans, Theo van Rooy, Christian Schönenberger, Herman Elswijk: *Decapitation of tungsten field emitter tips during sputter sharpening.* Surface Science Letters, 339 (1995) p. L925 – L930.

25: J. Bardeen: *Tunneling from a many-particle point of view.* Phys. Rev. Lett. Vol. 6, No. 12, page 57 – 59 (1961).

26: J. Tersoff and D.R. Hamann: *Theory and Application for the Scanning Tunneling Microscope.* Phys. Rev. Lett. Vol. 50, No 25, page 1998 – 2001 (1983).

27: J. Tersoff and D.R. Hamann: *Theory of the Scanning Tunneling Microscope.* Phys. Rev. B, Vol 31, No 2, page 805 – 813 (1985).

28: E.F. Schubert: *Doping in III-V Semiconductors,* chapter 8. Cambridge University Press, Cambridge (1993). This reference deals specifically with the redistribution of dopants during epitaxial growth. Similar effects can also occur for, for instance, Al atoms near a GaAs/AlGaAs interface.

29: D. Hull, D.J. Bacon: *Introduction to dislocations.* Pergamon Press, Oxford, third edition (1984). The 100 nm mentioned in this reference is an upper limit. Nevertheless, even when the sample thickness is in the order of only 10 or 20 nm, the electron beam still passes some 50 atomic layers.

30: H.P. Myers: *Introductory solid state physics.* Taylor and Francis, London (1990).

31: J.A. Appelbaum, D.R. Hamann: *Surface States and Surface Bonds of Si (111).* Phys. Rev. Lett, Vol. 31, No. 2, pp. 106 – 109 (1973).

32: O. Albrektsen, D.J. Ahrent, H.P. Meier, H.W.M. Salemink: *Tunneling microscopy and spectroscopy of molecular beam epitaxy grown GaAs-AlGaAs interfaces.* Appl. Phys. Lett, Vol. 57, Iss. 1, pp. 31 – 33 (1990).

33: M.B. Johnson, U. Maier, H.P. Meier, H.W.M. Salemink: *Atomic-scale view of AlGaAs/GaAs heterostructures with cross-sectional scanning tunneling microscopy.* Appl. Phys. Lett, Vol. 63, Iss. 9, pp. 1273 – 1275 (1993).

34: H.W.M. Salemink, O. Albrektsen: *Tunneling microscopy and spectroscopy on cross-sections of molecular beam epitaxy grown (Al)GaAs multilayers.* Journ. of Vac. Sci. and Tech. B, Vol. 9, Iss. 2, pp. 779 – 782 (1991).

35: O. Albrektsen, H.P. Meier, K.J. Arent, H.W.M. Salemink: *Terracing and step bunching in interfaces of molecular beam epitaxy grown (Al)GaAs multilayers.* Appl. Phys. Lett, Vol. 62, Iss. 17, pp. 2105 – 2107 (1993).

35: H.W.M. Salemink, O. Albrektsen: *Atomic scale survey of III-V epitaxial interfaces.* Journ. of Vac. Sci. and Tech. B, Vol. 10, Iss. 4, pp. 1799 – 1802 (1992).

36: H.W.M. Salemink, O. Albrektsen: *Atomic-scale composition fluctuations in III-V semiconductor alloys.* Phys. Rev. B, Vol. 47, No. 23, pp. 16044 – 16047 (1993).

37: M.B. Johnson, H.P. Meier, H.W.M. Salemink: *Dopant and carrier profiling in modulation-doped GaAs multilayers with cross-sectional scanning tunneling microscopy.* Appl. Phys. Lett, Vol. 63, Iss. 26, pp. 3636 – 3638 (1993).

38: M.B. Johnson, O. Albrektsen, R.M. Feenstra, H.W.M. Salemink: *Direct imaging of dopants in GaAs with cross-sectional scanning tunneling microscopy.* Appl. Phys. Lett, Vol. 63, Iss. 21, pp. 2923 – 2925 (1993).

39: J.F. Zheng, X. Liu, N. Newmann, E.R. Weber, D.F. Ogletree, M. Salmeron: *Scanning Tunneling Microscopy studies of Si donors (Si_{Ga}) in GaAs.* Phys. Rev. Lett, Vol. 72, No. 10, pp. 1490 – 1493 (1994).

CHAPTER 1: THEORY

1.1 Introduction

In this chapter, some key aspects of the theory behind atomically resolved STM on semiconductor surfaces are discussed. The treatment is mostly in qualitative terms. The interpretation of experimental results presented later in this thesis is also mostly qualitative, as some experimental parameters are not known in a typical STM-experiment (precise tip-sample distance, tip-state, etc).

First, a short outline of the Modified Bardeen Approach [4 (page 65)] is presented, on which the analytic expression for the tunneling current is based. Some properties of the tunneling current are evident from its analytic expression, which is shown in section 1.3. In that section we also establish the link between the tunneling matrix element and the amplitude of the sample wave function. For an s-like tip state, the tunneling matrix element is proportional to the absolute value of the sample wave function. This underlies the interpretation of atomically resolved STM-images of semiconducting surfaces. In the limit of small tip-sample voltage, this results in the Tersoff-Hamann theory [2,3].

We then discuss surface states in general and dangling bond states in particular, as well as the role these states play in atomically resolved STM on semiconductors. The role of the tip density of states (tip-DOS) in atomically resolved STM is well known [4 (p. 126), 11,12,13,14]. In Sect. 1.6, the role of non-s tip states is discussed, for which the theoretical interpretation of the tunneling current must be slightly modified. The p_z and d_z^2 –like states are particularly important as they enhance atomic corrugation. For tungsten tips ending in a single atom, it can be expected that a d_z^2 – like state dominates the tip-DOS [11,12].

When the tip and sample are at tunneling distance, there can be a significant tip-sample interaction. The main effects are modifications to, and energetic shifts of, the tip- and sample states, as well as a lowering of the potential barrier between the sample and the tip (see sections 1.7 and 1.8).

Finally, we will discuss the role of electro-static band bending. This effect is specific to STM on semiconductors and significantly changes the potential profile of the tunneling barrier and surface region of the sample. As chapter 4 will show, this effect can populate or de-populate states at the surface, which may influence the appearance of the atomically resolved lattice.

1.2 The tunnelling current

For the interpretation of STM-images, the following expression for the tunneling current is often used [4 (p. 69)]:

$$I \quad = \quad \frac{4\pi e}{\hbar} \int_0^{eV} \rho_S(E_F - eV + \varepsilon)\rho_T(E_F + \varepsilon)|M|^2 d\varepsilon \qquad (1.1)$$

The tunneling matrix element M_{ST} is given by [4 (p. 68)]:

$$M_{ST} \quad = \quad -\frac{\hbar^2}{2m_e} \int_\Sigma \left[\psi_S^* \vec{\nabla} \psi_T - \psi_S \vec{\nabla} \psi_T^*\right] \bullet d\vec{S} \qquad (1.2)$$

In these two equations, $\rho_S(E)$ is the electron density of states (DOS) of the sample surface at energy E, and $\rho_T(E)$ is that of the tip. ψ_T and ψ_S are the electron wavefunctions of the tip and sample, respectively. E_F denotes the Fermi energy of the tip and sample. The product *eV* equals the bias voltage that is applied between the tip and sample (multiplied by the electron-charge), and m_e equals the effective mass of the tunneling electrons. The tunnel matrix element is evaluated over a separation surface Σ which lies between the tip and sample. Its precise location is not critical [4 (p. 76)].

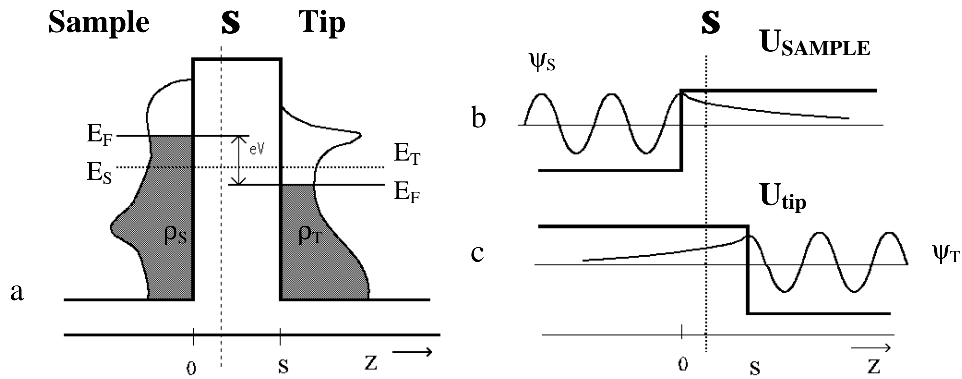

Fig. 1.1a: *Schematic view of a tunnel junction (see text).* ***b****: Potential* U_S *representing the sample, with the electron wavefunction* ψ_S*.* ***c****: The tip-potential* U_T *with associated wavefunction* ψ_T*. (see ref. 4, p23)*

Equations 1.1 and 1.2 have been derived following the *Modified Bardeen Approach*, of which a complete description is given in chapter 2 of ref. 4. The derivation is essentially an application of time-dependent perturbation theory. The sample is characterized by a potential U_S with associated wavefunctions ψ_S (figure 1.1 b). The wavefunctions satisfy the time-independent Schrödinger equation; $(T + U_S)\psi_S = E_S\psi_S$ where T is the kinetic energy operator. Likewise, the tip is characterized by a similar potential U_T and wavefunctions ψ_T (figure 1.1 c). The tip-potential now acts as a step-function perturbation which is absent for $t < 0$ and which equals U_T for $t > 0$. The wavefunction for the entire system $\Psi(\mathbf{r}, t)$ equals ψ_S for $t < 0$. At $t > 0$, $\Psi(\mathbf{r}, t)$ is the sum of ψ_S and various tip-states ψ_T, where the relative contributions of the various states ($c_V(t)$) to the total wavefunction are time-dependent. The total wave function $\Psi(t)$ satisfies the time-dependent Schrödinger equation for the entire system:

$$i\hbar \frac{\partial}{\partial t}\Psi(\vec{r},t) = (T + U_S + U_T)\Psi(\vec{r},t) \tag{1.3}$$

Notice that the sum of U_S and U_T forms a tunneling barrier. Fermi's Golden Rule can now be applied, which states that the transfer probability (w_{ST}) is given to first order by [4 (p. 67), 5 (p. 123)]:

$$w_{ST} = \frac{2\pi}{\hbar}|M_{ST}|^2\,\delta(E_S - E_T) \quad ; \quad M_{ST} = \int_{\Omega(tip)} \psi_T U_T \psi_S \; d\tau \tag{1.4}$$

The tunneling matrix element M_{ST} is evaluated over the volume of the tip since $U_T = 0$ everywhere else. The tunneling matrix element can be rewritten into the form in which it is presented in equation 1.2, as was first shown by Bardeen [1]. Equation 1.4 shows that electrons can only tunnel between two states if they have the same energy. This property is reflected in the arguments of $\rho_S(E)$ and $\rho_T(E)$ of equation 1.1 (see also figure 1.1a). Equation 1 itself is obtained after integration of w_{ST} over all possible initial and final states and taking the low temperature limit.

1.3 Some properties of the tunneling current

According to the Tersoff-Hamann theory, STM-images show the local density of states (LDOS) of the sample surface [2,3]. This result was derived under the condition that the relevant tip-state is an s-wave, and under the condition of small bias voltage. The latter is often the case for metals but need not be the case when imaging semiconductors. When the tip-state is (dominated by) an s-wave, it can be shown that the tunneling matrix element equals [2, 4 (p. 83)]:

$$M_{ST} = \frac{2\pi C\hbar}{\kappa m_e}\psi_S(\vec{r}_0) \qquad (1.5)$$

The amplitude of the sample wave function $|\psi|^2$ is evaluated at r_0 , the centre of the apex atom of the tip. C is a normalization constant, and $\kappa = (2m_e\phi)^{1/2}/\hbar$. For $|M|^2$ proportional to $|\psi_S(r_0)|^2$, it readily follows that the integrant in eq. 1 is proportional to the LDOS of the sample surface. For small bias voltage, the total tunneling current becomes proportional to $\rho_S(E_F)\rho_T(E_F)$, the DOS of the sample and tip at the (almost common) Fermi level. For larger bias voltage, provided that $|M|^2$ remains constant over the energy-range involved, equation 1 shows that the tunneling current becomes a convolution of the tip- and sample DOS. Combined with eq. 5, this yields an expression which represents the qualitative interpretation of topographic STM-data generally used:

$$I \sim \int_0^{eV} \rho_S(E_F - eV + \varepsilon)\rho_T(E_F + \varepsilon)\,|\psi_S(\vec{r}_0)|^2\,d\varepsilon \qquad (1.6)$$

If the tip-state is predomenantly p- or d-like, the tunnel matrix element is no longer proportional to $|\psi_S(r_0)|^2$. Rather, it becomes proportional to one of the spatial derivatives of $\psi_S(r_0)$ for p_x , p_y or p_z states, or to second derivatives of $\psi_S(r_0)$ for d-like states [4 (p. 83)]. This can have several effects on (atomically resolved) images, including an enhancement of atomic corrugation or an inversion of contrast [4 (p. 126, p. 138)]. The likelyhood of occurrence and consequenses of a non-s tip state will be discussed later in section 1.6.

One of the best-known features of tunneling is the exponential dependence of the tunneling current on the tip-sample separation. This dependence follows from equation 1.6, as it is a direct consequence of the proportionality of the tunneling current to $|\psi_S(r_0)|^2$. The sample wave functions decay exponentially as they extend into the vacuum barrier, behaving asymptotically like exp[-(2 m_e ΔE)$^{1/2}$ / $\hbar$ * z] (see figure

1.1), with ΔE equal to the energy difference between the sample state and the top of the tunneling barrier. The factor $|\psi_S(r_0)|^2$ is therefore proportional to $\exp[-2 (2 m_e \Delta E)^{1/2} / \hbar * |r_0|]$.

An other property is shown in figure 1.2: The DOS of a given sample surface can be made up of a number of different surface states (see figure 4.1). Each of those states has a wave-function $\psi_S(r)$, a (mean) energy and a density of states $\rho_S^i(E)$ associated with it. Also, the tunneling matrix element for each of the states will generally be different, as not all states extend equally far into the vacuum [6,8]. The total tunneling current then equals the sum of the contributions of the individual states.

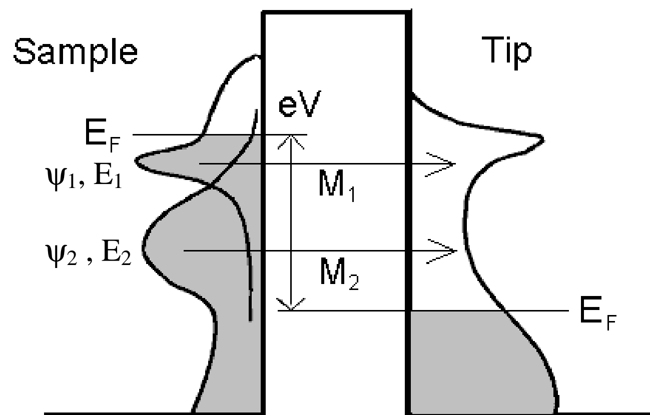

Fig. 1.2: *Tunneling current from more than one sample state.*

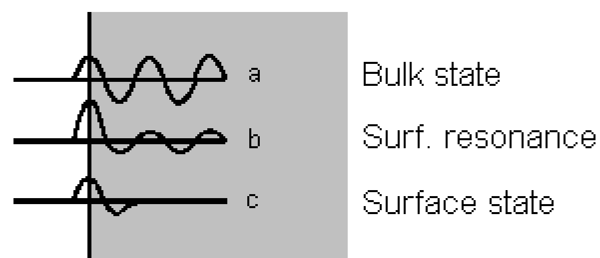

Fig. 1.3: *Three types of wavefunctions at surfaces (after ref 30, p. 19). Further details in section 1.4*

1.4 Atomically resolved STM-images

The ability to resolve the atomic lattice, for which STM has become famous, is due to its sensitivity to the *local* density of states. The LDOS of a crystalline surface reflects the periodicity of the underlying surface lattice, which results in an STM-image that contains a corrugation with the same periodicity as the surface lattice being imaged. This is the "atomically resolved" image.

The LDOS of a crystalline surface can be made up of three kinds of states: Bulk states, surface states and surface resonances (figure 1.3). The bulk states are Bloch waves terminated at the surface. They are periodic in the bulk of the crystal and become evanescent in the vacuum. The surface states are evanescent both in the bulk of the crystal and in the vacuum, and exist only near the surface of the crystal. Surface resonances are formed when a surface state and a bulk state combine, resulting in a state which is periodic in the bulk of the crystal, which decays exponentially in the vacuum, and which has an increased amplitude near the surface [30, 4 (p. 91)].

For an unreconstructed surface (*i.e.* the surface of a truncated bulk crystal) the surface states can be expected to lie energetically within the bulk band gap, as was shown for the first time by Tamm [4 (p. 99), 9] for a truncated Krönig-Penney potential. When a realistic three-dimensional (3-D) potential is concidered, surface states similar to the so-called "Tamm-states" are obtained, as was shown by Appelbaum and Hamann [6,7,10] for the {111}-surface of silicon. The unreconstructed configuration of a surface is often energetically unfavourable, so in many crystal surfaces, (some of) the atoms shift in position to reduce the free energy of the surface. The reconstructed surface can have a significantly different LDOS with respect to the unreconstructed surface. An example of this effect is the {110}-surface of GaAs [8] and other zincblende III-V semiconductors, or the {111}-surface of Si [4].

In ref. 6, three bands of surface states were found for the Si-{111} surface: One is located energetically inside the bulk band gap and had spatial lobes above and below each surface atom. The lobes are localized, with the top lobe extending only 1 Å in the directions parallel to the surface. In the reconstructed case, its integrated electron density is 0.7, indicating that the state is only partially filled. Unity corresponds to the state being fully occupied, in which case it contains two electrons (spin degeneracy). The state is identified as a "dangling bond" state. A second band of states was found to lie energetically within the bulk valence band, and is localized on the lines connecting each surface atom to its three nearest neighbors which lie slightly deeper inside the crystal. The integrated electron density for this band is 0.9. This is a back bond state. The third state which was found lies deep within the valence band (at –11 eV with respect to the top of the valence band) and is therefore unavailable to the tunneling process

There is an alternative way to consider dangling bond states: Many covalently bonded crystals form either the diamond lattice (Si, Ge, C) or the zinc-blende lattice (GaAs, InP, etc). The bonds in crystals of these structures are formed by sp^3 hybridized states which extend from each atom to its four nearest neighbors. Each such state contains two electrons. When such a crystal is separated into two parts, all bonds along one crystal-plane are broken. On the newly created surfaces the severed bonds form

localized states, each located at or above a surface atom and each containing one electron instead of two.

In atomically resolved STM on semiconductors, the dangling bond states are often the most important surface states, as they are localized and (usually) extend furthest into the vacuum. In ref. 33 it is shown for InP-{110} that the exponential decay-length of the dangling bond states is about 3.5 Å. According to equation 6, STM is sensitive to the local amplitude of the sample wave function ψ_S. When the tip is scanned across the surface at constant tip-sample separation, the two-dimensional array of dangling bond states present on the surface will cause the tunneling current to vary as a function of the position of the tip. As a result, the “current image”, which is a plot of I(x,y) (the z-axis is perpendicular to the sample surface, the x and y axes are both parallel to the surface), will be corrugated with each local maximum coinciding with a dangling bond. This mode of imaging is referred to as “constant height imaging”.

In practice, a second mode of operation, the “constant current mode”, is used most often (see figure 1.4). It makes use of the exponential dependence of the tunneling current on the tip-sample separation. Provided that certain experimental conditions are met, (low-noise electronics, a scanner and sample stage designed to be small and rigid and the absence of external vibrations) the tip can be held in position within a margin of less than 5 pm ($5 * 10^{-12}$ m). The STM can be operated such that the (feedback) electronics will extend or retract the tip in order to maintain the tunneling current at some preset value. The tip is moved by piezo-actuators (see chapter 2). The tip will then trace an oscillating path while scanning, such that the tunneling current is kept constant (figure 1.4). The corrugation amplitude (Δz), which is the distance over which the tip must be moved up and down in order to keep the tunneling current constant, is measured from the signal applied to the z-piezo actuator. In this mode, the STM-image is a plot of z(x,y).

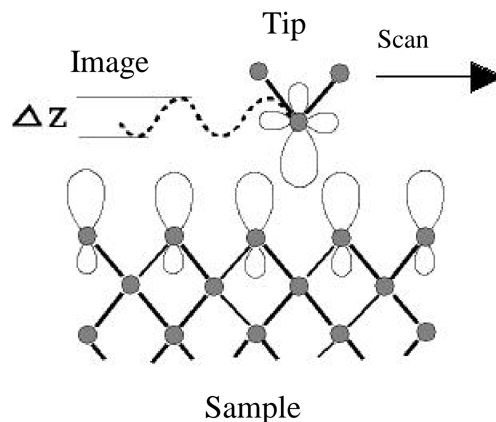

Fig. 1.4: *Constant current image mode. (See Ref. 4, p34)*

The response of the feed back loop present in any STM-system can be varied in order to optimize the image [1 (p. 1)]: It can be set to a slow response needed to keep the tip from crashing into the sample surface or drifting out of tunneling range, or to a fast one used to follow the surface (or rather: the contours of the surface-DOS) very accurately. When the feedback loop is set to a response which is too fast, it begins to oscillate. For constant current images, one would expect the feedback loop to be set just below the value at which oscillation sets in. In practice, the “best” z(x,y) images in constant current mode are obtained at an intermediate setting, for which some corrugation in the I(x,y) image is still visible [16].

1.5 Lateral motion of electrons and sample density of states

Although the surface states can be highly localized, as is the case for dangling bond states, the electrons that occupy them remain mobile. Their motion is, however, confined to the surface region. The lateral motion of the electrons can be described by two-dimensional Bloch-waves matching the two-dimensional lattice formed by the atoms in the surface region. For many surfaces, dispersion curves for the lateral motion of electrons occupying surface states have been determined [8, 4 (p. 106), 15 (p. 158, p. 176)]. The dispersion relations calculated for the relaxed GaAs {110} and AlAs (110) surfaces are shown as examples in chapter 6.

Figure 1.5 shows the calculated density of states (DOS) of InP {110} as an example. In general, the total DOS will be the sum of the individual densities of states of the different states present at the surface. The energy-dependence of each of those individual densities of states depends on the number of degrees of freedom available to the electrons, and on the dispersion curve associated with the state. In a first approximation, the DOS for the bulk valence band and bulk conduction band can be taken as $\rho_S(E) \sim |E|^{1/2}$ and $\rho_S(E) \sim |E-E_g|^{1/2}$, respectively (E measured is with respect to the Valance Band Maximum). Under the circumstances common for STM on semiconductors, only the band edges participate in the tunneling process. Near the band edges, the dispersion curves can be assumed parabolic. Since the bulk states allow the electrons to travel in all three directions, the DOS becomes proportional to $|E|^{1/2}$.

A similar argument does not apply to surface states. Unlike the dispersion curves for bulk bands, the surface-state dispersion curves do not extend over a very wide energy-range. Consequently, the entire energy-range of a surface-state dispersion curve can be accessible to tunneling using normal bias voltages [25], and the surface dispersion curve can therefore not be assumed to be parabolic. The different surface states on the GaAs {110}- surface manifest themselves as a series of peaks in the total surface DOS (see figure 1.5).

For the purposes of this thesis, two things are important to keep in mind: The first is that the total surface-DOS is composed of the contributions of the different electronic states that lie inside the relevant energy-window. The other is that the electronic states can have a lateral momentum, *i.e.* have a $k_{//}$-vector that lies at a certain

point in the surface-Brillouin zone (surface BZ). The latter will manifest itself as a periodicity of the state in a certain crystallographic direction. This underlies the voltage-dependent changes in atomic corrugation reported in chapters 4 and 6.

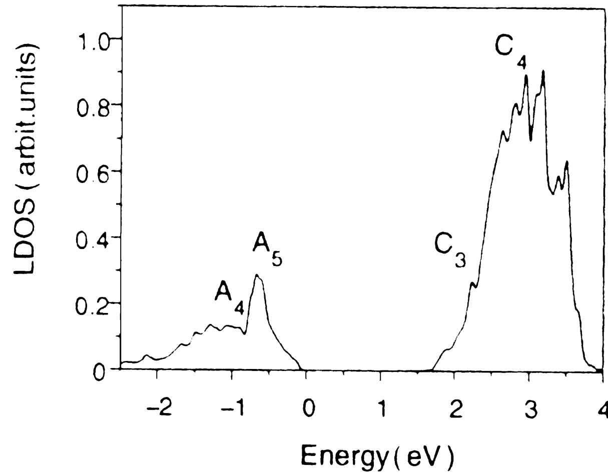

Fig. 1.5: *Calculated surface-DOS of the relaxed (110)-surface of InP. From Ref. 32. InP (110), GaAs (110) and AlAs (110) have four surface states, designated as Anion-4, Anion-5, Cation-3, and Cation-4. See also chapters 4 and 6.*

1.6 Tunneling for a tungsten tip: non-s tip states

As explained in Section 1.3, equations 1.5 and 1.6 are only valid if the tip-DOS is dominated by an s-like state. This is not always the case. In fact, Ohnishi and Tsukada showed that W_4 (tetrahedron) and W_5 (four-sided pyramid) clusters posess a molecular orbital at the apex atom which has a strong d_z^2 – component [11,12]. These levels are the Highest Occupied Molecular Orbital (HOMO) for the W_4 cluster and the molecular orbital just beneath the HOMO for the W_5- cluster. The result suggests that a real W-tip, ending in a single W-atom, will have a d_z^2-like electron state at its apex atom, located energetically just below the Fermi level of the tip [31]. The level is expected to have a band-width in the order of 1 eV [13]. Doyen *et. al.* showed that such a d-type state can also exist *at* the Fermi level, rather than just below it [14]. This means that for W-tips with a single atom at the apex, the tip-DOS near the Fermi level is dominated by a d-like state protruding from the apex. If the energy-band associated with the tip state crosses the Fermi level of the tip, the d-like state is important for both empty and filled states imaging.

The effect of a d_{z^2}-like tip-state is that (a component of) the tunneling matrix becomes proportional to the second derivative of the sample wave function with respect to z. The apparent corrugation of the surface being imaged can then be enhanced by more than a factor 10 [4 (p. 32, p. 131)]. The enhancement depends on the (average) lateral k-value of the state being imaged [4 (p. 126)]. The presence of other tip-states can lead to a lateral shift in apparent corrugation (p_x, p_y), or it can lead to an inversion of contrast (d_{xz}, d_{yz}, $d_{x^2-y^2}$,d_{zy}) [4].

In practice, it is frequently observed that the atomically resolved image suddenly changes (see ref. 4, figure 14.9 for an example). Chapter three will show that with the current techniques, the shape of the tip can be controlled down to a scale of 10 nm. Its shape at the atomic scale cannot be controlled, nor is it precisely known. During an STM-experiment which typically lasts up to six hours, the tip-DOS often goes through several spontaneous changes. The tip-DOS can also be changed on purpose by applying high voltage pulses (5 – 8 V for a few seconds at a time) to the tip while it is in tunneling condition over the sample surface. This is sometimes done with the purpose of changing the tip-DOS to a configuration that yields high resolution. This can lead to difficulties in interpreting atomically resolved images, as the influence of the tip on a given image is not *a priori* known. In the work presented in this thesis, the {110}-surfaces of GaAs and InP have been imaged many times, involving many different tips. We can thus make a distinction between "normal" and "anomalous" images based on our experience, or by comparison of our own results with existing literature. Besides, tip-changes always occur instantaneously, so any gradual change in appearance cannot be caused by a change in tip-DOS.

States with a large lobe extending along the axis of the tip (p_z or d_{z^2}) will enhance atomic corrugation [4 (p. 83, p. 126, p. 131)]. Moreover, the atomic image is not shifted laterally by these states, so the interpretation expressed by equation 1.6 remains valid in a qualitative sense: The image shows where the amplitude of the sample wave function is large, and where it is small. For many purposes (see chapters 4 and 6), that is sufficient. The p_z and d_{z^2} states are therefore very desirable for high-resolution STM.

Tip state	***Matrix element***
s	$\sim \psi_S (r_0)$
p_z	$\sim \partial/\partial z\, [\psi_S (r_0)]$
p_x, p_y	$\sim \partial/\partial x\, [\psi_S (r_0)]$, $\sim \partial/\partial y\, [\psi_S (r_0)]$
$d[z^2-(^1/_3)r]$	$\sim [\partial^2/\partial z^2\, [\psi_S (r_0)] - {}^1/_3\, \kappa^2\, \psi_S (r_0)]$

Table 1.1: *Tunneling matrix elements associated with different possible tip-states (taken from Ref. 4, page 83).*

1.7 Tip – sample interaction

When the tip and sample are far apart, they can be thought of as non-interacting. The tip states (ψ_T) and sample states (ψ_S) are then described by the wave-functions belonging to the *free* sample and tip. When the tip and sample are brought into distances typical for tunneling, they *do* have an interaction. As a consequence, the tip and sample exert an attractive force to each other, the tip- and sample states are modified and the potential barrier between the tip and sample gradually collapses as the two electrodes approach each other. The following discussion is based mainly on the theoretical treatment presented by Ciraci [18] and references therein [15, 20, 21]. Although Ciraci's treatment is applied to metal or graphite samples and metal tips, we will use it to provide a qualitative description of the interaction that takes place between a semiconductor sample and metal tip.

Three regimes of interaction can be identified [18 (p. 179, p. 182)]: For a tip-sample distance of roughly 10 Å, only the van der Waals interaction is important. For distances ranging from 3 - 7 Å (measured from the nucleus of the apex atom to that of the sample facing it) the tip- and sample wave functions begin to overlap. This leads to a short range, attractive force. At even shorter distance, when the separation between the apex atom and the nearest sample atom becomes comparable to the inter-atomic spacing *within* the tip- and sample material, the interaction becomes repulsive. This is the onset of mechanical contact. When at this point the (macroscopic) tip and sample are approached further (for example during a tip-crash), both electrodes will irreversibly deform.

In a tunneling experiment, the absolute tip-sample distance is not known. However, based on the results reported by Heinrich *et al.* [27,29] it is estimated to be about 6 – 7 Å. The experiments of Heinrich *et al.* were carried out on p-doped GaAs (Zn: 4 – 7 * 10^{19} cm^{-3}), using V_{SAMPLE} = -2.0 V and I = 300 pA. Although we generally use smaller tunneling currents (~ 100 pA) and sample material with a lower doping concentration (10^{18} cm^{-3}), it is reasonable to assume that in our experiments, the absolute tip-sample distance is usually similar to the tip-sample distances found by Heinrich *et al.* At a tip-sample distance of 6 – 7 Å, both the short-range interaction and the van der Waals interaction may have a role in the tip-sample interaction.

The short-range attractive interaction is a quantum-mechanical effect that occurs as a result of the wave functions of the tip and sample overlapping. What happens is that the electron state(s) extending from the outermost tip atom(s) combine with sample states to form bonding and antibonding combinations (see also chapter 4). In the simplest picture, the interaction takes place between one tip state and one sample state. A suitable model system for that situation is the hydrogen molecular ion (H_2^+) [4 (p. 177)]. The tip- and sample state can form two combinations, ($\chi_\nu + \psi_\mu$) and ($\chi_\nu - \psi_\mu$) with energies (E + M) and (E – M), respectively. E is the (common) energy of the two states (see eq. 4) and M is proportional to the tunneling matrix element (see equation 1.2). Both E and M are negative as they are measured with respect to the vacuum level, so the symmetric combination ($\chi_\nu + \psi_\mu$), *i.e.* the bonding state, has the lowest energy (E + M).

The tunneling process always involves one filled and one empty state, so the combined system of the tip- and sample state will always contain one electron. This

electron will occupy the state with lowest energy (the bonding state). As a concequence, the total energy of the combined system is reduced by an amount M when the tip and sample are brought at tunneling distance. The attractive force is then given by the derivative of M with respect to the tunneling distance:

$$F = -\frac{\partial}{\partial z}|M| \quad , \qquad M = \frac{1}{2}\int \left(\boldsymbol{c}\vec{\nabla}\boldsymbol{y} - \boldsymbol{y}\,\vec{\nabla}\boldsymbol{c} \right) \bullet d\vec{S} \tag{1.7}$$

According to eq. 1.7, the attractive force depends on the tunneling matrix element, and thus on the tunneling conductivity. If a tip is scanned across the surface, it may be expected that there is a lateral variation in the attractive force between the tip and sample that is similar to the lateral variation in the tunneling current itself. Ciraci *et al.* showed that for an Aluminium tip and Al-(001) surface, the resonance force indeed varies depending on whether the tip faces a surface atom or a hollow site between the surface atoms [18 (p. 182), 19].

The van der Waals force is electro-static in nature [4 (p. 174)], and therefore, it has a much longer range than the quantum-mechanical interaction described in the previous paragraph. The longer range also causes the interaction to extend over a much larger portion of the tip and sample than is the case for the short range attractive interaction. As a result, the van der Waals interaction depends very sensitively on the shape of the tip. In the short range interaction, only the last few atoms in the immediate vicinity of the tunnel junction are important. The van der Waals force ranges from less than 0.01 nN for sharp, conical tips to more than 10 nN for tips with a hemispherical end (at a tip-sample distance of 5 Å) [18 (p. 84), 26].

An important question that remains to be addressed, is which of the two interactions -short range force due to overlap of wave functions or van der Waals force- dominates the tip-sample interaction during a typical STM experiment. In ref. 4, the van der Waals force of both a neutral hydrogen molecule (H_2) and a hydrogen molecular ion (H_2^+) are calculated as a function of proton-proton distance [4 (p. 176)]. At the same time, the short range interaction energy in the hydrogen molecular ion was calculated as well. According to the results, the van der Waals interaction dominates the force in the hydrogen molecular ion when the two protons are further than 8 Å apart. At 6 Å, the decrease in energy due to the van der Waals interaction is about half of the interaction energy of the short range interaction. The van der Waals interaction in the neutral hydrogen molecule was neglegible compared to the short range interaction for all distances shorter than 8 Å. In ref. 4 Chen concludes that, as in STM-experiments the atoms near the gap are nearly neutral, the van der Waals interaction found in the neutral hydrogen molecule is a good representation for the van der Waals interaction between an apex atom and the sample atom facing it [4 (p. 176)]. Consequently, the results indicate that when only the few atoms immediately around the tunneling junction are considered, the van der Waals interaction is neglegible compared to the short-range interaction when tip and sample (atoms) are at distances common for STM.

This is, however, only part of the problem. As already mentioned, the van der Waals interaction has a longer range and so, the number of atoms in the tip and sample participating in the interaction will be (far) greater than the number of atoms involved in the short range interaction, for which only the few atoms in the immediate vicinity of the tunneling junction are important. Therefore, while the van der Waals interaction *per atom* is small compared to the short range interaction per atom involved, the total van der Waals force may well be comparable to, or even exceed, the total short range force. An other effect is that the short range force acts on the apex of the tip, while the van der Waals force, because of the greater number of atoms involved, acts on the part of the tip *behind* the apex. If the van der Waals interaction is sufficiently strong, the apex atom(s) may have a repulsive interaction with the sample while the tip and sample as a whole are still attracted to each other [24].

As Chapter 3 will show, the tips we make have a typical apex radius of 10 nm, which is supported by a conical shank with an inner half-angle of about 15°. For a tip-sample distance of 7.5 Å, this would mean that for our tips, the van der Waals force is in the order of 1 nN, which is quite comparable to the short range interaction [18 (p. 184, p. 182), 4 (p. 176), 26].

1.8 Effects of the tip-sample interaction

One obvious consequence of the tip-sample interaction, is that the tip and sample will deform. We will ignore the possibility of an avalanche effect as described by Smith *et al.*[28] as the resulting contact seems incompatible with atomic resolution. In atomically resolved STM, the deformation will cause a difference between the measured corrugation amplitude and the actual amplitude of the corrugated path traced by the apex. This is caused by the fact that the tip-sample interaction depends on the lattice-site facing the apex atom [19]: As the tip is scanned across the surface, it will relax in- and outward as it passes the different lattice sites, even if the back of the tip were held at the same height above the sample. When operating the STM in constant current mode, the extensions and retractions of the tip apex due to relaxation are added to the excursions that are applied to the back of the tip by the feedback mechanism of the STM.

At small tip-sample distance, the most important consequence of the tip-sample interaction is the modification of tip- and sample states, and the appearance of Tip Induced Localized States (TILS) [24, 18 (p. 182)]. When the tip and sample approach each other, the wavefunctions of the tip and sample overlap and form bonding and antibonding combinations. This is accompanied by a change in spatial distribution of the states and by a shift in energetic location of the states. Both effects have been described in detail by Ciraci, Baratoff and Batra for an Al tip and graphite sample [24]. The same authors have also studied the change in spatial distribution of the states for an Aluminum tip-atom and Al-(111) surface [19]. It was shown that the sample wave function differs from the wave function of the free sample surface for a tip-sample distance of 4.2 Å or less. At 2.6 Å, the electron resolution resembles that of an atomic bond [19]. The shift in energy for the different states as a function of tip-sample distance, studied in ref. 24 (see also ref. 18, p. 194), showed that as the tip-sample

distance is varied from 4.0 Å down to 1.4 Å, some states shift over 1 or 2 eV in energy. As some states move up in energy whereas others move down, crossings between states may occur.

A related effect is that as the tip and sample approach each other, the potential barrier gradually decreases. Due to exchange and correlation effects, electrons localized within the tunneling junction experience a potential that is lower than the vacuum level, which is the height of the potential barrier when the two electrodes are far apart. The effect is reproduced in the theoretical calculations presented in refs. 19 and 24. The top of the potential barrier may actually sink below the Fermi level of the tip or sample, creating a channel in which electrons are *classically* allowed. This is the onset of mechanical contact.

The lowering of the potential barrier is caused by an exchange and correlation potential modifying the tunneling barrier. It is thus a many particle effect. The image potential, which is the classical formalism to treat an electron in the presence of many other free charges, often used to evaluate the lowering of the potential barrier [4 (p. 56)]. For the model considered in ref. 4 (a "jellium" surface), the classical image potential provides an adequate approximation for the exchange- and correlation potential experienced by an electron localized in the vacuum region near a metal surface [4 (p. 94)].

Summarizing, we expect an attractive interaction between the tip and sample, either due to the short range interaction or due to the van der Waals interaction. If the van der Waals interaction is strong, the part of the tip behind the apex might be attracted to the sample while the apex has a repulsive interaction with the sample. As a result of the tip-sample interaction, the electron-states are deformed and shift in energy, and the potential barrier between the tip and sample is lowered.

Although at the tip-sample distances commonly encountered in STM (7 – 10 Å according to figure 4.8, see also refs. 27 and 29) there is a non-zero force between tip and sample, the tip-sample interaction is usually not essential in the interpretation of atomically resolved STM-images. Most of the results shown in chapters 4,6 and 7 can be interpreted without explicitely considering the tip-sample interaction apart from tip-induced band bending, which is discussed in the next section. However, in some cases the tip-sample interaction becomes essential in the interpretation of the images, as is the case for some of the results shown in chapter 4. In chapter 5, where we present an unusual image-form of GaAs (110) which is thought to arise when a chemical bond forms between the tip and sample, the tip-sample interaction obviously becomes very important as well.

1.9 Tip-induced band bending

In addition to the interaction-effects described in the previous section, tip induced band bending (TIBB) occurs when a semiconducting surface is being approached by a (metal) tip. The electro-static field between the tip and sample penetrates into the semiconductor surface, which rearranges the free charge carriers near the surface. The result is that a net charge is present on the surface, which will locally raise or lower the valence and conduction band of the semiconductor (see figure 1.6). Below the surface of the semiconductor, the net charge screens the field induced by the tip, and the valence and conduction bands lie at their normal positions with respect to the Fermi level. The effect is sensitive to the doping concentration of the semiconducting material: When the doping concentration increases, the width of the space-charge layer decreases as the screening becomes more effective. In metals, which have a far higher concentration of free carriers than semiconductors, the space-charge layer becomes exceedingly narrow [17]. At the same time, the electric field must remain continuous across the metal-vacuum interface meaning that the potential gradient near the interface must remain finite. Consequently, no band bending can occur in the tip.

The amount of band bending occurring between a metal tip and semiconducting sample can be calculated numerically by using a one-dimensional model [22,23]. The calculation consists of solving the one-dimensional Poisson-equation under the boundary condition that at the semiconductor-metal interface, the electric field (*i.e.* the potential gradient) be continuous. There are three possible situations for band bending in the semiconductor region, in both p- and n-type material: Depletion, inversion and accumulation (see figure 1.6 a). In the case of depletion, the resulting potential profile is parabolic since the charge in the depletion layer is generated by ionized dopants, which are immobile and assumed to be uniformly distributed throughout the semiconductor. When accumulation occurs, all dopants near the surface are unionized, and the band bending is caused by majority charge carriers that have accumulated near the surface. The amount of band bending, in turn, influences the charge density profile near the surface, causing the charge density and surface band bending to influence each other. In the case of inversion, the potential-profile is determined by the charge from the ionized impurities as well as from the charge of the minority carriers accumulated at the surface.

Using the model described in chapter 4, we have calculated the amount of TIBB (ϕ) as a function of applied bias voltage for a fixed tip-sample distance (figure 1.6 b). The regions of depletion, accumulation and inversion manifest themselves in the slope of the data-points. In case of depletion, the depletion width can be calculated from $w_\phi = (2\varepsilon_0\varepsilon_r/(Ne^2)\ )^{1/2}$, where N is the doping concentration [22]. Even for small amounts of band bending, the depletion layer can extend several tens of nanometers (nm) into the semiconductor ($N = 10^{18}$ cm^{-3}, $\phi = 0.2$ eV, $w_\phi = 169$ Å; $N = 10^{18}$ cm^{-3}, $\phi = 0.5$ eV, $w_\phi = 267$ Å). When analysing spectroscopic data, TIBB must be taken into account in order to interprete the results correctly [18]. Also, due to accumulation or inversion, certain surface-states may become populated or emptied depending on the applied bias voltage. This influences the morphology of the atomically resolved lattice. The voltage-dependent changes of the atomically resolved (110)-surface of GaAs and $Al_xGa_{(1-x)}As$, and the influence of TIBB on these changes, will be discussed at length in chapters 4 and 6, respectively.

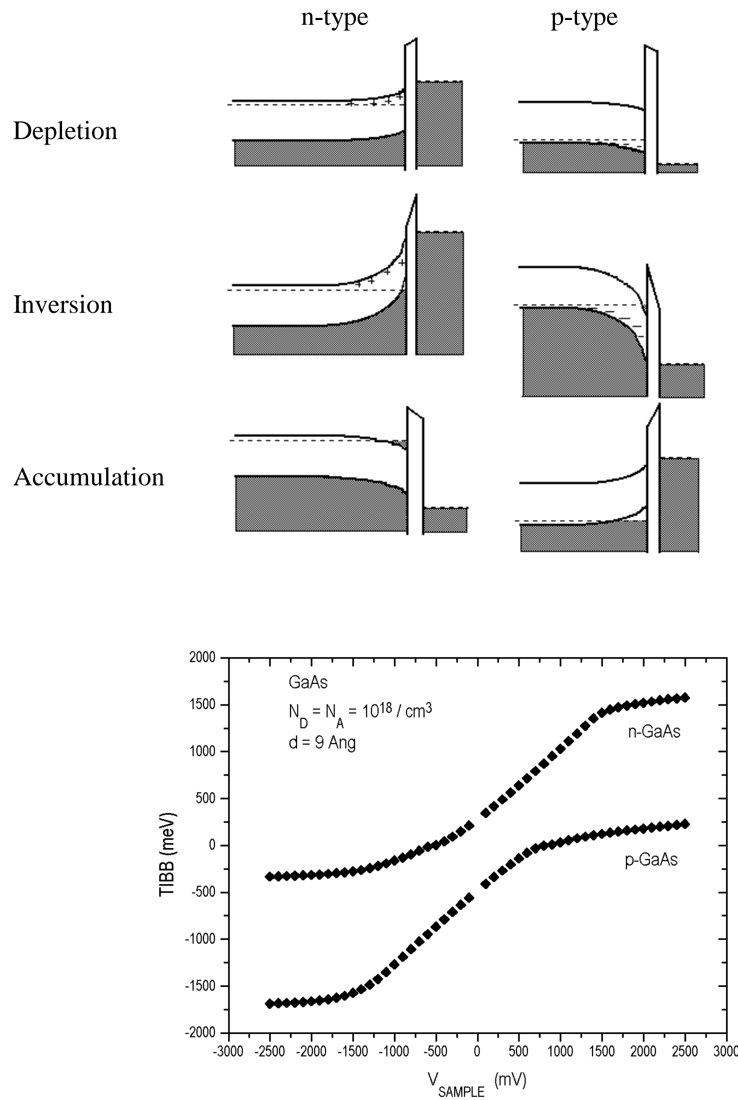

Fig. 1.6 a: *Tip-induced band bending.* **b:** *Tip-induced band bending (TIBB) as a function of sample voltage for n- and p-type GaAs (doped at 1 * $10^{18}/cm^3$). The quantity plotted equals the band bending at the semiconductor surface and is computed by numerical integration of the Poisson equation through the space charge region. The metal tip is biased at 0 V and is placed at 9 Å from the semiconductor surface. n-GaAs: depletion: -0.5 V < V < +1.5 V; inversion: V > +1.5 V; accumulation: V < -0.5 V. p-GaAs: depletion: -1.5 V < V < +0.75 V; inversion: V < -1.5 V; accumulation: V > +0.75 V. See also figure 4.2 b.*

1.10 Summary

The tunneling current is proportional to the convolution of the tip- and sample density of states. It is also assumed proportional to the local amplitude of the sample wavefunction(s) being probed, which causes the lateral variation in the tunneling current. When several states contribute to the total tunneling current, their contributions combine.

The surface-DOS of the sample is made up of different surface states and terminated bulk states. The different surface states manifest themselves as different peaks in the surface-DOS. The spatial distribution of the surface-DOS reflects the periodicity of the surface lattice, and as a consequence, STM images will reflect this periodicity as well. This is what makes atomically resolved STM possible.

For atomically sharp STM-tips, it is expected that the tip-DOS is dominated by a d_z-like state which protrudes from the apex. Although the proportionality to the sample wave function expressed in eq. 6 is only valid for s- like tip-states, it can still be used in a qualitative sense for p_z and d_z-like tip-states as well. Such states can significantly enhance atomic corrugation.

During tunneling, the tip and sample experience an attractive interaction, caused by the tip- and sample states combining into bonding and antibonding pairs. At distances typical for STM, the wave functions and the tip structure may be reversibly modified. The force between tip and sample varies as the tip faces different lattice-sites on the sample surface. Also, the top of the potential barrier may be lowered significantly.

Finally, the electro-static field between tip and sample causes band bending in the near-surface region of the sample when imaging semiconductors. Band bending can extend several tens of nm into the sample. At the surface, it causes the surface states to shift 1 eV or more in energy with respect to the sample Fermi level. The distortion of the bands can extend several tens of nm below the sample surface, depending on doping concentration.

At this point, we wish to introduce the term of “regular tunneling”. As is explained in section 1.3, atomically resolved images of semiconducting surfaces are usually thought to represent the local variation of the surface-DOS of the sample material, integrated over the energy-window between the tip Fermi level and the sample Fermi level. This view is represented mathematically by equations 1.5 and 1.6, and transforms into the Tersoff-Hamann theory in the limit of small bias voltage [2,3]. This interpretation, however, is only valid at larger tip-sample distances where the effects of the tip-sample interaction may be neglected. This interpretation implicitely also assumes an s-like tip-DOS, although it remains valid in a qualitative sense for a p_z- and $d[z^2-{}^1/_3r]$-like tip-state. “Regular tunneling” is tunneling under the conditions of finite voltage, neglegible tip-sample interaction (apart from tip-induced band bending) and a tunneling matrix-element that is proportional only to $\psi_S\ (r_0)$ or to spatial derivatives with respect to z of $\psi_S\ (r_0)$. Later in this thesis it will become apparent that many atomically resolved images of semiconductor surfaces can be explained within the framework of regular tunneling, although some experimental circumstances exist where other mechanisms for atomic corrugation have to be considered.

REFERENCES

1: J. Bardeen: *Tunneling from a many-particle point of view*. Phys. Rev. Lett. Vol. 6, No. 12, page 57 – 59 (1961).

2: J. Tersoff, D.R. Hamann: *Theory and Application for the Scanning Tunneling Microscope*. Phys. Rev. Lett. Vol. 50, No 25, page 1998 – 2001 (1983). For background to eq. 5, the reader is also referred to ref. 1, p. 83.

3: J. Tersoff, D.R. Hamann: *Theory of the Scanning Tunneling Microscope*. Phys. Rev. B, Vol 31, No 2, page 805 – 813 (1985).

4: C.J. Chen: *Introduction to Scanning Tunneling Microscopy.* Oxford University Press, New York, 1993.

5: A. Yariv: *Theory and Applications of Quantum Mechanics*. John Wiley and sons, New York, 1982.

6: J.A. Appelbaum, D.R. Hamann: *Surface states and surface bonds of Si (111).* Phys. Rev. Lett Vol. 31, No. 2, page 106 – 109 (1973)

7: J.A. Appelbaum, D.R. Hamann: *Surface Potential, Charge Density, and Ionization Potential for Si(111) – A self-consistent calculation.* Phys. Rev. Lett, Vol. 32, No. 5, page 225 – 228 (1973).

8: J.R. Chelikowski, M.L. Cohen: *Self-consistent pseudopotential calculation for the relaxed (110)-surface of Gallium Arsenide*. Phys. Rev. B, Vol. 20, No. 10, page 4150 – 4159 (1979).

9: I. Tamm: *Über eine Mögliche Art der Elektronenbindung und Kristalloberflächen.* Phys. Z. der Sowjetunion 1, page 733 – 746 (1932).

10: J.A. Appelbaum, D.R. Hamann: *Self-consistent Electronic structure of solid surfaces.* Phys. Rev. B, Vol. 6, No. 6, page 2166 – 2177 (1972).

11: S. Ohnishi, M. Tsukada: *Molecular orbital theory for the STM.* Solid State Comm., Vol. 71, No. 5, page 391 – 394 (1989).

12: M. Tsukada, K. Kobayashi, S. Ohnishi: *First-principles theory of the scanning tunneling microscopy simulation.* Journal of Vac. Sci. and Tech. A 8, No. 1, page 160 – 165 (1990).

13: M. Tsukada, K. Kobayashi, N. Isshiki: *Effect of tip atomic and electronic structure on STM/STS.* Surf. Sci. 242 page 12 – 17 (1991).

14: G. Doyen, E. Kötter, J.P. Vigneron, M. Scheffler: *Theory of STM.* Applied Physics A51, page 281 – 288 (1990).

15: W. Mönch: *Semiconductor surfaces and interfaces (2nd ed.),* Springer Verlag, Berlin, 1995.

16: The parameter which is varied when the feedback loop is set to a certain value, is its Unity Gain Bandwidth. See: SPM Control Unit Technical Reference Manual, version 2.3 (aug. 1995), page 14. This manual is supplied with our commercially bought STM-system (OMICRON STM-1).

17: For semiconductors, the free carrier concentration is in the same order as the doping concentration, typically 10^{18} cm^{-3} for the GaAs used in our experiments. For metals, it is in the order of the atom-density of the lattice, which is $6 * 10^{22}$ cm^{-3} for tungsten.

18: S. Ciraci: *Theory of tip – sample interactions,* in: *Scanning Tunneling Microscopy III*, (2nd edition) page 179 - 206, edited by R. Wiesendanger and H.J. Güntherodt. Springer Verlag, Berlin, 1996.

19: S. Ciraci, A. Baratoff, I. Batra: *Site – dependent electronic effects, forces and deformations in STM of flat metal surfaces.* Phys. Rev. B, Vol. 42, No. 12, page 7618 – 7621 (1990).

20: J. Wang, T.A. Arias, J.D. Joannopoulos, G.W. Turner, O.L. Alerhand: *Scanning Tunneling Microscopy signatures and chemical identifications of the (110)-surface of Si-doped GaAs.* Phys. Rev. B, Vol. 47, No. 16, page 10326 – 10334 (1993).

21: R.M. Feenstra, J.A. Stroscio, J. Tersoff, A.P. Fein: *Atom-selective Imaging of the GaAs (110)- surface.* Phys. Rev. Lett, Vol. 58, No. 12, page 1192 – 1195 (1987).

22: R.M. Feenstra, J.A. Stroscio: *Tunneling Spectroscopy of the GaAs (110) surface.* Journ. of Vac. Sci & Tech. B, Vol. 5, No. 4, page 923 – 929 (1987).

23: R. Seiwatz, M. Green: *Space Charge Calculations for Semiconductors.* Journ. of Appl. Phys, Vol. 29, No. 7, page 1034 – 1040 (1958).

24: S. Ciraci, A. Baratoff, I.P. Batra: *Tip-sample interaction effects in Scanning Tunneling and Atomic Force Microscopy.* Phys. Rev. B, Vol. 41, No. 5, page 2763 – 2775 (1990).

25: A “normal” bias voltage would be any voltage less than about 3 V in either polarity. When the bias voltage exceeds 5 V, the tunneling current signal becomes very noisy. Usually, the sample surface shows evidence of having been modified after an attempt to tunnel at high voltages. Also, the tip-DOS may change.

26: S. Ciraci, E. Tekman, A. Baratoff, I.P. Batra: *Theoretical study of short- and long-range forces and atom transfer in Scanning Force Microscopy.* Phys. Rev. B, Vol. 46, No. 16, page 10411 – 10422 (1992).

27: A.J. Heinrich: *Ordering in Ternary Compound Semiconductors on the Atomic Scale.* Cuvillier Verlag Göttingen. Phd-thesis presented by A.J. Heinrich at the university of Göttingen, Germany (1998).

28: J.R. Smith, G. Bozzolo, A. Banerjea, J. Ferrante: *Avalanche in Adhesion.* Phys. Rev. Lett, Vol. 63, No. 12, page 1296 – 1272 (1989).

29: A.J. Heinrich, M Wenderoth, M.A. Rosentreter, M.A. Schneider, R.G. Ulbrich: *Scanning Tunneling Microscopy of the atomic structure of the GaAs (110) surface at reduced tip-sample separation.* Appl. Phys. Lett. Vol. 70, No. 4, page 449 – 451 (1996).

30: F.J. Himpsel: *Angle-resolved measurements of the photoemission of electrons in the study of solids.* Advances in Physics, Vol. 32, No. 1, page 1 – 51 (1983).

31: Although an STM-tip can be made out of any conducting material, the two most commonly used materials are Tungsten (W) and a Platinum-Iridium alloy (Pt/Ir 90%/10%). We use polycrystalline Tungsten wire of 0.25 mm diameter.

32: Ph. Ebert, B. Engels, P. Richard, K. Schroeder, S. Blügel, C. Domke, M. Heinrich, K. Urban: *Contribution of surface resonances to Scanning Tunneling Microscopy images: (110) surfaces of III-V semiconductors.* Phys. Rev. Lett, Vol. 77, No. 14, pp. 2997-3000 (1996).

33: B. Engels, P. Richard, K. Schroeder, S. Blügel, Ph. Ebert, K. Urban: *Comparison between ab initio theory and scanning tunneling mircoscopy for (110) surfaces of III-V semiconductors.* Phys. Rev. B, Vol. 58, No. 12, pp. 7799 – 7815 (1998).

CHAPTER 2:

STM-SETUP AND SAMPLE PREPARATION

2.1 Introduction

In the following two chapters, we describe the experimental procedures and equipment used to perform the research presented in this thesis. In chapter 2, we will first briefly outline the entire sequence of tip- and sample preparation and subsequent measurement. We will then describe the STM-setup used, and we will give a more detailed description of the sample preparation and a typical STM measurement. In the second part of chapter 2, we will show the typical morphology of our cleaved sample surfaces, and we will discuss cleavage in general. A lot of experimental work has been spent on the implementation, and later improvement, of the tip-preparation method described by Albrektsen *et al.* [1]. The method of tip-preparation is therefore described separately in chapter 3. That chapter will also describe the research that we have carried out in relation to the preparation of tips.

2.2 Outline of measurement procedure

We fabricate our samples by cutting a small strip from the wafer we wish to investigate. The wafer often has an epitaxially grown structure on top of it. The strip is thinned down by mechanically polishing away part of the substrate. After a tin-contact (Sn) has been placed on the front side of the sample, it is mounted as shown in fig. 2.1. After mounting, we make a scratch on the sample surface to fix the point at which the fracture will start during cleaving. Parallel to this, several tips are prepared in the way described in the next chapter.

After loading the tips and samples into the vacuum system, these are outgassed. We can load four items at a time. The samples are now ready for use, the tips still receive further treatment. When the preparation of the tips and samples has been completed, they are placed in a storage caroussel in the STM-chamber which will hold up to eight items. During an STM-session we can investigate several samples and have several tips at our disposal. We can change tips or samples without breaking the vacuum of the STM-chamber, although the movement of the manipulator (wobble-stick) during tip-changing will cause a pressure-burst.

During the measurement, all mechanical pumps are switched off to avoid vibrations affecting the measurement. The STM-chamber is pumped down by an ion-getter pump, keeping base pressure below $4 * 10^{-11}$ torr. Other measures taken to minimize the effect of external vibrations are described in Sect. 2.3. At the start of the

measurement, the sample is cleaved by pushing gently against the top corner of the sample which then breaks off. After coarse positioning the sample is approached to the tip automatically until the tip and sample are at tunneling distance. Usually, between 5 and 20 minutes elapse between cleavage and first tunneling contact.

In order to image epitaxially grown layers, we have to move the tip to the edge of the exposed fracture surface. This takes about 10-15 minutes. The measurement then lasts as long as the tip(s) still yield(s) adequate resolution, or until contamination renders the surface useless. The latter is after about 6 hours, depending on the sample material and on the purposes of the measurement.

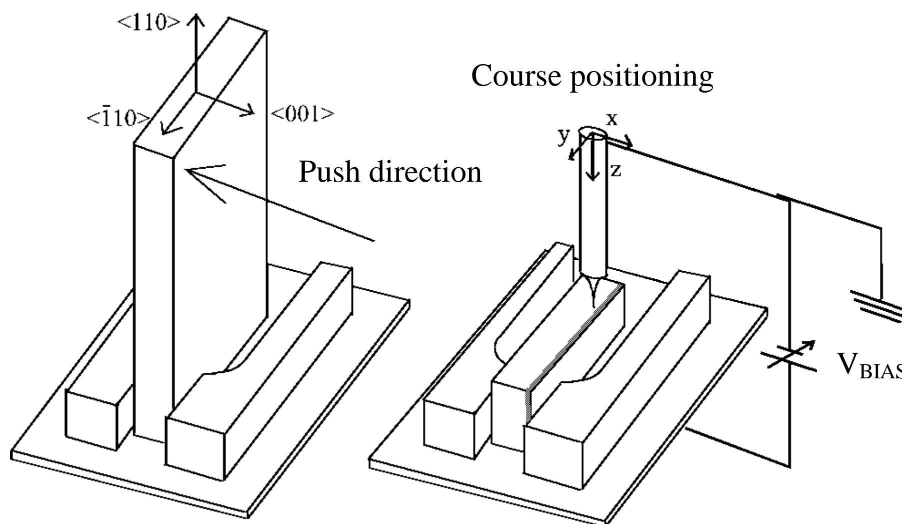

Fig. 2.1: *The sample is mounted upright in the holder. In vacuum, it is cleaved by pushing against the top part with a manipulator. The exposed plane is the (110)-plane. Any epitaxially grown structures (depicted grey) will be located near the edge of the sample. Bias voltage is applied to the sample. See also figure 2.2.*

2.3 The UHV-system and STM

We use a commercially available STM-system (OMICRON STM-1), around which a dedicated UHV system has been built. The system includes the STM itself as well as the control electronics. The vacuum system consists of a load-lock (10^{-6} torr), a preparation chamber ($5 * 10^{-10}$ torr) and the STM-chamber itself ($4 * 10^{-11}$ torr) (see figure 2.2).

The preparation chamber contains a heating stage in which samples and tips can be outgassed to a temperature of 150 – 200 ^{o}C. The heating is accomplished by passing a current through a tungsten coil placed near the sample or tip. The heat is then transferred by radiation. Apart from that, the preparation chamber contains a number of facilities for the preparation of tips. These are a filament for glowing tips, a counter electrode for characterization by field emission and self sputtering, an inlet for neon-gas, and an Ar^{+} ion gun (see chapter 3).

The STM itself really consists of two parts, the scanner and the sample stage (figure 2.2 b). We use a tripod scanner (TS-2 scanner). In order to minimize electronic noise, the I-V converter is integrated in the scanner, thus minimizing the length of cable over which the current signal must travel before amplification. The tip and sample holder are placed upright in the scanner and sample stage, respectively.

The scanning itself and fine positioning of the tip is carried out by three piezo-tubes placed perpendicularly to each other. In figure 2.2 b, the z-piezo lies horizontally and the x and y piezo are at a 45° angle next to and underneath the block that holds the tip. See figure 2.6 d for the resulting orientation of the STM-images with respect to the macroscopic shape of the sample. The scanner has a lateral range of 2 μm x 2 μm, and a vertical range of 60 nm.

The sample stage rests on three vertically placed piezo tubes. A sawtooth signal can be applied to the tubes, so that the sample stage can be moved in the x-z plane by stick-slip motion. This allows for coarse approach (z) and coarse positioning along a line perpendicular to the epitaxial side of the sample (x). This line coincides with the growth direction of our samples. There is no possibility for coarse movement in the y-direction.

One very important factor affecting the performance of an STM-system is adequate vibration isolation. The floor on which the system is built has a vibration accelleration of about 30 μm/s^{2} (base level), with some peaks at various frequencies ranging up to 150 μm/s^{2}. The peak lowest in frequency occurs at 7 Hz. The entire frame is placed on four air-damped feet, and the table on which the STM is built rests on eight rubber tabs which are placed between the frame and the table (figure 2.2). Inside the vacuum system, the STM-unit itsef (*i.e.* the scanner and sample stage) is placed on a small table. When the STM is in operation, the table hangs from four springs. Along the rim of the table, a series of copper fins falls partly between a row of magnets to provide a damping mechanism. The resonance frequency of this arrangement is about one hertz. The entire arrangement, combined with the electronics, is such that we can measure apparent height differences of down to 5 pm. In spite of the vibration-isolation present on our system, we often carry out our STM-measurements at night.

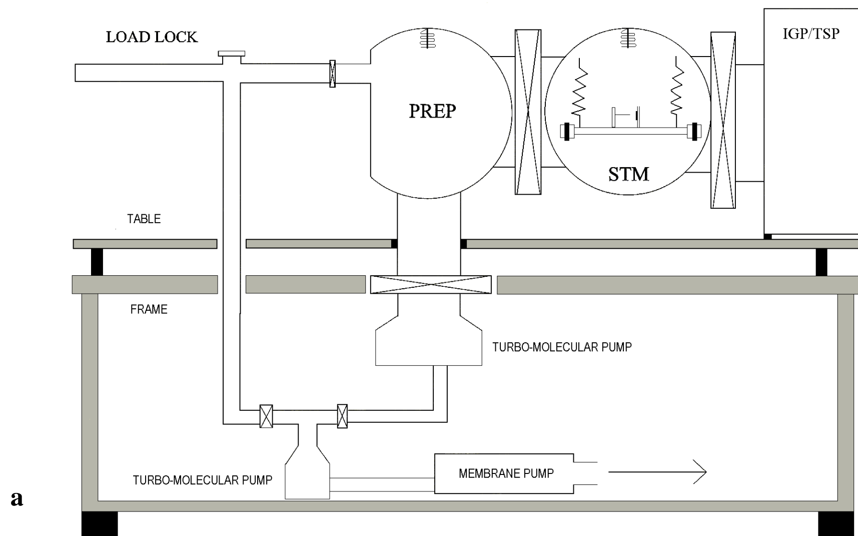

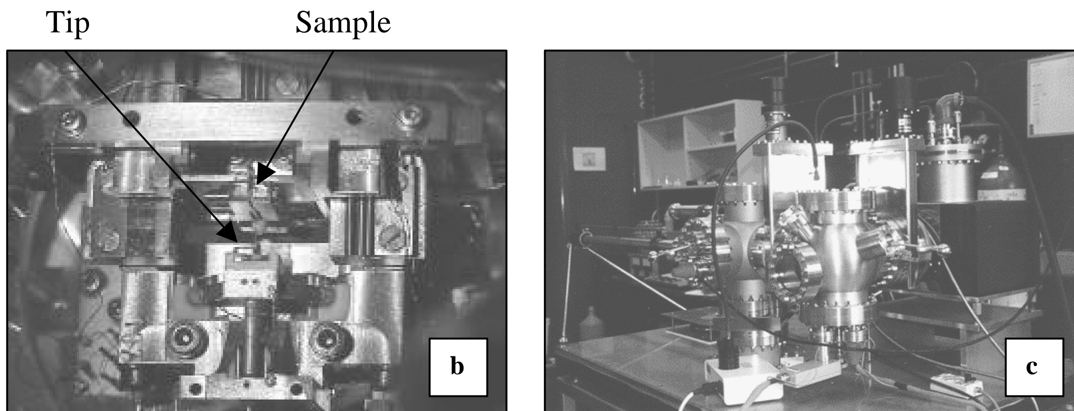

Fig. 2.2a: *Schematic outline of the UHV-system. The figure shows the preparation chamber (PREP) and load-lock, which are both pumped by turbomolecular pumps. During STM-operation, the turbomolecular pumps are switched off. The STM-chamber is pumped by an ion-getter pump (IGP/TSP), both during STM operation and while the system is on stand-by. During STM-operation the pumping speed is temporarily increased by filling the cooling shroud mounted in the ion-getter pump with liquid nitrogen. The frame rests on four air-damped feet.* ***b:*** *Top view of the STM, showing the scanner and tip and sample. The entire arrangement is placed on a (round) eddy current damped table inside the STM-chamber (not shown in photograph).* ***c:*** *Photograph of the entire UHV-system. The round chamber in the middle is the STM-chamber. To the left is the preparation chamber (6-way cross with spherical body). To the right, the ion-getter pump is seen (black).*

2.4 Sample preparation

The first step in sample preparation consists of cutting the sample out of the wafer. The sides of the sample must be well aligned with the natural cleavage planes (the {110}-planes) of the sample, so that the sample itself can be properly aligned with the holder during mounting. The wafer is broken in four equal parts as shown in figure 2.3a. From a quarter-wafer, we then cut a 3.5 x 10 mm strip as is shown in figure 2.3b. The central idea is that the scratch is only used to initiate the crack. After initiation, the crack must be free to find its own way through the material. This way, it will follow a natural cleavage plane. We do not break the sample along a scratch made along the entire intended path of the crack, as the scratch is often misaligned by 1 or 2 degrees. In that case, the sides cannot be used for alignment with the holder.

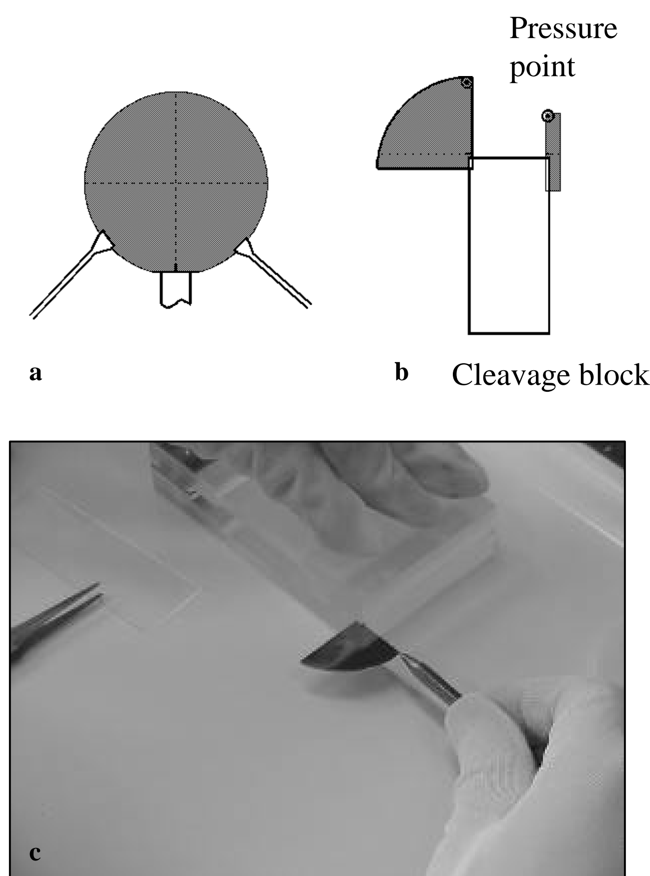

Fig. 2.3a: *Arrangement used for cleaving samples out of the wafers. The entire wafer is taken with two pincers and then gently bent until it snaps in two. It is often helpful to rest the wafer on a third, preferably round object.* **b:** *Strips are cleaved from the quarter wafers in the manner shown on the right.* **c:** *Photograph of a strip of GaAs being cleaved out of a quarter wafer. In the end, a strip of 3.5 x 10 mm becomes the sample.*

The wafers we use typically have a thickness of 350 – 450 µm. In order to obtain a better cleave we polish away part of the substrate, until the sample has a thickness of about 100 µm for GaAs and 120 µm for InP. Thinner samples become too fragile to be handled in a practical manner. In order to polish the sample, it is mounted onto a copper block using wax. After polishing, the wax used for mounting the sample is removed with ethanol.

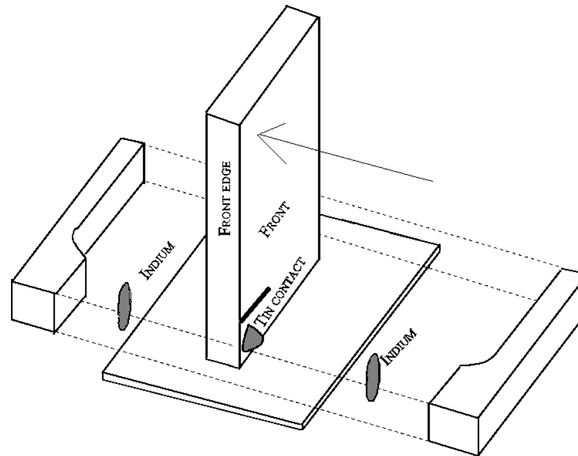

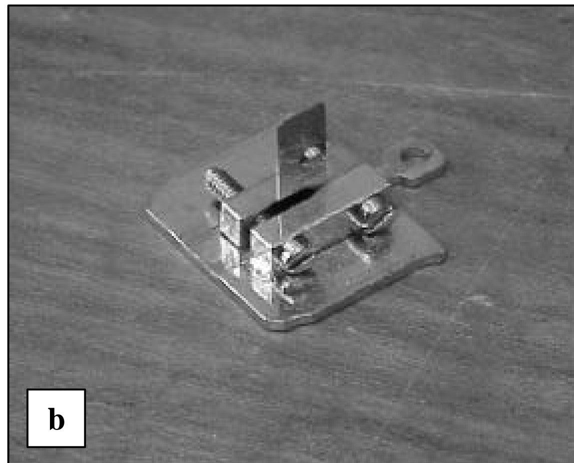

Fig. 2.4a: *The arrangement of the tin contact and pieces of indium when mounting a sample. The clamps of the sample holder are tightened by screws on the front and back ends of the clamps.* **b:** *Photograph of a finished sample just before loading into the vacuum system. The base plate of the sample holder measures 19 x 18 mm. The photograph clearly shows how the sample is clamped at one corner.*

The third step in the process is the application of an electrical contact. Due to the oxide-layer present on the semiconductor, a simple mechanical contact between the sample and sample holder is not sufficient to provide a good electrical contact. We make the contact by placing a small ball of tin (Sn) on the front side of the sample. The tin is then partly diffused into the semiconductor by heating the sample and tin ball in a N_2/H_2 atmosphere (80 % / 20 %). The sample is heated to 300 ^{o}C for typically two or three minutes. The contact is placed in the lower corner of the sample, at the point where the sample is clamped in the holder. In the ideal case, the contact, the scratch and the point at which the sample is pushed during cleaving, are along one line extending along the front edge of the sample.

The samples are now ready for mounting. They are usually kept under ethanol for up to 30 minutes, while in the meantime the sample holders and the tools to handle them are cleaned. Cleaning is done ultrasonically in four consecutive liquids: a warm, aquaous solution of soap, warm water, distilled water, and ethanol. Between the steps, the items are carefully rinsed with the same liquid as the one that is used for the following cleaning-step.

During the early stages of this project we used thick samples (400 μm), which can simply be clamped. Thin samples (150 μm or less), however, will break if the clamps of the sample holders are fastened too tight. At the same time, if they are set too loose, there is a high probability that the sample will fall out of the holder when inside the vacuum system. We solve this by placing a small amount of indium metal between the sample and the holder, on both sides (figure 2.4). The clamps of the sample holder are opened widely, and we press some indium onto the inner sides of the clamps where it will stick to the sample holder. The sample is then placed in between, allowing it to hang towards the back side. Then the contraption is put onto a heating plate, until the indium melts [4]. We then gently slide the loose clamp up against the fixed one, and tighten the two screws. During this stage, it is also important to check if the sides of the sample are well aligned with the holder itself. If that's the case, the cleavage plane is well aligned with the top of the clamps. After the sample is allowed to cool off, the screws are very gently tightened some more. Basically, we just check whether the screws have not loosened as the different parts of the holder contracted during cooling off. When the indium melts during mounting, the tin appears to mix with it. After mounting, a rather thin layer of metal is present between the front and back sides of the sample and the clamps, and the tin ball is no longer there. The applied temperature itself, however, is below the melting point of tin. The whole procedure can be carried out with relative ease after some practice.

The last part of mounting is the placement of the scratch, just above the top of the clamp on the epilayer side (see figure 2.1). This is a tricky moment, since the samples become very fragile after they have been thinned down. When making the scratch by hand it is quite easy to break the sample by accidentally applying too much force. After mounting, the samples are loaded into the vacuum system. Inside the preparation chamber, they are outgassed for about an hour at a temperature between 150 ^{o}C and 200 ^{o}C. The indium used for keeping the sample in its place will melt, but since molten indium is quite sticky, the sample remains in place. When the outgassing is completed, the sample is placed in the carrousel until the start of the measurement.

Since part of the experimental work consists of the study of the spatial distribution of dopants (chapter 7), it is essential to ensure that the temperature treatments applied during sample preparation do not cause diffusion of the dopants. During preparation, the samples are subjected to 300 ^{o}C for 3 minutes or less while the electrical contact is applied, and to less than 200 ^{o}C for up to an hour as they are outgassed in the vacuum. To our knowledge, these treatments will not cause significant diffusion.

2.5 The measurement

At the start of the measurement, the sample is cleaved by pushing against the top corner of it with the wobble-stick (see figure 2.1). We can choose the position of the pressure-point on the sample within a margin of 0.5 mm. Again, the thought behind the way we cleave is that we want the crack to be free to find its own path through the material. Clamping the sample at only the front edge helps to ensure that, even if the alignment with the top of the sample holder is less than perfect. Another condition we try to avoid during cleavage, is the presence of torque along the long axis of the sample. This can occur during cleavage if the back edge of the sample is caught accidentally in one of the fixation screws, or if the pressure-point is misplaced. One of the topics that we are still investigating is at which point exactly the pressure should be applied during cleavage in order to obtain the smoothest possible surface. Up to now, we always choose the top corner of the sample as our pressure-point, in the way that is indicated in figure 2.1. Recent experiments have shown that placing the pressure-point at the corner of the sample *does* induce torque in the sample during cleavage. If torque is to be minimized, the pressure-point should be chosen at the top edge of the sample, at about $^{1}/_{3}$ of the width of the sample from the corner. The effects of the chosen location of the pressure-point on the quality of the cleaved surface is at present still under investigation.

After cleavage, the sample is taken out of the carousel and placed in the sample stage of the STM (the top part that was broken off remains in the carousel). The movement of the wobble-stick and of the STM itself, which has to be lowered from its locked position into its operating position, causes a pressure-burst. We estimate it to be less than $2 * 10^{-10}$ torr. The tip and sample are aligned using a CCD-camera. An experimental trick to carry out the alignment quickly is to place the camera such that the reflection of the tip will show in the sample surface. When the alignment is satisfactory, we use the automatic approach provided with the electronics to bring the tip in tunneling contact.

After first contact, we can either start imaging right away, or we can move to the edge of the sample to image epitaxially grown structures. We locate the edge by retracting the tip, moving the sample a short distance (between 250 nm and several μm) and extending the tip again to establish tunneling contact. When the tip can be extended

over the entire range of the (fine) z-piezo actuator without coming within tunneling range to the sample, the tip has been moved past the edge and is moved back a bit. We can locate the edge to within 250 nm this way, within 10-15 minutes after first contact. For this method to work properly, the (macroscopic) shape of the tip is quite essential. The important features are the absence of many different microtips, and a long, reasonably thin shank. The macroscopic shape of electrochemically etched tungsten tips is ideal for this method. We have not been able to locate the edge with mechanically cut Pt-Ir tips, probably because such tips *do* posess many microtips near the apex. Occasionally, the shank of the tip comes into tunneling contact with the edge of the sample. We have not observed this to be harmful as long as it is not attempted to scan the tip in this condition.

We apply a background correction to the images that involves a “line-by-line tilt correction”: from the height along each fast scan-line (horizontal in the images) a linear fit is made, which is then subtracted from the original height-curve along that scan-line. This same type of correction is commonly applied as an on-line correction during the acquisition of the data. In our measurements, the tip is usually scanned with a frequency between 2.5 and 5 Hz. External vibrations with a frequency of a few Hz tend to raise or lower a fast scan-line, and also to tilt it. When the scanning-frequency of the tip is larger than 4 times the frequency of the external vibration, the vibration introduces only little curvature into the height-profile along the scan-line. This line-by-line correction is then very effective in filtering out the effects of such low-frequency external vibrations without otherwise altering the data. The effectiveness increases when the method is applied to smaller cut-outs of a frame.

The same background correction can also be applied to all pixels lying in a line perpendicular to the fast scan-direction (vertical in our images). Some of the images shown in this thesis are cut-outs from larger frames, where the top right corner is chosen inside a depression in the surface (see chapter 5). The height-surface [z(x,y)] is thus warped instead of planar. We eliminate much of this warping by applying the line-by-line correction first in the horizontal direction and then in the vertical direction, which allows us to show details of the atomic lattice in all portions of the frame. In some images in chapters 5 and 7, details of the atomic lattice around dopants or other features are shown by applying a (high-pass) fast-Fourier transform filter. Whenever this technique is used, it will be stated clearly in the figure caption.

2.6 Typical morphology of cleaved surfaces

The preparation of samples for cross-sectional STM in UHV is a non-trivial task, as a poorly prepared sample will have a rough fracture-surface. On such surfaces, only steps with atomically resolved terraces in between can be imaged meaningfully. The contrast of a given STM-image is determined by the maximum height-differences present in the data. If a mono-atomic step (Δz = 260 pm) is present in the frame, the resulting contrast is such that other features like dopants (Δz = 50 - 70 pm) or interfaces between different materials (Δz = 20 pm) cannot be recognized. Atomic corrugation, in spite of the small difference in apparent height associated with it (Δz = 20 pm) can often be recognized on one of the terraces of a rough image if the colour scale is adjusted appropriately. This is the case because atomic corrugation is a short-range effect, recognizable even if a small patch of it is visible, and also because atomic corrugation extends throughout the frame, so it is always possible to optimize the contrast for a given terrace. To a lesser extent, the same is true for interfaces between different materials. Dopants, on the other hand, manifest themselves as a gentle rise in the atomically resolved image and lie scattered as isolated points in the image. In practice, this makes them very hard to recognize in rough images. Even if a few dopants are found in a rough image, the study of the spatial distribution of dopants in, for example, a δ-doped layer, becomes quite meaningless.

Our sample preparation procedure has become rather elaborate in order to produce fracture surfaces that are as smooth as possible, especially near the edge on the epitaxial side of the sample. The “art” of creating smooth surfaces by cleavage in UHV remains a topic of applied research, both in our group as well as elsewhere [2,3].

Figure 2.5 shows two limiting cases of the macroscopic* morphology that we observe on our cleaved samples (figure 2.5b: rough morphology, figure 2.5 c: smooth morphology). In all cases, the area adjacent to the scratch contains a high density of steps, and is useless for STM. The remaining part of the sample surface can be devided into two regions: The first is the “edge region”, a narrow strip along the edge of the sample which usually looks optically flat. The second region is the “bulk region”, which can be either optically flat or which can show steps that fan out from the edge region.

* We define “macroscopic” as anything observable by the naked eye or optical microscope.

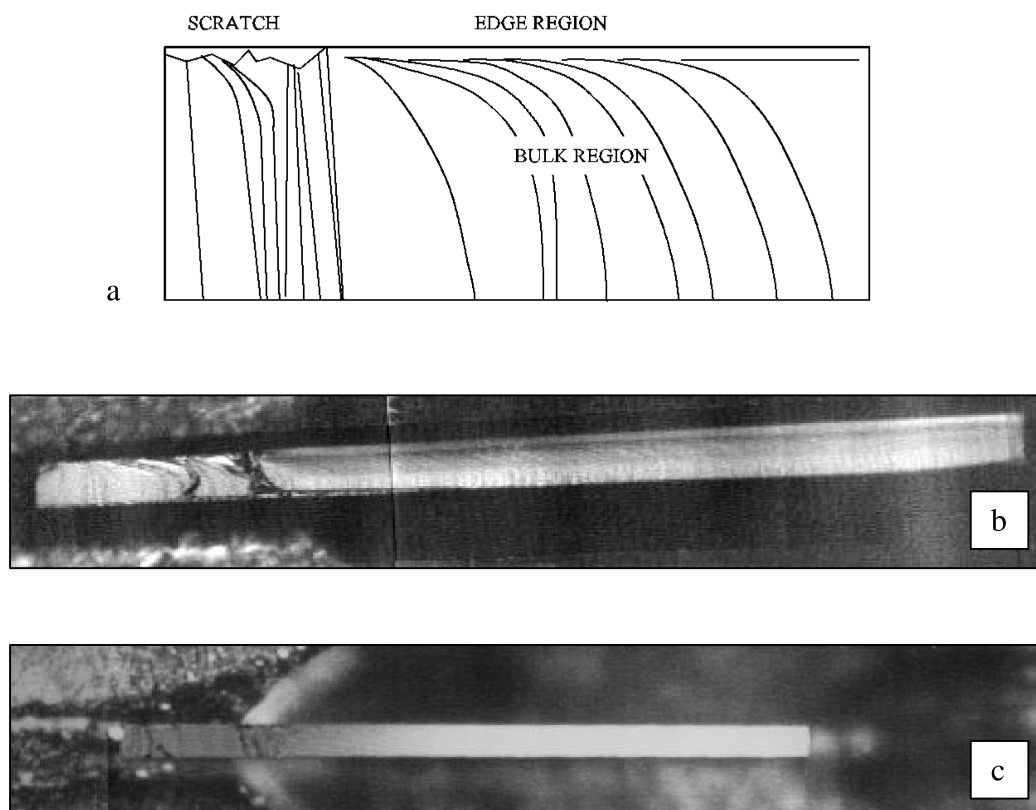

Fig. 2.5 a: *Schematic drawing of typical macroscopic morphology of a cleaved sample, showing the area adjacent to the scratch and the edge and bulk regions.* **b:** *LSM image of a sample with rough macroscopic morphology. The line-pattern is a bit difficult to see, but the image clearly shows the edge and bulk regions.* **c:** *Sample with a smooth macroscopic morphology. The bulk and edge regions cannot be seen separately. The only rough area is the area adjacent to the scratch.*

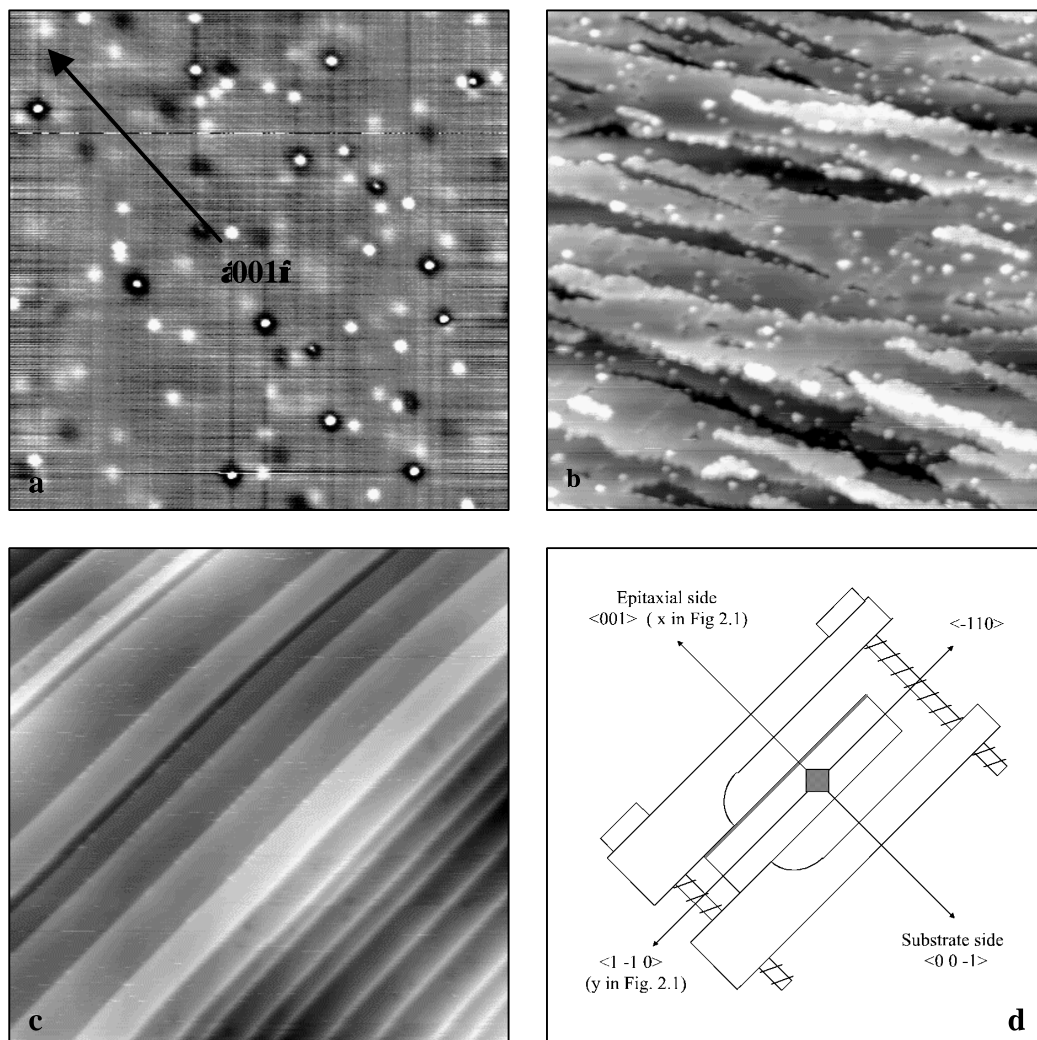

Fig. 2.6 (a,b,c): *Examples of sample surface morphologies frequently observed on GaAs (110) (frame size 100 x 100 nm).* **a:** *Atomically flat surface approximately 15 minutes after cleavage. The white hillocks are subsurface dopants, the bright spots with a dark ring may be adsorbates or suface-layer dopants (see chapter 7). V = -1.871 V, I = 79 pA, greyscale: 0 – 34 pm.* **b:** *Furrow morphology on a rough sample surface as is often seen on the bulk region of the sample surface. Greyscale: 0 – 89 pm, V = -1.861 V, I = 85 pA.* **c:** *Morphology typical for the edge region. The width of the parrallel terraces can vary from several nm (see frame) to far more than 100 nm in which case an atomically flat surface is observed with STM. AFM-results (not shown here) show that the steps can run parrallel without bunching for several μm. Greyscale: 0 – 150 pm, V = -1.667 V, I = 69 pA.* **d:** *Orientation of the STM-frames with respect to the macroscopic world. This orientation holds for all STM-frames shown in this thesis. The fast scan direction is horizontal in all STM-images.*

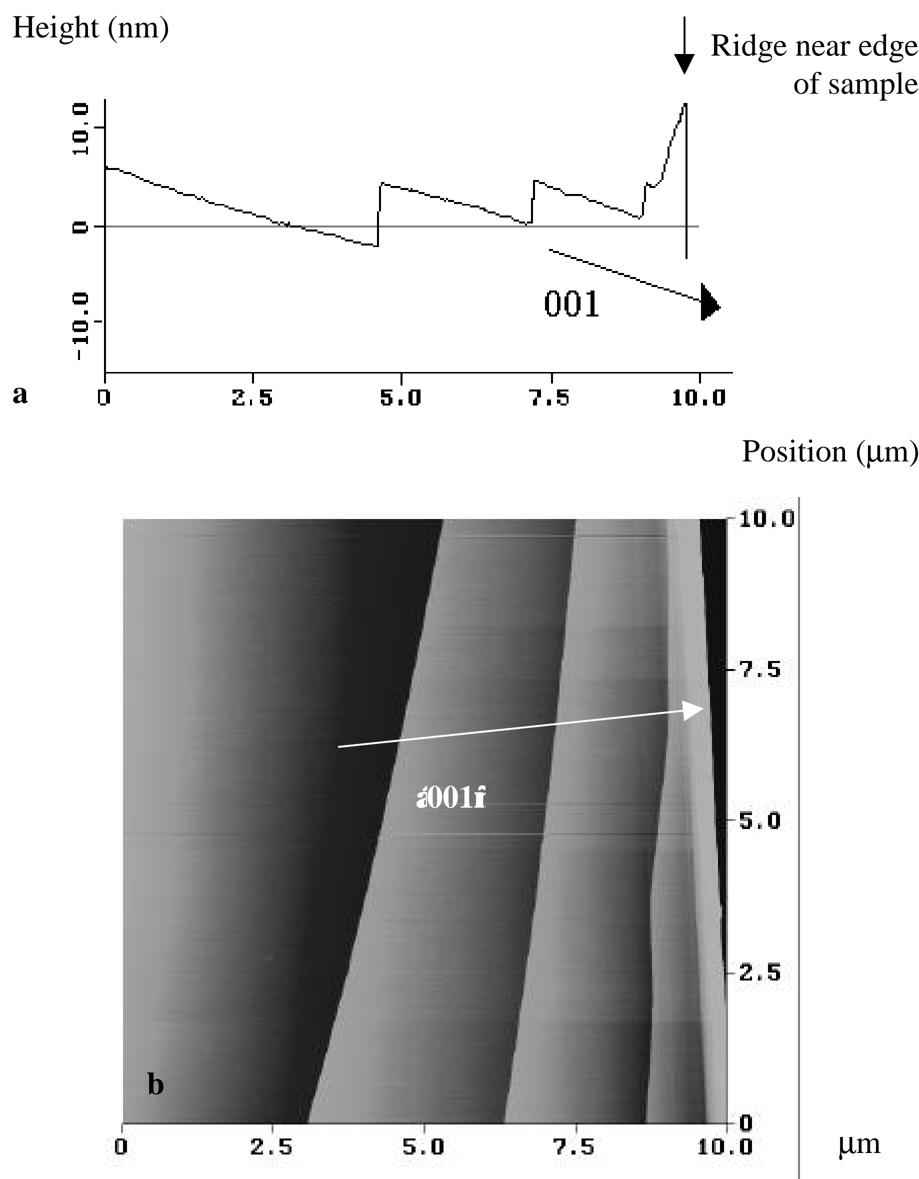

Fig. 2.7 a: *Height-profile taken from a contact-mode AFM-image along the* ⟨001⟩ *direction. The profile shows that near the edge of the cleaved surface, a ridge is present.* **b:** *Contact-mode AFM image of the edge region (frame 10 x 10* **m***m, colour scale 0 – 20 nm). The height-profile shown in a) was taken along the white arrow. The image shows some large steps branching off from the ridge running along the edge of the sample. The edge itself is seen on the right (sharp interface between between bright and dark). Notice that the AFM-image has a different orientation with respect to the STM-images shown in Fig. 2.6.*

On a scale of 10 μm down to the atomic scale, the trends in the macroscopic morphology are reproduced. Near the edge, the steps run mostly along the ⟨-110⟩ direction, parallel to the edge and, if these are present, to the epitaxial layers. Between the steps are very long, straight terraces. The width of the terraces varies from far more than 100 nm down to 10 or 20 nm (figure 2.6 c). STM-frames of 100 x 100 nm taken in the bulk region of the sample show either an atomically flat surface (figure 2.6 a), or they can show mono-atomic steps in STM (figure 2.6 b). These steps are often V-shaped, forming what is called the "furrow morphology" in recent literature [2,3]. If steps are present in the bulk region, the general direction of the steps gradually changes from ⟨-110⟩ near the edge region to ⟨001⟩ as one moves towards the back of the sample. In the bulk region, we encounter atomically flat surfaces and V-shaped steps about equally often. We observe that usually the edge region lies somewhat higher than the rest of the sample surface, forming a sort of ridge (figure 2.7 a,b).

Finally, the macroscopic morphology is often smoother as one moves away from the scratch (the right end of the sample surface shown in figure 2.5 b,c). We have the impression that also on the atomic scale, the surface tends to become smoother as one moves further away from the scratch, but we have no experimental results to confirm this notion. We sometimes observe significant differences in morphology when changing tips. This indicates that there are differences in morphology as a function of position on the sample, since the tips contact the sample at a different location.

For the study of epitaxial layers, it is desirable that the terraces are as wide as possible. For the study of δ-layers, a terrace width of about 100 nm or more is desirable. For the study of interfaces, the width can be somewhat smaller. When the average terrace width is about 10 nm, the study of any kind of epitaxial structure becomes quite difficult.

2.7 Discussion on the cleavage process

As the precise nature of the cleavage process is at best only partially understood [2], the preparation of usable sample surfaces by cleavage in UHV is mostly done by trial and error. The following section will discuss some of the literature on cleavage that we are aware of, along with some observations of our own. Most of the considerations concern the region near the epitaxial side of the sample (epilayer region) since our main interest is in imaging epitaxially grown layers. Our own understanding of cleavage is by no means complete. At present, cleavage and how to obtain smooth sample surfaces by cleavage remains a topic of ongoing research [2,3].

It has been shown by Rosentreter *et al.* that at room temperature, the surface morphology obtained by cleavage does not correspond to the morphology expected for a surface that has reached thermal equilibrium. The article concludes that the morphology is created by the fracture-process and that "relaxation towards thermal equilibrium is not the dominant mechanism responsible for the arrangement of the steps" [2]. Another very important point is that the crack tip may propagate either

smoothly through the material, or in an oscillatory manner [5,6,9,10,11]. According to ref. 5, the crack propagates through a (triangular) lattice smoothly when the external strain is below a critical value. If the strain exceeds this value, smaller cracks branch off from the main crack periodically, creating a rough surface morphology. The same calculations also predict a rather complex relation between the external strain and the crack tip velocity [5].

The motion of a crack propagating through a GaAs sample has been investigated by Sauthoff *et al.* [3]. The results showed that the entire cleavage process takes about 14 to 20 μs. The samples were 3.6 mm (fracture length) by 0.3 mm (sample thickness). During cleavage, the crack-front proceeds along the front edge of the sample from the edge towards the bottom end of the sample. After the crack has reached the bottom end of the sample, it takes about 5 to 8 μs more before the crack reaches the back side of the sample. The experiment showed that as the crack approaches the back side of the sample, it travels perpendicularly to it. The cleavage process thus involves a change of the propagation direction of the crack by 90 ^{o}. Observed crack velocities ranged from 250 m/s to 3000 m/s. Those samples that had a low crack propagation velocity ($v < 600$ m/s) had a smooth morphology, both on the macroscopic and on the atomic scale [3]. When breaking an entire wafer into four quarts in the manner shown in figure 2.3, we sometimes observe a behaviour which is consistent with Sauthoff's results: We bend these wafers very gently, gradually increasing pressure until the wafer snaps. Sometimes, before the wafer actually breaks, a very thin line appears in the surface of the wafer extending from the scratch along the intended cleavage path. It usually traverses ¾ of the wafer and does not reach the rim of the wafer opposite from the scratch. At this point the wafer is still one integral body: One can hold it at one side and the other half of the wafer remains in place. When more pressure is applied, the wafer breaks in two.

Before we started using the sample holders shown in figure 2.1 which only clamp the sample at the front edge, we used sample holders that clamped the sample along the entire length of the bottom end, similar to the one drawn in figure 2.8 b. The following STM-image (figure 2.8 c) shows the effect of poor alignment of the sample cleavage plane with respect to the top edges of the clamps holding the sample.

The STM-image shown in figure 2.8 c was taken within a distance of 250 nm from the epitaxial side of the sample. The image shows many V-shaped terraces. Traveling in the [-110] direction (from the lower left corner towards the upper right corner) one moves up a staircase, the steps of the stairs appearing very pointed and jagged. This is a clear contrast to the typical morphology shown in figure 2.6 c, where the steps do not seem to terminate anywhere on a scale of several hundred nm, and which does not have any kind of staircase in the [-110] direction. The propagation direction of the crack was from the lower left corner towards the upper right one for both images as both frames were taken within the edge region of the sample. The work of Sauthoff *et al.* [3] shows that in the edge region, the crack proceeds in the [-110] direction along the entire length of the sample. Notice that the image also shows a staircase morphology in the perpendicular direction, with the steps rising as one moves in the [001] direction (from the bottom right towards the upper left corner). This is consistent with the presence of a ridge similar to the one shown in figure 2.7 a,b.

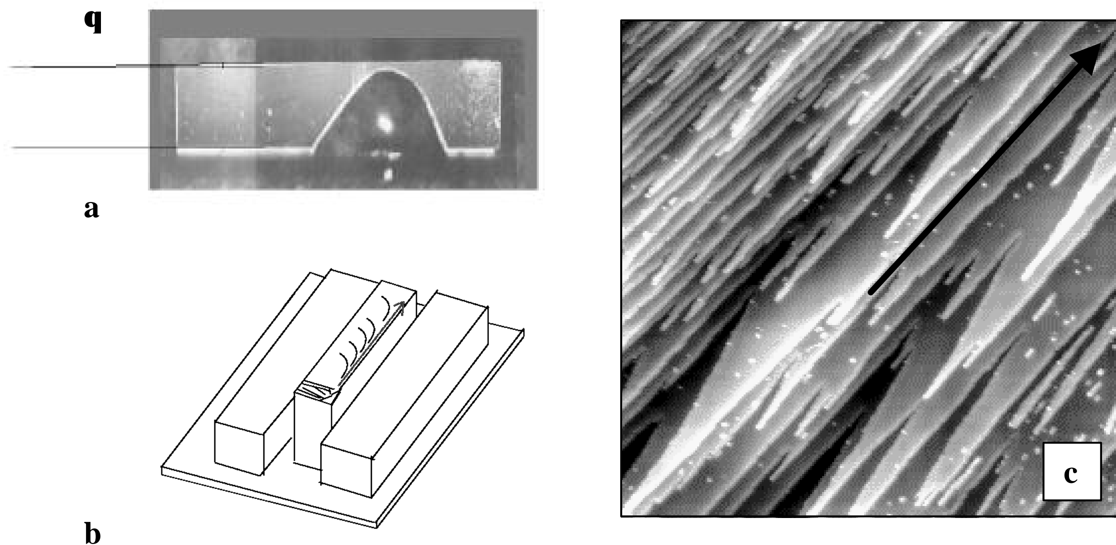

Fig. 2.8a: *Laser scan microscope (LSM) image taken from a sample after its use in STM (side view). The image shows the epitaxial side of the sample. The big round structure is an indium droplet (see text). The scratch is on the right side of the sample near the concentration of bright specks seen on the sample. The visible part of the sample is bounded by the fracture surface at the top, and by the top of the clamp at the bottom. The clamp itself could not be imaged clearly. Notice that the fracture surface and the top of the clamp are not quite parallel, indicating that the sample was misaligned during mounting by an angle* **q**. **b:** *Schematic drawing showing the form of the (old) sample holder. The grey arrow indictates the propagation direction of the crack in the edge region.* **c:** *STM-image (frame: 250 x 250 nm, greyscale 0 – 93 pm, V = -2.234 V, I = 104 pA). The bottom left corner lies at less than 250 nm from the edge of the sample near the epilayer side. The arrow shows the expected propagation direction of the crack (see text).*

The laser scan microscope image (figure 2.8 a) taken after the STM-measurement shows that the sample surface was misaligned with respect to the top of the sample holder. On the right, near the scratch, the top of the sample is higher than on the left. The bright horizontal line coincides with the top of the sample holder. The round structure is a droplet of indium metal which spilled out from between the sample and the clamp as the clamps were tightened. The sample is about 3 mm long.

If during cleavage the natural cleavage plane is misaligned with respect to the sample holder, the propagation of the crack is influenced by the presence of the clamps. The two limiting cases are that the crack follows the natural cleavage plane, creating an

atomically flat surface which is at an angle with respect to the sample holder. The other extreme is that the crack follows the top of the clamp, creating a vicinal surface that is macroscopically parallel to the sample holder. The sample morphology shown in figure 2.8 is an intermediate case.

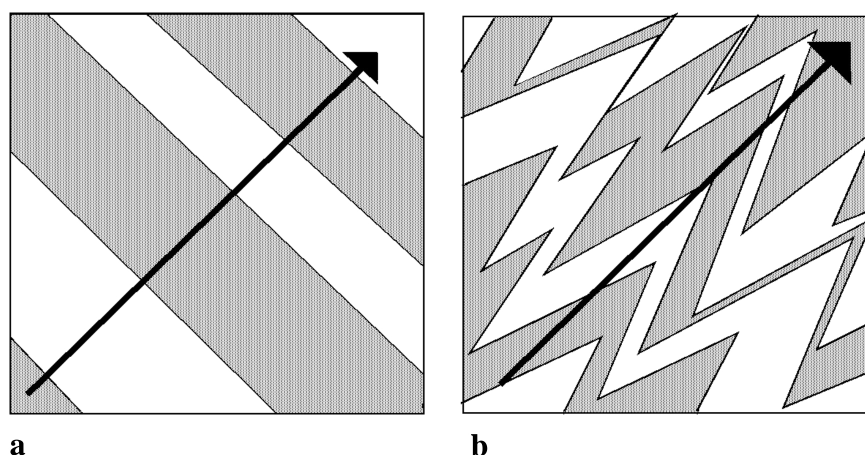

Fig. 2.9 a: *Vicinal surface with steps perpendicular to the crack propagation direction (dark grey arrow). This arrangement minimizes the number of step atoms. The terraces are shown alternatingly white and grey for clarity.* **b:** *Vicinal surface with V-shaped terraces and steps more or less aligned with the propagation direction of the crack (See also figure 2.8 c).*

There is another interesting point to be made about figure 2.8: As the propagating crack was forced upward by the presence of the clamps, it created a vicinal surface. One might have expected the steps and terraces to run along [001] as sketched in figure 2.9 a, which would minimize the number of step atoms per unit area while still creating a surface with the macroscopic orientation shown in figure 2.8 a. Such steps would run perpendicular to the propagation direction of the crack. Apparently the system does not favour this arrangement as the steps run more or less along [-110]. The terraces making up the vicinal surface are V-shaped with the steps running more or less parallel to the propagation direction of the crack (figure 2.9b). This arrangement is created at the expense of having far more step atoms per unit area than would be needed in the case of straight steps running perpendicular to the crack propagation direction. As the steps gradually change direction when moving from the epilayer region towards the bulk of the sample (see refs. 2 and 3, and figure 2.6) the direction of the steps does not seem to be related to any given crystallographic direction. We thus conclude that as the steps are formed during the cleavage process, they have a tendency to align themselves to the propagation direction of the crack. This can lead to the parallel steps typical for the epilayer region (figure 2.6c) when clamping the sample at one corner, or it can cause the V-shaped steps shown in figure 2.8c when the dynamics of the cleavage process force the advancing crack tip to deviate from the natural cleavage plane.

In practice, it is difficult to mount the sample in such way that the natural cleavage plane is perfectly aligned with the top of the sample holder [7]. This is why we use sample holders that clamp the sample only at one corner: Away from the corner that is clamped, the crack is free to propagate through the material without influence from the clamps of the sample holder. Although long, parallel steps as shown in figure 2.6c are seen frequently in the epilayer region when using the modified sample holders (see figure 2.1), we have never observed V-shaped terraces in the epilayer region when clamping the sample only at one corner.

Interpreting the foregoing, it is clear that the cleavage process involves a crack propagating through the epitaxial side of the sample from the scratch towards the other end of the sample. Either at the same time or slightly afterwards, the crack also propagates through the bulk of the sample. The experiments by Sauthoff *et al.* [3] indicated that the crack reaches the back side traveling in the [00-1] direction. The cleavage process thus involves a change in the propagation direction of the crack by 90 degrees.

The pattern of long, parallel terraces extending in the propagation direction of the crack typical for the edge region (figure 2.6 c) shows that in this region, the crack travels smoothly through the material. Any oscillatory behaviour of the crack-tip as discussed in the literature [5,6,9,10,11] would result in steps perpendicular to the propagation direction of the crack, or in V-shaped terraces like the ones shown in figure 2.8 c. The external strain acting on the crack tip is apparently small enough in order to avoid oscillatory behaviour of the crack. We thus propose that the parallel steps are created as the atomic plane through which the crack propagates, is shifted by one or more unit cells for different positions along the advancing crack-front (figure 2.10).

The main remaining challenge regarding cleavage is to cleave in such a way that the parallel steps in the epilayer region lie as far apart as possible. A rough morphology in the bulk region presents less of a problem, as the bulk material takes up most of the sample surface. This gives more possibilities to move around on the sample in order to find an area with a suitable morphology. Should that fail, then there is usually enough material available to make a new sample. For the study of epitaxial layers this is not the case: The available area on the sample surface is limited by the extent of the epitaxial layer in the [001] direction and by the range of the scanner (2 μm). Also, the amount of sample material available is often limited to one (2 inch) wafer or one quarter wafer, allowing only a certain number of samples to be made.

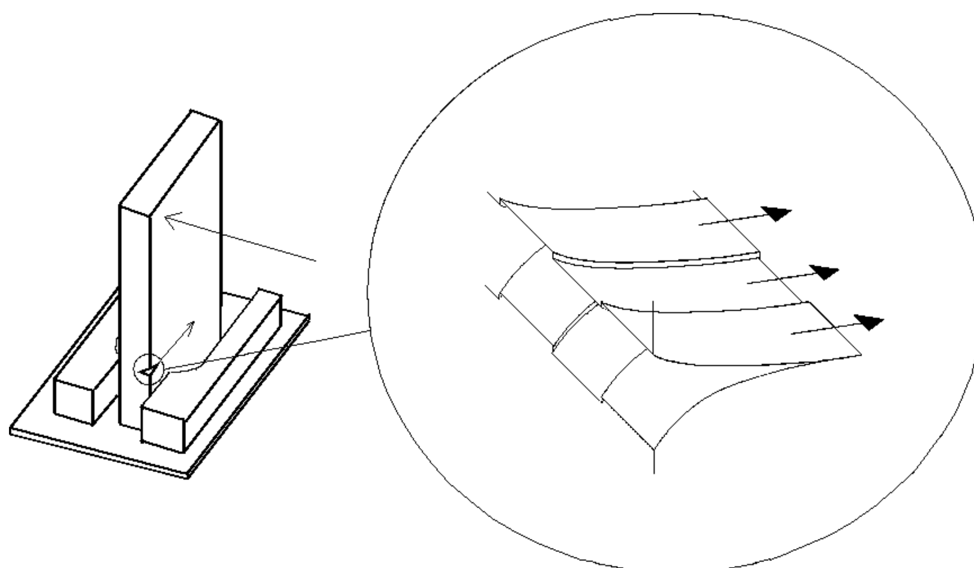

Fig. 2.10: *Possible geometry for the formation of parrallel steps in epilayer region (see text). The arrows in the large scale sketch (left) show the pushing direction and the propagation direction of the crack, respectively.*

2.8 Summary

The experimental method used in this thesis is cross-sectional scanning tunneling microscopy in ultra-high vacuum ($4 * 10^{-11}$ torr). The surfaces we prepare by cleavage have a characteristic morphology which shows an edge region and a bulk region. Near the edge of the sample on the epitaxial side, we observe long, parallel steps running along the [-110] direction. The width of the terraces between these steps varies from 10 nm to far more than 100 nm. Further towards the bulk of the sample, we observe that the atomic steps gradually change direction, running along [001] in the middle of the sample. At this point, creating smooth cleavage surfaces remains the topic of ongoing research.

REFERENCES

1: O. Albrektsen, H.W.M. Salemink, K.A. Morch, A.R. Thölen: *Reliable tip preparation for high-resolution scanning tunneling microscopy.* JVST B12 (6) page 3187 (1994)

2: M.A. Rosentreter, M. Wenderoth, N.H. Theuerkrauf, A.J. Heinrich, M.A. Schneider, R.G. Ulbrich: *Non-equilibrium configurations of mono-atomic steps on cleaved GaAs (110) surfaces.* Phys. Rev. B, Vol. 56, No. 16, pp 10538 – 10543 (1997).

3: K. Sauthoff, M. Wenderoth, M.A. Rosentreter, K.J. Engel, T.C.G. Reusch, R.G. Ulbrich: *Non-linear dinamic instability in brittle fracture of GaAs.* Phys. Rev. B, Vol. 60, No. 7, pp. 4789 – 4795 (1999).

4: The temperature of the sample during mounting lies between 156 ^{o}C (melting point of indium) and 200 ^{o}C (set-point of the heating plate).

5: M. Marder and Xiangming Liu: *Instability in Lattice Fracture.* Phys. Rev. Lett, Vol. 71, No. 15, pp 2417 – 2420 (1993).

6: R. Blumenfeld: *Nonequilibrium brittle fracture propagation: Steady state, oscillations, and intermittency.* Phys. Rev. Lett Vol. 76, No. 20, pp 3703 – 3706 (1996).

7: When taking special measures, it is possible to align the sample with its cleavage direction parrallel to the sample holder accurately enough to produce a satisfactory surface: Phd-thesis presented by O. Albrektsen, Laboratory of Applied Physics (LTF), Technical University of Denmark (Supervisor: Prof. Lic. Tech. K.A. Mørch). Also: Personal communication with dr. H. Salemink, IBM-Zürich.

8: W.D. Callister: Materials science and engeneering (2nd ed.), John Wiley and sons, New York, p. 199 (1985).

9: J. Fineberg, S.P. Gross, M. Marder, H.L. Swinney: *Instability in dynamic fracture.* Phys. Rev. Lett. Vol. 67, No. 4, pp. 457 – 460 (1991).

10: M. Marder, J. Fineberg: *How things break.* Phys. Today, Sept. 1996, pp. 24 – 29.

11: J. Fineberg, S.P. Gross, M. Marder, H.L. Swinney: *Instability in the propagation of fast cracks.* Phys. Rev. B, Vol. 45, No. 10, pp. 5146 – 5154 (1992).

CHAPTER 3:

PREPARATION OF STM-TIPS AND RELATED EXPERIMENTS

3.1 Introduction.

One of the most important experimental aspects of Scanning Tunneling Microscopy (STM) is the manufacture of high quality tips. Tips that are used in UHV conditions are commonly made out of tungsten (W), which can be either polycrystalline or monocrystalline. A good tip is mechanically rigid, free of surface contaminants or oxides and has a very sharp end. For atomic resolution on GaAs {110} the radius of curvature at the apex has to be in the order of 15 nm. The electrochemical process usually applied to etch tungsten tips into their basic shape produces tips which narrow down to a straight cylinder of about 50 nm radius. The apex can be a hemisphere with a radius of curvature equal to the diameter of the cylinder [1], but it can also have a more truncated form. Moreover, the tip is covered with an oxide layer that is produced during the etching process, which can have a thickness of up to 15 nm at the apex [2]. Exposure to air also causes the tip to be covered by an oxide layer. It is therefore clear that high quality W-tips need additional treatment after they have been etched.

This subsequent treatment is aimed at removing the oxide layer as well as at sharpening the tip apex. It can consist of heating the tip in vacuum or *ex situ* immersion in a concentrated HF solution [3] to remove the oxide, self-sputtering which sharpens the apex, or an ion-bombardment that cleans and sharpens the tip at the same time [4]. Also, applying voltage pulses to the tip when it is in tunneling condition over the sample surface is sometimes used in the hope to change the tip density of states (DOS) at the apex to a more favorable one.

This chapter explains the methods we use to prepare and characterize polycrystalline tungsten STM-tips. During implementation of our tip preparation method, further research was necessary, and the results of that research are presented as well. Much of the content of this chapter is also described in ref. 16.

We have used the method of heating and subsequent self-sputtering with Ne^+-ions as described by Albrektsen *et al.* [5,18]. At a later stage, an Ar^+-ion gun was installed as well. First, we will describe our experimental procedures for tip preparation and tip characterization. We choose to mention many details while describing our method, since the ignorance of such "insignificant" details is often the factor that complicates the implementation of a new experimental method. Tip preparation involves a fair amount of alchemy, and we think it is important to mention those details that may be useful to those who start making tips.

During self-sputtering, we record the evolution of the sputtering voltage as a function of time. We have discovered a highly specific and very reproducible pattern,

which we will show to be associated with the decapitation process described earlier for ⟨111⟩-oriented monocrystalline tungsten tips by Schiller *et al.* [1]: During the self-sputter process, a “head-and-neck” structure forms just behind the apex. At some point, the head is torn off, which leaves a very sharp tip. We can recognize the moment at which the head is torn off from the pattern in the sputtering voltage. By terminating the self-sputter process immediately after the decapitation as observed from the pattern in the sputtering voltage, we are able to produce high-quality STM-tips by self-sputtering with high reliability (success-rate is about 75 %). Our tips routinely yield atomic resolution on the {110}-surfaces of GaAs and InP.

We will also present a model that is used to interpret field emission characterization measurements. This model allows us to estimate the apex radius of a tip from field emission measurements within a margin of 5 nm. The field emission measurements suggest that the polycrystalline, nominally unoriented tungsten wire that we use for the manufacture of STM-tips, has a preferential orientation of the ⟨110⟩-crystal axis along the long axis of the wire. Such orientation is a known effect of wire production [12,13].

An experimental complication when using the self-sputtering method is the possible occurrence of vacuum-arcs, which can completely destroy the apex of a tip. Our experience on vacuum-arcs and their prevention is explained. Finally, we make comments on our experiences with regards to the Ar^+-ion bombardment and its combination with the self-sputtering technique.

3.2 Tip preparation method.

Our method of tip preparation has four steps, which will each be described in detail in this section. First the tips are etched. Inside the UHV-system, the tips are outgassed (see section 2.3) after which they are heated to remove the oxide layer. The third step in the preparation process is self-sputtering in order to decrease the radius of curvature of the apex from about 50 nm, which is usual for an etched tip, to about 10 – 15 nm. A lot of experimental effort has been devoted to the proper implementation of this step, and it will therefore be described in much detail. The last step is a light Ar^+-ion bombardment. After these treatments have been completed, the tip can be used for STM. In the last part of this section we will explain the characterization measurements that we carry out on our tips (*in situ* field emission measurement and *ex situ* characterization by SEM for a limited number of tips). We will also describe the method that we use to regenerate tips that have been used in a previous measurement, in order to use them a second time.

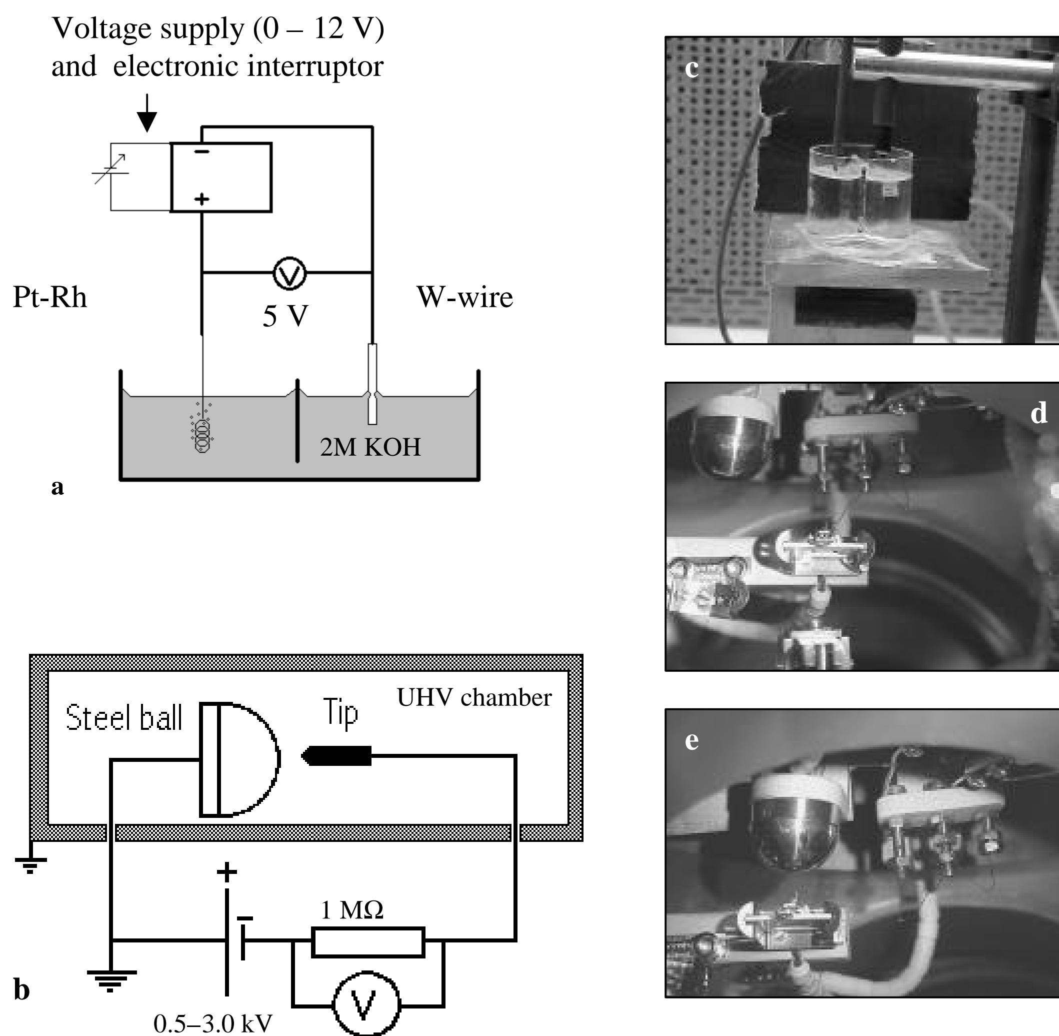

Fig 3.1a: *Schematic drawing of etching-setup.* **b:** *Set-up for self-sputtering. The system is electrically isolated from the UHV system.* **c:** *Photograph of the beaker-glass with the tip (left) and counterelectrode (right).* **d:** *Position of the tip during heating. The L-shaped filament is oriented more or less vertical. The shaft of the tip is placed such that it catches underneath the filament when the tip is raised with the manupulator. During the treatment, the tip (including the shaft) glows brightly orange. The filament itself glows white. We have two filaments in the system, one serves as backup.* **e:** *Photograph showing the tip and hemispherical counterelectrode (diameter 20 mm) during self-sputtering. The tip and tipholder are placed in a carrier plate used for transport inside the UHV system.*

3.2.1 Tip etching

Our tips are made out of 99.98% pure polycrystalline tungsten wire [7] (∅ 0.25 mm), of which a 1 cm piece is spotwelded onto a tipholder. The wire is then etched two times: the first etch is meant to remove the end of the wire which has been split by the mechanical cutting, the second etch produces the actual tip. The tips, carrier plates (see figure 3.1 d,e) and the pincers to handle the tips are cleaned ultrasonically between the first and second etch in the same way as the sample holders are cleaned (see Sect. 2.4). We use the standard DC-drop off method [8 (p. 283)] for etching with the following characteristics: The electrolyte is a 2 M. KOH solution, etching voltage is 5 V, the counter electrode is a small Pt-Rh spiral. The process is carried out in a beaker-glass that has a partition in the middle which ensures that the flow around the W-wire is not disturbed by the H_2-gas produced at the counterelectrode. As the reaction products (mainly $WO_4{}^{2-}{}_{(aq)}$) [8 (p. 282)] dissolve in the etchant, they sink down along the wire. The effect is visible since the reaction products locally changes the diffractive index of the liquid. We found the effect very useful for monitoring the etching process. The “tail” of reaction products drooping from the wire being etched should hang straight down from the wire, or at least, look stable in time. The process is cut by an electronic interruptor which opens the circuit when the current drops below a preset value (switching time is about 10^{-6} sec). The tip is then immersed in de-ionized water for a few minutes to remove any remnants of the KOH-solution. After inspection with an optical microscope it is stored under ethanol for up to a few hours until a complete batch of 4 tips is ready for loading into the UHV-system.

We found that it is necessary to pay a lot of attention to the quality of the etching solution. For instance, when the etchant is stored in a plastic bottle over longer periods of time, the tips that are etched with it are partly covered with a contamination that looks like sea-weed in Scanning Electron Microscopy (SEM). We suspect that this contaminant consists of strands of the plastic of which the storage bottle in which we kept our etchant, was made. The contaminant shows up dark in SEM, which is consistent with the contaminant being a non-conductive material. Furthermore, the notion that a 2M KOH-solution would dissolve small amounts of (certain) plastics is a plausible one as well [19]. Also, it seems that small quantities of dissolved metal accallerate the etching process. When using a metal spoon to weigh and stir the solution, the etching process proceeds a lot faster than usual and the normal flow of reaction products around the wire does not form. The resulting tip shape is quite peculiar (sort of step-like) and the apex is blunt. As countermeasures, we do not keep any etching solution ready for use for longer than a day and we use only glass objects to prepare and handle the etchant. Such “alchemistic” effects however, may well differ from one laboratory to the next.

After loading into the UHV-system the tips and carrier plates are outgassed in the same fashion as the samples (see Sect. 2.4). After that, the subsequent steps in the preparation process (heating, self-sputtering and Ar^+-ion bombardment) are carried out.

3.2.2 Heating

For heating, the tip is brought into mechanical contact with a hot filament in UHV. The filament is heated by passing 4 - 5 A dc current through it. The energy needed to heat the tip is entirely provided by heat-conduction from the filament to the tip: No current flows through the tip itself. The filaments are made out of the same material as the tips themselves (figure. 3.1 d). During the treatment, the tip glows brightly orange [25]. From its colour, we estimate the temperature of the tip to be in the order of 1000 ^{o}C. The treatment lasts 20 minutes. Figure 3.1 d,e shows the filaments. The filaments have the shape of the letter Λ. The tip is placed between the two vertical legs the filament and raised until the tip is catches underneath its point. The tip has to be pressed rather firmly against the filament, otherwise the thermal contact does not allow enough heat to be transferred in order to heat the tip to a sufficiently high temperature. Some of the tips we etch have a shaft which is too short to make adequate contact. These tips are bombarded with 500 – 750 eV Ar^{+} ions for about 1 hour instead.

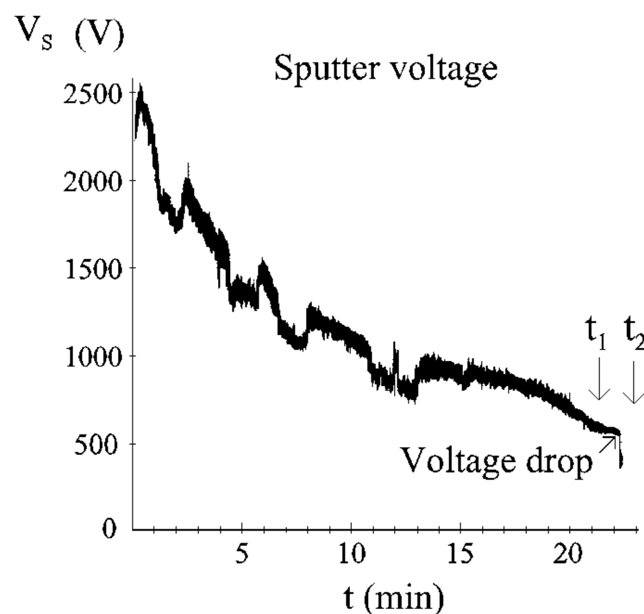

Fig. 3.2: *Typical behaviour of the sputter voltage $V_S(t)$ as a function of time (see subsection 3.2.3). The sputter voltage is usually 1.0 – 2.5 kV at the start and drops to about 600 V. In this case, the noise in the V_S-signal starts to decrease after 17 minutes. The drop occurs after 22 minutes, after which the sputter process continued for a few seconds. This created the mark observed right after the drop. After sputtering the tip radius was estimated to be 13 nm (V_{FE}(1 nA) = 262 V).*

3.2.3 Self-sputtering

After removal of the oxide layer, the tip is placed in front of a 10 mm radius stainless steel hemisphere acting as a counterelectrode, to carry out the self-sputter process (figure 3.1 e). This process has been used earlier by Albrektsen *et al.* [5,18] and by Ekvall *et al.* [17]. The distance between the tip and the counterelectrode is 5 ± 1 mm. Neon gas is let into the vacuum chamber to a pressure of about 1.5 – 2.0 x 10^{-5} torr (base pressure is less than 1 x 10^{-9} torr), and a negative voltage is put on the tip. This sputter voltage (V_S) is typically about 2 kV and is chosen such that a field emission current of 10 μA is generated. Our high voltage supply (Fug HCN 14-12500) is operated in constant current mode. We monitor the sputter process by recording the sputter voltage as a function of time [$V_S(t)$]. The typical behaviour is shown in figure 3.2. As the tip sharpens during sputtering, the voltage decreases to about 600 V. In this regime a very specific pattern consisting of a decrease of the noise-amplitude of the sputter voltage, followed by a very fast drop in the order of 50 V, occurs. After this drop the process is cut off.

We can carry out the self-sputtering process with high reliability. Presently we achieve a success-rate of about 75 %, which was estimated from about 100 attempted sputtering treatments carried out as part of our normal use of the STM-setup, over a period of 10 months. In this estimate, the regenerated tips have been included. Achievement of the reported success-rate during self-sputtering, however, depends strongly on several experimental conditions: Firstly, the tip must have a certain sharpness at the beginning of the sputter process. If prior to sputtering the field emission voltage of a tip [V_{FE}(1 nA)] exceeds 2 kV, we will not attempt to sputter it. Secondly, the sputtering-gas must be free of contaminants to avoid vacuum-arcs (see section 3.6). For the same reason, it is important that the oxide layer present on the tip is adequately removed. Lastly, the setup for self-sputtering (tip holder and manupulator, counter electrode and wiring) must be designed in such a way that no significant amount of current can leak away from those parts of the setup that are at high voltage. For this reason, placing the setup well away from the walls of the vacuum chamber and avoiding a design having many sharp edges or corners, is preferable.

3.2.4 Argon ion bombardment

The last step in the preparation process is a light, head-on Ar^+-ion bombardment. We currently favour the following parameters: 750 eV, 6 μA/cm^2, and between 7 and 10 minutes of sputter-time depending on the initial sharpness of the tip. The width of the ion-beam is 0.5 cm, so positioning the tip with respect to the ion-gun is not very critical. The purpose of the ion-bombardment is to increase the stability of the tip: According to ref. 1, the tips that are self-sputtered in the way as we described it have a very small "tail" at the apex. The ion bombardment is applied to remove any such structures in a controlled way. Tips that had a V_{FE} (1 nA) of more than 300 V at the start of the ion bombardment tend to get slightly sharper during the bombardment, whereas tips that had a V_{FE} (1 nA) of less than 300 V become slightly blunter. The difference in field

emission voltage before and after the treatment is usually less than 20 V. The ion-bombardment is not needed to obtain high resolution on GaAs {110} or InP {110}. Before the installation of the ion-gun, we routinely obtained atomic resolution with tips that had been only heated and self-sputtered. We show figure 3.3 as an example, which was obtained with a tip that had been heated and self-sputtered, but which was not bombarded with Ar^+-ions.

3.2.5 Tip characterization

The self-sputtering technique features an inherent possibility for characterization of the tips by field emission. In the same geometry as in which a tip is self-sputtered, we measure the voltage needed to draw 1 nA of field emission current [V_{FE}(1 nA)]. The field emission current is limited to 1 nA because at higher currents, the tip apex is frequently altered during the measurement. The voltage is kept constant and the current typically fluctuates by a factor 0.3. After etching and heating, the tips generally emit 1 nA at V_{FE} = 1.0 ± 0.5 kV, indicating a radius of the order of 50 nm. The self-sputter process decreases this voltage to between 200 and 400 V. In that case, the apex has an estimated radius of 8 – 15 nm. This radius is also typical for our completed STM-tips. Our tips give good topographic results on *in situ* cleaved GaAs and InP (110) surfaces, with the best tips having a V_{FE}(1 nA) value of about 250 V.

A limited number of tips has been investigated using Scanning Electron Microscopy (SEM). The tips were transported to the SEM (JEOL JSM-6400F FEGSEM operated at 15 kV) through the ambient air, involving an exposure of about 30 minutes.

3.2.6 Regeneration of tips

We often regenerate tips that have been used in previous measurements. This practice yields good tips and saves time. We estimate that at present, between a fourth and one half of our measurements are carried out using regenerated tips. The regeneration process consists of repeating the self-sputter process and Ar^+-ion bombardment. In both steps the same parameters are used as during the preparation of a new tip. After its use in STM, the field emission voltage of a tip is usually around 300 - 400 V. We favour repeating the self-sputter process for a used tip, even if the field emission voltage is low. The reason is that during the measurement, the tip may have been deformed or contaminated during the measurement. This might show in the field emission measurement, but if the damage is on the atomic scale, it also might not. The observation that the tip shows “normal” sputtering behaviour is used as an indication that this is not the case, and that the tip can be expected to behave as a new one does. Sputtering a used, already sharp tip often takes longer as the sputter voltage is lower than for a new tip (300 – 500 V). This decreases the energy of the incident ions, which in turn decreases the sputtering yield of the ions. After being used in a measurement for

the first time, most tips go through 2 or 3 cycles of regeneration and new measurement. The tip is discarded when self-sputtering fails to produce a good tip.

The tips that we produce routinely show clear atomic corrugation of the {110} surfaces, in both the ⟨-110⟩ and the ⟨001⟩ direction. Many of them show minor mechanical instabilities which manifest themselves as horizontal stripes coinciding with the fast scan direction (which is horizontal). We have to correct for this by subtracting the slope from each scan-line (see figure 3.3 and Sect. 2.5). We have the impression that tips which have been self-sputtered and bombarded with Ar^+-ions are mechanically somewhat more stable than tips that have only been self-sputtered.

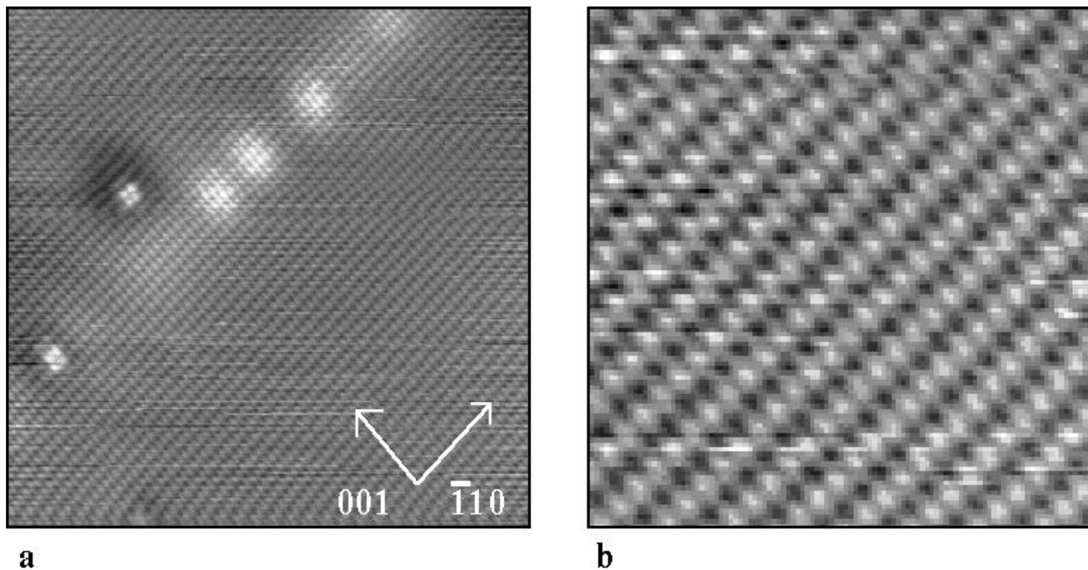

Fig. 3.3 a: *STM-image of a Si δ-layer (10^{13} cm^{-2}) in GaAs. The layer was grown by MBE on a Si-doped (10^{18} cm^{-3}) GaAs wafer. Tip preparation: etching, heating, self-sputtering (V_{FE} (1 nA) = 336 V). The frame (25 x 25 nm^2, greyscale 0 – 96 pm) shows a number of Si donors (white hillocks). The horizontal stripes are a sign of minor tip-instability for which is corrected as explained in the text. V_{SAMPLE} = -1.93 V, I = 96 pA, 400 x 400 data points.* **b:** *Cut-out from the lower right portion of the left frame showing the crystal lattice, on which no further background corrections were carried out (6.6 x 6.8 nm^2, greyscale 0 – 46 pm). Corrugation amplitudes are 23 pm along ⟨-110⟩ and 25 pm along ⟨001⟩.*

3.3 Description of the self-sputtering behaviour.

As outlined in the previous section, we monitor the sputter voltage during the process. A typical sputter curve (V_S as a function of time) is shown in figure 3.2, along with an STM-image on GaAs {110} as we typically obtain it with tips made as described in this chapter (figure 3.3). The behaviour of the sputter voltage typically consists of three phases: First, V_S drops from its initial value to about 600 V. Then the amplitude of the noise in the V_S signal decreases. Finally, V_S suddenly drops. The time-scale of the drop is far less than one second. If the sputter process is then allowed to continue, the sputter voltage often slowly increases to a value compareble to the value of V_S at the time just before the voltage drop. The noise level has then increased again to its old value. After a varying amount of time the whole sequence of a decrease in noise followed by a sudden drop can be repeated.

It has been shown by Schiller *et. al.* that during the self-sputter process which we use, it is possible that a "head and neck" structure forms just behind the apex of the tip [1]. Their tips were etched from ⟨111⟩-oriented monocrystals. At some point during the sputter process, the neck becomes too thin to withstand the electrostatic force that acts on the head, and the head breaks off. The existence of the head and neck structure was shown by Transmission Electron Microscopy (TEM), the head measures 20 by 50 nm. Its formation is accompanied by a very specific pattern in the angular distribution of the emitted electrons which Schiller and his co-workers studied using a phosphor screen as the counter electrode. When the head breaks off, the emission pattern changes radically and a drop in sputter voltage is also observed. In its final shape, the tip has a very small "tail" at the apex. The formation of the "neck-and-head" structure occurs only for relatively sharp tips (apex radius less than about 100 nm) and low field emission currents ($I_{FE} < 20\ \mu A$) [1].

We now show SEM-micrographs of two tips for which the sputter process was terminated at different times (figure 3.4): For the first tip (figure 3.4 a), the sputter process was terminated during the decrease of the noise amplitude, at the moment that we thought the expected drop of the sputter voltage was eminent (t_1 in figure 3.2). For the second tip (figure 3.4 b), the sputter process was allowed to progress until immediately *after* the expected voltage drop (t_2 in figure 2), in the same manner that we normally use for manufacturing STM-tips.

Figure 4a clearly shows that a neck and head structure has formed, similar to the structure reported by Schiller *et. al.* After the drop in V_S(t)-signal, the head and neck structure is no longer there (figure 3.4b). We therefore conclude that the decapitation process as it is described by Schiller *et al.* [1] occurs during the sputter treatment that we apply to our tips, and that this is accompanied by an observed decrease in noise in the V_S-signal. As the formed head is torn away from the tip, the sputter voltage suddenly drops. This gives us the possibility to recognize the moment at which the head is torn off, and thus the most favourable moment to terminate the sputter process, *without* the use of a phosphor screen.

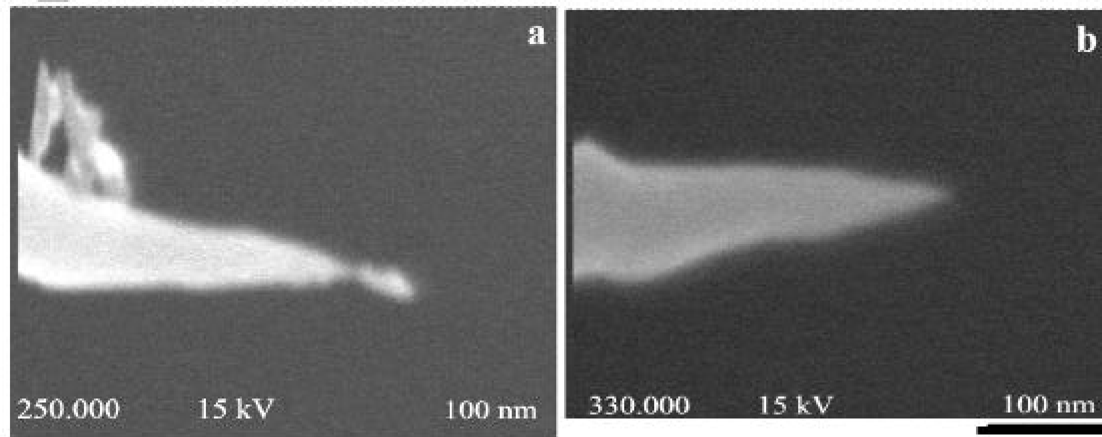

Fig. 3.4 **a**: *Tip for which the sputter process was cut off at t_1: A neck and head structure has formed on the tip. The structure on the tip shaft (left) is a contamination, possibly a remnant of the KOH-solution used for etching the tip. The images are slightly deformed along the left edge, this is an artefact of the SEM. Magnification: 250000 times, acc. voltage: 15 kV.* **b:** *Tip for which the sputter process was cut off at t_2: The apex has no neck at all. V_{FE} (1 nA) = 268 V. Magnification: 330000 times, acc. voltage: 15 kV.*

3.4 Characterization of STM-tips by field emission.

We use field emission measurements as a quick and simple way to characterize our tips, both between the different stages of the *in vacuo* treatment as well as after the completion of the preparation process. As we have standardized the parameters (field emission current: 1 nA, tip – counter electrode distance: 5 mm) of the measurement, we can more or less predict the performance of a tip in STM from the field emission measurement based on our experience alone. We have nevertheless developed a model which allows us to estimate the radius of the tip from the field emission measurements.

The model is based on the Fowler-Nordheim relation for field emission of electrons from a metal [6]:

$$J_{FN}(E,\Phi) \quad = \quad 1.537\cdot 10^{14}\,\frac{E^2}{\Phi t^2(y)}\exp\left[-\frac{0.683\cdot\Phi^{3/2}}{E}v(y)\right] \qquad (3.1)$$

$$y \quad = \quad \frac{3.79\sqrt{E}}{\Phi} \qquad \begin{array}{l} v(y) = 1.0029 - 0.1177y + 1.1396y^2 - 0.2561y^3 \\ t(y) = 0.9967 + 0.0716y + 0.0444y^2 \end{array}$$

J_{FN} is the current density (A/m^2), E is the electric field at the surface of the emitter (V/Å), ϕ is the work function (eV). The numerical values for $t(y)$ and $v(y)$ are also given in ref. 6, from which we obtained the polynomial fits given along with equation 1. To calculate the electric field at the surface of the emittting tip, we use the potential distribution as it is calculated by Dyke *et. al.*[9,10] for a small sphere on top of a narrow cone:

$$V \quad = \quad \left(\frac{V_R}{R^n}\right)\left(r^n - a^{2n+1}\cdot r^{-n-1}\right)P_n(\cos\boldsymbol{q}) \qquad (3.2)$$

The shape of one of the equipotential surfaces surrounding this sphere-on-cone closely follows the contour of an actual emitter tip [9,10]. In the used geometry, the sphere-on-cone is at ground, the equipotential surface representing the tip is at a potential V and the counter electrode is represented by an other equipotential surface at a potential V_R. The origin of the coordinate system *(r,* ***q****)* lies at the centre of the small sphere, the axis $\boldsymbol{q}$ = 180° coincides with the axis of the cone. The (shortest) distance between the centre of the sphere and the anode is along $\boldsymbol{q} = 0$ and equals R. The difference V_R-V equals the applied voltage between the experimental tip and counterelectrode, V_m. The constants a and n together define the shape of the tip: a is the radius of the small sphere, and n is to be chosen such that the Legendre-polynomial $P_n(cos\boldsymbol{q})$ vanishes when $\boldsymbol{q}$ equals the exterior half-angle of the cone, *i.e.* where the cone and the small sphere meet. We use n = 0.10 and a= 0.30875×r_0. The distance r_0 (measured along $\boldsymbol{q} = 0$) between the centre of the sphere and the equipotential surface V equals the radius of curvature of the emitter tip that the equipotential surface V represents, as the apex of the equipotential

surface is nearly a hemisphere. The electric field at the emitter surface can be calculated from the potential. Dyke *et.al.* found that close to the tip the field can be described by the relation [9,10] :

$$E = \frac{\boldsymbol{b}}{\boldsymbol{b}_0} E_0 \tag{3.3}$$

The factor $\boldsymbol{b}_0$ gives the ratio V_m/E for $\boldsymbol{q} = 0$, and $\boldsymbol{b}/\boldsymbol{b}_0$ describes the variation of the electric field as a function of $\boldsymbol{q}$, where r varies as a function of $\boldsymbol{q}$ to follow the shape of the emitter. We determined $r(\boldsymbol{q})$ by solving eq. 2 for r using a discrete set of values for $\boldsymbol{q}$. We then obtained a fit for the different $(\boldsymbol{q},r)$ points. $\boldsymbol{b}_0$ depends on (r_0, R, n, a) and $\boldsymbol{b}/\boldsymbol{b}_0$ depends on $(r(\boldsymbol{q}), r_0, n, a, P_n cos(\boldsymbol{q}))$. Exact expressions for $\boldsymbol{b}_0$ and $\boldsymbol{b}/\boldsymbol{b}_0$ are given in ref. 9 and 10. The Legendre-polynomial $P_{0.1}(cos\boldsymbol{q})$ is evaluated using a power-series [11].

We now have all the information needed to calculate the electric field at the emitter surface as a function of $\boldsymbol{q}$. That yields the following fit for $E(\boldsymbol{q})$ for $n = 0.1$ and $a/r_0 = 0.30875$:

$$E = 0.368 \frac{V_m \left(1 + 0.00425\boldsymbol{q} - 0.137\boldsymbol{q}^2\right)}{r_0^{0.9}\left(R^{0.1} - 0.75 r_0^{0.1}\right)} \tag{3.4}$$

The next step is to insert the now known electric field into the Fowler-Nordheim relation (eq. 1). V_m and R are known from the experiment, and r_0 is assigned a value since it is used as the free parameter. We assume an average work function of 4.5 eV which seems justified from figure 16 in ref. 9, in spite of the known differences of work function for the various crystallographic planes of tungsten [9]. We can thus obtain $J_{FN}(\boldsymbol{q})$ (figure 5a) and integrate this quantity over the entire frontal hemisphere of the tip to obtain the total field emission current. We have also used this to determine the theoretical relation between the tip radius (r_0) and V_{FE}(1 nA) (figure 5b).

In order to test our model experimentally, we measured a series of field emission currents for different voltages for one tip and constructed a Fowler-Nordheim plot from the data (figure 6a). In such a plot, $\log(J/E^2)$ is plotted against $1/E$ and the data points are expected to form a straight line (for fields ranging from 0.3 V/Å to 0.5 V/Å) [6]. To account for the fluctuation in the field emission current, we recorded the current-signal

to determine the lower and upper bound of the current. These upper and lower bounds of the field emission current correspond to the upper and lower ends of the error bars in figure 6a. As the field and current density change as a function of θ, we use E_0 and J_0 (E resp. J for $\boldsymbol{q} = 0$) to make the Fowler-Nordheim plot. We estimate the experimental value for J_0 from:

$$J_0^{\exp} = \frac{I_{measured}}{\int_0^{P/2} \frac{J^{theory}(\boldsymbol{q})}{J_0^{theory}} d\boldsymbol{q}} \tag{3.5}$$

While making the plot, we have used the tip radius as the free parameter to optimize the agreement between the theoretical and experimental data. As the assumed radius was varied, the intersection between the theoretical line and the line formed by the experimental points shifted from the bottom right for r_0 = 17 nm to the upper left for r_0 = 20 nm. We therefore estimate the tip radius to be 18 ± 2 nm. This is in good agreement with the value for the tip-radius that we estimate from the SEM-micrograph (figure 6b) which is 17 ± 5 nm. We have repeated the same field emission experiment for a tip which was etched from a ⟨111⟩-oriented monocrystal. The fluctuations in the current were less than 5 % for all but one data point, which is much less than is typical for polycrystalline tips, so no error-bars are drawn for the monocrystalline tip.

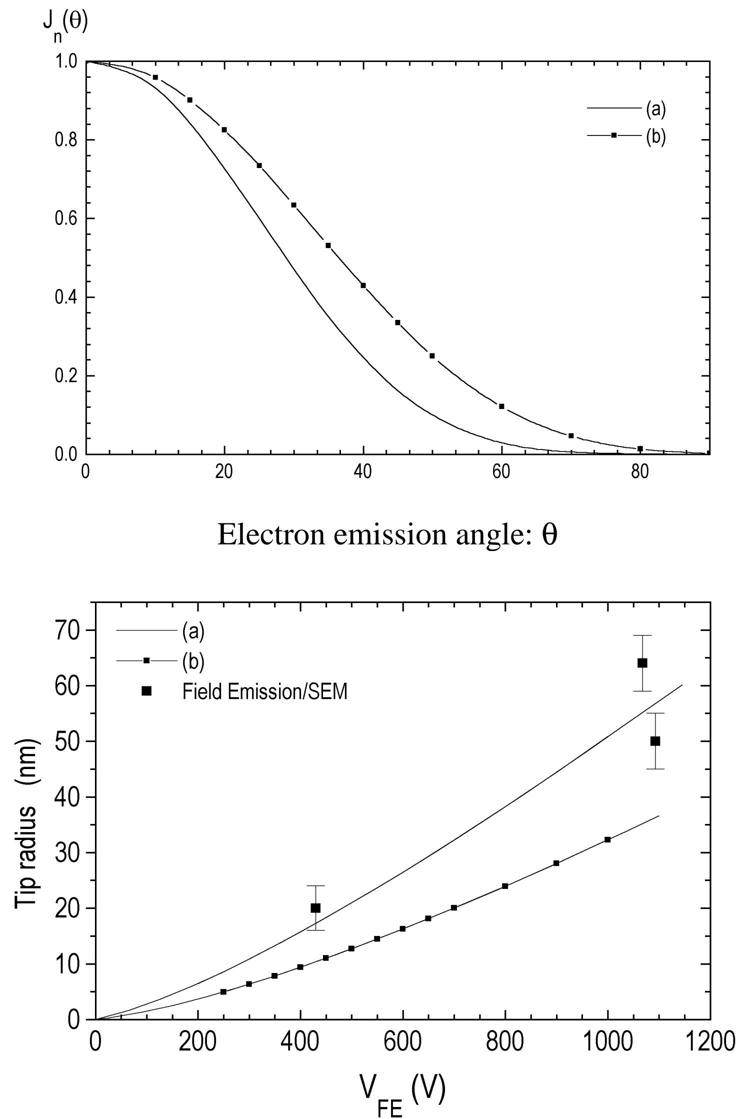

Fig. 3.5a: *Field emission current density vs.θ as predicted by the model (normalized so that $J(\theta = 0)$ equals 1). Curve (a): $I = 1$ nA, $V_{FE} = 400$ V. Curve (b): $I = 10$ μA, $V_{FE} = 689$ V. The squares on curve (b) have no other meaning than as a way to distinguish the two curves. Note that for the higher voltage, the current is emitted over a wider area on the tip. The current density vanishes for $\theta > 60^o$, meaning that practically no current is emitted from the tip shank. The tip radius is 16 nm.*
b: *Theoretical relationship between the tip radius (r_0) and field emission voltage. Curve (a): $I = 1$ nA. Curve (b): $I = 1$ μA. The squares on curve (b) have no other meaning than as a way to distinguish the two curves. For three tips, we plotted the experimental V_{FE} (1 nA) against the tip radius obtained by SEM for comparison. The left point (430 V, 1 nA) was generated by the same tip that was used for figure 6. The other two points come from tips that were etched and heated, but not sputtered.*

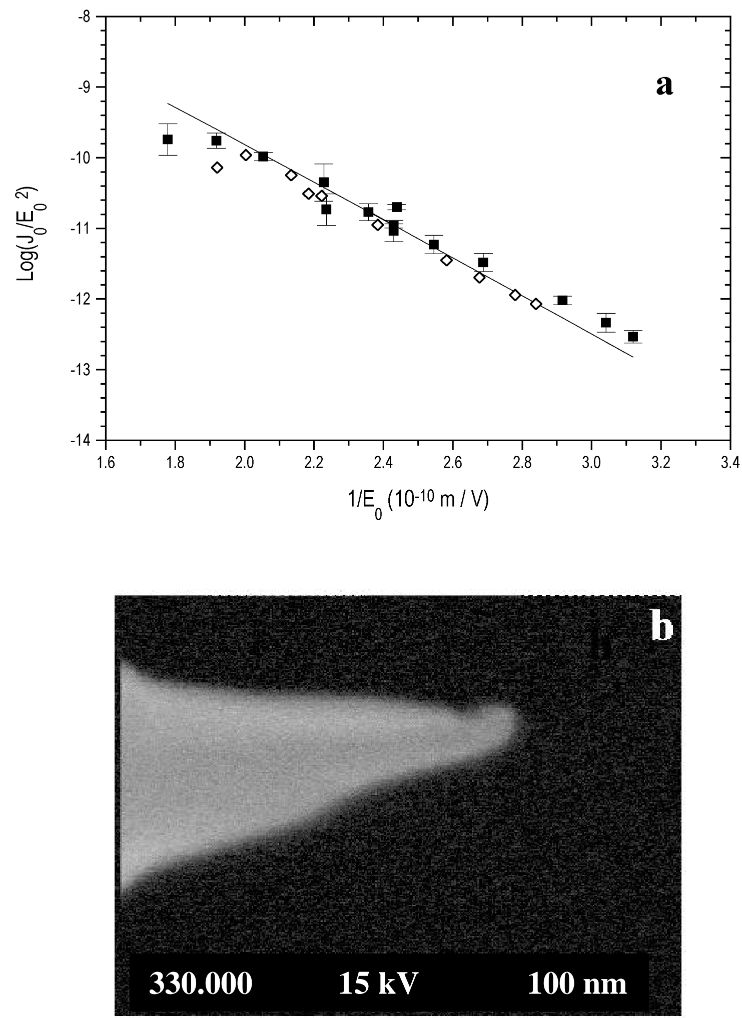

Fig. 3.6a: *Fowler-Nordheim plot taken from a typical STM-tip (squares with error-bars). The estimate for the tip radius is 18 ± 2 nm. We have included the results of the same measurement taken from a tip which was etched from a* **á111ñ**-*oriented monocrystal for comparison (diamonds). Radius of the* **á111ñ**-*oriented tip was 8 nm. We attribute the deviation of the data point on the far left to the fact that the measurement may have altered the tip. The point corresponds to the last (I,V) point taken, which had the highest applied voltage.* **b:** *SEM-micrograph of the same tip taken ex situ. From the micrograph we estimate the radius to be 17 ± 5 nm (magnification 330.000 times, acceleration voltage 15 kV).*

3.5 Discussion on self-sputtering behaviour and field emission characterization.

In spite of the good agreement between the tip radius obtained by SEM and the one extracted from the field emission measurements, figure 6a shows that the slope of the theoretical line does not fully match the data. This mismatch is quite typical. Since the slope of a Fowler-Nordheim plot depends on the work function of the emitting surface, one's first thought would be that the (effective) work function of our tips is not 4.5 eV, but rather, slightly less. Repeating the calculation for a different work function, however, does not lessen the mismatch in these slopes: Both the theoretical and the experimental data are affected by a change in this parameter and the mismatch remains. For a given set of field emission data, the best fit for the radius *will* of course change if a different work function is assumed. It is in fact possible to obtain a continuous range of tip radii simply by adjusting the work function. Therefore, the work function has to be determined independently in order to obtain a reliable value for the tip radius. We have always used $\Phi = 4.5$ eV which is commonly used as the (average) work function for clean tungsten [6,9,10]. The agreement in radii obtained from field emission data and those determined by SEM (figure 3.5 and 3.6 a, b) shows that $\Phi = 4.5$ eV is a realistic value.

If a tip is contaminated, its work function is changed and the estimate for the tip radius will change as well. This is particularly important in case a single (I,V) point is taken like we often do when we carry out a quick and simple characterization of our tips during and after preparation. In that case, a low V_{FE} (1 nA)-value caused by a tip having an unusually low work function cannot be distinguished from a tip which has a sharp, but clean apex. A barium covered tungsten surface can have a work function as low as 2.44 eV [9]. On one occasion we observed a tip in SEM to have a radius of 94 nm while this tip had a V_{FE} (1 nA) voltage of 688 V, indicating a radius of 33 nm for $\Phi = 4.5$ eV or a radius of 94 nm for $\Phi = 2.6$ eV. This tip had been glowed in UHV, but had not received any sputter treatment. We expect, however, that particularly after sputtering most surface contaminants are removed from the apex and its immediate vicinity.

To look for a possible explanation of the difference between the experimental and theoretical slope in the Fowler-Nordheim plot, let us look at the two ways in which our tips differ from the model tip which is used by Dyke and Dolan: Its physical shape on a scale of about 100 nm may be different from the shape concidered in the model, as is shown in figure 6b. Secondly, the emission current density distribution may differ from the distribution shown in figure 5 since the model assumes a uniform work function across the entire surface of the tip. Modifications to the emission pattern as a result of the different facets of the apex having different work functions are not taken into account. SEM micrographs of our tips indicate that the apex usually consists of a single grain; occasionally a grain boundary intersects the apex [24]. A very special case of such a modification of the emission pattern occurs when the central facet of the apex is a {110} plane. This plane has a high work function (6.11 eV) [9], so that at the apex itself very little electrons are emitted. The electrons are mostly emitted from the other facets surrounding the {110}-facet, so that the emission pattern more or less forms a ring around the apex (figure 3.7) [9].

This geometry could be quite common as the process of wire drawing induces a preferential orientation of the crystal-grains along the wire-axis [12]. In bcc metals like tungsten, this is the ⟨110⟩ direction [12]. At the same time, the crystals become thin and elongated with the long axis parallel to the wire axis. Since the polycrystalline, nominally unoriented tungsten wire that we use is drawn through holes ("dies") to thin it down to size [7,13], we expect that the crystal grains in the wire are oriented with the ⟨110⟩ direction along the wire axis, causing the central facet of the tip to be a {110}-facet. The thin, fibre like structure expected for such wires we have also observed by studying the fracture surface of a split tungsten wire by optical microscope. We would like to emphasize that the wire we use is commercially available, standard tungsten wire. If one orders polycrystalline tungsten wire of a given diameter without any further specifications, this is the type of wire one is likely to get.

For all our tips, the circumstances of wire production have been the same as they have all come from the same roll of tungsten wire. This orientation leads to a field emission current density distribution which is significantly different from the one predicted by the model. For this reason, we suspect that the mismatch between the theoretical and the experimental slope is caused by it. Moreover, since all our tips have come from the same wire, this could also explain why this mismatch occurs with the high reproducibility that we have observed. If the mismatch were to be caused by the shape of the tip, we would expect more variation in the mismatch. This notion is also supported by the fact that the mismatch does not occur in the Fowler-Nordheim plot that we took from a ⟨111⟩ oriented monocrystalline tip, which has an emission pattern that agrees much better to the pattern assumed in the model [14]. The mismatch that we just discussed still allows us to estimate the tip radius from the field emission measurements as figures 3.5 and 3.6 show. We have also found that the V_{FE} (1 nA) voltage is a good indicator of a tip's performance in STM.

The formation of the "neck and head" which leads to the decapitation during sputtering can be caused by one of several mechanisms, three of which are mentioned by Schiller *et al.* and references therein: 1) The density of impinging ions is larger on the shank, 2) the ions strike the tip surface at an angle instead of perpendicularly, which gives them a higher sputtering yield, and 3) the high-index planes making up the sides of the ⟨111⟩ oriented monocrystal used by Schiller *et.al.* are preferentially sputtered [1].

In case polycrystalline wire is used which is oriented with a ⟨110⟩ direction along the wire axis, most of the electrons will be emitted from a ring just behind the apex. Such an orientation can be either intentional or the accidental result of of thinning down the wire. The density of impinging ions will then also be highest in that area of the tip, which could easily cause a neck and head structure to form. At this point, we have no indication as to which of these mechanisms should be dominant. The ring-like emission pattern of a ⟨110⟩ oriented wire can certainly cause a neck and head to form during sputtering, but the results from Schiller *et al.* show that a ring-like electron emission pattern is no necessary condition for the decapitation process to occur.

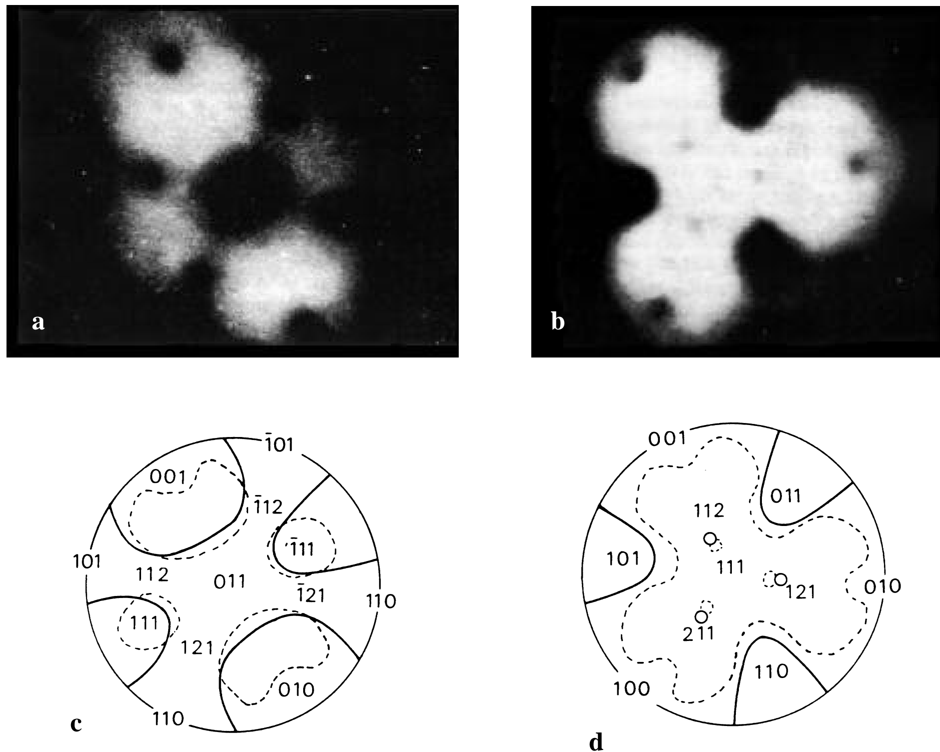

Fig 3.7a, b: *Field emission microscopy images of a* ⟨110⟩*-oriented tip and a* ⟨111⟩*-oriented tungsten tip, respectively.* **c, d:** *Diagram showing the various facets making up the apex for the* ⟨110⟩*-oriented tip and* ⟨111⟩*-oriented tip (from ref. 14).*

We have no clear ideas about the mechanism that connects the formation of the neck-and-head structure to the decrease of the noise in the sputter voltage. The results that we present in figures 3.2 and 3.4 merely show *that* the two effects accompany each other, not *why* this is the case. As already stated in the previous section, the field emission voltage signal from the ⟨111⟩-oriented monocrystalline tip showed remarably little noise in comparison to the field emission voltage of a polycrystalline tip. Possibly, the amount of noise in the field emission voltage signal depends on which of the crysstallographic planes making up the apex emits (most of) the current, or on the geometry of the emission pattern. An emission pattern which is unstable as a function of time could well be a cause for noise in the field emission voltage. One might suspect that the emssion pattern of a ⟨111⟩-oriented tip is more stable than the ring-like emission pattern of a ⟨110⟩-oriented tip, but it is at present unknown to us whether this is really the case or not. It is interesting to note that Schiller *et al.* report that during the neck-and-head formation, part of the current is emitted from the neck and from the back of the head [1].

A possible hypothesis is that during the formation of the neck-and-head structure, the emission pattern changes to a more stable configuration due to the presence of the head. In order to clarify the mechanics behind the decapitation process and the accompanying decrease in the noise of the sputter voltage, an obvious next step would be to study the emission pattern of a polycrystalline tip by means of a phosphor screen during self-sputtering. Such a test would confirm or disprove our expectation that polycrystalline tungsten wire has a preferential orientation along the ⟨110⟩-axis, it would show which crystallographic planes contribute to the total field emission current at different stages of the process, and finally, it would indicate if the stability of the emission pattern changes during the formation of the neck-and-head structure. This experiment, however, lies outside the capabilities of our set-up.

A final remark to make about the characterization measurements by field emission, is that the field emission process and the tunneling process involve different length-scales. For the field emission process, the apex as a whole matters, involving distances in the order of 10 nm. It may therefore be insensitive to features on the apex that are of atomic scale, such as two atoms sitting at the very apex instead of one, or an apex with an unusual local density of states. In principle, this can cause discrepancies between the performance of a tip as predicted by field emission measurements and the actual performance of the tip in STM. Although we generally do not observe such descrepancies, this point is important to remember when interpreting field emission results.

3.6 The occurrence and prevention of vacuum-arcs.

A phenomenon well documented in literature on field emission (microscopy) is the vacuum-arc [9 (p. 122 - 128)]. Several possible causes or initiating factors are listed in ref. 9 and references therein. Our experience is that inadequately heated tips are particularly prone to experience vacuum-arcs, and we therefore regard the mechanism described by Bennett [15] as the most plausible explanation for the vacuum-arcs that occasionally occur when we prepare tips. The mechanism involves an excess amount of positive ions that are generated near the tip apex. As the ions and electrons move in opposite directions, they have an attractive Lorentz interaction. This can cause the volume through which the charge travels between the tip and counterelectrode to contract into a very narrow cylindre. The resulting high current density heats the tip apex which then emits yet more electrons by thermionic emission. In this runaway process the temperature of the apex quickly rises to beyond the melting point of the tip material, (partially) melting the apex (see figure 3.8). The occurrence of vacuum-arcs (or preferably: their absence) is often the factor that limits the success-rate of the self-sputter process. If the wrong experimental procedures are adhered to, persistently occurring vacuum-arcs can decrease the success-rate of the tip preparation procedure to less than 25 %.

In our setup, the vacuum-arc manifests itself as a very large, instanteneous increase in the sputter voltage (ΔV > 1 kV). Afterwards, the tip either has a very high field emission voltage (several kV) or it will emit no field emission current at all for voltages of up to 4 kV. Inspection of some of the tips that have shown this pattern by SEM showed that the tips were melted at the apex. Similar events have also been reported elsewhere [17]. It seems that in some cases the damage sustained by the tip is limited and the sputter process can continue after a vacuum-arc. We have observed on some occasions that the sputter voltage rose instanteneously by 500 V or more, after which the sputter process could be continued to produce a working STM-tip in the end. We attribute this to the occurrence of a "mild" vacuum-arc. In most cases, however, the vacuum-arc ruins the tip completely.

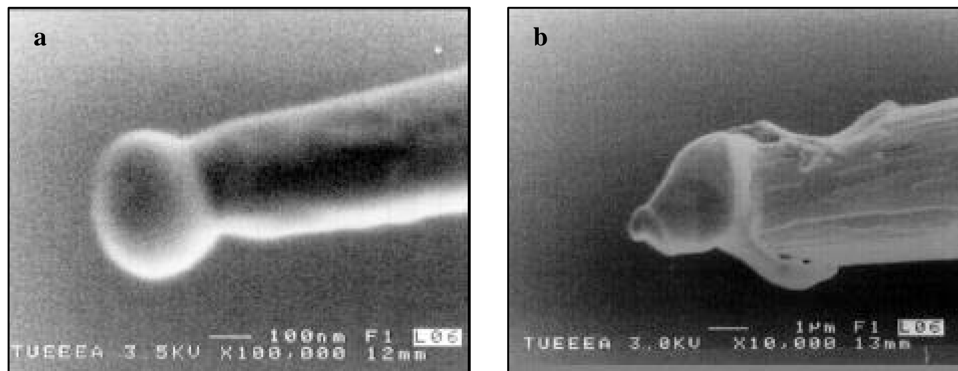

Fig 3.8 a,b: *The effects of a vacuum-arc. During sputtering, the effect manifests itself by an abrubt decrease of the field emission current to zero while at the same time, the high-voltage supply turns out the maximum voltage (as preset by the adjustable voltage limit). Afterwards, the tip will not emit any current for voltages of up to 4 kV. The extent of the damage sustained during a vacuum-arc can vary.*

In our experience, there are two experimental circumstances that strongly increase the chance of a vacuum-arc occurring during the sputter process: Contamination of the sputtering atmosphere, and the tip having a (not adequately removed) oxide layer.

The importance of a clean sputtering atmosphere is best demonstrated by an anekdote: At some point the neon gas-bottle fitted to our UHV system was nearly empty, but the pressure-gauge of the bottle failed to indicate it. As normal operation of the UHV-system continued, ambient air seeped into the supply line through some of the couplings and contaminated the sputtering gas. Over the course of a few weeks, we

observed a very high incidence of vacuum-arcs. The problem was solved by changing the gas-bottle and heating the supply-line for a few hours while flushing it with neon.

We also find it important to keep the supply line at overpressure (0.6 bar with respect to the ambient). The fact that it is needed to heat the supply line after it has been exposed to the ambient (this happens when changing gas bottles or removing the gas bottle during bake-out of the system) suggests that water vapour is involved in the initiation of vacuum-arcs. An other measure currently in place is that we only initiate the sputtering process when the background pressure of the vacuum chamber is below 2.0 x 10^{-9} torr.

There are various ways to clean a tip prior to self-sputtering [2,5,17]: When we started to implement our method of tip preparation, we chose to heat the tips by electron bombardment (see refs 5 and 17 for a description of the method). Vacuum-arcs occurred very frequently during that time. About 3 out of 4 sputter attempts would end with a vacuum-arc. That ended when we adopted the heating method described in Sect. 3.2. We suspect that during the electron bombardment, the tips were not heated enough to desorb the oxide layer completely. Field emission measurements taken before and after such electron bombardment showed that the tip apex generally did not melt significantly during the treatment. At the same time, we never observed the apex to glow as has been reported elsewhere although the effect is difficult to observe [18 (p. 67)].

Heating tips by electron bombardment is a fairly common way to desorb the oxide layer from etched tungsten STM-tips [5,17]. We do not favour this method because it is difficult to assess the temperature of the tip during heating and because only the apex is heated [17]. When the tip is pressed against a hot filament for heating, the colour of the tip can be observed easily. This can be used to assess the temperature or to carry out the heating process reproducibly. Also, the tip is cleaned over a wide area, so that no adsorbed contaminants can migrate to the apex after cleaning. A drawback of our method is that positioning the tip against the filament is a bit tricky.

The presence of an oxide layer can be recognized very easily by a specific behaviour of the tip when characterized by field emission for the first time: As the field emission voltage is gradually increased, an oxide covered tip will not show any field emission until at a certain voltage, the oxide layer experiences a local voltage breakdown somewhere on the apex. This manifests itself by a sudden increase of the field emission current, typically to 10 – 100 nA. After that, the tip shows more or less stable field emission with V_{FE} (1 nA) significantly below the voltage at which field emission first set in. When the voltage is decreased to zero and then gradually increased a second (or subsequent) time, no such hysteresis is observed. The tip then shows the same value for V_{FE} (1 nA) as it did after breakdown on the first attempt. The effect is often accompanied by an unusually low field emission voltage: V_{FE} (1 nA) is about 400 V rather than 750 V < V_{FE} (1 nA) < 1200 V which is typical for a clean, unsputtered tip. The latter is possibly due to a decrease in tip work function caused by the oxide layer. At the time that we still heated our tips by electron bombardment, this hysteresis-like field emission behaviour was very typical for our tips. Presently, we will heat the tip a second time before attempting to sputter it if we observe the hysteresis effect during field emission characterization of the tip.

The measures that we currently apply to prevent vacuum-arcs, are: 1) We ensure adequate heating of the tip. The temperature of the tip is assessed from its colour which must be bright orange. 2) We maintain the neon gas supply line at overpressure. 3) We heat the supply line for several hours while flushing it with neon whenever the inside of the supply line has been exposed to the ambient. 4) We do not initiate the self sputter process if the background pressure of the vacuum chamber exceeds 2.0 x 10^{-9} torr. These measures seem effective in preventing vacuum-arcs, which we experience only occasionally.

3.7 Comments on the argon-ion bombardment.

Head-on sputtering by Ar^+-ion bombardment is a widely used technique to clean and sharpen STM-tips [2,4,17,20]. During such ion-bombardment the sides of the apex are sputtered faster than the apex itself, because ions striking a given surface at an angle have a higher sputtering yield at a given energy than normally incident ones [4,21,23]. The sputtering yield of Ar^+-ions on tungsten is for the energies used in our setup in the order of 1 [22].

For the experimental parameters stated in section 3.2, we estimate that the ion bombardment removes 7 monolayers of tungsten from the tip, assuming that the sputtering yield of the ions equals 1. When a tip is sputtered for a long time, it becomes sharper at first, then reaches a point where the apex radius is minimal, after which the tip becomes blunter as sputtering continues. This observation was made when two tips were sputtered for a prolonged time at 1500 eV and 12 μA/cm^2 while the sputtering process was periodically interrupted to perform a field emission measurement. Minimum V_{FE} (1 nA) values were 552 V and 474 V, which were attained after 1^h 45^{min} and 1 hour of sputtering time, respectively. When the tips are sputtered with lower energies, however, they become sharper. Those tips that we sputter with Ar^+-ions in order to clean them have been observed to have a V_{FE} (1 nA) value of about 250 V (500 – 750 eV, 6 – 8 μA/cm^2, 1 hour). During subsequent self-sputtering, such tips show quite normal sputtering behaviour. We have at present not tried out a tip in STM that was cleaned and sharpened by Ar^+-ion bombardment alone, but there is no reason to suspect that such a tip would *not* give atomic resolution. We have presently not yet fully explored all possibilities for tip preparation by Ar^+-ion bombardment, but it seems that ion-energies between 0.5 keV and 1.0 keV are well-suited for sharpening tips.

It may seem redundant to equip a UHV-system with both an Ar^+-ion gun and a setup for self-sputtering. When the UHV-system was designed, we in fact intended to use the self-sputter process alone. As problems to reliably produce working STM-tips persisted, the decision was taken to install an ion-gun as an alternative to self-sputtering. By the time the ion-gun was installed, however, our understanding of self-sputtering had increased sufficiently in order to use the self-sputter process reliably.

In hindsight, it has proven very useful to posess both sputter techniques. They can be used very well in a complementary fashion, since in both cases the trajectories of the incoming ions are quite different. Ref. 14 shows typical ion-trajectories during self-sputtering. The ions from an ion-gun travel in straight, parallel lines. The ion-gun can be used to clean the tip from contaminants over a much wider area than can be treated with the self sputter process. Especially the very sharp tips [V_{FE} (1 nA $<$ 200 V)] are at times mechanically unstable, and it is then disirable to have a technique that can make a tip slightly blunter in a controlled way. An advantage of the self-sputter process is its inherent possibility for characterization, both by dedicated field emission measurements as well as by observation of anomalities during self-sputtering. Even if only the ion-gun is relied upon to sharpen and clean the tips after etching, the tips still have to be characterized during and after preparation. As far as we know field emission is by far the most practical method to do that. When the setup for field emission characterization is already in place, implementation of the self-sputter process requires very little extra equipment: The hardware needed for characterization is the same as that needed for the self-sputter process, except for a second needle valve and a bottle of neon-gas.

We think that having the two sputter techniques available offers a lot of possibility in the field of preparing high-quality STM-tips: As the understanding of the sputter process in general increases with experience, it should in the future be possible to recognize certain conditions of the tip (presence of oxide layer, whiskers, etc.) from field emission measurements or perhaps other simple characterization methods. This would allow to tailor the preparation method to that particular tip, rather than relying on a standard preparation method as we do now. This would further improve the reliability of our tip preparation.

3.8 Summary.

In this chapter, the tip preparation method is described. We also describe the research that we carried out in relation to the preparation of tips. Our preparation method consists of four steps: electro-chemical etching, heating, self-sputtering with Ne^+-ions and bombardment with Ar^+-ions.

The electro-chemical etching is carried out in a similar way as is described in ref. 8, p. 283. Heating the tip is accomplished by pressing the tip against a hot filament. Adequate removal of the oxide layer during heating is essential in order to reliably carry out the self-sputter process that follows heating. The self-sputter process has been described earlier by Albrektsen *et al.* [5] and involves the tip emitting electrons by field emission. These electrons ionize the neon atoms that are let in the UHV-chamber, which in turn sputter the tip. After completion of this process, the apex radius has decreased to 7 – 15 nm [200 V $<$ V_{FE}(1 nA) $<$ 400 V]. This is sharp enough to obtain atomic resolution on GaAs-{110} and InP-{110}. Nevertheless, we apply a light Ar^+-ion bombardment to the tip in order to make them slightly more stable. We characterize our tips by field emission measurements and occasionally by SEM. We often regenerate tips

used in previous measurements by repeating the self-sputter process and ion-bombardment.

We have shown that during our sputter process, the Schiller-decapitation process can occur [1]. Furthermore, it is accompanied by a highly specific, reproducible pattern in the evolution of the sputtering voltage as a function of time. We recognize the occurrence of the decapitation process from the pattern in the sputter voltage alone, and we use this to determine the most favourable moment to terminate the self-sputtering process, which is immediately after the decapitation process has occurred.

We also present a theoretical model based on field emission from a metal surface, which allows us to calculate the apex radius of an experimental tips from field emission measurements. The results are correct within a margin of 5 nm. A slight, but systematic deviation between our experimental results and the results predicted by the model suggests that the tungsten wire that we use posesses a preferential orientation with its ⟨110⟩-direction along the long axis of the wire. The process of wire-drawing is known to induce such orientation [12].

We have discussed the phenomenon of vacuum-arcs, which occasionally occur during self-sputtering and which can ruin a tip. In order to prevent their occurrence, the oxide layer must be adequately removed from the tip and the sputter-gas should be free of contaminants (neon pressure / background pressure ~ 10^4). Water vapour appears to play a role in the initiation of vacuum-arcs.

The Ar^+-ion bombardment is meant to make the tips slightly more stable. We think that using the self-sputter technique and the Ar^+-ion bombardment in a complementary fashion offers great opportunities to make high-quality STM-tips with high reliability. Although our present tip preparation method and success rate are quite adequate in the for the purposes of our measurements, we lack the understanding to make full use of the possibilities offered by having both the self-sputter technique and the ion-gun available.

REFERENCES:

1: Christoph Schiller, Arie Koomans, Theo van Rooy, Christian Schönenberger, Herman Elswijk: *Decapitation of tungsten field emitter tips during sputter sharpening*. Surface Science Letters, 339 (1995) p. L925 – L930.

2: K.N. Eltsov, V.M Shevlyuga, V.Yu. Yurov, A.V Kivit, M.S. Kogan: *Sharp tungsten tips prepared for STM study of deep nanostructures in UHV.* Physics of Low Dimensional structures, 9/10 (1996) p. 7 - 14.

3: Lisa A. Hockett, Stephen E Creager: *A convenient method for removing surface oxides from W STM tips.* Rev. Sci. Instr, 64, (1) Jan 1993 p. 263

4: Joel A. Kubby and Benjamin Siegel: *High resolution strucuturing of emitter tips for the gaseous field ionization source.* Journ. of Vac. Science and Technology B4 (1) Jan/Feb 1986. p. 120.

5: O. Albrektsen, H.W.M. Salemink, K.A. Mørch, A.R. Thölen: *Reliable tip preparation for high-resolution STM.* Journ. of Vac. Sci. and Technology B12 (6) Nov/Dec 1994 page 3187

6: A. Modinos: Field, Thermionic, and Secondary Electron Emission Spectroscopy. Plenum Press (New York and London, 1984), p. 13 – 18.

7: Personal communication with manufacturer of our tungsten wire: Johnson Matthey represented by Alfa, Zeppelinstrasse 7, D-76057 Karlsruhe, Germany.

8: C.J. Chen: Introduction to Scanning Tunneling Microscopy. (Oxford University Press, 1993).

9: W.P. Dyke and W.W. Dolan: *Field Emission*, in Advances in Electronics and Electron Physics, vol VIII (1956) page 89 – 185. (Academic Press, New York, 1956).

10: W.P. Dyke, J.K. Trolan, W.W. Dolan, George Barnes: *The Field emitter: Fabrication, Electron microscopy, and Electric Field calculations.* Journal of Applied Physics vol 24, No 5 (May 1953) page 570.

11: W.R. Smythe: Static and Dynamic Electricity. 3rd ed. (McGraw-Hill, New York, 1968), p. 157

12: R. Gomer: Field emission and field ionization. (Harvard Univ. Press, 1961), p. 45

13: Stephen W.H. Yih, Chen. T. Wang: Tungsten: Sources, Metallurgy, Properties and Applications. (Plenum Press, New York and London, 1979) p. 209-222

14: J.Y. Cavaille and M. Drechsler: *Ion impact on field emitter crystals.* Revue de Physique Appliquée, TOME 12, octobre 1977, p. 1631.

15: W.H. Bennet: *Magnetically self-focusing streams.* Physical Review, Vol. 45 (1933) p. 890

16: De Raad, Koenraad, Wolter: *Use of the Schiller-decapitation process for the manufacture of high-qualtity tungsten STM tips.* Journal of Vac. Sci. and Tech.-B, Vol. 17, No. 5, pp. 1946 – 1953 (1999).

17: I. Ekvall, E. Wahlström, D. Claesson, H. Olin, E. Olsson: *Preparation and characterization of electrochemically etched tungsten tips for STM.* Meas. Sci. Technol. 10 (1999), p. 11 – 18.

18: O. Albrektsen: *Scanning Tunneling Microscopy and Spectroscopy on III-V semiconductors and their interfaces.* Phd-thesis presented by O. Albrektsen, Laboratory of Applied Physics (LTF), Danish University of Technology, Lyngby, Denmark (1990).

19: Personal communication with ir. R.J. Bruls, Technical University of Eindhoven (Chemistry dept.).

20: M.A. Rosentreter, M. Wenderoth, N.H. Theuerkrauf, A.J. Heinrich, M.A. Schneider, R.G. Ulbrich: *Nonequilibrium configurations of monoatomic steps on cleaved GaAs (110) surfaces.* Phys. Rev. B, Vol. 56, No. 16, pp. 10538 – 10543.

21: H. Oechsner: *Untersuchungen zur Festkörperzerstäubung bei schiefwinkligem Ionenbeschu***b** *polykristalliner Metalloberflächen im Energiebereich um 1 keV.* Z. Physik, 261, 37 – 58 (1973).

22: H.H. Andersen and H.L. Bay : *Sputtering yield measurements,* in Sputtering by particle bombardment I, edited by R. Behrisch, Springer Verlag, Berlin, 1981, p. 184.

23: This is the general trend. When the incident ions strike the surface of a monocyrstal parrallel to certain crystal directions, the sputtering yield may deviate. See “Sputtering yields of single cyrstalline targets” by H.E. Roosendaal, in *Sputtering by particle bombardment I,* edited by R. Behrisch, Springer Verlag, Berlin, 1981, p. 220.

24: The presence of a grain boundary intersecting the surface near the apex can cause a “split tip”. Such grain boundaries have a rough surface morphology, which decreases the workfunction (see ref. 9, p. 116). As the grain boundary is preferentially sputtered, two adjacent microtips are formed. We have observed such tips in SEM occasionally. The effect seems not to degrade the performance of the tip in STM, possibly because one microtip is always a little closer to the surface than the other.

25: The colour should be a little brighter than that of a sodium street-light.

CHAPTER 4:

TUNEABILITY OF THE SURFACE-CORRUGATION ON GaAs (110) SURFACES: THE PRECISE ROLE OF TIP-INDUCED BAND BENDING

4.1 Introduction

As was shown by Ebert *et al.* [1] for GaAs, GaP and InP, the apparent direction of the atomic rows on the (110)-surfaces of these materials can change from the [-110] direction to the [001] direction as a function of applied bias voltage, when imaged by atomically resolved Scanning Tunneling Microscopy (STM). The (110)-surface of these semiconductors is made up of zig-zag rows of alternating anions and cations extending along [-110] (figure 4.1a). It was shown that the apparent direction of the atomic rows is governed by different surface states contributing in varying relative amounts to the total tunneling current. These states have a different location and spatial extent within the surface unit cell. When the relative contributions of these states to the total tunneling current change, so does the appearance of the surface in atomically resolved STM.

Exactly which of the surface states contributes to the total tunneling current depends on the applied bias voltage, as well as on the amount of tip-induced band bending (TIBB). The influence of TIBB was already demonstrated qualitatively by Jiang *et al.* [2] who observed local changes in the atomic corrugation around Ag nano-clusters deposited on a GaAs (110) surface. In order to understand the voltage-dependent changes in atomically resolved STM-images of GaAs (110), knowledge of the electronic structure of the surface and information about the amount of TIBB as a function of applied bias voltage, are both essential. To obtain the latter, we calculate the amount of tip-induced band bending from a one-dimensional model.

In the energetic range accessible with STM, the surface-density of states (DOS) of these surfaces is dominated by four states (A5, A4, C3 and C4) [1,3,4]. For the relaxed, free InP (110)-surface Ebert *et.al.* identify the following energy ranges for the states with respect to the valence band maximum (VBM): A5: 0 eV to –0.95 eV, A4: -0.95 eV to –1.77 eV, C3: 0 to +2.27 eV, C4: +2.27 eV to 2.81 eV. These same states with similar energetic location are also found on GaAs (110) [3]. The surface-DOS of InP has recently been described in great detail by Engels *et al.* [4]. The A5 and A4 states are both localized on the anions and extend along [-110]. The A5 state has a dangling bond character and the A4 state is a back-bond state [1,4]. The C3 state is localized on the cations and extends along the [001] direction [1,4]. The state is an empty dangling bond with p_z character [4]. The state commonly designated as C4 in reality consists of several empty surface resonances with different spatial extent and slightly different energetic location [4]. Close to the surface ($2.23\ a_0 = 1.1$ Å from the outwardly rotated P

atoms), the C4 state is localized on both the cations and anions and appears as a zig-zag row. Further away from the surface (6.53 a_0 from the surface anion) the state shows as maxima centered on the cations extending along [-110] [1,4]. Refs. 1 and 4 also show that if both the C3 and C4 states contribute to the tunneling current, the C4 state will dominate in the STM-image. Consequently, the atomic rows will appear to run along [001] if the contribution from the C3 state dominates the tunneling current. If any of the other states dominates, the rows will appear to run along [-110]. In intermediate cases, the image will show clear atomic corrugation in both directions.

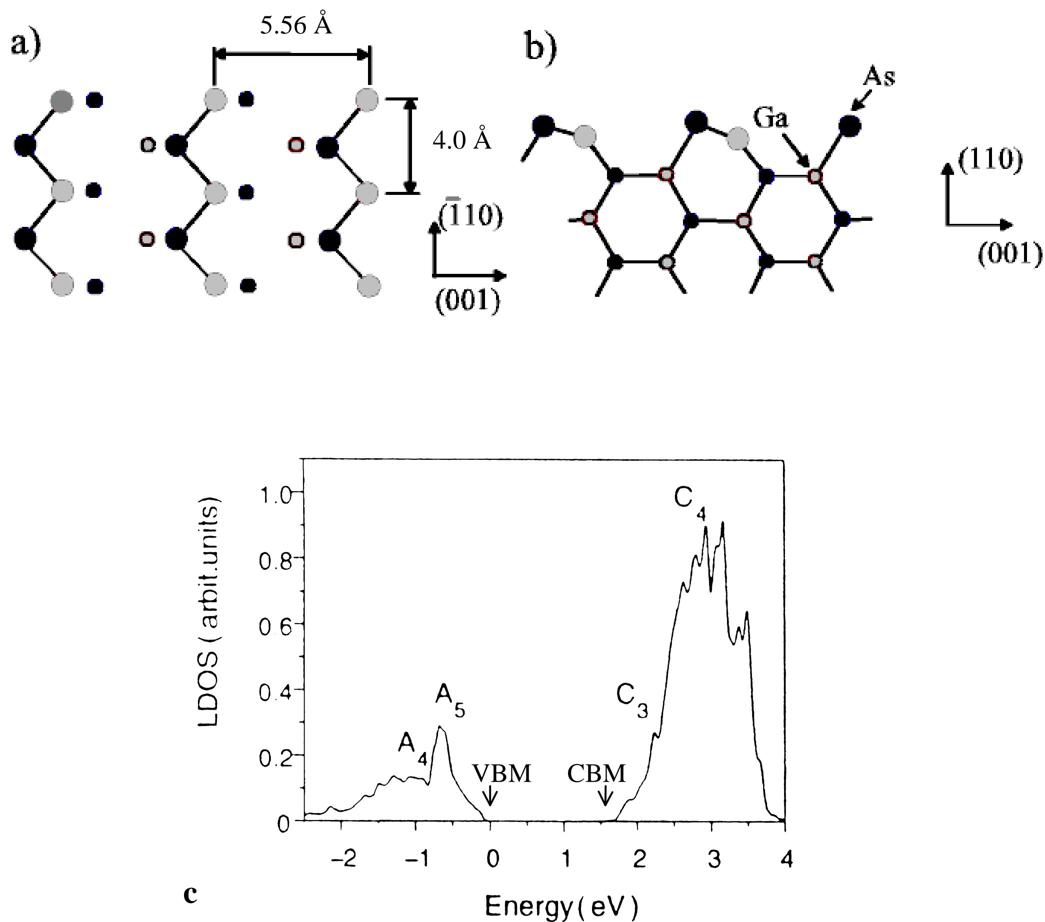

Fig. 4.1a: *Relaxed GaAs-(110) surface (top view).* **b:** *Side view.* **c:** *Energetic location of the four most important surface states. C4: CBM + 1.1 eV, C3: CBM + 0.6 eV, A5: VBM – 0.6 eV, A4: VBM – 1.3 eV (From refs. 1 and 2).*

Another important point to note is that, although no surface state on the GaAs (110) is centered inside the bulk bandgap, the shoulder of the unoccupied surface states *does* extend into the bandgap [4,5]. Chelikowski had already noted that the bottom of the "empty cation derived surface band" had its localization along the ⟨001⟩ bulk direction and showed that the onset of this surface band lies at about 0.7 eV below the Conduction Band Minimum (CBM) [5]. However, the portion of the surface-DOS lying within the bulk bandgap does not extend very far into the vacuum: At 6.53 a_0 from the relaxed anions, the integrated local surface-DOS shows no sign of a shoulder extending into the bandgap any more [4].

Atomic resolution on semiconductor surfaces is usually understood in terms of electrons tunneling directly into or out of surface states. The STM-images are then essentially microscopic maps that show the lateral variation in intensity of the DOS associated with (combinations of) the surface states (Tersoff-Hamann theory) [6]. In this view, only those states that lie energetically between the TFL and SFL are available to the tunneling process. Another important point in this theory is that the tunneling matrix element is proportional to the local sample surface DOS evaluated at the position of the centre of the tip apex atom [7]: The STM-image shows the vacuum-tails of the surface states. A direct consequence is that in the framework of the Tersoff-Hamann theory, features in the sample-DOS that lie within the surface layer do not appear in the STM-image. This is the way in which most often, atomic resolution on semiconductor surfaces is understood. We will refer to this process as "regular tunneling" (see section 1.10).

Ebert *et al.* reported that the change in the direction of atomic corrugation was most apparent when imaging the empty states on n-doped material [1]. When imaging p-doped material in filled states mode, no dramatic changes in atomic corrugation were reported. In this paper, we report voltage-dependent changes for the GaAs (110) surface for both p-type and n-type material, for both polarities of the applied bias voltage. We will show that these changes can be understood when the electro-static band bending induced by the electric field between tip and sample is taken into full account. We will also demonstrate that some of the voltage-dependent changes cannot be understood if only the four surface states of the GaAs (110) surface are considered: When imaging p-GaAs at small negative bias voltage, the electrons tunnel from bulk states near the top of the valence band, through a depletion zone several nm wide, to the tip. In this voltage regime, all of the four surface states lie outside the energetic window between the tip Fermi level and the sample Fermi level which defines the interval of tip-DOS and sample-DOS available to the tunneling process. In spite of that, we observe an atomically resolved STM-image for such voltages that is similar in appearance to the lateral distribution of the A5 state. When imaging n-type GaAs at small positive voltage, we can observe the lateral distribution of the low energy shoulder of the C3 state as electrons tunnel resonantly through this shoulder into the bulk states near the bottom of the conduction band.

4.2 Experimental

The STM-work was performed in UHV (OMICRON STM-1 setup operated at 4 * 10^{-11} torr) on *in situ* cleaved GaAs samples. Doping concentrations were 10^{18} cm^{-3} Si for n-doped material (n-doped substrate) and 10^{18} cm^{-3} Be for p-doped material (1 μm thick MBE-grown layer on p-doped substrate). Our tips are etched electrochemically from ø 0.25 mm polycrystalline tungsten wire. After heating, Ne^{+}-ion self-sputtering and bombardment by Ar^{+} ion-gun, our tips routinely yield atomic resolution on GaAs/InP (110) (apex radius ~10 nm) [8] (see also chapter 3). The bias voltage is applied to the sample. Our STM-setup is equipped with a "dual mode" feature, which enables us to apply one set of scan parameters (bias voltage, tunneling current, feedback parameter) on the forward scan and another set of parameters on the backward one. We can thus image a given area of sample simultaneously for two different sets of parameters. All images shown in this chapter are height-images [z(x,y)] that were obtained while operating the STM in constant current mode.

Changes in the atomic corrugation are commonly expressed as the ratio of corrugation amplitudes along the [-110] and [001] directions [1]. We deviate from that, as changes in the appearance of the lattice occur not only as changes in the corrugation amplitude along a given axis, but also as changes in the spatial extent of the maxima. To our opinion, a number that is sensitive to both effects is then more appropriate. Our "corrugation number" (CN) is calculated from two line profiles, which are taken along [-110] and [001], respectively, and which both pass through the atomic maxima of the image. We calculate the average height along both profiles. The difference in average height is divided by the corrugation amplitude along either [-110] or [001], whichever is largest. The resulting CN lies between –0.5 and 0.5, corresponding to a corrugation appearing as straight, parallel lines along [-110] for CN = +0.5, and to one appearing as straight, parallel lines along [001] for CN = -0.5. A CN close to zero corresponds to a clearly resolved atomic corrugation in both directions.

During high-resolution STM, tip changes which alter the appearance of the atomically resolved lattice are a common occurrence. Such changes are easily recognized as a sudden and spontaneous change in apparent corrugation and tip-sample separation. If during the acquisition of a series of voltage-dependent images (one column in figure 4.4) a tip-change is observed to irreversibly change the corrugation, we only compare those images that were recorded either *before* or *after* the tip change in order to ensure that only those images are compared that were recorded while the tip had the same tip-DOS. Another way to verify that the changes in atomic morphology are not influenced by a change in the tip-DOS during the measurement, is to record a reference image at some fixed voltage at regular intervals during the measurement, or on the backward leg of the tip motion while operating the STM in dual mode. A tip-change will manifest itself as a change in the reference image.

In practice, tip changes do not present much of a problem. A good tip usually yields stable and reproducible images throughout most of the intended voltage region. Most of the tip changes occur near the extremities of the intended voltage range where either the tip-sample distance becomes small or the electric field between the tip and sample becomes large. If a tip is observed to yield unstable images, it is exchanged for

another one. By choosing the temporal order in which the images are recorded sensibly, one can avoid the event that an unfortunate tip-change renders one half of the images within a measurement incomparable to the other. In many cases, a tip-change causes a (slight) shift in the voltage at which the change in atomic corrugation occurs. The general trends usually remain the same.

As an aid in the interpretation of the results, we also calculated the amount of TIBB (ϕ) and the tunneling current (I_T) for GaAs/$Al_xGa_{(1-x)}As$ surfaces during tunneling. Main parameters are bias voltage (V), tip-sample distance (z), tip work function (W_{TIP}), sample surface electron affinity (χ), bulk doping level (N_D, N_A), aluminum concentration (set 0 for GaAs), and density and energetic distribution of surface states. It is a one-dimensional model, which only describes the tunneling junction in the direction perpendicular to the sample surface (z-axis). It is based on the model presented by Feenstra *et al.* [9].

Based on a given bias voltage and tip-sample distance, the model calculates the amount of TIBB and the length over which the band bending extends into the semiconductor surface. Based on the tip work function and sample electron affinity, the entire potential profile can then be constructed. To calculate the potential profile, the Poisson-equation is solved under the constraint that the potential-gradient (electric field) be continuous throughout the region of interest. The resulting potential profile has a trapezoidal shape in the vacuum barrier. To account for effects due to the image charge, the (z-dependent) image potential felt by an electron between two metal plates is subtracted from the calculated potential in the vacuum barrier. In our model, the image-charge lowers the potential barrier but does not affect the amount of TIBB in the semiconductor. Then the tunneling probability as a function of energy is calculated and integrated over the energy-window between the tip- and sample Fermi level. The tunneling probability is calculated using the Tersoff-Hamann theory [6,7], thereby implicitely assuming an s-like tip-state. The resulting tunneling current density is multiplied by a fictitious “tip surface” which we have set at 10 x 10 Å to obtain the total tunneling current. Part of the tunneling current is generated by electrons tunneling from bulk valence band (BVB) states or into bulk conduction band (BCB) states. These electrons tunnel through the vacuum barrier and the depletion layer near the semiconductor surface. The contributions from the BVB states and BCB states are calculated by our model in the same way as in ref. 9 (see figure 4.2).

Most important “unknowns” affecting the model calculations are the absolute tip-sample distance, tip work function and the tip-state involved in tunneling. The densities of surface states are assumed constant ($4.42 * 10^{14}/cm^2$). We have assumed a 1 eV wide surface states band extending from the CBM up into the conduction band, and a 1 eV wide surface states band extending from the VBM down into the valence band.

In the depletion regime, screening is provided by ionized dopants which are distributed homogeneously throughout the sample material. Solving the Poisson-equation is then quite straightforward, leading to a parabolic potential-profile. When the sample surface is in accumulation or inversion, screening is provided by accumulated majority or minority carriers, respectively. In these two regimes, the charge density near the surface is determined by the 3-dimensional (3-D) densities of states of the conduction- and valence band of the semiconductor. This allows for higher charge-

densities near the surface than in the case of depletion, causing relatively little TIBB when the surface is in accumulation, and causing the amount of TIBB to level off when the regime of depletion has been passed and inversion sets in. Our model results are in good agreement with the results obtained by Feenstra for TIBB [9]. Only at large voltage (-2.5 V and +2.5 V) a deviation from Feenstra's results is apparent since our model includes the influence of the two surface-states bands. When these two bands are left out, the model accurately reproduces Feenstra's results.

It should be noted that the shoulder of the conduction band surface states which extends into the bandgap has an influence on TIBB: The occupation or depopulation of surface state shoulder provides the surface with an additional screening mechanism. This is not considered in neither our own model nor that of Feenstra's. To assess the importance of this mechanism, we calculated TIBB for p-GaAs with a surface states band ($4.42 * 10^{14}$ cm^{-2}) extending from CBM - 0.5 eV to CBM + 0.5 eV. This simulates a surface states band that is partly resonant with the conduction band, and which partly extends into the bandgap. We compared the results with those obtained for "normal" p-GaAs, in which the surface states band extends from the CBM to CBM + 1.0 eV. For both cases, simulated sample voltage was –0.9 V, and the tip-sample distance was optimized to obtain a calculated current of 55 pA. The presence of a surface donor band which extends partly into the bandgap decreases TIBB from –1202 meV to –1127 meV, confirming that this mechanism has no significant effect on TIBB. For the rest of this chapter we will ignore this screening mechanism.

As a result of some of the incertainties in the model (tip state, absolute tip-sample distance, relation between calculated tunneling current density and total current emitted by a real tip), a direct, quantitative agreement between the model and our experiments cannot always be obtained. The main feature of the model is that it calculates band bending realistically. In this work, we use the model to calculate the effects of TIBB as a function of bias voltage, while varying the tip-sample distance at the same time to maintain an in principle arbitrary, but constant tunneling current for each of the different bias voltages.

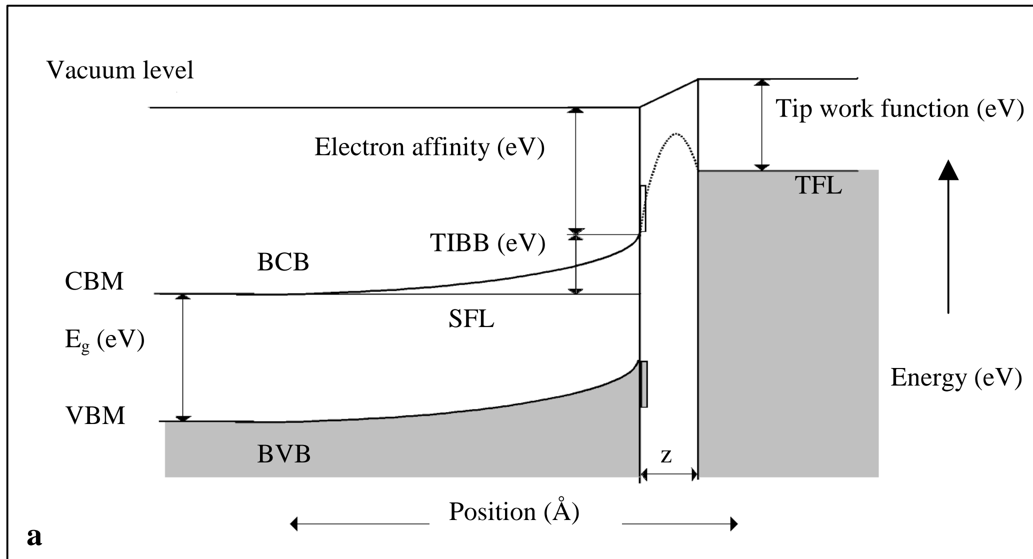

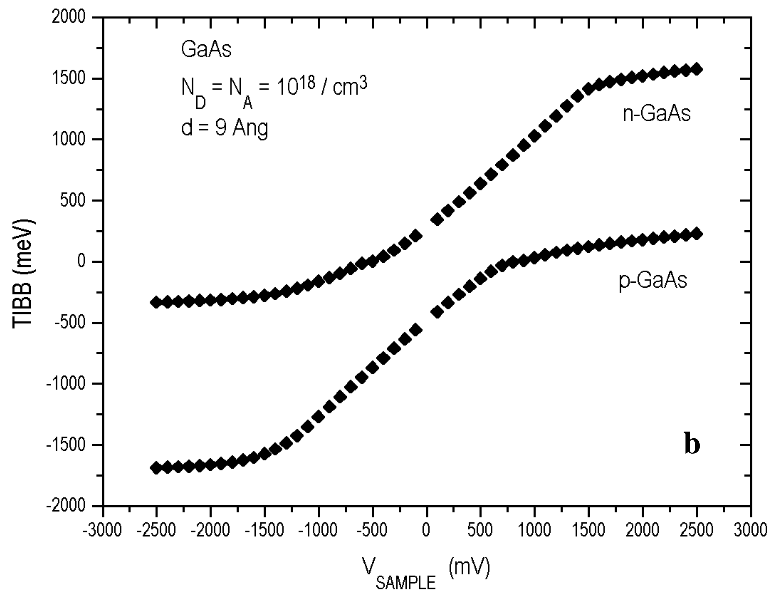

Fig. 4.2a: *Definition of the various constants used in the model. The dotted line indicates the potential inside the vacuum-barrier when the image-charge is taken into account. This is the potential barrier used to calculate the tunneling current. The two bands of surface states are also indicated.* **b:** *Calculated TIBB for n-GaAs and p-GaAs for a fixed tip-sample distance (9 Å).*

4.3 STM: Corrugation-change on n-GaAs and p-GaAs-(110)

We now present voltage-dependent images of p-GaAs and n-GaAs (110), which show clear changes in the apparent direction of the atomic rows as the bias voltage is changed. We have also expressed the changes in terms of the corrugation number (CN) defined in section 4.2 (figure 5). On p-type material, the corrugation change is only partial: For large bias voltage of either polarity, the corrugation is in the [001]-direction (CN > 0, atomic rows are along [-110]). At intermediate voltage, there is a mixed corrugation. This is also reflected by the CN which close to zero at these voltages. At small voltage, the corrugation is again in the [001]-direction, similar to the corrugation observed for large voltage. On n-type GaAs there is a complete change in the direction of atomic rows: For large voltage the corrugation is in the [001]-direction, and for small voltage it is in the [-110]-direction. We have not observed significant differences between the empty states frames obtained at small tunneling current (50 pA), and those aquired using a larger current (254 pA). When using tunneling currents in the range of 50 – 75 pA, we have repeatedly observed that the resolution gradually deteriorates for V > +1.5 V. The reason for this is that as the bias voltage increases, so does the tip-sample distance. With that, the apparent height of the atomic corrugation decreases, until at some point, the corrugation is lost in the background noise. This problem was solved by choosing the larger tunneling current (254 pA). On one occasion while using a small tunneling current, we have observed that the corrugation-change reverses for very low voltage (figure 4.4: n-GaAs, I = 50 pA, V = +0.346 V and V = +0.305 V; figure 4.5 b: open circles with dark rim). We present this as an interesting, but non-typical result that we will discuss later in this chapter.

Another feature of the empty-states results on n-GaAs is that we switched from one value for the applied bias voltage to the next one shortly *after* the start of a new frame, rather than between consecutive frames as was done for the other STM-images (see figure 4.3b). By including the transition from one value of the applied bias voltage to the next, we can observe shifts in the position of the atomic maxima, should these occur. From the changes in the tip-sample distance (see figure 4.3a) we can calculate the quantity |dz/dV|. We will show later in this chapter that the value of |dz/dV| can change dramatically as a function of applied bias voltage, and that from these changes conclusions may be drawn about the amount of TIBB as a function of applied bias voltage.

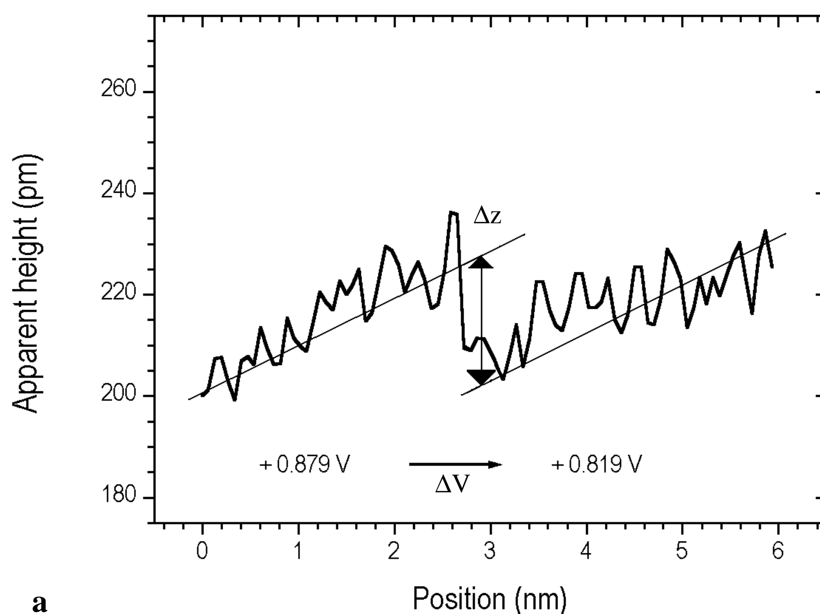

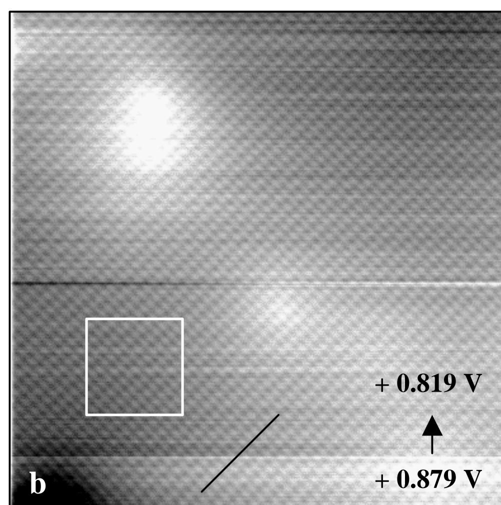

Fig. 4.3a:.*Height-profile taken along [-110] (see black line in figure 4.3 b). From the change in apparent height and the voltage difference between the upper and lower parts, |dz/dV| is calculated.* **b:** *Typical STM-image of n-GaAs: Applied bias voltage: 0.879 V -> 0.817 V , I = 254 pA. Frame size: 20 x 20 nm, gray scale 0 - 120 pm. The corrugation numbers and representative frames in figures 4.4 and 4.5 are obtained from cut-outs (white rectangle). The horizontal stripes in the image are caused by noise. On the cut-out we apply a background correction on each individual (horizontal) scan-line*

p-GaAs, filled states	p-GaAs, empty states	n-GaAs, filled states	n-GaAs, empty states	
-1.364 V, 55 pA	+ 2.493 V, 55 pA	-2.400 V, 96 pA	+1.698 V, 254 pA	+1.608 V, 50 pA
-1.200 V, 55 pA	+2.039 V, 55 pA	-1.800 V, 82 pA	+1.268 V, 254 pA	+1.315 V, 50 pA
-0.879 V, 55 pA	+ 1.761V, 55 pA	-1.600 V, 55 pA	+0.929 V, 254 pA	+0.848 V, 50 pA
-0.693 V, 55 pA	+ 1.667 V, 55 pA	-1.300 V, 45 pA	+0.706 V, 254 pA	+0.408 V, 50 pA
-0.499 V, 55 pA	+ 1.550 V, 55 pA	-1.100V, 45 pA	+0.299 V, 254 pA	+0.346 V, 50 pA

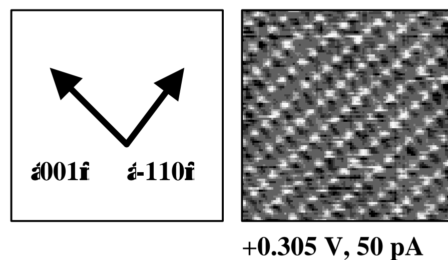

+0.305 V, 50 pA

Fig. 4.4: *Voltage-dependent changes in atomic corrugation on GaAs. The frames have been selected from the larger collection of STM-frames represented in fig. 4.5. Frame size: 5 x 5 nm. Examples of corrugation number (n-GaAs, empty states, I = 254 pA): V = +1.698 V: CN = 0.34; V = +1.268 V: CN = 0.19; V = +0.929 V: CN = +0.085; V = +0.706 V: CN = -0.21; V = +0.299: CN = -0.31.*

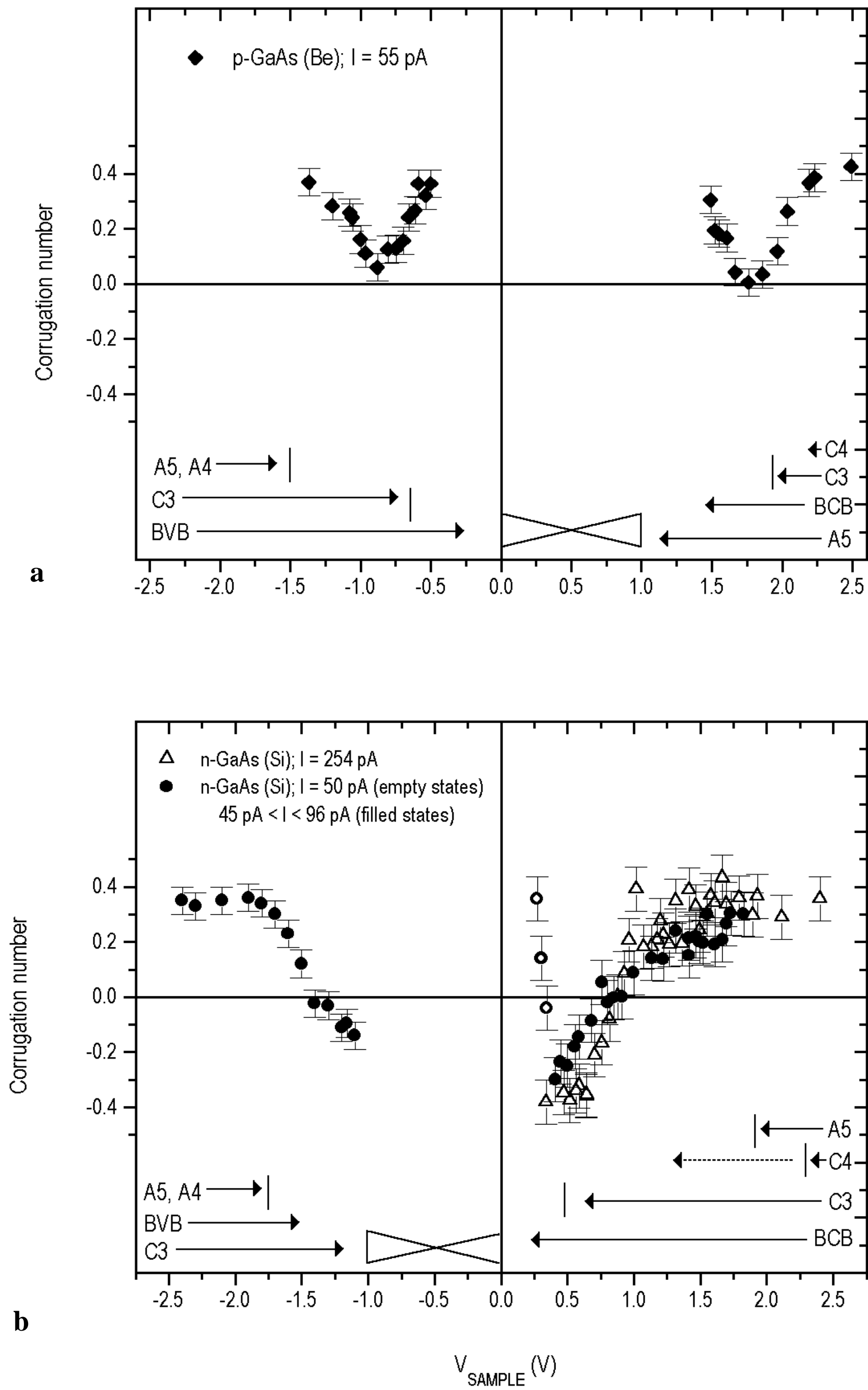

(figure caption on next page)

Fig. 4.5 *(preceeding page)* **a:** *Corrugation number (CN) for p-GaAs. Each point represents one STM-frame. The arrows represent the voltage-intervals over which we expect contributions from the various surface states (see details in section 4.5).* **b:** *CN for n-GaAs. At low positive voltage, three a-typical data points are plotted (open circles). These are discussed in sect. 4.5. The arrows represent the voltage-intervals for which we expect contributions from the various surface-states. The dotted line which is drawn to show the contribution of the C4 state (empty states) signifies that at these voltages, we expect the contribution to be from the low-energy shoulder of the C4 state (see further details in sect. 4.5).*

4.4 Model results: Different scenarios of band bending

Tip-Induced Band Bending (TIBB) is the main factor that determines which of the surface states contributes to the tunneling current at a given bias voltage, and thereby determines the appearance of the atomic corrugation. For this reason we have used our model to calculate the amount of TIBB, given the bias voltages that we applied in our experiments. We have chosen the tip-sample distances in such a way that the total tunneling current calculated by the model equals the currents used in (most of) our measurements. In our discussions, we use an absolute scale for the applied bias voltage (-2 V > -1 V).

The commonly used value of the (average) work function of polycrystalline tungsten is 4.5 eV [10]. However, the different crystal facets of tungsten are known to possess different work functions, varying between 4.3 eV (116) [10,11] and 5.22 eV (110) [11]. We have reasons to suspect that the polycrystalline wire from which we fabricate our tips, has a preferential orientation along ⟨110⟩, which could be a cause for a higher work function than the value used in the model [8]. On the other hand, a contamination near the apex of the tip could well lower the work function. Also, a rough morphology of the surface is known to decrease the work function [10,12], suggesting that for a tip apex, the work function is inherently reduced. The assumption of a tip work function different from the average value of tungsten is therefore not at all unrealistic. As a working hypothesis, we assume that the work function of our tips usually lies between 4.0 and 4.6 eV.

From figure 4.2 can be seen that an increase (decrease) in tip workfunction will bend the bands of the semiconductor upwards (downwards). To illustrate the very strong influence that the tip work function has on the band bending behaviour, we show the calculated amount of TIBB for several tip work functions (4.45 eV and 4.6 eV for p-GaAs and 4.3 eV, 4.35 eV, and 4.6 eV for n-GaAs). Other parameters, such as the tip-sample distance (chosen tunneling current) and the doping concentration also have an influence. However, in the simulations, the influence of the tip work function is much stronger than the influence of the chosen value for the tunneling current. We do not vary

the doping concentration in our simulations since the doping concentration of a given sample is usually known in an experiment [13].

The quantity plotted in figures 4.6 and 4.7 is the amount of TIBB relative to the Sample Fermi Level (SFL). The amount of TIBB is indicated by the solid symbols. For p-GaAs, the amount of TIBB equals the energetic position of the surface-VBM and for n-GaAs that of the surface-CBM (see figure 2). The surface-CBM for p-GaAs and the surface-VBM for n-GaAs have also been indicated (open symbols). We assume that the energetic positions of the surface-states remain constant relative to the surface-VBM and surface-CBM. Consequently, the energetic location of the four surface-states is assumed to vary with the applied bias voltage in the same way as the amount of TIBB itself, except for an offset. The band bending plots shown in figures 4.6 and 4.7 should thus be read in the following way: the part of the surface-DOS that falls within the sharp triangle formed between the lines denoting the SFL and TFL (Tip Fermi Level), lies between the TFL and SFL and is thus energetically available to the tunneling process.

For p-GaAs, we identify 6 different situations, which we label (1) type II inversion, (2) type I inversion, (3) type I depletion, (4) dead region, (5) type I accumulation, and (6) type II accumulation. The potential-profiles of each of these different situations have been sketched in figure 4.6 c. The significant difference between type I and type II inversion is that in the latter case, the (absolute) bias voltage exceeds the amount of TIBB. This means that the Tip Fermi Level (TFL) lies energetically below the sample Valence Band Maximum (VBM), so that the valence band surface states (A4 and A5) can contribute to the tunneling current. A similar distinction is made between type I and type II accumulation and type I and type II depletion.

We will now discuss the band bending behaviour of p-GaAs from the fig. 6a (W_{TIP} = 4.6 eV): Suppose one is to change the bias voltage between a tip and a p-GaAs sample from large negative value down to zero, and then from zero towards large positive values. First, the surface will be in type II inversion. The filled states current consists of three contributions: One from the A5 and A4 states, one from the bulk valence band states (BVB) and one from the conduction band surface state (C3), which has become populated due to the inversion. As the voltage is decreased, the tip fermi level (TFL) rises above the VBM of the sample, and the contribution of the A4 and A5 states is no longer there (type I inversion). When the voltage is decreased even further, the conduction band minimum (CBM) rises above the sample fermi level (SFL), and only the contribution from the BVB states is left (type I depletion). When the bias voltage is reversed, there is still a voltage region for which the surface band bending is negative. For a free GaAs surface, band bending is such that the Fermi level lies in the middle of the bandgap, irrespective of the type of doping of the material. For very small positive voltage, no tunneling of any kind is possible (dead region).

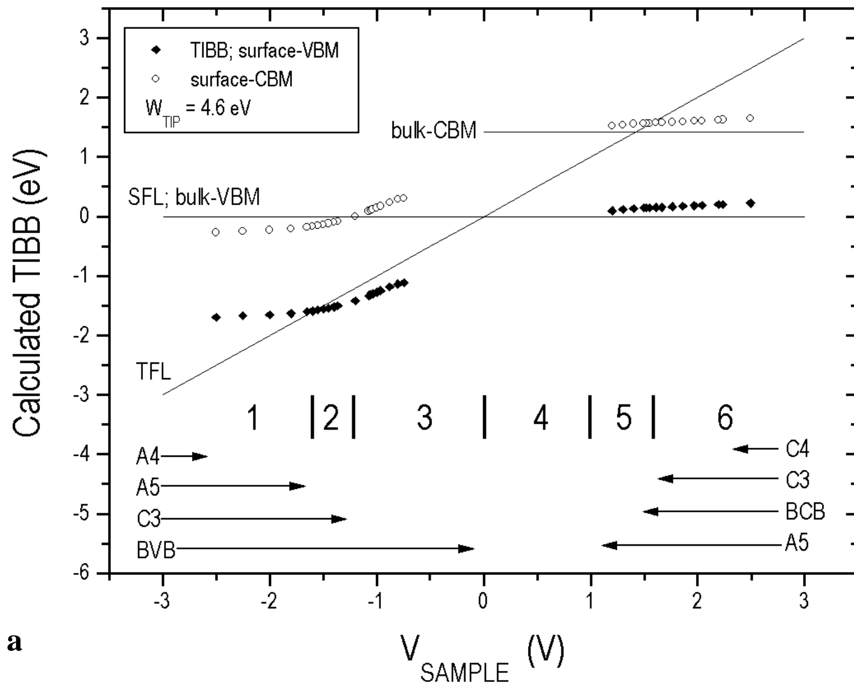

a

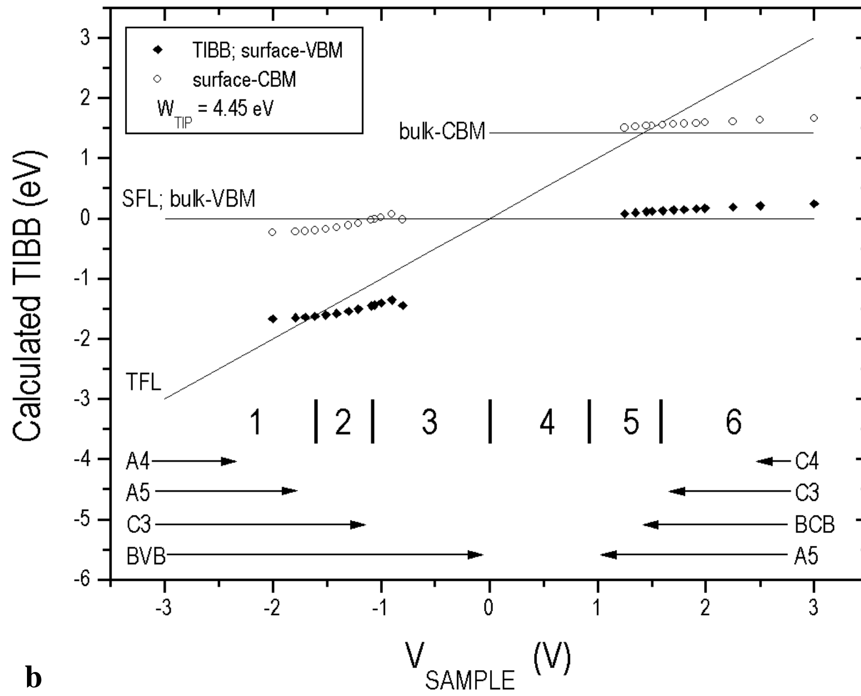

b

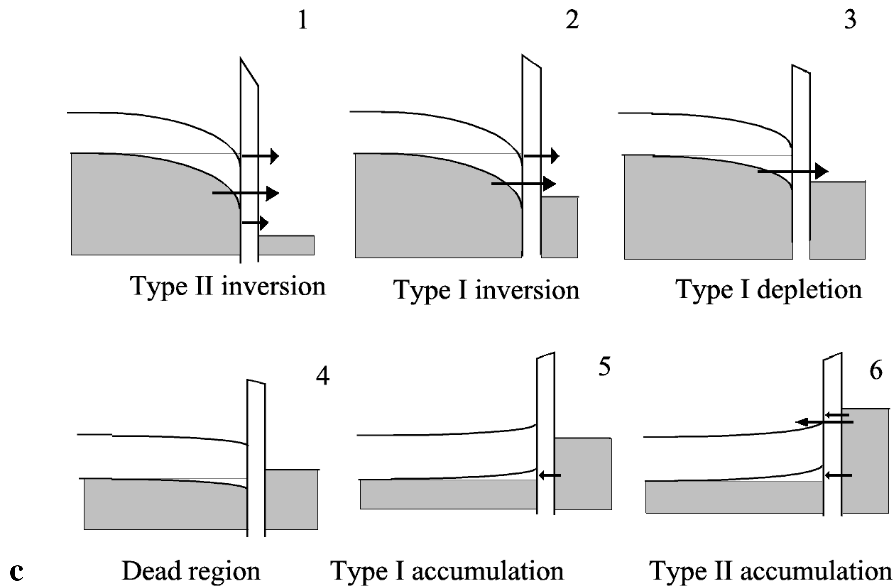

Fig. 4.6 *(both pages)* **a:** *Tip-induced band bending calculated for p-GaAs, W_{TIP} = 4.6 eV, I = 55 pA, N_A = 10^{18} cm^{-3}.* **b:** *TIBB calculated for p-GaAs, W_{TIP} = 4.45 eV, I = 55 pA.* **c:** *Different possible band bending configurations on p-GaAs.*

After the flat band condition has been passed and TIBB is positive, electrons can tunnel into the now depopulated A5 state, and at slightly higher voltages, into the bulk conduction band (BCB). This is the regime of type I accumulation. The exact voltage at which tunneling into the BCB states becomes apparent depends on the width of the surface depletion layer of the semiconductor as a function of bias voltage. The onset must in any case lie above the level of the CBM in the bulk, which is at V = +1.42 V for GaAs. Type II accumulation sets in when the TFL passes the sample CBM, allowing the C3 and later the C4 state to contribute.

For the lower value of the tip work function (W_{TIP} = 4.45 eV, figure 4.6 b) a similar scenario is found, although some of the transitions between the different regimes of band bending shift to different voltages. The most apparent difference is that the regime of type I inversion extends to smaller negative voltage (V = -1.05 V). For W_{TIP} = 4.6 eV, the transition lies at V = -1.2 V. For V < -1.05 V (on the absolute voltage scale) there is a narrow voltage-interval for which the surface is in type I depletion. At very low voltage (V ~ -0.8 V), the amount of TIBB increases with decreasing voltage, and the surface shows a tendency to go back into type I inversion. This effect is understandable, since for small values of the applied bias voltage, the tip-sample distance becomes quite sensitive to changes in the applied bias voltage. If a decrease in applied bias voltage is accompanied by a large decrease in tip-sample distance the

electric field between tip and sample may increase, causing the amount of TIBB to increase as well. In figure 6b, we have chosen to abort the calculation for V = -0.8 V and less: In the model, the tunneling current originates completely from the surface states in the conduction band that are populated by inversion for those voltages. In the model, the density of surface states is assumed constant, whereas in reality the DOS associated with the surface states is very much reduced near the edges of the bandgap of the semiconductor. The calculated value for the tunneling current may thus well be an overestimation.

For n-GaAs (see figure 4.7), we can work out the various band bending situations the same fashion as was done for p-GaAs. For large negative voltage, the surface is type II accumulated and we expect contributions from the A4 and A5 states, the BVB states and the C3 state which has become populated due to the downward band bending. When the bias is decreased, the TFL passes the sample VBM and type I accumulation sets in. In this regime, there is a contribution from the C3 state and the BVB states, but the A4/A5 contribution is gone. As the bias voltage is decreased further, the contribution from the BVB states slowly diminishes and for small negative voltages, only the contribution from the C3 state is left. For very small negative voltage, there is a dead region similar to the one found for p-GaAs. Except for a slight shift in the voltage at which the transition between type I and type II accumulation occurs, there are no differences in the filled-states band bending behaviour of n-GaAs for the different model parameters.

For positive values of the applied bias voltage, on the other hand, the band bending behaviour of n-GaAs becomes very strongly dependent on the assumed values for the model parameters, the tip work function in particular. For the lower two values of the assumed tip work function (4.30 and 4.35 eV), electrons tunnel into the BCB states for V < 0.5 V (type I depletion). When the applied bias voltage exceeds 0.5 V, the TFL passes the CBM and type II depletion sets in. The voltage-regime of type II depletion is rather large. For V > 1.8 V, type II inversion sets in. For the type II inverted surface, we expect contributions from the A5 state, the BCB states, the C3 state, and for larger voltages, the C4 state.

For the higher value of the tip work function, the amount of TIBB remains comparable to the bandgap of the semiconductor for all voltages. For a small applied bias voltage, the surface is predicted to be in type I depletion. For the current chosen in the calculation, the voltage at which the TFL passes the CBM coincides with the voltage at which inversion sets in. Therefore, as the bias voltage is increased, the surface goes directly from type I depletion into type II inversion. If a larger tunneling current (smaller tip-sample distance) is used, TIBB at a given voltage is stronger. If the bias is then gradually increased, inversion sets in before the TFL passes the CBM of the sample, causing type I inversion similar to what is seen on p-GaAs. For a smaller current, inversion will set in *after* the TFL has passed the sample CBM, causing type II depletion (see figure 4.7 d, configuration 5). The surface shows a tendency towards type I inversion for very small positive voltage, in a similar way to what is observed for p-GaAs in figure 4.6 b.

Given the fact that the band bending behaviour of the GaAs (110) surface can be so strongly dependent on the assumed value of the tip work function, the obvious question to address at this point is whether such model calculations can be used to interprete any given set of experimental STM-images. The work function of the tip used is usually not known from the experiment.

We can base our interpretation of the results on p-GaAs on the images themselves without having to make explicite assumptions about the tip work function, as will be shown in section 4.5. However, the corrugation-change in the empty-states results on n-GaAs is caused by a shifting balance between the contributions of the energetically adjacent C3 and C4 surface states. The voltage at which the contributions from both states are equally balanced, and thus the voltage for which the corrugation change is observed, critically depends on the value of the tip work function. In order to reliably interprete the empty states results on n-GaAs, we therefore have to validate our choice for the tip work function using additional information.

This additional information is provided by the voltage-dependent changes in the tip-sample distance that we have measured for the empty states results on n-GaAs (see figure 4.3). When calculating the amount of TIBB, the tip-sample distance has to be adjusted for each data-point in order to maintain a constant value for the tunneling current. As a result, the calculations also produce a theoretical z(V)-curve. Since the absolute tip-sample distance is unknown in an STM-experiment, we calculate a theoretical value for $|dz/dV|$ by differentiating the adjacent z(V)-points. What is apparent from comparing figures 4.8a-f is that the tip-sample distance becomes more sensitive to changes in the applied bias voltage at low voltage, where type I depletion sets in. This manifests itself in a marked increase of $|dz/dV|$ at the onset of type I depletion. That same increase at low voltage is also observed in the experimental values of $|dz/dV|$, indicating that the transition between type I depletion and type II depletion occurred for $V \sim +0.5$ V for both the series of images taken at $I = 254$ pA and the series taken at $I = 50$ pA, respectively. The model calculations were carried out assuming a tip work function of 4.3 eV for $I = 254$ pA, and assuming a tip work function of 4.35 eV for $I = 50$ pA. Based on this information, we conclude that in our measurements, the transition between type I depletion and type II depletion occurred for $V = +0.5$ V, and that for a wide voltage-region, the surface was in type II depletion. The relevant band bending scenarios are shown in figures 4.7 a and c.

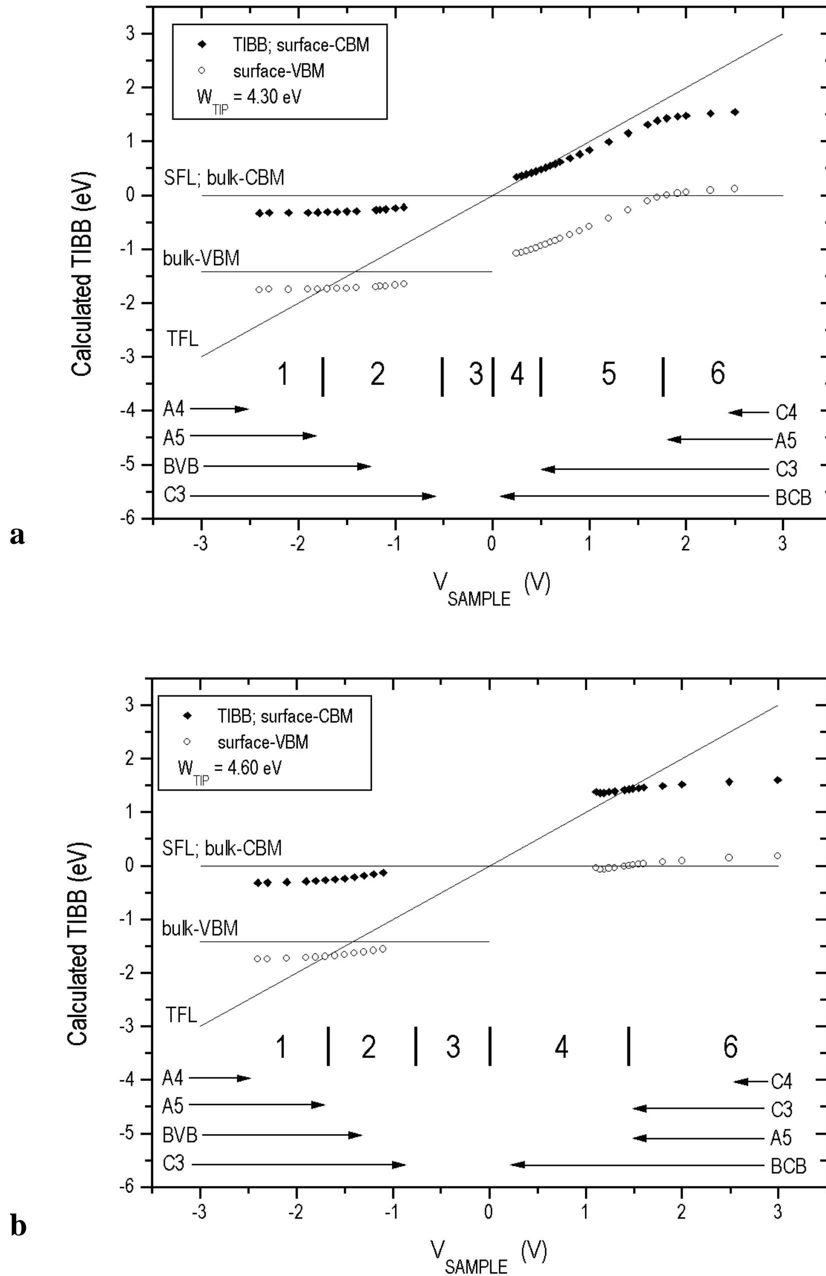

Fig. 4.7 *(both pages)* **a:** *Tip-induced band bending calculated for n-GaAs (W_{TIP} = 4.3 eV, $N_D = 10^{18}$ cm^{-3}). Simulated currents: 45 pA < I < 96 pA (filled states), 254 pA (empty states). We have varied the value of the tunneling current in the filled states simulation in order to mimick the corresponding measurement.* **b:** *TIBB calculated for n-GaAs (W_{TIP} = 4.6 eV, $N_D = 10^{18}$ cm^{-3}). Simulated currents: 45 pA < I < 96 pA (filled states), 65 pA (empty states). For these parameters, the model predicts a direct transition from type I depletion to type II inversion (see text).*

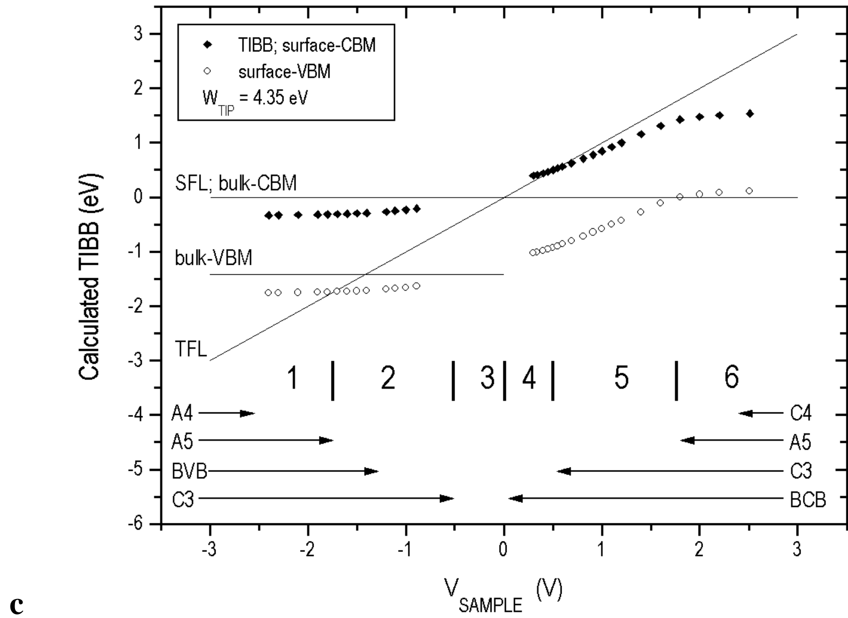

c

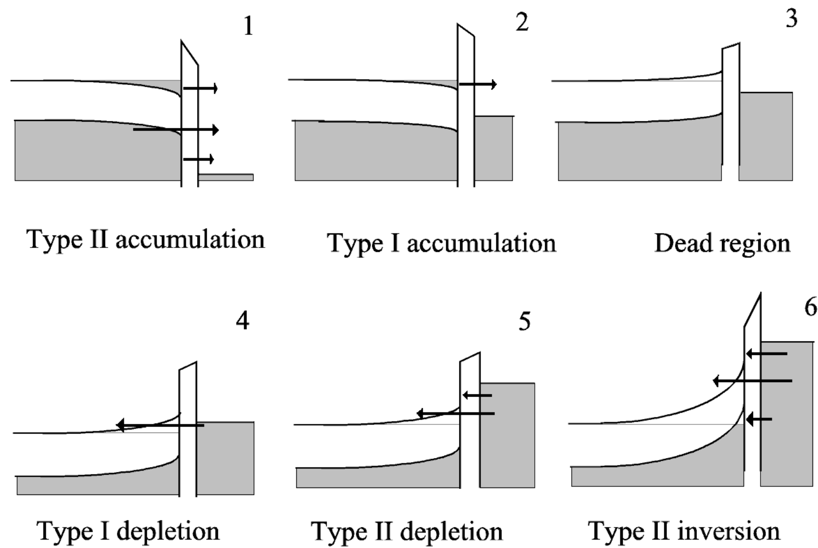

d

Fig. 4.7 *(continued)* **c:** *TIBB calculated for n-GaAs (W_{TIP} = 4.35 eV, N_D = 10^{18} cm^{-3}). Simulated currents: 45 pA < I < 96 pA (filled states), 50 pA (empty states).* **d:** *Different possible band bending configurations on n-GaAs.*

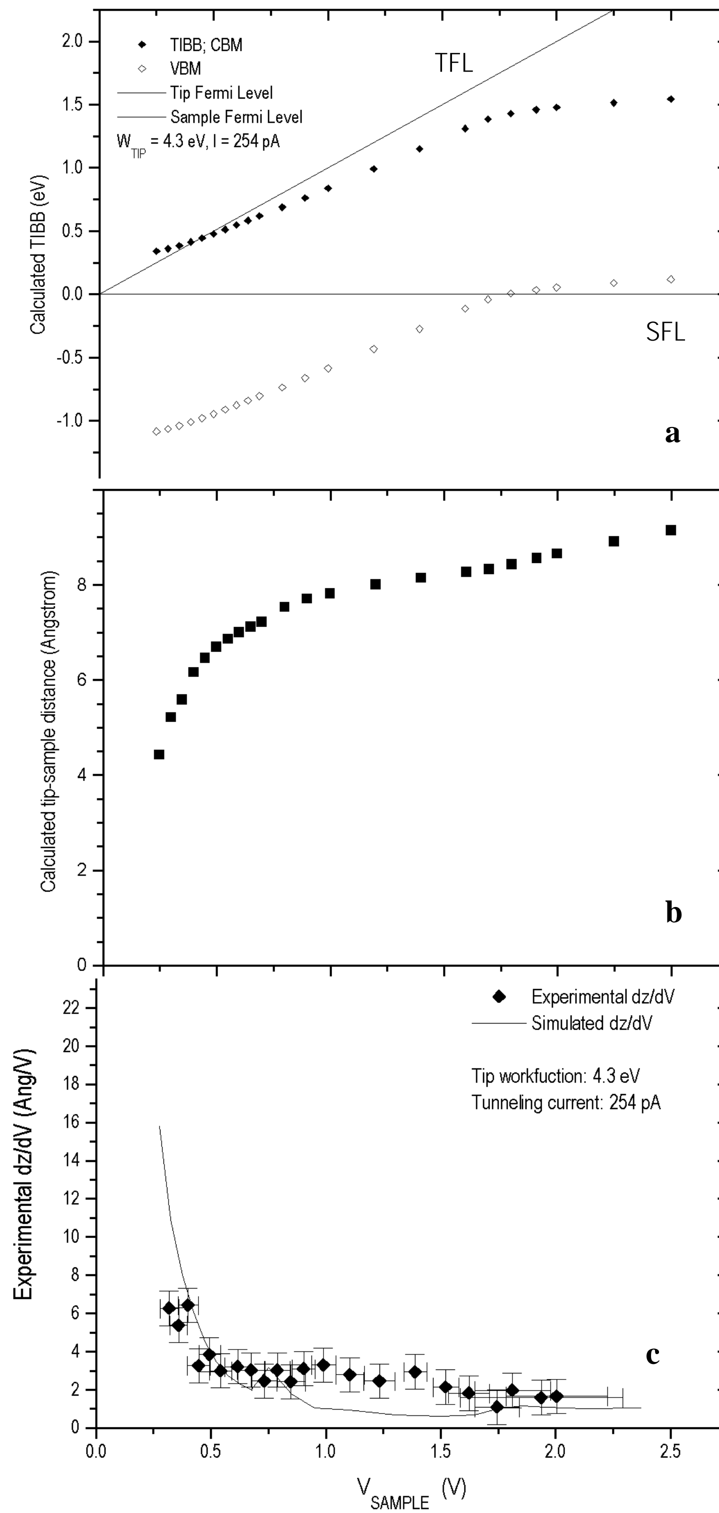

(figure caption on page 88)

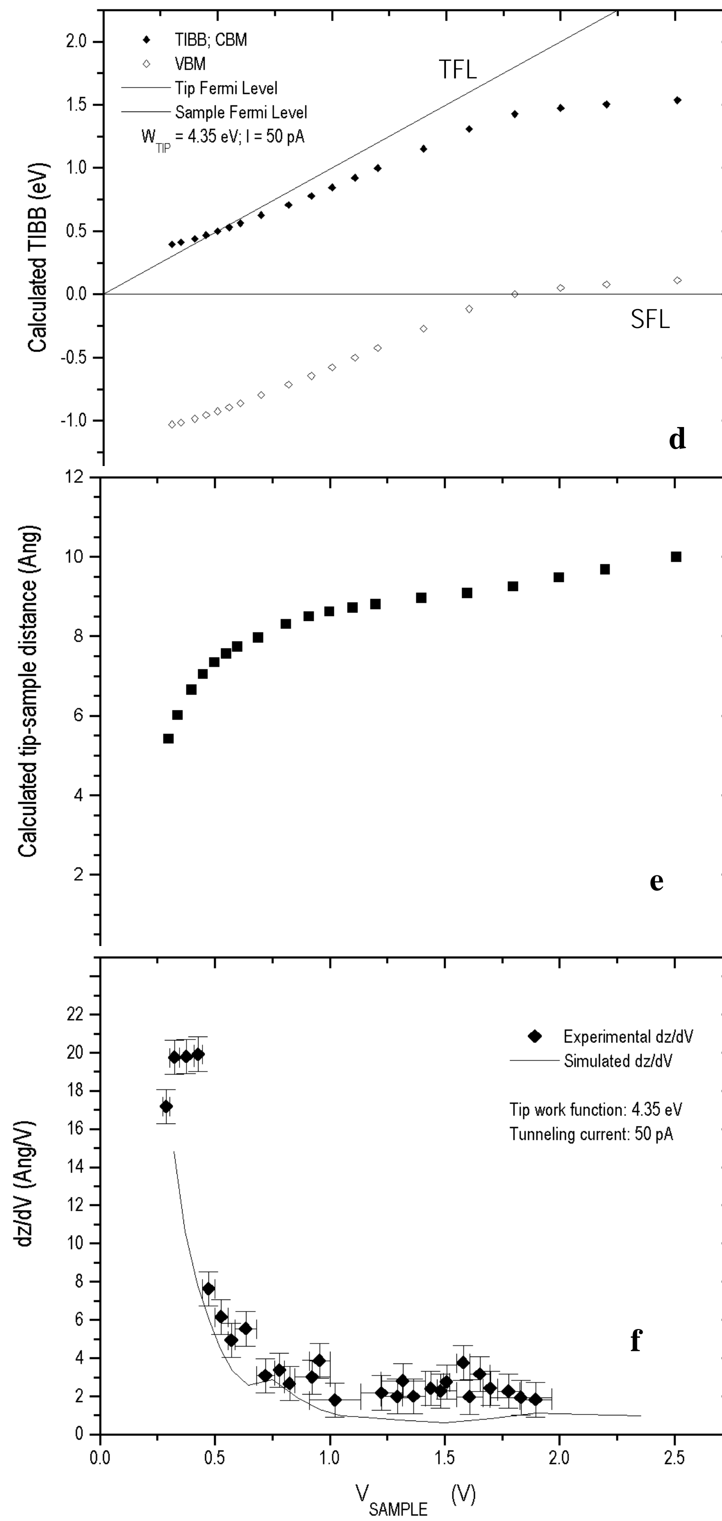

(figure caption on page 88)

Fig. 4.8 *(previous two pages)* **a:** *Calculated TIBB for n-GaAs, empty states. I = 254 pA, W_{TIP} = 4.3 eV (see also fig. 7).* **b:** *Tip-sample distance as function of bias voltage z(V). At V = 0.75 V and at V = 1.5 V respectively, the onset of contributions from the surface states inside the conduction band and the onset of inversion manifest themselves as small discontinueties in the z(V) curve.* **c:** *Comparison between the experimental and calculated dz/dV. For V < 0.5 V, the sharp decrease in |dz/dV| indicates the transition from type I depletion to type II depletion. The left and right ends of the horizontal error-bars correspond to the two voltages between which we switched during the transition. The points are centered on the mean value of the two voltages. The length of the vertical error-bars has been estimated from the noise in the raw STM-images.* **d:** *Calculated TIBB for n-GaAs, empty states. I = 50 pA, W_{TIP} = 4.35 eV (see also fig. 7).* **e:** *Tip-sample distance as fucntion of bias voltage z(V). At V = 0.75 V and at V = 1.7 V respectively, the onset of contributions from the surface states inside the conduction band and the onset of inversion manifest themselves as small discontinueties in the z(V) curve.* **f:** *Comparison between the experimental and calculated dz/dV. For V < 0.5 V, the sharp increase in |dz/dV| indicates the transition from type I depletion to type II depletion. The error-bars were estimated in the same way as in c.*

From figures 4.6 and 4.7 some general trends concerning TIBB may be discovered. First of all, accumulation (empty states for p-GaAs and filled states for n-GaAs) involves small amounts of band bending which are relatively insensitive to the experimental parameters. The observed strong dependence of TIBB on the experimental conditions occurs mainly when the surface is in depletion. The voltages at which the transitions between the various regimes occur can also strongly depend on the chosen experimental parameters. Whether bulk states, surface states, or a combination of bulk and surface states contribute to the tunneling current, mainly depends which of the transitions occurs at which voltage. This makes the influence of TIBB on voltage-dependent STM-images rather subtle.

It should also be noted that in our work, we use samples with a relatively low doping concentration ($1 * 10^{18}$ cm^{-3}). Other samples with a higher doping concentration ($4*10^{18}$ cm^{-3}, $1 * 10^{19}$ cm^{-3}) will show much less TIBB in the depletion regime. We suspect that for such surfaces, type I depletion or type I inversion may not occur for “common” experimental parameters.

The model calculations also show, that there are voltage regimes for which (most) of the tunneling current is associated with bulk states, rather than surface states. Feenstra *et al.* report that at these voltages, they were not able to obtain meaningful topographic STM-results on GaAs (I = 0.1 nA) [9]. In the previous section we have presented voltage-dependent STM-images of clean n-GaAs and p-GaAs. Given the model results on TIBB and the morphology of the different surface states on the GaAs (110) surface [1,4], we will show that for some of the images, the surface was in type I

depletion, suggesting that the tunneling process involved bulk states. In spite of that, the images taken at these voltages show a clear atomic corrugation, which in its appearance is not significantly different from the corrugation associated with surface states.

V_{SAMPLE} (V)	I (pA)	TIBB (eV)	V_{SAMPLE} – TIBB (eV)
W_{TIP} = 4.30 eV			(TFL - CBM)
+ 1.700	254.0	+ 1.384	+ 0.316
+ 1.200	254.1	+ 0.993	+ 0.207
+ 0.900	254.0	+ 0.763	+ 0.137
+ 0.700	254.0	+ 0.621	+ 0.079
+ 0.300	253.9	+ 0.361	- 0.061
W_{TIP} = 4.35 eV			
+ 1.600	50.0	+ 1.310	+ 0.290
+ 1.400	50.0	+ 1.153	+ 0.247
+ 1.200	50.0	+ 0.999	+ 0.201
+ 0.810	50.0	+ 0.709	+ 0.101
+ 0.400	50.0	+ 0.441	- 0.041
+ 0.300	50.0	+ 0.396	- 0.096

Table 4.1: *Some numerical values of the model results shown in figures 7a,c and 8a,b. We also show the calculated energetic difference between the TFL and the position of the CBM at the surface. This difference determines the part of the (conduction-band related) surface-DOS available to the tunneling process, and hence the corrugation in the image. This data can be compared directly to figure 4. Notice that the transition from type I depletion to type II depletion can be recognized in the last column from the change in sign of the numbers.*

4.5 Discussion

In this discussion, several questions will be addressed: First we will compare the STM-images with the model-results concerning TIBB in order to interprete the voltage-dependent changes in atomic corrugation that we have observed. The empty-states results on p-GaAs (subsection 4.5.1) and the filled-states results on n-GaAs (4.5.2) are treated first, since these cases involve accumulation and are thus very simple to interpret. Then we will discuss the empty-states results on n-GaAs (4.5.3) and the filled-states results on p-GaAs (4.5.4). After discussing the experimental results we will make comments on the validity and reliable use of our model (4.5.5). In subsections 4.5.3 and 4.5.4 it will be made clear that at some voltages, the surface is in type I depletion. For these voltages, the atomic corrugation that is observed in the images must be attributed to a tunneling current that is associated with bulk states rather than surface states. Atomic corrugation which is observed while the surface is in type I depletion cannot be explained within the framework of “regular tunneling”. The last subsection (4.5.6) therefore theorizes about possible alternative mechanisms for atomic corrugation on the (110)-surface of GaAs.

4.5.1 p-GaAs, empty states

The empty-states results of p-GaAs are shown in the first column of figure 4.4. They show that the atomic corrugation is in the [001]-direction for large positive voltage (+ 2.5 V), or equivalently, that the atomic rows appear to run in the [-110]-direction for large, positive voltage. Then the atomic corrugation partly changes into an atomic corrugation that is clearly resolved in both directions for intermediate voltage (+ 1.8 V). At small positive voltage (+ 1.5 V), the corrugation is again in the [001]-direction. The interpretation of the empty states behaviour of p-GaAs is quite straightforward as the amount of TIBB remains relatively constant throughout the voltage range of interest (see figure 4.6). At the lowest voltage (V = +1.5 V), tunneling occurs into the A5 state which has become depopulated by the upward band bending (type I accumulation). The corrugation is then in [001]. When the bias voltage is increased, the BCB states contribute more and more to the tunneling current. Somewhere in the range between V = +1.5 V and V = +1.8 V, the TFL passes the CBM (type II accumulation) and the C3 state starts to contribute as well. This is reflected by the change in CN. When the bias voltage is increased further, the C4 state starts to contribute, causing the corrugation to change back again. For the highest voltage (V = +2.5 V) the corrugation is completely in [001].

In subsection 4.5.3, it will be shown that the contribution from the BCB-states is accompanied by a corrugation in the [-110]-direction. The effect is caused by electrons tunneling resonantly through the low-energy shoulder of the C3-state, of which it is known that it extends into the bandgap [5]. In this case, the effect of the contribution from the BCB-states to the tunneling current is that the contribution of the C3-state

appears slightly stronger than would otherwise be the case. One can also expect the corrugation-change to appear at slightly lower voltages due to this effect. In this case, however, these effects are unimportant.

It is worth to note that at the lowest voltage at which we measured, the value of the CN indicates that there still is a minor contribution from the (shoulder of the) C3 state. It is also clear that at V = +1.8 V, where we expect a simultaneous contribution from the C3- and the A5-states, a mixture of the atomic corrugation occurs: The C3-state causes a corrugation in the [-110]-direction whereas the A5-state causes an atomic corrugation in the [001]-direction. The simultaneous contribution of both states results in an atomic corrugation that is clearly resolved in both directions.

4.5.2 n-GaAs, filled states

The filled states results on n-GaAs show that for high voltage, the corrugation is in [001]. As voltage is decreased, the corrugation appears not to change very much until V = -1.8 V. Below this voltage, the corrugation changes until for V = -1.1V, it has completely changed to a corrugation in [-110]. In contrast to what is seen for p-GaAs, the change in the direction of the atomic corrugation is monotonous as a function of bias voltage.

At high voltage, the surface is in type II accumulation and we expect contributions from the A5 and A4 states, from the BVB states and a minor contribution from the C3 state which is populated due to the downward band bending. As the A5 and A4 states and BVB states dominate, corrugation is in [001]. As will be shown in subsection 4.5.4, the contribution from the BVB-states is (very likely to be) accompanied by an atomic corrugation in the [001]-direction. When the voltage is decreased, the TFL will rise with respect to the sample surface states as in this voltage regime, TIBB is relatively constant. The contribution of the A4 and A5 states will thus gradually decrease. At lower voltages where type I accumulation sets in, the contribution from the BVB states will decrease as well. At low voltages, only the contribution from the populated C3 state is left. For these voltages, the corrugation has clearly changed towards one in the [-110] direction, as is indicated by the negative CN.

4.5.3 n-GaAs, empty states

The empty-states images of n-GaAs show a gradual corrugation-change: At large voltage, the corrugation is in the [001]-direction, and at low voltage it is in [-110]. The change is most apparent between V = +0.706 V and V = +1.268 V. In the recorded transitions between the applied voltages we have not observed any shifts in the atomic rows (see figure 4.10 for an example of such a shift). This indicates that the atomic maxima seen in the images are centered on the same atom-species throughout the entire range of applied bias voltages. For the lower voltages, we can identify the corrugation unambiguously as being associated with the C3 state. Since the local maxima in the

DOS associated with this state are centered on the Ga atoms, the atomic maxima in the rows along (-110) which are observed at higher voltage are also centered on the Ga atoms. This confirms that the corrugation observed for higher voltage is associated with the C4 state. Also, the images are in qualitative agreement with the results obtained by Ebert *et al.* [1], although in our work the corrugation change occurs at a slightly lower voltage. We thus attribute the corrugation-change to a shifting balance between the competing contributions of the C3 and C4 states. The empty-states results obtained on n-GaAs also contain a non-typical rise of the CN for very low voltage (V < 0.4 V, 50 pA). This result will be discussed in sub-section 4.5.6.

The point at which the CN changes sign lies near V = +0.9 V. According to the model calculations the TFL lies 137 meV above the CBM for that voltage. This is energetically below the energies at which both the C3 and C4 states are centered. This fact appears strange: If the corrugation change is supposed to be caused by the contributions from two competing states, it would seem logical that the corrugation change takes place at a voltage for which the TFL lies energetically between the (peak positions of) two states. According to figures 4.7a and b, that situation is only expected to occur for V > 2.0 V, since the TFL rises very slowly in energy with respect to the sample surface states as the bias voltage is increased. Since the model calculations reproduces the voltage-dependent-changes in the tip-sample distance quite well (see figure 4.8) we are convinced that the model calculations describe the band bending behaviour correctly, at least in qualitative terms. The slow rise of the TFL with respect to the sample surface predicted in the model is also consistent with the experimental observation that the corrugation changes quite gradually as a function of applied bias voltage.

One possible explanation is the hypothesis that the low energy shoulder of the C4 state extends to much lower energies than one might at first glance expect. From the calculated surface-DOS on InP (110) (see figure 1 in ref. 1), the C3 state appears as a small peak superimposed on a some background. If the low energy shoulder of the C4 state forms a background on which the DOS associated with the C3 state is superimposed, it is conceivable that the C4 state influences the corrugation even for energies that lie below the value at which the lower lying C3 state is centered. For energies below CBM + 150 meV, the low energy shoulder of the C3 state would then dominate the surface-DOS, causing the corrugation to change.

From figure 4.7 it is clear that for V < +0.5 V, the surface was in type I depletion as the images were recorded. For these voltages, the atomic rows run along [001]. We interpret this as the influence of the low energy shoulder of the C3 state, from which it is known that it extends into the bandgap [4,5]. We do not think that the low energy shoulder of the C3 state is imaged by the process of regular tunneling. The portion of the DOS associated with the C3 state that lies inside the bandgap only extends 4.4 a_0 (2.2 Å) into the vacuum [4]. According to the Tersoff-Hamann theory, this would mean that for these images, the tip-sample distance would also be around 2 Å [7]. This seems an unlikely event since at these small tip-sample distances, a non-neglegible influence from the tip-sample interaction is to be expected. Theoretically it is expected that a chemical bond forms between the tip and sample at such short tip-sample distances [14,15,16,17]. From figure 4.7b the tip-sample distance is expected to be larger than 2 Å as well. To our opinion, the following interpretation is much more plausible: If the

electrons tunnel from the tip into the sample while the surface is in type I depletion, they can tunnel resonantly through the low energy shoulder of the C3 state (figure 4.9). This will enhance the tunneling current when the tip apex faces a maximum in the lateral distribution of the C3 state, and suppress the tunneling current when the tip faces a minimum. This way, it is possible to image the low energy tail of the C3 state which extends into the bandgap, even at tip-sample distances that are large enough for the tip-sample interaction to remain small.

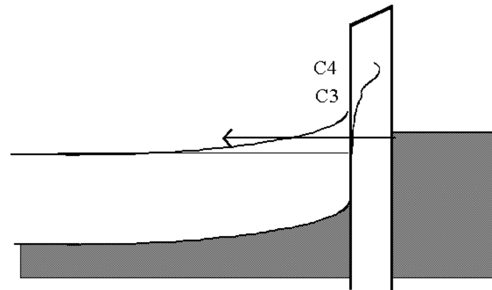

Fig. 4.9: *Interpretation for the empty states results of n-GaAs, obtained for V < +0.5 V: The electrons tunnel resonantly through the low energy portion of the C3 state. Further details in text.*

4.5.4 p-GaAs, filled states

The filled states results obtained on p-GaAs shown in figures 4.4 and 4.5 show that at large negative voltage, the atomic corrugation is in the [001]-direction. A mixed corrugation appears at intermediate voltage (V = -0.9 V), and at low voltage (V = -0.5 V) the corrugation is again in the [001]-direction. The observed changes in atomic corrugation can be explained in a very straightforward manner if one accepts the following hypothesis: That the contribution of the BVB-states is spatially modulated so as to produce an atomic-like corrugation in the [001]-direction (see figure 4.4: p-GaAs, V = -0.499 V).

Let us start by considering the minimum in the CN that occurs for V = -0.9 V. This partial change in corrugation indicates that the C3-state is populated and contributes to the total tunneling current, since the C3-state is the only surface state that causes an atomic corrugation in the [-110]-direction. On p-GaAs, the C3-state can only become populated if the surface is in inversion. At the same time, it is clear from the fact that a mixed corrugation is observed, that there must be a second contribution from another state which causes a corrugation in the [001]-direction. Together, the two contributions cause a mixed corrugation to appear in the image. At first sight the logical interpretation would be that the mixed corrugation is caused by the combined

contributions of the A5-state and the C3-state, assuming that the latter has become populated by inversion.

However, it becomes clear that this interpretation must be wrong when the voltage at which the mixed corrugation occurs, is considered. If the C3-state is to contribute to the filled-states tunneling current, it must lie energetically below the Sample Fermi Level (SFL). The fact that the C3-state lies energetically near the SFL implies that the A5 and A4-states must lie well below the Tip Fermi Level (TFL) and thus cannot contribute to the total tunneling current. The reason for this is that the bias voltage at which the mixed corrugation occurs, equals –0.9 V. This is less than the energetic separation of the A5 and C3 states, which lie on either side of the bandgap of the semiconductor. It is thus certain that at V = -0.9 V, the surface is in type I inversion. From figure 4.6 we now identify the BVB-states as the origin of the second contribution to the total tunneling current at V = -0.9 V. In order to explain the fact that we observe a mixed corrugation at this voltage, we have to assume that the contribution from the BVB-states is associated with an atomic-like corrugation in the [001]-direction.

When the voltage is decreased from V = -0.9 V to V = -0.5 V, the corrugation changes to one in the [001]-direction. According to figure 4.6 the amount of TIBB gradually decreases with decreasing (absolute) voltage. Consequently, the C3-state becomes less and less populated, causing a gradual decrease of the contribution to the total tunneling current from the C3 state relative to the one from the BVB-states. This causes the corrugation to change. At some point, the C3-state rises above the SFL and only the contribution from the BVB-states is left. At V = -0.5 V, we thus expect that the total tunneling current originates purely from the BVB-states.

As the voltage increases from V = -0.9 V to V = -1.4 V, the CN increases as well. Our explanation is that, as the voltage increases, the contribution from the BVB states increases more rapidly than the contribution from the C3 state, thus leading to a corrugation which is stronger in [001]. This is understandable from the fact that the amount of TIBB levels off at the onset of inversion: When inversion sets in, the contribution from the C3-state remains more or less constant whereas the one from the BVB-states increases with increasing voltage. It is quite obvious that a stronger contribution from the A5 state would also lead to a corrugation in [001]. However, for the A5 state to contribute, the TFL has to lie energetically below the VBM. Since the surface must be in type I inversion for V = -0.9 V and larger (absolute) bias voltages, the A5 state must lie energetically at –1.4 eV or more below the SFL. Consequently, we cannot expect to observe the A5 state for 0 < V < -1.4 V. The change in corrugation between V = -0.9 V and V = - 1.4 V must therefore occur entirely while the surface is in type I inversion.

Summarizing, we interpret the filled-states images obtained on p-GaAs in the following way: At low voltage (V = -0.5 V), we expect to observe only a contribution from the BVB-states. We assume that the contribution from the BVB-states has an atomic-like corrugation to it in the [001]-direction. At intermediate voltage (V = -0.9 V), inversion sets in and the resulting contribution from the C3-state causes a partial corrugation-change. At large negative voltage, both the BVB-states and the C3-states contribute to the total tunneling current, but we expect the contribution from the BVB-states to dominate, causing a corrugation in the [001]-direction.

The idea that a tunneling current from the BVB-states would be accompanied by atomic corrugation is a somewhat radical one, since it assumes a mechanism for atomic corrugation that lies outside the framework of the Tersoff-Hamann theory (see section 1.10). In the following we will therefore give two supporting arguments for this assumption. In subsection 4.5.6, we will comment on the possible nature of corrugation-mechanisms that lie outside the framework of the Tersoff-Hamann theory.

The most compelling supportive argument is that we have based our interpretation on a bandbending behaviour that is consistent with the results presented by Feenstra *et al.* [9]. In that paper, the authors compare experimental I(V)-spectra of GaAs-(110) with model calculations. The model very specifically considers the effects of electrons tunneling into or out of bulk states through a surface depletion layer caused by TIBB. The authors find that the experimental results can only be reproduced by the model if the current generated by electrons tunneling through a surface depletion layer into or out of bulk states, is included. It is thus clear that it is very well possible to obtain a measurable tunneling current from electrons tunneling out of bulk states through a surface depletion zone. In fact, the phenomenon seems a very common occurrence from ref. 9. When this band bending behaviour is combined with the assumption that a contribution from the BVB-states is somehow associated with atomic-like corrugation in the [001]-direction, the explanation of our own experimental results follows in a very straightforward and natural way.

A second argument can be made by attempting to explain the measured corrugation-changes within the framework of regular tunneling, *i.e.* assuming that atomic corrugation can only be caused by electrons tunneling directly into or out of surface states. The remainder of this subsection will show that such an alternative explanation is strictly speaking possible, but necessarily involves a band bending behaviour that is very questionable.

Since the surface is in inversion at V = -0.9 V, we can exclude any contribution from the A4 and A5 states in the voltage-range –0.9 V < V < -1.4 V. At lower voltage where we no longer expect inversion, we can exclude a contribution from the A4 and A5 states for the following reason: The partial corrugation change at V = -0.9 V very strongly suggests that there is a simultaneous contribution from two states, one with a corrugation in [-110] (the C3 state) and one with a corrugation in [001]. The change in corrugation at low voltage further suggests that of these two states, only the one with corrugation in the [001]-direction remains at lower voltage. It thus seems that the electronic state that determines the atomic morphology of the images at V = -0.5 V, also must contribute to the total tunneling current at V = -0.9 V.

Besides, a contribution of the A5 state at V = -0.5 V combined with a contribution from the C3-state at V = -0.9 V would imply a very sharp, almost discontinuous decrease in the amount of TIBB with decreasing voltage. The decrease in TIBB would actually have to exceed the decrease in the applied bias voltage. From figures 4.6 and 4.7, such sharp changes in TIBB are not to be expected. Such a sharp decrease in TIBB would also imply that at V = -0.9 V, only the C3-state would contribute to the tunneling current as the A5- and A4-states lie too low in energy. A contribution of only the C3 state at V = -0.9 V would manifest itself in a corrugation in [-110] rather than the mixed corrugation that is observed in the images. We can thus

exclude a contribution from the A4 and A5-states for the entire range of applied bias voltages.

In the absence of the A4- and A5-states, the only remaining surface-state that would cause a corrugation in the [001]-direction is the C4-state. The alternative explanation would therefore involve the following band bending scenario: At large voltage (V = -1.4 V), the surface would have to be in type I inversion to such an extent that the C4-state becomes populated and contributes to the *filled* states current. For V = -0.9 V, TIBB would have to decrease slightly so that the contribution from the C3-state would become somewhat stronger. At lower voltage, still, the amount of TIBB would have to *increase* in order to re-populate the C4-state.

In our model, an increase of TIBB with decreasing absolute voltage can occur if the decrease in voltage is accompanied by a larger relative decrease in tip-sample distance. Note that our measurements were obtained a fixed tunneling current, and therefore the tip-sample distance changes from one frame to the next. We have no indications that such a non-monotonous behaviour of TIBB indeed occurs under normal experimental circumstances, but we will assume that it might occur for the sake of the argument.

We first have to consider whether or not it is possible for the C4-state to become populated by inversion in the first place. It would seem that no circumstances exist for which the C4-state becomes populated by inversion as it is centered 1.1 eV above the CBM. According to our model, the amount of TIBB levels off at the onset of inversion, populating the conduction-band related surface states only up to some 300 meV. This is consistent with our filled-states images of n-GaAs: For V = -1.1 V, the conduction-band related surface states are populated due to (type I) accumulation. At the same time, the atomic corrugation seen in the filled-states images of n-GaAs shows no sign of a contribution from the C4-state. However, from the empty-states images of n-GaAs in which the conduction-band related surface-DOS of the GaAs-surface is probed directly, it seems that the influence of the C4-state in the surface-DOS manifests itself even at energies that lie slightly above the CBM: In the empty-states images of n-GaAs (see subsection 4.5.3), it is seen that the corrugation does not change when the TFL lies somewhere between the peaks of the C3 and C4 states: Rather, the corrugation changes when the TFL lies at a far lower energy relative to the sample surface-DOS, about 140 meV above the CBM. Apparently the low energy shoulder of the C4 state extends to relatively low energies and makes up a significant part of the surface-DOS, even at energies that lie below the value at which the lower lying C3 state is centered. From figures 4.6 a and b it can be seen that it is very well possible to populate the conduction band up to 150 meV above the CBM by inversion. It is thus *perhaps* possible that due to inversion of the surface, the low-energy shoulder of the C4-state can become populated and thus influences the atomic corrugation of the filled-states images of p-GaAs.

The other crucial element in the alternative explanation is that the band bending behaviour must be non-monotonic in order to reproduce the corrugation-changes that we have observed experimentally. For some parameters, we have observed that the amount of TIBB increases slightly with decreasing voltage. Such effects, however, are minor and always occur near the transition from type I inversion to type I depletion (see figures 4.6 b, 4.7 b). The reason for this is that the transition from type I inversion to type I depletion usually involves a large decrease in tip-sample distance. If the relative

decrease in tip-sample distance is larger than the relative decrease in the bias voltage, the electric field present between the tip and sample increases and the amount of TIBB increases as well.

In our model, we found no set of parameters which produces a non-monotonous change in the amount of TIBB at the right voltage: It is possible in the model to populate the conduction-band by inversion at V = -0.9 V and I = 55 pA when a tip workfunction of 4.0 eV is assumed. The calculated amount of TIBB is then –1.572 eV, implying that the CBM at the surface lies 148 meV below the SFL. Since the empty-states results on n-GaAs suggest that the corrugation changes when the TFL lies about 140 meV above the surface-CBM, we assume for the moment that this situation would produce an atomic corrugation similar to the mixed corrugation that we have observed experimentally. To account for the fact that near the CBM the surface-DOS decreases asymptotically to zero, we also set the density of the surface-state bands to 4.42 * 10^{13} cm^{-2}, which is $^{1}/_{10}$ of the usual value. For these parameters, the amount of TIBB varies monotonically from –1.450 eV at V = -0.55 V to –1.702 eV at V = -1.5 V. This type of scenario would therefore cause a monotonous change in the atomic corrugation rather than a partial change which is reversed. This argument also holds if a different value for the work function is assumed in the model. In order to mimick the experimentally observed mixed corrugation at V = -0.9 V, the tip-sample distance has to be adjusted in order to reproduce the same amount of TIBB (-1.572 eV). The (constant) simulated current will then change accordingly. If then the bias voltage is varied in order to simulate the entire measurement, the same monotonous change in the amount of TIBB is predicted.

Whether or not such a non-monotonous behaviour of the TIBB can be excluded for a real inverted surface as well, is not fully certain. In a real inversion layer the electrons are confined and thus occupy quantized energy-levels. These levels lie near the top of the tip-induced potential well, which is near the SFL. In our model, the large changes in tip-sample distance that cause a non-monotonous behaviour of the amount of TIBB only occur when the CBM passes the SFL. In the presence of quantized levels, the lowest occupied electron-states do not lie at the surface-CBM, but rather, at a slightly higher energy. As a consequence, the non-monotonous changes in the amount of TIBB are expected to occur when the lowest quantized level passes the SFL. Very strictly speaking, this might create the non-monotonous band bending behaviour at the right tip-sample voltage needed to complete the alternative explanation. However, the argument seems quite far-fetched, and we therefore regard it as implausible.

It is clear that the alternative explanation for our experimental results is strictly speaking possible, but that it crucially depends on two assumptions that are very much open to debate: it is possible, but by no means certain, that TIBB can invert the p-GaAs surface to such an extent that the C4-state becomes populated. In fact, based on our filled-states images of n-GaAs we expect the opposite. Secondly, it remains to be seen whether or not the non-monotonous band bending behaviour can really occur. In our model, a non-monotonous change in band bending that occurs at the right voltage in order to explain our experimental results, could not be simulated. We thus conclude that the only reasonable explanation for the corrugation changes that we have shown in figure 4.4, involves electrons tunneling from the BVB-states into the tip through a surface depletion layer. This tunneling current is spatially modulated in such a way that

when the contribution from the BVB-states dominates the total tunneling current, an atomic-like corrugation in the [001]-direction is observed in the STM-image.

4.5.5 The reliable use of the model

The use of a one-dimensional model to describe band bending seems justified from the distances over which TIBB extends into the semiconductor. For typical parameters, the effects of TIBB extend between 10 and 50 nm into the semiconductor. If the band bending extends over similar distances laterally, it will appear uniform on the scale of one or two surface unit cells. Furthermore, the model relies on the Tersoff-Hamann theory to calculate the tunneling probability. Consequently all problems that are usually associated with the application of this theory will also be relevant for this model. Whenever the simulated tip-sample distance decreases to less than about 4 Å, we expect deviations from the model due to significant tip-sample interaction. We observe that for very low voltages in the band bending situation of type I depletion, the model sometimes fails to reproduce experimentally observed I(V) points. Instead, the model indicates that no tunneling current can be measured for those parameters. We attribute this deviation to the effects of tip-sample interaction, possibly a collapse of the tunneling barrier [18].

Another approximation that is made in the model is that the tip and surface states have constant densities of states as a function of energy. The latter approximation can cause small discontinueties in the calculated tip-sample distance (figure 4.8b, d) or kinks in the band bending behaviour. Such features occur at the transitions between the different band bending situations. Experimentally, sharp peaks in the tip-DOS can cause one portion of the surface-DOS to contribute more strongly to the total tunneling current than the rest of surface-DOS that lies inside the energetically accessible window between the TFL and SFL. The consequence of that is that the model can only be used to determine which of the surface states might contribute to the tunneling current on the basis of whether they are energetically avialable or not. Questions about which surface state is likely to dominate over the others at a given voltage cannot be answered from the model alone.

In the light of the assumptions and approximations made in the model it would seem problematic to obtain a meaningful comparison between the experimental and theoretical z(V) points for a given measurement. Fortunately, however, many of the unknown parameters in the model (such as the tip-state) are constant throughout the range of applied bias voltages. Thus a theoretical z(V) curve should at least be proportional to its experimental counterpart, so that voltage-dependent changes in z(V) can still be interpreted meaningfully. Besides, the agreement between the experimental |dz/dV| points and the theoretical |dz/dV| curve indicates that the accuracy of the model is quite reasonable.

We are convinced that when the limitations of the model are kept in mind, it can be used reliably. The most important issue when applying the model, is finding the appropriate values for some of the parameters, in particular the tip work function. At present, we base our interpretation of the results on the experimental STM-images

themselves, and then use the model to verify whether the interpretation is realistic from the point of view of band bending. Notice that our main conclusions do not critically depend on assumptions for any of the model parameters: The conclusion that a contribution from the BVB states is associated with atomic corrugation is based on the observation that for a particular voltage the surface must be inverted. That inversion is seen directly from the observed corrugation. The complementary argument that excludes a contribution from the C4 state in those circumstances also remains valid for different sets of model-parameters. The interpretation of the results for n-GaAs pivots around the fact that the transition from type I depletion to type II depletion occurs for V = +0.5 V. This transition can be seen experimentally from the increase in |dz/dV|. The interpretation of the results for n-GaAs therefore does not depend on assumptions made in the model, either. In case of accumulation (filled states results for n-GaAs and empty states results for p-GaAs) the band bending behaviour itself does not depend very strongly on the assumed parameters.

4.5.6 Atomic resolution on GaAs (110) in type I depletion

Atomic resolution on semiconductor surfaces is usually understood in terms of regular tunneling of electrons into or out of surface states. In this view, only those states that lie energetically between the TFL and SFL are available to the tunneling process. For most of the experimental results presented in this paper, the concept of regular tunneling is perfectly adequate to understand the observed corrugation. However, when tunneling takes place while the sample surface is in type I depletion, alternative mechanisms for atomic corrugation have to be considered. In this subsection we will theorize on such possible mechanisms for atomic corrugation while tunneling takes place between a tip and the bulk states of a sample in type I depletion.

It is in any case clear that the corrugation observed in the type I depletion regime must be associated with the surface of the crystal. At the surface, there is a clear distinction between the top row As sites and the bottom row As sites (figure 4.1b). Inside the crystal, the As atoms located on a [110]-axis below a top row As surface atom are equivalent to the As atoms located below a bottom row As surface atom. If the inside of the crystal (more specifically: the spatial distribution of the valence band charge in the bulk) could be imaged by electrons tunneling through the depletion layer, this would manifest itself as a doubling of the periodicity in the observed lattice. From figure 4.4 it is evident that this is in conflict with our experimental observation.

Besides, it is doubtful whether the bulk of the crystal can be imaged with adequate resolution: In order to image the atomic scale variations of the bulk valence band charge through a depletion zone of some 5 nm, the electrons participating in the tunneling process have to travel almost perpendicularly to the surface. If the cone of "allowed" directions of travel has a half-angle of more than about 1 degree, atomic resolution will be lost. It is known from Ballistic Electron Emission Microscopy (BEEM) that such channeling of electrons can indeed occur due to the existence of a "critical angle" [19]. However, for typical circumstances this critical angle is slightly too

large (about 6 degrees) [19]. Moreover, this effect is caused by the constraint that the lateral momentum of the tunneling electrons must be conserved across a metal-semiconductor interface. This interface manifests itself as a potential-step which is lower than the energy of the tunneling electron itself. In our situation, no such low potential step exists near the tunneling junction. We therefore suspect that the current of electrons tunneling from the BVB states contain no (observable) information about the inner structure of the crystal. However, as the tip is scanned across the surface, the surface structure may modulate the tunneling current by some other process than regular tunneling.

In the case of type I depletion on n-GaAs we can explain the observed corrugation by assuming that the tunneling current is modulated by resonant tunneling through the low energy shoulder of the C3 state, which extends into the bandgap [4,5] (see sub-section 4.5.3). For p-GaAs, on the other hand, it is not clear whether the same argument can be applied. According to ref. 5, the A5 state does not have a shoulder that extends into the bandgap as is the case for the C3 state. The same is evident from refs. 1 and 4 for the (110) surface of InP. The plotted surface-DOS of GaAs (110) in ref. 3, however, *does* suggest that the A5 state has a small high-energy shoulder which extends into the bandgap, although no specific reference or comment about this is made by the authors of the paper. It is therefore not clear to us whether on GaAs (110) the A5 state has a (small) shoulder extending into the bandgap or not. If the A5 state does not have any such shoulder, we have to consider alternative mechanisms that can cause atomic corrugation when electrons tunnel from BVB into the tip.

The non-typical result in the empty states images on n-GaAs ($V < +0.4$ V, 50 pA) can certainly not be explained by resonant tunneling through the low-energy shoulder of the C3-state. At these very low voltages, the corrugation is in the [001]-direction. At the same time, we have observed that the positions of the atomic maxima has not shifted during the corrugation-change, indicating that the atomic maxima in the corrugation are centered on the top row Ga sites. This identifies the observed corrugation as the one being associated with the C4 state. For a tunneling junction between a tip and an n-GaAs (110) surface, it is sometimes possible for the amount of TIBB to become negative for very small positive values of the applied bias voltage. This will cause the C3 state to sink below the SFL, so that only a contribution from the C4 state is left. For this to occur, however, the tip work function has to be less than the electron affinity of the semiconductor (4.07 eV for GaAs [20]). Given the fact that we could reproduce the experimentally observed values for $|dz/dV|$ in that measurement for $W_{TIP} = 4.35$ eV (figure 4.8d), this mechanism cannot be used to explain the observed increase of the CN at low voltage. In order to explain the involvement of the C4 state in the tunneling process at these very low voltages, we have to consider alternative mechanisms for atomic corrugation as well.

One possible mechanism is that the corrugation is caused by atomic-scale variations of the tunneling barrier-height. Such variations have been observed experimentally for different reconstructions of the Si (111) surface and for the 2xn-reconstruction of Si (001) [21,22]. Two other possible mechanisms are caused by the interaction between the tip- and sample electronic states that becomes important when the tip and sample are sufficiently close. This interaction, and the resulting appearance of Tip-Induced Localized States (TILS), has been described by several authors

[23,24,25,26]. The interaction can be understood in qualitative terms from the molecular orbitals that exist in di-atomic molecules.

In ref. 7 (p. 177 and further), the tip-sample interaction for tip-sample distances between 4 Å and 8 Å is modeled by considering a hydrogen molecular ion (H_2^+). As the H_2 molecule is formed from two separated H-atoms, the two 1s levels of the atoms combine into a bonding and an antibonding molecular orbital [27]. The bonding orbital is shifted downward in energy with respect to the unperturbed 1s levels, whereas the antibonding orbital shifts upward. An attraction between the two hydrogen-nuclei exists because the hydrogen molecule only contains two electrons which can both be accommodated in the bonding orbital, which lowers the energy of the entire system. In ref. 7, the H_2^+-ion rather than the neutral H_2 molecule was chosen as the model since that mimicks the fact in STM that tunneling always involves one occupied and one empty state. A similar interaction, only more complicated, exists between the 1s orbital of a hydrogen atom and the 2p orbital of a fluorine atom when they combine to form hydrogen fluoride (HF) [27]. The significant difference between H_2 and HF is that for HF, the interacting atomic orbitals do not have equal energies. Also, the molecular orbitals that result from the interaction between the 1s and the 2p orbital do no necessarily lie energetically between the two parent states: One molecular HF-orbital lies energetically below the two non-interacting parent states, some have the same energy as the unperturbed 2p-states, and one lies energetically above the two non-interacting parent states.

In a real tunneling junction, the same type of interaction takes place between the (molecular) states of the atom-cluster that makes up the apex of the tip [28] and the surface states of the sample. In general, these states do not have equal energies, so that the interaction between a real tip and sample may be compared to the formation of molecular orbitals in di-atomic, *heteronuclear* molecules such as HF. A significant difference is that the distance between tip and sample in STM is usually larger than the bond length found in these molecules (0.9 Å for HF) [27]. The tip-sample interaction in STM is therefore similar to the *onset* of molecular orbital formation as the atoms approach each other. Furthermore, the tip-sample interaction is site-dependent as it is the result of a spatial overlap of the interacting states: If the tip faces a maximum in the sample-DOS, the interaction will be stronger than in the case that it faces a minimum (see also ref. 7, sect. 7.3 and ref. 23).

In the case that tunneling takes place between the bulk states of a semiconductor (surface) in type I depletion and a tip, this interaction has two important consequences: The first is that the interaction may cause new states to appear inside the energetic window between the TFL and SFL, since in general the molecular orbitals do not have the same energies as the non-interacting (parent) states. The electrons involved in the tunneling process can then tunnel resonantly through such a "molecular orbital" formed between tip and sample if it happens to lie at the appropriate energy. Because the tip-sample interaction is site-dependent, this effect will modulate the tunneling current as the tip is scanned across the sample. The resulting STM-image will reflect the lateral variations in the tip-sample interaction. It will thereby also reflect the lateral distribution of the sample state with which the tip state interacts. This is the first mechanism.

The second mechanism is related to the first one in the sense that it is also based on the site-dependency of the tip-sample interaction. As the tip is scanned across the

surface, it will relax under the influence of the site-dependent interaction. If the interaction is attractive, the tip apex will approach the sample surface where the interaction is strong, and it will be pulled away by the elastic forces inside the body of the tip where the interaction is weaker. If the STM is operated in the constant height mode, this will cause a modulation in the current. If the STM is operated in the constant current mode, the feedback mechanism will try to compensate for the modulations in the current by retracting or extending the (back of) the tip, causing a corrugation in the height-image.

If the tip-sample interaction indeed provides an alternative mechanism for atomic corrugation, it might have an observable feature to it: The interaction between electronic states is likely to be stronger if the two states are closer in energy [27]. At the same time, an STM-tip often has an electronic state just below the Fermi Level that dominates the tip-DOS [28,29,30]. In the case of type I depletion on p-GaAs, the A5-state is closest to the TFL, so that an atomic corrugation caused by the interaction of the electronic states of the tip and sample is likely to reflect the spatial distribution of the A5 state. In the case of type I depletion on n-GaAs, on the other hand, the TFL lies closest to the conduction band related states, C3 and C4. Of these two states, the C3 state lies closest to the TFL, but it is also weak in comparison to the C4 state. In any case, the atomic corrugation that the interaction might cause, must have its local maxima centered on the Ga-sites of the surface. If atomic-scale variations in the work function of the sample surface were to cause the observed corrugation, we do not expect to observe a selection between the different surface states of the GaAs (110) surface based on whether p-GaAs or n-GaAs is imaged in type I depletion.

From our measurements, it appears that such a selection between the surface states indeed occurs: We suspect that the non-typical result observed in the empty states-images of n-GaAs may have been caused by an interaction between the C4 state of the sample and the dominant electronic state of the tip. The corrugation associated with the BVB-states is similar in its appearance to the corrugation caused by regular tunneling out of the A5 state, but since we have not recorded the transitions from one value of the applied bias voltage to the next, we do not know whether the atomic maxima have shifted or not. We are thus unable to determine with certainty whether the atomic maxima observed the images are centered on the As atoms or the Ga atoms.

The hypothesis that the interaction between the electronic states of the tip and sample surface causes the observed corrugation would provide a very natural explanation for the apparent similarity between the atomic corrugation observed in the type I depletion regime and the atomic corrugation associated with regular tunneling. However, the matter is made more complicated by the fact that resonant tunneling through the low energy shoulder of the C3 state also causes corrugation (on type I depleted n-GaAs). This mechanism seems to dominate in most cases. Whether the tip-sample interaction really can cause atomic corrugation in STM-images in the regime of type I depletion, and whether there are circumstances in which this mechanism is the dominant one, still remains to be determined.

The above considerations can at best give a qualitative insight into the tip-sample interaction between a tip and a semiconducting sample, and into the mechanisms by which such interaction might lead to atomic corrugation in the absence of regular tunneling into or out of surface states. The real proof for any possible mechanism must

come from rigorous calculation. In the case of type I depletion on n-GaAs, resonant tunneling through the low energy shoulder of the C3 state is an important mechanism for atomic corrugation. Whether such resonant tunneling through a similar high-energy shoulder of the A5 state might occur for p-GaAs in type I depletion is as yet unclear. In any case, the results shown in figures 4.4 and 4.5 show that regular tunneling of electrons into or out of surface states is not the only possible mechanism for atomic resolution on the GaAs (110) surface. Therefore, the way in which people usually understand atomic resolution on semiconductor surfaces, can no longer be regarded as complete.

4.6: Some other examples of corrugation-change on GaAs (110)

During our experiments, some of which are not directly related to the work presented in this chapter, we have observed corrugation-changes many times. In this section, we show three illustrative examples.

The first example shows the transition from filled states imaging to empty states imaging on an n-GaAs substrate. For this measurement, we operated the STM in “dual mode”. The scanning voltages are shown in figure 4.10. As the frame was recorded, we changed the scanning parameters for the backward frame from V = +1.018 V, 54 pA to V = -1.930 V, 83 pA, which resulted in a clearly visible change in the corrugation. The parameters for the forward scan remained unchanged. In the backward frame, the sudden change in parameters constitutes an abrubt transition from empty states imaging (bottom part) to filled states imaging (top part). In our STM-setup, the slow scan direction is from the bottom of the frame towards the top. The forward scan, which remains unchanged, shows that the tip-DOS remained the same during the voltage change in the backward scan.

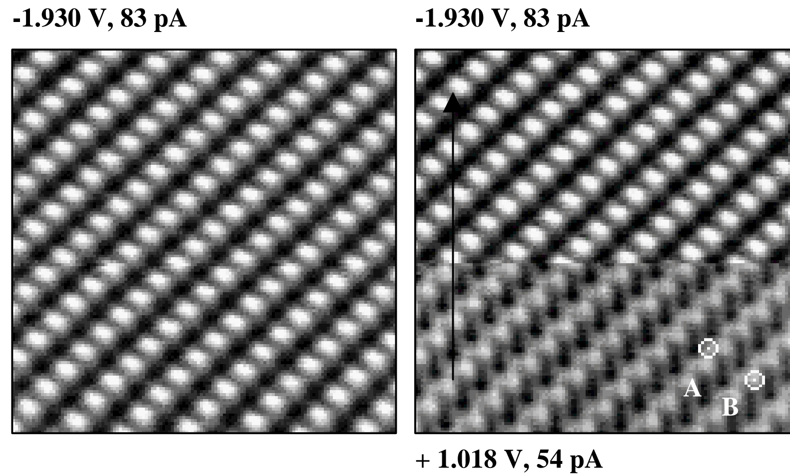

Fig. 4.10: *Left: STM-image of n-GaAs in filled states. Right: Same area, for which scanning paramters were switched (see text). The slow scan direction is from bottom to top. We identify the corrugation in the left frame and the upper part of the right frame as being related to the A5 and BVB states. The corrugation in the bottom part of the right frame is identified as related to the C4 state. Frame size: 5 x 5 nm. See further details in text.*

The forward frame and the top of the backward frame have been imaged in filled states mode. From figure 4.7a-c it is clear that the corrugation must be associated with the A5 state. We can thus identify the atomic maxima as As-sites. In the bottom part of the backward scan, the principle maxima (B-sites) appear to have shifted slightly with respect to the maxima in the top part. This places the maxima on the Ga-sites. Also, the atomic corrugation consists of zig-zag rows of which the A-sites coincide with the maxima of the top part of the image. This identifies the corrugation in the lower part of the backward frame as associated with the C4-state, as this state is centered mainly on Ga-sites, extends along [-110] and has some localization on As-sites as well as on the Ga-sites [1,3]. The possibility of the C4 state appearing as a zig-zag row is also mentioned by Ebert *et al.* [1].

The second example which we show is the local corrugation change associated with dopants or adsorbates (figure 4.11). For a detailed discussion on how dopants and adsorbates appear in STM, and how these two may be distinguished from each other, we refer to ref. 32 and to chapter 7 of this thesis. The example shown here also illustrates how the local corrugation-change around an atomic-scale defect may be used to determine its charge-state. The two images are cut-outs from two different areas of the same STM-frame, in which a Si δ-layer ($1 * 10^{13}$ cm^{-2}) in GaAs was imaged. Figure 4.11a shows several of the dopants, figure 4.11b shows a nearby feature that appears to

be an adsorbate (see also chapter 7). Applied bias voltage was V = -1.93 V, tunneling current was 96 pA. For these conditions, the donor atoms are unionized since the surface is in accumulation (see figure 4.7). If, however, the tip approaches the Si atom to within the Bohr-radius of the bound electron, the positive charge associated with the Si atom core will no longer be screened completely. This positive charge will locally decrease the potential for electrons, resulting in a local increase of the downward band bending. That enhances the contribution from the C3 state relative to the ones from the BVB states and the A5 state, which manifests itself as a change in corrugation near the dopant atoms.

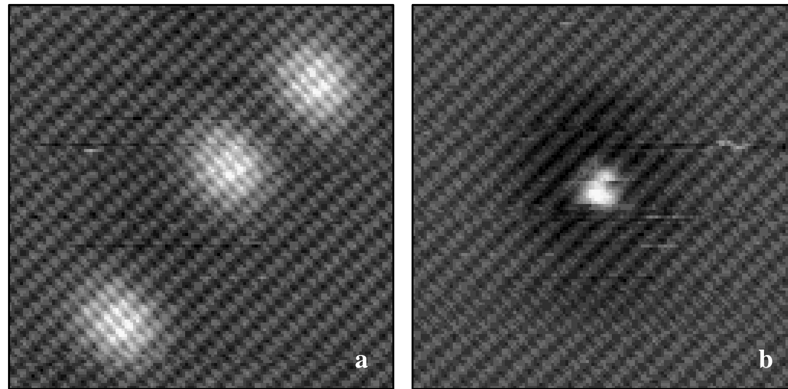

Fig. 4.11a: *Three Si donor atoms which form part of an n-type ddoped layer in GaAs (1 * 10^{13} cm^{-2}). Around the dopants, the rows appear to run more along (001), as the local positive charge associated with the dopants locally changes the amount of TIBB (see text). Frame size: 11.7 x 11.7 nm. Gray scale: 146 pm.*
b: *Corrugation change around an adsorbate. The adsorbate is charged negatively which also locally changes the amount of TIBB (see text). Here, the rows run more along (-110). Frame size: 11.7 x 11.7 nm. Gray scale: 180 pm.*

Around a negatively charged adsorbate, the same mechanism leads to a corrugation change which is opposite to the change observed for the dopants. We regularly observe adsorbates like the one shown in figure 4.11b in our experiments. For filled states, they look as shown. For empty states, they appear as depressions in the image. We also observe that their density increases as the experiment progresses. This voltage-dependent behaviour has been reported for oxygen-atoms adsorbed onto an n-doped GaAs (110) surface [31]. The oxygen atom aquires some negative charge as it is adsorbed, which creates a depletion zone around it [31,33]. This causes the dark ring

around the adsorbate. The negative charge locally raises the potential, raising the amount of TIBB in the vicinity of the adsorbate. This decreases the contribution from the C3 state relative to the contributions of the BVB states and the A5 state, which causes a change in corrugation as shown.

The last example that we wish to show is the corrugation change around a pn junction (figure 4.12). This junction was formed by a Be δ-layer ($1 * 10^{13}$ cm^{-2}) and an n-doped cap layer (Si: $4 * 10^{18}$ cm^{-3}) that was grown on top of it. The δ-layer was overgrown by 27 nm of non-intentionally doped GaAs and then by n-type GaAs. Somewhere between the Be δ-layer and the the cap layer, a p-n junction formed which we recognized in our image from the depletion zone that is associated with such a junction (figure 4.12). The bright spot near the depletion zone is a Si dopant. Near the bottom of the frame, where the depletion zone is curved, there is a second Si dopant which falls just outside the frame. The image was obtained at V = -1.698 V, 85 pA.

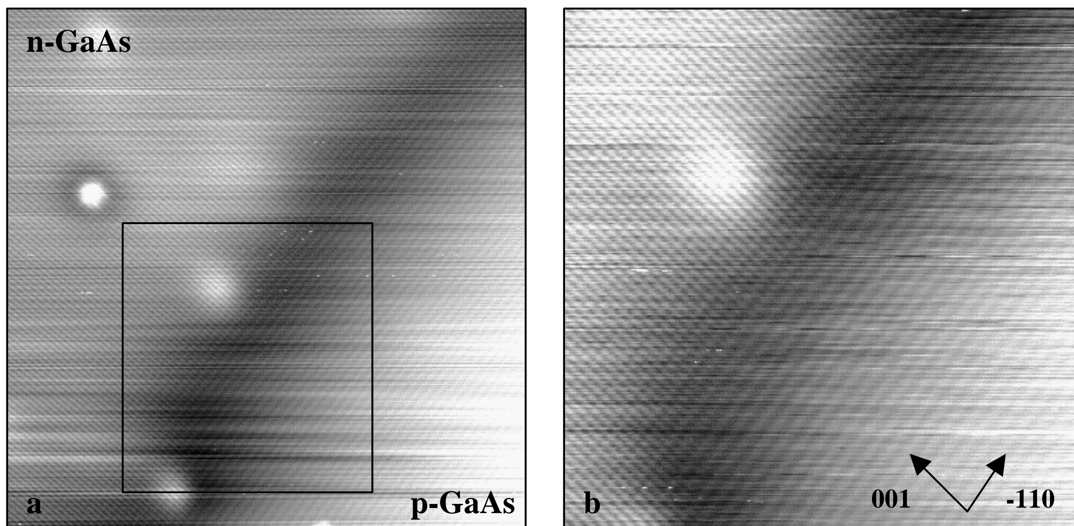

Fig. 4.12 a: *STM-image of a pn-junction in GaAs (see text). Frame size: 35 x 35 nm, V = -1.698 V, I = 85 pA. The depletion region associated with the pn-junction is visible as a dark band running from the lower left part of the frame towards the upper right corner. The bright features in the n-GaAs part of the frame are subsurface Si dopants, the bright feature surrounded by a dark ring can be either a surface layer dopant or an adsorbate (see chapter 7).* **b:** *The local change in atomic corrugation on either side of a pn-junction. The area shown in (b) is indicated in (a) by the black box. Frame size: 20 x 20 nm, grey scale: 0 – 236 pm.*

The n-GaAs portion of the image shows rows running along (001) whereas the p-GaAs portion shows rows running along (-110). The interpretation is relatively straightforward: Due to the downward band bending, the n-GaAs portion of the surface is in accumulation. This populates the C3 state and causes the corrugation to be in the [-110]-direction. For the p-type portion of the surface, we expect contributions from the BVB states or possibly the A5 state, causing the corrugation to be in [001]. The quantitative treatment of TIBB given earlier in this chapter is not very well applicable since the model was developed for bulk materials. Due to the presence of the junction, the bandbending behaviour of the two portions of the frame may differ from the TIBB expected for bulk material. Also, the fact that for the p-type material all dopants are concentrated in a single δ-layer located at some distance from the junction may influence the band bending behaviour.

4.7 Summary

In this chapter, we have combined voltage-dependent images of the GaAs (110) surface with calculated values for tip-induced band bending obtained from a one-dimensional model, in order to study the influence of Tip-Induced Band Bending (TIBB) on voltage-dependent STM-images of GaAs-(110). For the empty-states results on n-GaAs we have validated the model by comparing measured and theoretical values for |dz/dV| as a function of applied bias voltage. The work shows that TIBB influences the morphology of the observed atomic lattice quite profoundly. Furthermore, for both p-GaAs and n-GaAs a voltage-regime exists for which no surface state lies inside the window of energetically accessible states between the Tip Fermi Level (TFL) and Sample Fermi Level (SFL) (type I depletion). Instead, tunneling occurs between the tip and bulk states of the sample. In spite of that, atomic, surface-like corrugation is observed in this voltage regime, both on p-GaAs and on n-GaAs. In the case of n-GaAs, the observed corrugation can be explained by resonant tunneling of electrons through the low-energy shoulder of the C3 state, for which it is known that it extends into the bandgap. For p-GaAs, several possible mechanisms exist. The corrugation might arise from resonant tunneling through a high-energy shoulder of the A5 state, if the A5 state has a shoulder which extends into the bandgap like the shoulder of the C3 state. The corrugation might also be caused by atomic-scale variations in the tunneling barrier-height as shown in refs. 21 and 22, or by the interaction between tip- and sample electronic states. In any case, the corrugation observed for the type I depletion regime cannot be explained by regular tunneling, which is the common way to understand atomic resolution on semiconductor surfaces.

Looking ahead, a few things are apparent: In previous articles on voltage-dependent images of III-V semiconductor (110)-surfaces, band bending is only

considered qualitatively [1,2,4]. In this work, we have established a connection between the amount of TIBB and the corrugation observed in the image, which can be very helpful for the interpretation of existing and future STM-data. Local changes in the corrugation provide a straightforward way to determine the charge-state of an atomic-scale surface defect. Another very exciting prospect is the fact that some of our STM-images show atomic corrugation in the absence of regular tunneling into or out of surface states. Understanding the mechanisms by which atomic corrugation might occur in the band bending regime of type I depletion represents a clear challenge.

REFERENCES:

1: Ph. Ebert, B. Engels, P. Richard, K. Schroeder, S. Blügel, C. Domke, M. Heinrich, K. Urban: *Contribution of surface resonances to Scanning Tunneling Microscopy images: (110) surfaces of III-V semiconductors*. Phys. Rev. Lett, Vol. 77, No. 14, pp. 2997-3000 (1996).

2: C.S. Jiang,T. Nakayama, M. Aono: *Tip-induced occupation of an unoccupied surface state in Scanning Tunneling Microscopy imaging of a GaAs (110) surface with Ag clusters*. Japn. Journal of Appl. Phys, Vol. 36, pp. L1336-L1339 (1997).

3: J.R. Chelikowski, M.L. Cohen: *Self-consistent pseudopotential calculation for the relaxed (110) surface of GaAs*. Phys. Rev. B, Vol. 20, pp. 4150-4159 (1979).

4: B. Engels, P. Richard, K. Schroeder, S. Blügel, Ph. Ebert, K. Urban: *Comparison between ab initio theory and Scanning Tunneling Microscopy for (110)-surfaces of III-V semiconductors*. Phys. Rev. B, Vol. 58, No. 12, pp. 7799 – 7814 (1998).

5: J.R. Chelikowski, S.G. Louie, M.L. Cohen: *Relaxation effects on the (110) surface of GaAs*. Phys. Rev. B, Vol. 14, No. 10, pp. 4724 - 4726 (1976).

6: J. Tersoff and D.R. Hamann, Phys. Rev. Lett. Vol. 50, No. 25, page 1998 – 2001. Also: Phys. Rev. B, Vol. 31, No. 2, page 805 – 813.

7: C.J. Chen: *Introduction to Scanning Tunneling Microscopy*. Oxford University Press, Oxford, 1993. Chapter 3 explains that for an s-like tip state, the tunneling matrix element is proportional to the surface-DOS of the sample evaluated at the centre of the tip apex atom. The concept of "regular tunneling" is summarized by equations 2.36 and 3.26.

8: G.J. de Raad, P.M. Koenraad, J.H. Wolter: *The use of the Schiller-decapitation process for the manufacture of high-quality tungsten STM-tips*. Journal of Vac. Sci. and Tech.-B, Vol. 17, No. 5, pp. 1946 - 1953 (1999).

9: R.M. Feenstra, J.A. Stroscio: *Tunneling Spectroscopy of the GaAs (110) surface*. JVST-B, Vol. 5, No. 4, page 923 (1987).

10: W.P. Dyke and W.W. Dolan: *Field Emission*, in Advances in Electronics and Electron Physics, vol VIII (1956) page 89 – 185. (Academic Press, New York, 1956). See p. 114.

11: Handbook of Chemistry and Physics, Ed. 79, page **12**-124.

12: R. Smoluchowski: *Anisotropy of the electronic work function of metals.* Physical Review, Vol. 60, pp. 661 – 674 (1941).

13: We use commercially available n-doped GaAs wafers with a nominal doping concentration of $1 * 10^{18}$ cm^{-3}. The actual doping concentration may lie between 1 and $2 * 10^{18}$ cm^{-3}.

14: S.H. Ke, T. Uda, R. Perez, I. Stich, K. Terakura: *First-principles investigation on GaAs (110) surface: Implications for atomic force and scanning tunneling microscopies.* To be published in Phys. Rev. B, issue of oct. 15, 1999. In the work presented in refs 9, 14 and 15, the tip is represented by a 4-atom Si tetrahedron. On the back side of the tetrahedron, the dangling bonds have been saturated with hydrogen atoms.

15: R. Perez, I. Stich, M.C. Payne, K. Terakura*: Surface-tip interactions in non-contact atomic-force microscopy on reactive surfaces: Si (111)*. Phys. Rev. B, Vol. 58, No. 16, pp. 10835 – 10849 (1998).

16: J. Tobik, I. Stich, R. Perez, K. Terakura*: Simulation of tip-surface interactions in atomic force microscopy of InP (110) surface with a Si tip*. To be published in Phys.Rev. B, issue of oct. 15, 1999.

17: G.J. de Raad, D.M. Bruls, P.M. Koenraad, and J.H. Wolter: *Observation of a new image-form on GaAs-(110) showing the top- and bottom zig-zag rows of the surface.* Submitted to Phys. Rev. B.

18: Ciraci in: Scanning Tunneling Microscopy III, ed: Wiesendanger and Günteroth, Springer Verlag Berlin,p. 182, p. 197 (1996).

19: L.D. Bell, W.J. Kaiser, M.H. Hecht: *Ballistic Electron Emission Microscopy,* in Scanning Tunneling Microscopy. (pp. 307 - 348). Edited by J.A. Stroscio and W.J. Kaiser. Academic Press, San Diego (1993).

20: E.F. Schubert: *Doping in III-V semiconcductors.* Cambridge University Press, Cambridge, p. 541 (1993).

21: N. Horiguchi, K. Yonei, M. Miyano: *Local tunneling barrier height on Si (111) reconstructed surfaces.* Japn. Journ. of Appl. Phys, Vol. 37, Part 1, No. 6B, pp. 3782 – 3784 (1998).

22: H. Fukumizu, S. Kurokawa, A. Sakai, Y. Hasegawa: *Barrier-height imaging of Si (001) 2xn.* Japn. Journ. of Appl. Phys, Vol. 37, Part 1, No. 6B, pp. 3785 – 3788 (1998).

23: S. Ciraci, A. Baratoff, I.P. Batra*: Site-dependent electronic effects, forces and deformations in STM on flat metal surfaces.* Phys. Rev. B, Vol. 42, No. 12, pp. 7618 – 7621 (1990).

24: S. Ciraci, A. Baratoff, I.P. Batra*: Tip-sample interaction effects in Scanning Tunneling Microscopy and Atomic Force Microscopy.* Phys. Rev. B, Vol. 41, No. 5, pp. 2763 – 2775 (1990).

25: E. Tekman, S. Ciraci: *Atomic theory of Scanning Tunneling Microscopy.* Phys. Rev. B, Vol. 40, No. 15, pp 10286 – 10293 (1989).

26: P.I. Arseev, N.S. Maslova: *Features of tunneling in microjunctions.* Sov. Phys. JETP, Vol. 75, No. 3, pp. 575 – 581 (1992).

27: R.L. DeKock, H.B. Gray: *Chemical strucuture and bonding.* The Benjamin/Cummings Publishing Company, Menlo Park, CA (USA). (1980). See p. 193, 253.

28: S. Ohnishi, M. Tsukada*: Molecular orbital theory for Scanning Tunneling Microscopy.* Solid state comm. Vol. 71, No. 5, pp. 391 – 394 (1989).

29: M. Tsukada, K. Kobayashi, S. Ohnishi*: First principle theory of Scanning Tunneling Microscopy simulation.* Journ. of Vac. Sci. and Tech. A, Vol. 8, No. 1, pp. 160 – 165 (1990).

30: A.L. Vázquez de Parga, O.S. Hernán, R. Miranda, A. Levy Yeyati, n. Mingo, A. martín-Rodero, F. Flores: *Electron resonances in sharp tips and their role in tunneling spectroscopy.* Phys. Rev. Lett, Vol. 80, No. 2, pp. 357 – 360 (1998).

31: J.A. Stroscio, R.M. Feenstra, A.P. Fein: *Local state density and long-range screening of adsorbed oxygen atoms on the GaAs (110) surface.* Phys. Rev. Lett, Vol. 58, No. 16, pp. 1668 – 1671 (1987).

32: Ph. Ebert: *Nano-scale properties of defects in compound semiconductor surfaces.* Surf. Sci. Reports, Vol. 33, pp. 121 – 303 (1999).

33: J.A. Stroscio, R.M. Feenstra: *Scanning tunneling spectroscopy of oxygen adsorbates on the GaAs (110) surface.* Journ. of Vac. Sci. and Tech-B, Vol. 6, No. 4, pp. 1472 – 1478 (1988).

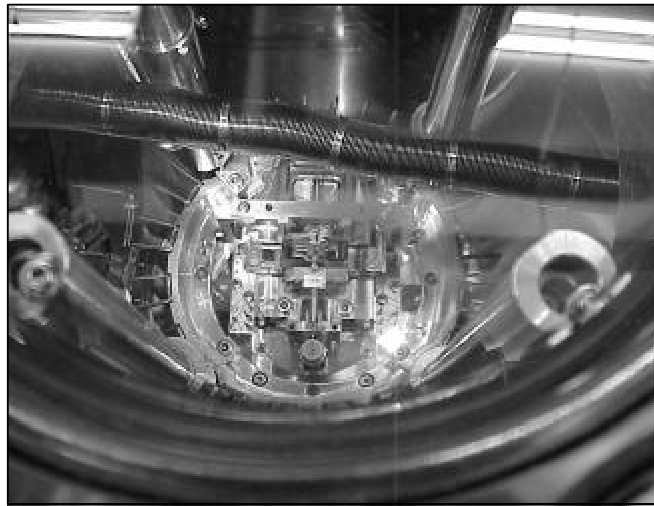

Top view of the STM. The photograph shows a slightly larger field of view than figure 2.2b. The STM is mounted on a round, eddy current damped table which is suspended from four vertical poles. On the foreground, the bellows of the wobble-stick can be seen.

CHAPTER 5:

OBSERVATION OF A NEW IMAGE-FORM OF GaAs-(110) SHOWING THE TOP- AND BOTTOM ZIG-ZAG ROWS OF THE SURFACE

5.1 Introduction

Since the work of Feenstra *et al.* [1], the common way to interpret atomically resolved Scanning Tunneling Microscopy-images (STM) of GaAs (110) has been that the image shows either the Ga atoms or the As atoms in the top rows of the surface, depending on the polarity of the applied bias voltage (figure 5.1). At that time it was already known that the (110)-surface of GaAs posesses four surface states, which are all located energetically outside the fundamental bandgap of the semiconductor [2,3]. Two of these states lie energetically inside the valence band (A5, A4) and two lie inside the conduction band (C3, C4) (see also figure 4.1). The same work also shows that the A5 and A4 states are localized on the top row anions (As) of the surface, whereas the C3 state is localized on the top row cations (Ga). The C4 state is localized mainly on the top row cations, but it also has some localization on the top row anions as well as on both atom-species in the bottom rows of the surface [2].

The (110)-surface of several III-V zincblende semiconductors has been studied in more detail by Ebert *et al.*[4], who showed that the different surface states each have a different localization and spatial extent within the surface unit cell. As a result, the atomically resolved STM-image of such surfaces may change very significantly in appearance as a function of applied bias voltage [4,5]. The (110)-surface of InP has recently been described theoretically by Engels *et al* [6] in great detail. The work explains that the surface state usually designated as C4 in reality consists of several empty surface resonances, each having a different spatial extent and slightly different energetic location [6]. Close to the surface (2.23 a_0 = 1.1 Å from the outwardly rotated P atoms), the C4 state is localized on both the cations and anions and appears as a zig-zag row. Further away from the surface (6.53 a_0 from the surface anion) the state shows up as maxima centered on the cations extending along [-110] [4,6]. In the literature, several papers exist that report bias voltage-dependent changes in the morphology of atomically resolved STM-images of the GaAs (110) surface (see also chapter 4). These changes are interpreted in terms of the four surface states contributing in varying relative amounts to the total tunneling current [4,5,8]. The usual Tersoff-Hamann theory [9,10] provides an adequate basis for this interpretation.

However, some types of atomic morphology are reported which have more than one atomic maximum per surface unit cell, and which therefore cannot be interpreted in

terms of different surface states contributing to the total tunneling current [11,12,13]. In one such case, it is shown explicitely that the image-form involves a reduced tip-sample distance [11]. The result is interpreted in terms of tip-induced electronic states (TILS) that are formed between the tip and sample as these two approach each other closely [11,14,15,16,17]. At the same time, recent theoretical results indicate that a chemical bond may form between the apex atom of the tip and the nearest Ga atom in the top row of the sample surface, if the tip-sample distance is sufficiently reduced [18]. It is thus clear that occasionally, effects are observed in atomically resolved STM on GaAs (110) that cannot be explained within the framework of the usually applied Tersoff-Hamann theory.

In this chapter, we report an unusual image-form of the GaAs (110) surface that we have observed when imaging the empty states of the sample surface. It clearly shows the zig-zag chain formed by the Ga atoms and As atoms in the top row, as well as traces of the second zig-zag chain formed by the Ga and As atoms in the bottom row of the surface. In doing so, it closely resembles the true atomic lattice which is usually depicted by the ball-and-stick models of the GaAs (110)-surface found in many textbooks. We think that this image-form arises when a chemical bond forms between the tip and sample in the way that is described by Ke *et al.*[18]. To our knowledge, no STM-images of GaAs (110) that show both the top and bottom row of the surface have been reported in the literature until now.

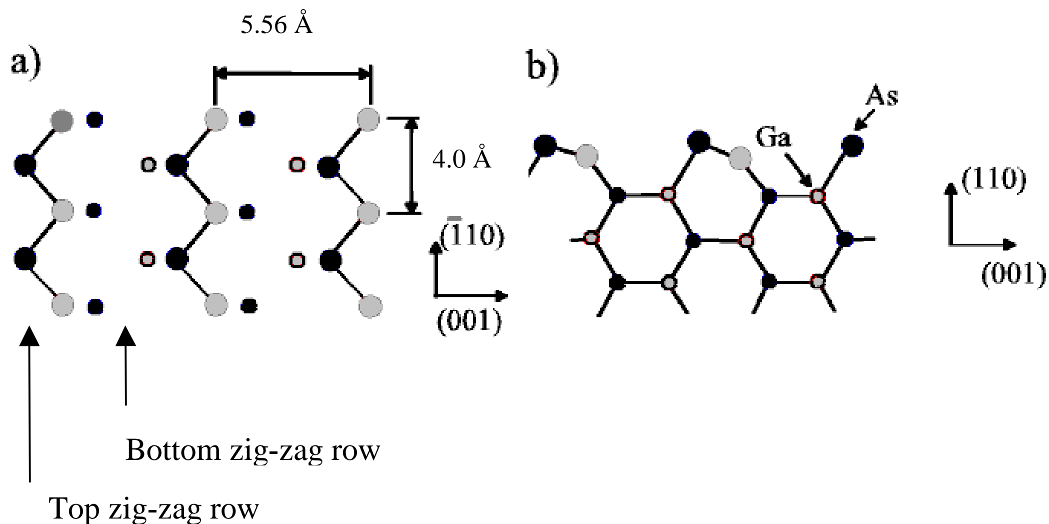

Fig. 5.1a: *Relaxed GaAs-(110) surface (top view).* **b:** *Side view: The surface reconstructs by allowing the top row As atoms to rotate outwara and the top row Ga atoms to move inward toward the bulk of the crystal. The process is known as "buckling".*

Notice that the appearance of the bottom zig-zag row of the surface cannot be explained within the framework of regular tunneling (see section 1.10). An important point in the Tersoff-Hamann theory is that the tunneling matrix element is proportional to the local sample surface DOS evaluated at the position of the centre of the tip apex atom [7]: The STM-image shows the vacuum-tails of the surface states. A direct consequence is that in the framework of the Tersoff-Hamann theory, features in the sample-DOS that lie within the surface layer do not appear in the STM-image.

5.2 Experimental

The STM-work was performed in UHV on *in situ* cleaved GaAs crystals. The samples were doped n-type (Si) to a dopant concentration [19] of 10^{18} cm^{-3}. The bias voltage is applied to the sample. All images shown in this chapter were obtained while operating the STM in constant current mode. To most of the images, we have applied a background correction to the images that involves the "line-by-line tilt correction", which is descibed in detail in section 2.5. For figure 5.3 d we used a band-pass fast Fourier transform (FFT) filter to show details of the lattice in all parts of the frame.

5.3 True Lattice Resemblant Corrugation

The novel image-form that we report occurs occasionally as an anomaly when we make voltage-dependent images of GaAs (110). So far, we have observed the image-form, which we label "True Lattice Resemblant Corrugation" (TLRC: see figure 2a), when imaging the empty states of n-GaAs (110) using a small value for the bias voltage (0 V $< V_{bias} < 0.5$ V). The image-form is stable for a variable amount of time: It sometimes lasts no longer than several seconds or a minute, or it can last for up to 30 minutes as we have observed on one occasion. The image-form TLRC can be reproduced, but we cannot obtain it at will or in a very controlled manner. The method that we apply to obtain TLRC is by imaging the (110) surface of GaAs at positive sample voltage so as to produce normal-looking atomic resolution, which we can obtain routinely. From that point, we gradually decrease the applied bias voltage and/or increase the tunneling current, so as to decrease the tip-sample distance. Some of these attempts produce TLRC, the others simply fail with a tip-crash.

The appearance of TLRC always involves a sudden transition from the normal imaging mode in which the atomically resolved lattice of the GaAs-(110) surface appears as it usually does (see *e.g.* refs. 1, 5, 20), to an anomalous mode which involves TLRC. An example of such a transition is shown in figure 2c. In this particular case, the onset of TLRC involved a sudden transition from the normal morphology of the

atomically resolved lattice (bottom of the frame) to an anomalous form which we have called the “preform” (top of the frame). TLRC itself occurred when the applied bias voltage was further reduced after the appearance of the preform. During other measurements, we have also observed transitions from the normal to the anomalous tunneling regime in which there was a direct change from the normal-looking image to TLRC, without the preform appearing first. The change from the normal tunneling regime to the anomalous tunneling regime does not necessarily occur at the same moment as the moment at which the bias voltage is changed: In figure 2c, for instance, the transition occurred some time later, *i.e.* at a moment that the bias voltage was constant. The difficult part of obtaining TLRC is causing this transition to occur.

The image-mode that we have called TLRC is shown in figure 2a. The atomic lattice consists of parallel zig-zag rows (A-B sites). Between these rows, a second set of zig-zag rows appears as well (C-D sites). These rows lie 10 pm below the rows belonging to the first set. This arrangement closely resembles the true atomic lattice shown in figure 1a. It is possible to switch between TLRC (figure 2a) and its pre-form (figure 2b) by changing the bias voltage (+0.25V and +0.45 V at 35 pA). Furthermore, the effect is very sensitive to the tip-sample distance: At V = +0.35 V, the image shows the pre-form with TLRC in the dark areas (figures 3 a,b). The change from pre-form to TLRC occurs over several nm (36 Å). When imaging a Si-dopant, the dopant shows the pre-form while the surrounding lattice shows TLRC (figures 3 c,d and figure 2d). It is thus clear that TLRC and the pre-form are related, and that the pre-form involves a slightly larger tip-sample distance than TLRC. As the fast scan direction is horizontal, the images also show very clearly that the transition between TLRC and its pre-form is reversible.

Close comparison of the lower and upper parts of figure 5.2c shows that the B-sites in the pre-form coincide with the atomic maxima in the bottom part of figure 5.2c. We can thus identify the B-sites in the pre-form (see figure 5.2b) as top row Ga-sites. A line drawn along [001] through the B- and C-sites in the pre-form would thus pass through the top-row Ga-sites of the surface. From figure 5.2b it is evident that such a line would pass through the atomic maxima of the pre-form, as well as over the bridges connecting the B- and C-sites. We have drawn such a line from the central maximum of the dopant shown in figure 5.3 c,d. In figure 5.3 d it can be seen that the line coincides with the B-sites of the TLRC, which we thus identify as Ga sites in the top row of the surface. The A-sites would then correspond to the As-sites in the top row.

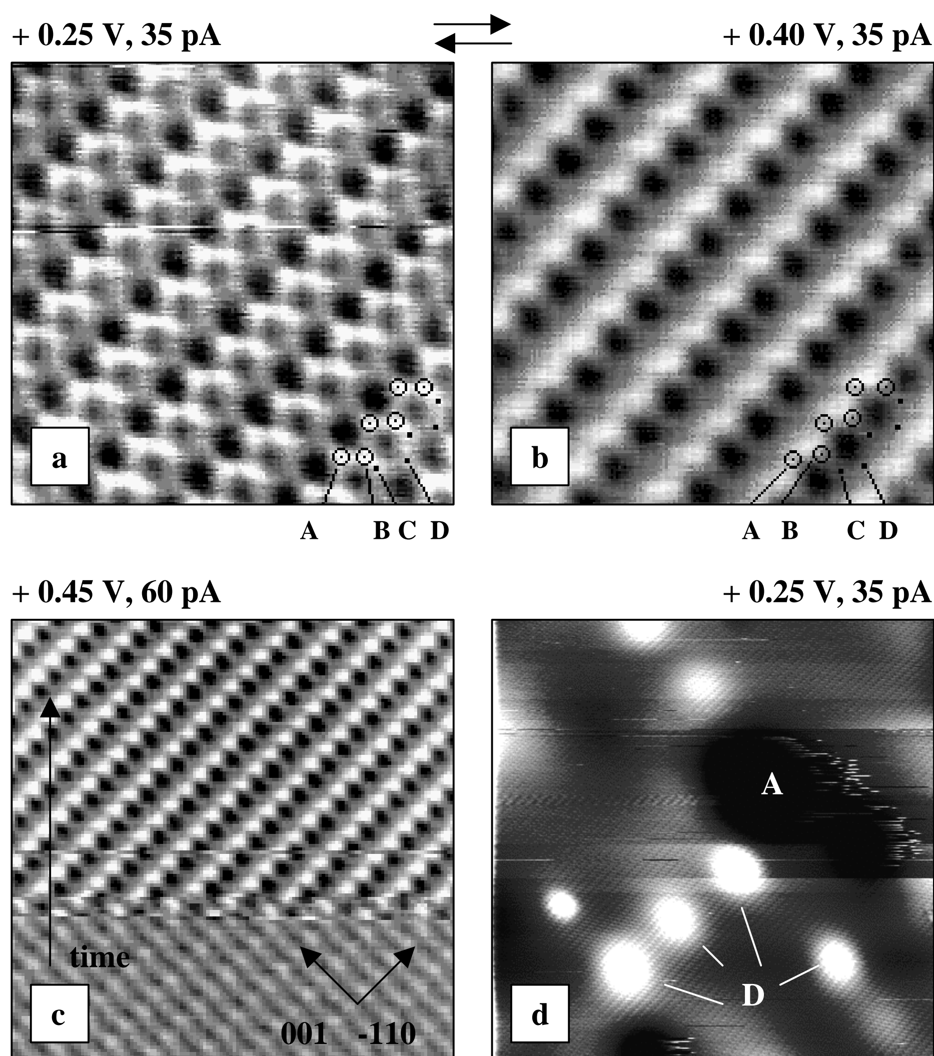

Fig. 5.2 a: *True Lattice Resemblant Corrugation (TLRC) on n-GaAs (3.2 x 3.2 nm^2). V=+0.25V, I=35pA. Greyscale: 0 – 32 pm. The circles identify the top-row atoms (A, B), the dots identify the bottom row atoms (C, D).* **b:** *Pre-form of TLRC. Frame size: 3.2 x 3.2 nm, greyscale: 0 – 41 pm. Figures 2a and 2b have been obtained simultaneously using dual mode imaging. The A,B,C and D-sites of the TLRC have been projected into the image.* **c:** *Transition from normal imaging (lower part) to pre-form of TLRC (upper part). Slow scan direction is from bottom to top (6.7 x 6.7 nm). Greyscale: 0 – 39 pm. In the (raw) image, the atomic maxima of the pre-form lie 16 pm higher than the atomic maxima in the bottom part of the image.* **d:** *Large-scale image of the GaAs (110) surface showing TLRC. Frame size: 35 x 35 nm. We interprete the bright features (D) as Si dopants. The dark areas (A) are interpreted as negatively charged adsorbates* [28].

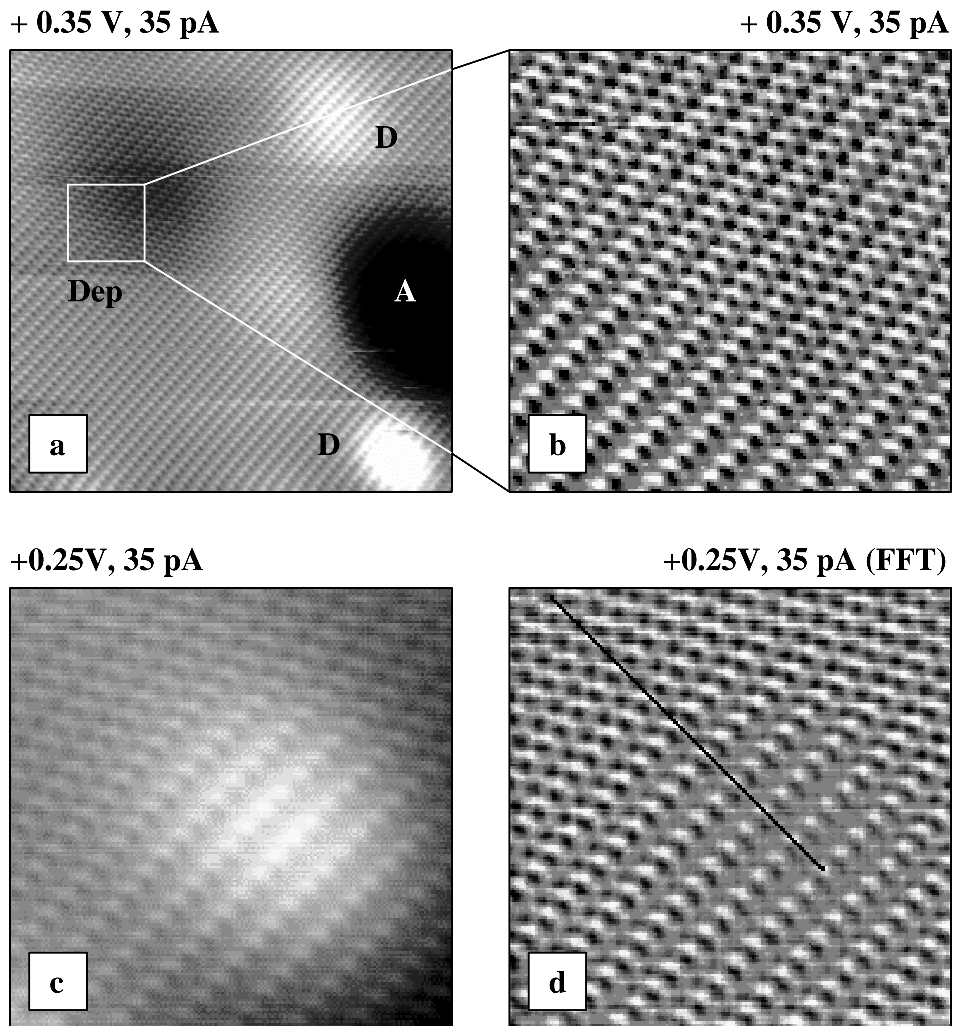

Fig. 5.3 a,b: *Transition from the pre-form to TLRC (V = 0.35 V, I = 35 pA). Such transitions occur in areas where the local tunneling probability changes, which causes an adjustment in the tip-sample distance. The top right corner of figure 3b is part of a shallow, circular depression that lies 78 – 108 pm below the surrounding lattice (Dep). The depression is about 10 nm in diameter, and possibly represents a (negatively charged) subsurface* Si_{As} *acceptor. Similar transitions from the pre-form to TLRC occur near adsorbates (A). Figure a: frame size: 20 x 20 nm; figure b: frame size: 6.7 x 6.7 nm, greyscale: 0 – 34 pm.* **c:** *High-resolution image showing one of the Si dopant shown in figure 2d in detail. Near the dopant, the pre-form is seen while around the dopant the image shows TLRC. The apparent height of the dopant is 149 pm with respect to the surrounding lattice. V = +0.25 V, I = 35 pA, frame size: 5.8 x 5.8 nm, greyscale: 0 – 199 pm.* **d:** *Same as (c), after application of a band-pass fast Fourier transform filter. Greyscale: 0 – 27 pm. A line drawn along [001] from the maxima of the pre-form coincides with the B-sites of the TLRC.*

5.4 Discussion

In earlier literature, STM-images obtained in the filled states mode showing both the Ga and As atoms in the top row of the surface have been reported by Jäger *et al.*[12] and Heinrich *et al.*[11]. In ref. 11 it was shown that this type of imaging involves a significantly smaller tip-sample distance than usual. To our knowledge, however, no STM-images of GaAs-(110) that also show traces of also the bottom zig-zag row have been reported in the literature. An image-form similar to TLRC has also been observed on InAs (110) [13].

From the model and experimental results presented in chapter 4 concerning "normal" atomically resolved images of GaAs-(110), it is clear that for small positive sample bias, the distance between the tunneling tip and an n-type sample becomes very sensitive to changes in the applied bias voltage (figure 4.8). Also, the tip-sample distance can rapidly decrease to a few Å at small bias voltage (figure 4.8 b,e). The voltage at which the rapid decrease in tip-sample distance sets in, depends on the exact value of the tip work function [5]. The tip work function, in its turn, varies from one experiment to the next and usually also changes when a spontaneous change in the tip-DOS occurs. However, given the fact that TLRC occurs for low bias voltage, the hypothesis that the mechanism behind it involves a short tip-sample distance is logical.

Recent theoretical calculations predict that the-(110)-surface of GaAs undergoes some very significant changes as it is being approached closely by a tip. The calculation has been carried out in order to model the atomic resolution recently obtained in non-contact AFM on GaAs-(110). Using a four-atom Si cluster to represent an AFM-tip, it has been predicted by Ke *et al.* that under influence of the tip-sample interaction, the nearest Ga atom in the top row can relax outward: When the tip approaches the sample surface to within 3 Å, a chemical bond may form between the Si apex atom and one of the Ga atoms in the top row of the surface. The vertical displacement of the Ga atom in this configuration can be up to 1 Å. This decreases, or even partly reverses the buckling angle of the surface, since the displacement of the nearest As atom in the top row, for a tip-sample distance of 3 Å, is less than the displacement of the Ga atom [18]. If the tip is withdrawn again, the tip-sample distance has to be increased to about 5 Å before the bond between the apex atom and the Ga atom is ruptured. When, after the formation of the bond, the tip is approached further still, the Ga atom and Si apex atom relax slightly further. For a tip-sample distance of less than about 2 Å, the interaction becomes repulsive [18]. The method used by Ke *et al.* has been based on earlier work by Perez *et al.*[21] in which the tip-sample interaction between a similar Si tip cluster and a Si-(111) surface has been modeled in great detail. A calculation similar to the one performed by Ke *et al.* has also been carried out for InP-(110) by Tobik *et al.*[22], showing that the relaxation of the InP-(110) surface under the influence of tip-sample interaction differs from the relaxation predicted for GaAs-(110).

The decrease of the buckling angle by itself has a profound effect on the electronic structure of the GaAs-(110) surface: As has been shown by Chelikowski, the C3 state moves up in energy whereas the C4 state comes down [2,3]. For the unrelaxed (truncated bulk) surface, the C4 state lies energetically near the middle of the bulk bandgap whereas the C3 state lies in the bulk conduction band. The significance of this is that it thus becomes possible to image only the C4-state at small positive bias voltage

(and thus small tip-sample distance) due to the tip-induced structural modification of the sample surface. The C4 state is localized on both the top zig-zag row Ga and As atoms [4,6], and also has a localization on the atoms of the bottom zig-zag row of the surface [2]. Refs. 4 and 6 predict that if the C4-state is imaged at small tip-sample distance, the top zig-zag row would appear in the images, showing both the top row Ga and As atoms. If the localization of the C4 state on the bottom zig-zag row were to show as well in the image, the result would be an image similar to TLRC. Due to the upward tip-induced band bending that we expect for n-GaAs being imaged at small positive sample bias, a significant semiconductor barrier (depletion layer) will be present between the tip and the bulk conduction band states involved in the tunneling process [5]. We propose that the electrons tunnel resonantly through the C4 surface state, so that the C4 state spatially modulates the tunneling current so as to produce TLRC. For this to occur, the C4-state would have to lie energetically well inside the bandgap, which is exactly the expected energetic location of the C4 state if the buckling of the surface is eliminated due to the tip-sample interaction (see figure 5.4). It must, however, be kept in mind that the above considerations are based on calculations for the GaAs-(110) surface with an altered surface reconstruction, while it is in all other respects assumed to be unperturbed [2,3,4,6]. If the tip-sample interaction has other significant effects besides a decrease of the buckling angle, the interpretation will become more complicated. A more rigorous treatment than given here will then be needed.

Notice that if the tunneling current is spatially modulated due to resonant tunneling through a surface state, it becomes possible to image the spatial variations of that state *inside* the surface layer, which provides a straightforward explanation for the fact that also the bottom zig-zag row is seen. Since at some distance from the surface (3 Å or more), the surface-DOS shows no characteristic of the structure of the bottom row of the surface [4,6], there is no way in which the imaging of the bottom row could be explained within the framework of regular tunneling.

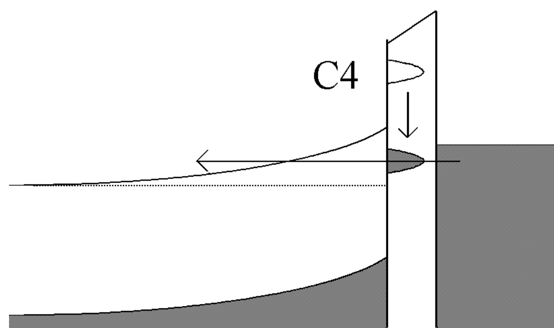

Fig. 5.4: *Our interpretation of TLRC: Due to the tip-sample interaction, the buckling angle of the surface is decreased. This causes the C4 state to come down in energy. Electrons can now tunnel resonantly through the displaced C4 state, giving rise to TLRC.*

If an atomic bond is formed between the tip and sample, and this bond is dragged along the surface as the tip is scanned, the Ga atoms over which the tip apex passes will relax outward, modifying the electronic structure of the surface accordingly. The sudden formation of an atomic bond would provide a very natural explanation for the sudden onset of the pre-form of TLRC which is seen in figure 5.2c. It would also explain why the image mode remained stable afterward, as the formation and rupture of this bond involves hysteresis. Although the hysteresis is reported to be strongest at low temperature, it is still expected to be there at room temperature as well [18]. Finally, since the Ga atom and Si apex atom in the model relax slightly more if the tip and sample approach each other even more closely after the formation of the bond [18], it would also explain the many smooth transitions between TLRC and the pre-form that we have observed. It is clear that once the atomic bond between the tip and sample has formed, the interpretation of the resulting STM-image must be done in terms of tip-induced localized states (TILS) [15,17], in a fashion similar to the way that the results in ref. 11 are interpreted. All in all, it seems plausible that the formation of a chemical bond between the apex atom of the tip and the Ga atoms of the sample is the underlying mechanism of TLRC and its pre-form.

We have considered alternative possible explanations for TLRC. The most important one is the hypothesis that TLRC is caused by an unusual tip-state. The central idea is that somehow, the tip-DOS is such that the regular surface-DOS of the GaAs-(110) surface is imaged twice. If the two atomically resolved images are shifted with respect to each other, the resulting image might show two maxima and two minima per unit cell. An unfortunate arrangement of these two images could, in theory, result in an image similar to the one shown in fig. 2a. Although it is unclear to us how this mechanism might explain the observed dependence of TLRC on the tip-sample distance and bias voltage, the thought in itself is hardly surprising: The sudden transition shown in figure 5.2c looks very similar to the image obtained when a spontaneous tip-change occurs during scanning. It is also known that, for instance, monoatomic steps are sometimes imaged twice, indicating that the tip has a double apex. Other examples of such “double imaging” have been reported by Mizes *et al.* [23] and Park *et al.* [24].

In our experiments it sometimes occurs that the tunneling tip has a double apex. The presence of such a double apex is easily recognized because in that case mono-atomic steps, adsorbates, dopants and other features of a larger scale than the atomic lattice appear in pairs in the image. Moreover, the features in one such pair have a fixed distance and relative orientation. If the tip used in the measurement would have had a double apex, this would have manifested itself in the larger-scale images (figures 2d and 3a) that we aquired during the same measurement. These images show no sign of a tip with a double apex. Besides, on those occasions that the tip does have a double apex, it is observed that the atomic lattice of the surface can be imaged quite normally, because one of the two apeces is (almost) always slightly closer to the sample surface than the other. We are thus convinced that the images presented in this paper have been acquired with a tip that only had a single apex. Moreover, the atomic resolution that we obtained both before and after the sudden onset of the pre-form (figure 5.2c), suggests that the apex of the tip that was used ended in a single atom rather than a micro-facet.

For a tip that ends in a single atom, some electronic states exist that have two spatially separated lobes extending equally far towards the sample surface (see *e.g.* the d_{xz}-state) [10]. Let us now consider the likelihood of occurrence and possible effects on the STM-image of such a "double lobed" tip state with regards to TLRC. Based on the results of cluster (W_4 and W_5) calculations [10,25,26,27] it is generally agreed that for a tungsten tip ending in a single apex atom, a $d_z{}^2$-like surface state dominates the tip-DOS near the Fermi level. In the same energetic region a d_{xy}-state is also predicted, but this state only carries a fraction of the total tunneling current (10^{-4}) when such a cluster is brought close to a model surface. Even when a tip-sample distance of 3 Å is assumed in these calculations, the $d_z{}^2$-dominates the d_{xy}-state. Furthermore, Sachs and Noguera [30] show for a clean tungsten tip that s- and d- type states dominate the DOS of a tungsten tip apex near the Fermi level, although a p-type state may dominate the tip-DOS if a foreign atom is adsorbed on the apex.

A very important point has been made by Kobayashi *et al.* [31] by simulating the tunneling process between a graphite surface and the bonding and antibonding molecular orbitals of the H_2-molecule: If the active tunneling orbital has two spatially separated lobes which both carry a portion of the tunneling current, the resulting STM-image need not be a superposition of the two independent images. The two tunneling currents interfere with each other. In the case of tunneling between the bonding orbital and the graphite surface, the calculated STM-image was similar to the ideal STM-image of graphite. For tunneling between the antibonding orbital and the graphite surface, the image was severely distorted, the distortion depending on the orientation of the orbital with respect to the graphite surface. In neither of the two cases, a period-doubling of the graphite lattice was found. A distorted image similar to the one found for the antibonding orbital is predicted for a d_{zx}-like orbital [31] and for the tunneling active orbital of a ⟨110⟩-oriented W-tip with a missing apex atom [26,32].

These results are in apparent conflict with the experimental results reported by Park *et al.*[24], who reports the occurrence of two superimposed, independent images of the adatom pattern of the (7x7)-reconstruction of Si-(111). Some of the shifts between the images are as small as 4 Å. It must however be noted that the tips used in their experiment were used immediately after ac etching, without further *in vacuo* treatment. This means that their tips must certainly have had a thin oxide layer on them. We do not know how this affects the interference effect described by Kobayashi, but it is clear that an oxide layer with saturated bonds does not represent the situation considered in ref. 31. Furthermore, the adatoms in the 7x7 reconstruction of Si (111) studied by Park *et al.* lie relatively far apart (7.68 Å). It is possible that the tip has imaged each of the adatoms separately, rather than having an interaction with the electronic structure of the surface *lattice* as is the case for tunneling on an atomically flat surface. This may also explain the difference between their conclusions and the predictions made in ref 31.

We expect that our own tips, given the elaborate *in vacuo* treatment [20] that we apply and the fact that we routinely obtain atomic resolution on GaAs {110} [5,20], are sharp and free of oxides. From the larger-scale images taken during the same measurement it seems very unlikely that the tip used in our measurement had a double apex. For a clean tungsten tip ending in a single apex atom, the presence of a tip-state with two lobes extending to the surface does not lead to a superposition of two independent images [25,26,27,31]. We therefore conclude that the interpretation of TLRC

in terms of a chemical bond forming between the tip apex and the Ga atoms in the surface is the most plausible one.

At this point, the physical meaning of atomically resolved STM-images of the (110)-surface of GaAs and other zincblende III-V semiconductors seems well understood as long as the tip-sample interaction remains small enough for the Tersoff-Hamann theory to apply [4,6]. However, once the tip-sample interaction does become significant, the images can change in drastic and poorly understood ways. Although the recent theoretical work on the interaction between a semiconductor surface and a nearby tip [18,21,22] was meant to explain the recently obtained atomic resolution on zincblende-(110) surfaces by dynamic Scanning Force Microscopy [29], it certainly has equally much relevance to STM-images as well. The occasional occurrence of TLRC and related image-forms [11,12,13] on such zincblende-(110) surfaces shows that the tip-sample interaction can profoundly influence the appearance of the atomically resolved lattice in STM. Although this influence is often unwanted, it can in principle also be used to obtain new image-forms. Understanding these new image-forms and making use of the tip-sample interaction to obtain them, holds interesting challenges for theorists and experimentalists alike.

5.5: Summary and conclusion

We report an unusual image-form of the GaAs (110) surface that occasionally occurs when imaging the empty states of that surface. It closely resembles the true atomic lattice. We propose that the image-form arises when a chemical bond forms between the tip and sample in the way that is predicted theoretically by Ke *et al.*[18]. This involves a significant reduction of the buckling angle of the surface. For the *free* GaAs (110) surface, such a reduction of the buckling angle is known to shift the C3 and C4 surface states, causing the C4-state to lie well inside the bandgap of the semiconductor [2]. If electrons then tunnel resonantly through the shifted C4 state, the resulting image will show the localization of the C4 state within the surface layer, resulting in TLRC.
We have considered the possibility that the image form that we have observed might have been caused by an unusual electronic state present at the apex of the tunneling tip. From simulations of tunneling between a multi-lobed tip-state and a sample surface that are reported in the literature, it seems unlikely that such a tip state will lead to an image-form with more than one atomic maximum per surface unit cell [31]. The results show a clear perspective to a new and very interesting way to image the (110)-surface of GaAs.

RERENCES:

1: R.M. Feenstra, J.A. Stroscio, J.A. Tersoff, A.P. Fein: *Atom-selective imaging of the GaAs (110) surface*. Phys. Rev. Lett, Vol. 58, No. 12, pp. 1192 – 1195 (1985).

2: J.R. Chelikowski, M.L. Cohen: *Self-consistent pseudopotential calculation for the relaxed (110) surface of GaAs.* Phys. Rev. B, Vol. 20, pp. 4150-4159 (1979).

3: J.R. Chelikowski, S.G. Louie, M.L. Cohen: *Relaxation effects on the (110) surface of GaAs*. Phys. Rev. B, Vol. 14, No. 10, pp. 4724 - 4726 (1976).

4: Ph. Ebert, B. Engels, P. Richard, K. Schroeder, S. Blügel, C. Domke, M. Heinrich, K. Urban: *Contribution of surface resonances to Scanning Tunneling Microscopy images: (110) surfaces of III-V semiconductors.* Phys. Rev. Lett, Vol. 77, No. 14, pp. 2997-3000 (1996).

5: G.J. de Raad, D.M. Bruls, P.M. Koenraad, J.H. Wolter: *Interplay between tip-induced band bending and voltage-depending surface-corrugation on GaAs-(110) surfaces*. (To be published). The series of frames preceeding TLRC is an early measurement similar to the results shown in this reference. See also chapter 4 of this thesis.

6: B. Engels, P. Richard, K. Schroeder, S. Blügel, Ph. Ebert, K. Urban: *Comparison between ab initio theory and Scanning Tunneling Microscopy for (110)-surfaces of III-V semiconductors.* Phys. Rev. B, Vol. 58, No. 12, pp. 7799 – 7814 (1998).

8: C.S. Jiang,T. Nakayama, M. Aono: *Tip-induced occupation of an unoccupied surface state in Scanning Tunneling Microscopy imaging of a GaAs (110) surface with Ag clusters*. Jap. Journal of Appl. Phys, Vol. 36, pp. L1336-L1339 (1997).

9: J. Tersoff and D.R. Hamann, Phys. Rev. Lett. Vol. 50, No. 25, page 1998 – 2001. Also: Phys. Rev. B, Vol. 31, No. 2, page 805 – 813.

10: C.J. Chen: *Introduction to Scanning Tunneling Microscopy.* Oxford University Press, Oxford, 1993. Chapter 3 explains that for an s-like tip state, the tunneling matrix element is proportional to the surface-DOS of the sample evaluated at the centre of the tip apex atom. The usual interpretation of STM-results is well summarized by equations 2.36 and 3.26

11: A.J. Heinrich, M. Wenderoth, M.A. Rosentreter, M.A. Schneider, R.G. Ulrich: *Scanning Tunneling Microscopy of the atomic structure of the GaAs (110) surface at reduced tip sample separation.* Appl. Phys. Lett, Vol. 70, No. 4, pp 449 – 451 (1996). See also*: Ordering in Ternary compound Semiconductors on the atomic scale*. PhD-thesis by A.J. Heinrich, Cuvillier Verlag, Göttingen, Germany (1998). The thesis shows that for small tip-sample distance, the bandgap evident in I(V)-spectra taken at normal tip-sample distances disappears.

12: N.D. Jäger, X. Liu, J.F. Zheng, N Newman, D.F. Olgletree, E.R. Weber, M. Salmeron*: Scanning Tunneling Microscoy of the GaAs (110) surface at low bias.* 23rd International Conference on the Physics of Semiconductors (World Scientific, Berlin), pp. 847 – 850.

13: A. Depuydt *et al,* University of Leuven, Belgium. Private communication.

14: Ciraci in: Scanning Tunneling Microscopy III, ed: Wiesendanger and Günteroth, Springer Verlag Berlin,p. 182, p. 197 (1996).

15: S. Ciraci, A. Baratoff, I.P. Batra*: Site-dependent electronic effects, forces and deformations in STM on flat metal surfaces.* Phys. Rev. B, Vol. 42, No. 12, pp. 7618 – 7621 (1990).

16: S. Ciraci, A. Baratoff, I.P. Batra*: Tip-sample interaction effects in Scanning Tunneling Microscopy and Atomic Force Microscopy.* Phys. Rev. B, Vol. 41, No. 5, pp. 2763 – 2775 (1990).

17: E. Tekman, S. Ciraci: *Atomic theory of Scanning Tunneling Microscopy.* Phys. Rev. B, Vol. 40, No. 15, pp 10286 – 10293 (1989).

18: S.H. Ke, T. Uda, R. Perez, I. Stich, K. Terakura: *First-principles investigation on GaAs (110) surface: Implications for atomic force and scanning tunneling microscopies*. Phys. Rev. B, Vol. 60, Iss. 16, pp. 11631 - 11639 (1999). In the work presented in refs 9, 14 and 15, the tip is represented by a 4-atom Si tetrahedron. On the back side of the tetrahedron, the dangling bonds have been saturated with hydrogen atoms.

19: We use commercially available n-doped GaAs wafers with a nominal doping concentration of $1 * 10^{18}$ cm^{-3}. The actual doping concentration may lie between 1 and $2 * 10^{18}$ cm^{-3}.

20: G.J. de Raad, P.M. Koenraad, J.H. Wolter: *The use of the Schiller-decapitation process for the manufacture of high-quality tungsten STM-tips.* Journ. of Vac. Sci. and Tech-B, Vol. 17, Iss. 5, pp. 1946 – 1953 (1999).

21: R. Perez, I. Stich, M.C. Payne, K. Terakura*: Surface-tip interactions in non-contact atomic-force microscopy on reactive surfaces: Si (111).* Phys. Rev. B, Vol. 58, No. 16, pp. 10835 – 10849 (1998). See also chapter 3 of this thesis.

22: J. Tobik, I. Stich, R. Perez, K. Terakura*: Simulation of tip-surface interactions in atomic force microscopy of InP (110) surface with a Si tip.* Phys.Rev. B, Vol. 60, pp. 11659 (1999).

23: H.A. Mizes, S.I. Park, W.A. Harrison: *Multiple-tip interpretation of anomalous Scanning Tunneling Microscopy images of layered materials.* Phys. Rev. B, Vol. 36, No. 8, pp. 4491 – 4494 (1987).

24: S.I. Park, J. Nogami, C.F. Quate*: Effect of tip morphology on images obtained by Scanning Tunneling Microscopy.* Phys. Rev. B, Vol. 36, No. 5, pp. 2863 – 2866 (1987).

25: S. Ohnishi, M. Tsukada*: Molecular orbital theory for Scanning Tunneling Microscopy.* Solid state comm. Vol. 71, No. 5, pp. 391 – 394 (1989).

26: M. Tsukada, K. Kobayashi, S. Ohnishi*: First principle theory of Scanning Tunneling Microscopy simulation.* Journ. of Vac. Sci. and Tech. A, Vol. 8, No. 1, pp. 160 – 165 (1990).

27: M. Tsukada, N. Shima, S. Ohnishi, Y. Chiba: *Effect of the tip/sample surface electronic states and the electron-phonon coupling on the current in Scanning Tunneling Microscopy.* Journal de Physique, Colloque 6, Suppl. 11, Tome 48, nov. 1987.

28: J.A. Stroscio, R.M. Feenstra, A.P. Fein: *Local state density and long-range screening of adsorbed oxygen atoms on the GaAs (110) surface.* Phys. Rev. Lett, Vol. 58, No. 16, pp. 1668 – 1671 (1987).

29: A. Schwarz, W. Allers, U.D. Schwarz, R. Wiesendanger: *Simultaneous imaging of the In and As sublattice on InAs (110) 1x1 with dynamic scanning force microscopy.* Appl. Surf. Sci, Vol. 140, pp. 293 – 297 (1999).

30: W. Sacks, C. Noguera*: Generalized expression for the tunneling current in Scanning Tunneling Microscopy.* Phys. Rev. B, Vol. 43, No. 14, pp. 11612 – 11622 (1991).

31: K. Kobayashi, M. Tsukada*: Effect of microscopic tip electronic state on Scanning Tunneling Microscopy image of graphite.* Journ. of Phys. Soc. of Japan, Vol. 58, No. 7, pp. 2238 – 2241 (1989).

32: M. Tsukada, K. Kobayashi, N. Isshiki: *First-principles theory of Scanning Tunneling Microscopy.* Surface Science Reports 13 (1991), pp. 265 – 304.

CHAPTER 6:

VOLTAGE-DEPENDENT CHANGES IN THE FILLED- AND EMPTY-STATES IMAGES OF $Al_xGa_{(1-x)}As$ (110) AND OF GaAs/$Al_xGa_{(1-x)}As$ THIN LAYERS

6.1 Introduction

Cross-sectional Scanning Tunneling Microscopy (STM) in Ultra-High Vacuum (UHV) is by now recognized as a valuable tool for the study of the atomic-scale structure of ternary III-V semiconductor compounds, as well as for the study of interfaces in heterostructures made up of layers of different III-V materials [1,2,3,4,5,6]. However, in many cases the information about such materials is extracted from topographic images that have been aquired at only a few values of the applied bias voltage. In this chapter, we will show voltage-dependent images of $Al_{0.2}Ga_{0.8}As$ and of a 5 nm / 5 nm GaAs/$Al_{0.33}Ga_{0.67}As$ superlattice, both doped n-type (Si). The images that we present have been taken in both the filled and empty states imaging mode.

GaAs and AlAs have nearly equal lattice constants [7], and it is thus possible to epitaxially grow lattice-matched interfaces between layers of GaAs and $Al_xGa_{(1-x)}As$ for almost all Al concentrations (x). Also alloy-fluctuations within layers of $Al_xGa_{(1-x)}As$ will involve only minimal lattice strain because of this reason. Consequently, there should be no structural relaxation of the surface other than the process of “buckling” which is the common reconstruction for the (110)-surfaces of III-V zincblende semiconductors. The cleaved, cross-sectional surface of a GaAs/ $Al_xGa_{(1-x)}As$ heterostructure should therefore contain no physical height-differences. The same is expected for the cleaved surface of $Al_xGa_{(1-x)}As$, in which alloy-fluctuations can give rise to Ga-rich and Al-rich areas. The consequence is that the contrast between GaAs and $Al_xGa_{(1-x)}As$ observed in cross-sectional STM is almost entirely due to electronic effects, and may therefore be expected to be highly dependent on the applied bias voltage. This is in contrast to STM-images of *e.g.* InAs self-assembled quantum dots embedded in GaAs. In that case, the quantum dot can to bulge out of the surface by about 500 pm after cleavage due to the fact that it is compressively strained [26]. The contrast in the STM-image of the InAs quantum dot against the GaAs matrix must therefore contain an important geometrical component, beside the contrast caused by electronic effects [26].

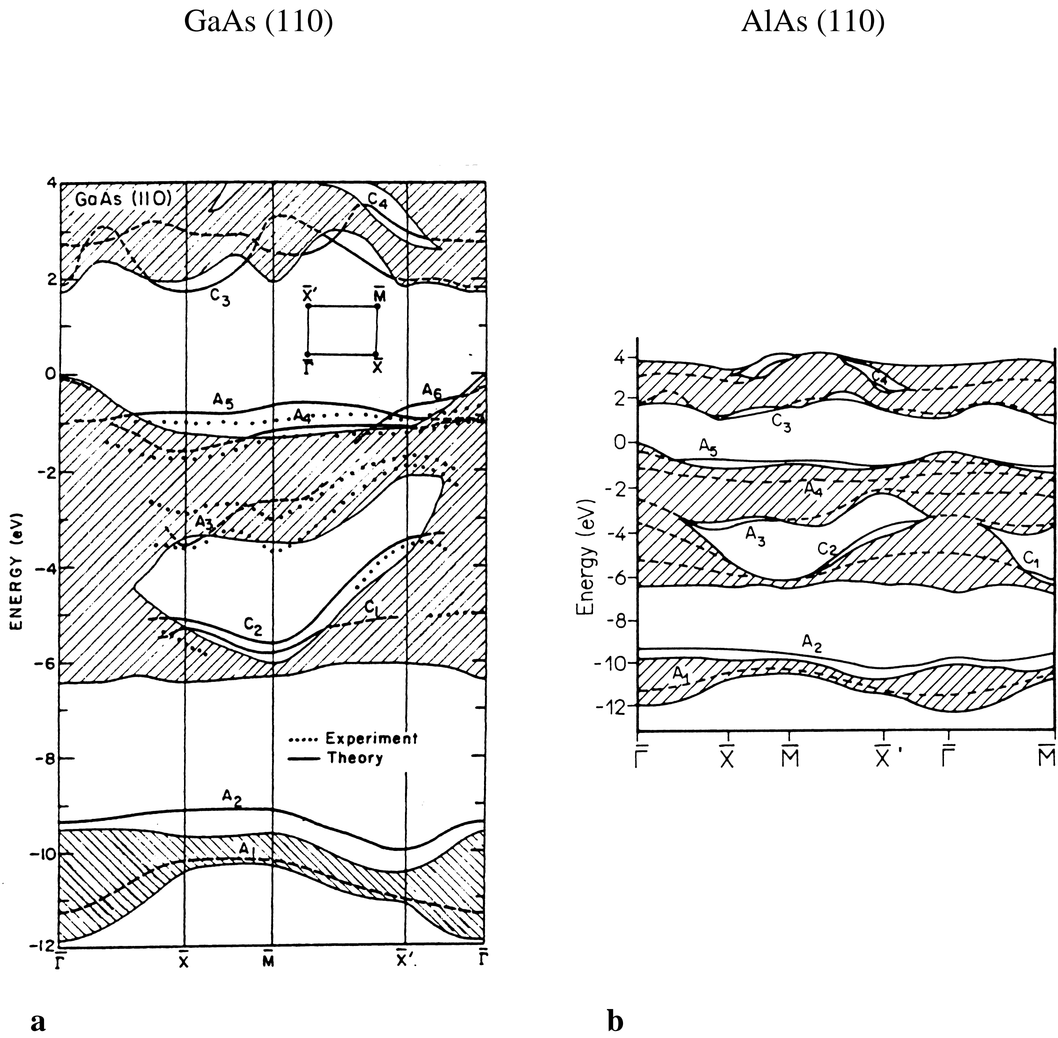

Fig. 6.1a: *Calculated electronic band structrure of the GaAs-(110) surface. The projected bulk band structure is shown as the hatched regions. Taken from ref. 12.* **b:** *Calculated electronic band structure of the AlAs-(110) surface. The projected bulk band structure is represented by the hatched regions. Taken from ref. 24.*

To our knowledge, no theoretical STM-images have been calculated for the (110)-surface of $Al_xGa_{(1-x)}As$ or AlAs, although the band structure and relaxation of the AlAs (110) surface has been described by Grossi *et al.* [24] (figure 1). The electronic structure of AlAs is very similar to that of GaP [15,16]. In both semiconductors the top of the valence-band lies at the Γ-point of the Brillouin zone (BZ), whereas the bottom of the conduction-band lies at or near the X-point. In a direct semiconductor like GaAs or InP, both the valence band maximum (VBM) and the conduction band minimum (CBM) occur at the Γ-point of the bulk BZ [15]. In ref. 8, voltage-dependent changes in atomic morphology are presented for GaP, InP and GaAs (110). In qualitative terms the changes are the same for all three compounds, and can be compared meaningfully to theoretical STM-images that the authors calculate from the surface-density of states (surface-DOS) of InP (110).

The (110)-surface of GaP has been described theoretically by Manghi *et al.* [19]. Comparison of that article with the work of Chelikowski *et al.* [20] and with that of Grossi *et al.* [24] shows that the surface-DOS of the relaxed (110)-surfaces of GaAs, GaP and AlAs are similar to each other. Near the fundamental bandgap, the same suface states exist (A4, A5, C3, C4). They also have the same relative energetic positions, although for GaP (110) the energetic location of the surface states is only given at the four symmetry-points of the surface-BZ. We can thus assume that for AlAs (110) and $Al_xGa_{(1-x)}As$ (110), the same voltage-dependent changes in the atomic morphology will occur as for GaAs (110), InP (110) and GaP (110). A significant difference between the surface electronic structure of GaP (110) and that of GaAs (110) is the fact that the conduction-band related surface states (C3 and C4) of GaP lie energetically inside the upper part of the bandgap of the semiconductor [19,20]. This appears not to influence the voltage-dependent changes in atomic corrugation reported in ref. 8. For AlAs (110), the dispersion-curve of the C3-state has its minimum near the X-point in the surface Brioullin zone [24]. For most k-points in the surface Brioullin zone, the dispersion-curve of the C3 –state lies near the bulk-CBM [24].

Since in our experiments the nominal Al fractions were 0.20 and 0.33, the $Al_xGa_{(1-x)}As$ layers that we studied should still be "GaAs-like", having a direct bandgap with the smallest energetic distance between the conduction-band and valence-band at the Γ-point of the BZ [15]. However, the material may be "AlAs-like", *i.e.* have an indirect bandgap, in areas where the local Al fraction exceeds 0.33 [15]. When interpreting the voltage-dependent changes in the atomic corrugation that we observe on n-AlGaAs (110), we make the assumption that the surface-DOS is essentially like that of GaAs (110). The complete similarity of the corrugation-changes observed for n-AlGaAs with those that we have seen on n-GaAs is consistent with that assumption [11]. From ref. 24, it seems likely that for $Al_xGa_{(1-x)}As$ (110), the influence of (the lower part of) the C3-state on the corrugation in the image is stronger than it is for GaAs (110).

The voltage-dependent images presented in this chapter show that the atomic morphology of $Al_xGa_{(1-x)}As$ and thin $GaAs/Al_xGa_{(1-x)}As$ layers indeed very strongly depends on the value of the applied bias voltage, and involves several other effects besides the changes in the apparent direction of the atomic rows which are also observed on binary III-V semiconductors [8,9,10,11]. When an n-type semiconductor is imaged at small, negative sample voltage, an accumulation layer of electrons occupies the electron-states located just above the bottom of the conduction-band. At small,

negative voltage we observe for AlGaAs (110) a morphology that we interprete in terms of fluctuations in the density of electrons in this accumulation layer. Moreover, we observe for the superlattice an inversion of contrast between GaAs and AlGaAs for low voltage of either polarity. In the empty-states mode at intermediate voltage, an apparent widening of the GaAs layers in the GaAs/AlGaAs superlattice indicates that we image the confined electron-level of the quantum wells that are formed by the GaAs layers sandwiched between the AlGaAs layers.

We also observe that the positions of local maxima and minima associated with alloy-fluctuations do not coincide when the same area of AlGaAs-surface is imaged simultaneously in filled and empty states mode. This means that the surface-DOS of the valence-band related surface states (A4 and A5) [10,12,13] significantly differs from the surface-DOS of the conduction-band related surface states (C3 and C4), and that the relation between the atomic structure and the resulting surface-DOS is far more complicated than is often assumed. Until this relation is fully known, unambiguous statements about the atomic structure of $Al_xGa_{(1-x)}As$ cannot be made from atomically resolved STM-images.

6.2 Experiment

The STM-work was performed in UHV (OMICRON STM-1 setup operated at 4 * 10^{-11} torr) on *in situ* cleaved samples. These samples consisted of a GaAs substrate (nominal doping concentration 10^{18} cm^{-3} Si), on which a GaAs/AlGaAs superlattice and subsequently a bulk AlGaAs layer were grown by Molecular Beam Epitaxy (MBE). The superlattice was n-doped (Si), GaAs: 10^{18} cm^{-3}, $Al_{0.33}Ga_{0.67}As$: 6.67*10^{17} cm^{-3}. The GaAs and AlGaAs layers in the superlattice were each 50 Å, the total thickness of the superlattice was 1 μm. On top of the superlattice, a 4 μm $Al_{0.2}Ga_{0.8}As$ layer (doping concentration: 5 * 10^{17} cm^{-3} Si) was deposited. The bias voltage is applied to the sample. All images shown in this chapter are height-images [z(x,y)] that were obtained while operating the STM in constant current mode. We use a one-dimensional model to calculate the amount of tip-induced band bending (TIBB) that we expect in our experiments on AlGaAs (see chapter 4). We have used another model to calculate the band offsets and position of the Fermi level in the superlattice (figure 6.11). While discussing the voltage-dependent changes in our images, we use an absolute scale for the applied bias voltage (-1 V < -2 V).

6.3 Results

We now present voltage-dependent images of n-type $Al_{0.2}Ga_{0.8}As$ (110) (figures 6.2: filled states; figure 6.3: empty states). In figure 6.4, we present cut-outs showing details of the atomically resolved lattice. It can be seen that the atomic morphology of the AlGaAs-surface depends quite strongly on the applied bias voltage. The voltage-dependent changes in the apparent direction of the atomic rows are similar to what is reported in chapter 4 for GaAs (110). However, due to the heterogenic nature of $Al_xGa_{(1-x)}As$, other voltage-dependent effects are seen as well. We will also present filled and empty-states images of the same area of $Al_{0.2}Ga_{0.8}As$ (figure 6.6). In these images, it is seen very clearly that the shapes and locations of the alloy-related minima change as a function of the polarity of the applied bias voltage. Finally, we present voltage-dependent images of an n-type GaAs/$Al_{0.33}Ga_{0.67}As$ superlattice (5 nm / 5 nm). These images also consist of both filled and empty states images (figures 6.7 and 6.8).

The filled-states images (figure 6.2) were taken on roughly the same patch of sample surface, although we did experience some drift as the images were aquired. From the last four images where adsorbates can be used as reference-points, it is evident that the bright areas do not shift in position on the surface as the voltage is changed. The height-profiles shown in fig. 5 show that the height-differences associated with the bright spots are larger than the height-differences associated with the Al-related depressions observed at higher voltage.

The empty-states images (figure 6.3) have been aquired at a different location on the same AlGaAs-layer. The bright, sharp-bordered feature is interpreted as an adsorbate in analogy with figure 6.9 d,e where a similar feature appears in the image during scanning. We interprete the fuzzy, bright feature above it as a Si dopant. The entire sequence of empty-states images has been obtained in "dual mode": On the forward leg of the tip-motion the voltage was varied, on the backward one it was kept constant at V = -2.193 V. We can thus directly compare the filled and empty states images of $Al_{0.2}Ga_{0.8}As$. We have analyzed one such pair of a filled-states and an empty-states image of the same area as a representative example (-2.193 V, 75 pA / +1.222 V, 54 pA).

In order to correlate the dark and bright areas in the two frames, we have projected varying sets of contour-lines of the filled-states image into the empty-states image and vice versa (figure 6.6). In the empty-states image we have drawn the contour-line z = 9 pm, which encloses all minima, and z = 23 pm, which encloses all maxima (see inset in figure 6.6a). A second contour line at z = 75 pm encloses the adsorbate and is used for alignment. For the filled states image, similar contour lines were drawn for z = 8 pm and z = 18 pm. At low positive voltage, small ridges oriented along the [-110]-direction appear in the image. Figures 6.6 g and 6.6 h are used to compare the position of these ridges with the position of the alloy-related maxima and alloy-related minima that appear at large, positive voltage.

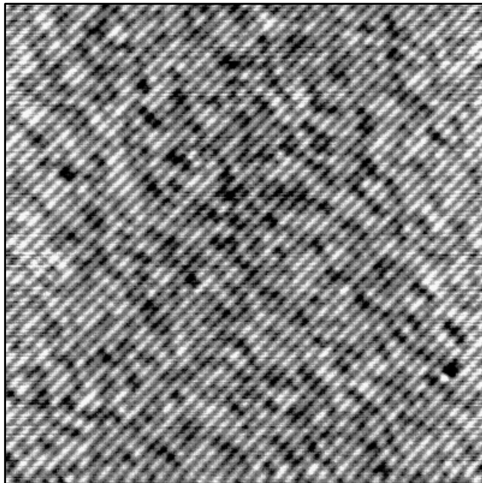

a: -2.493 V, 95 pA (4)

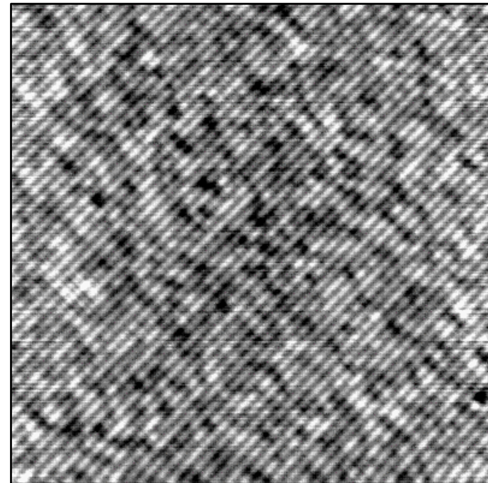

b: -2.275 V, 95 pA (3)

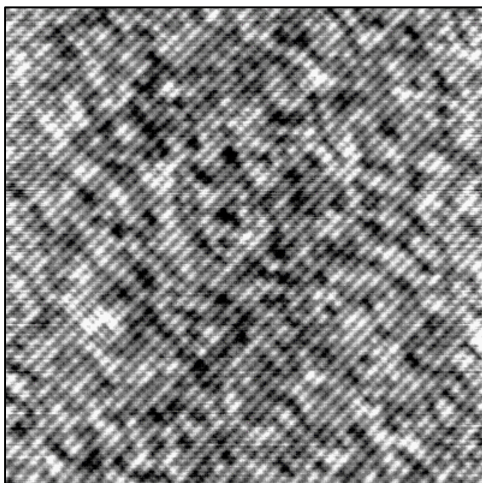

c: -2.115 V, 95 pA (2)

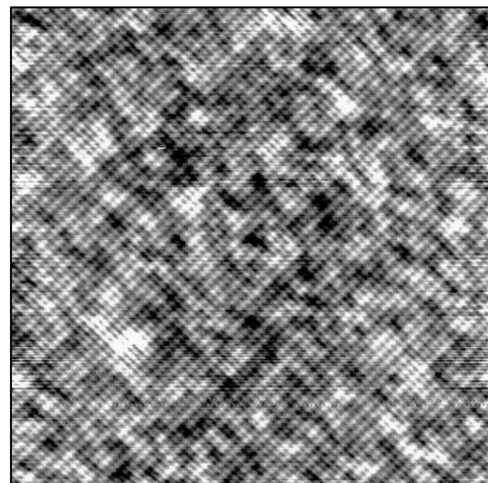

d: -1.966 V, 95 pA (1)

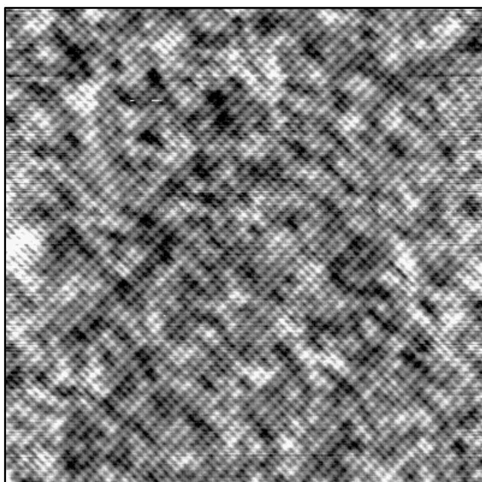

e: -1.930 V, 95 pA (5)

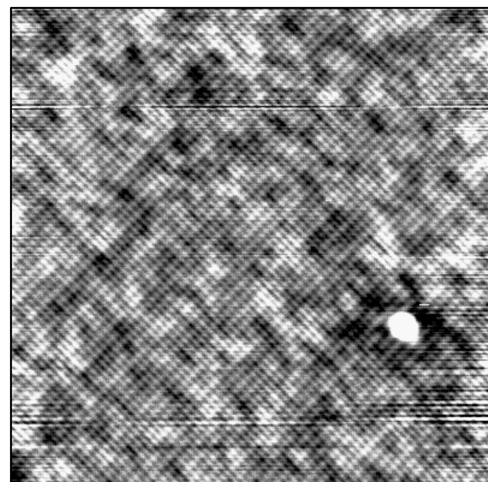

f: -1.895 V, 95 pA (6)

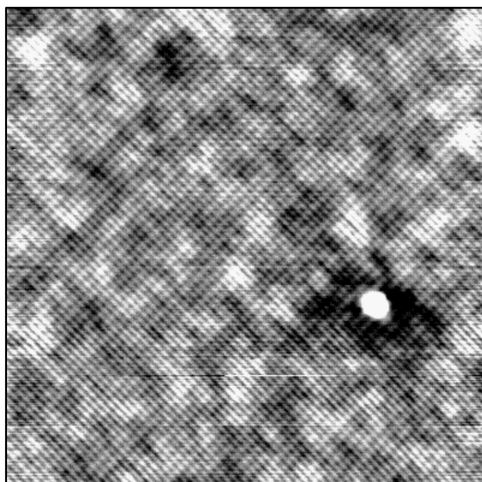

g: -1.827 V, 95 pA (7)

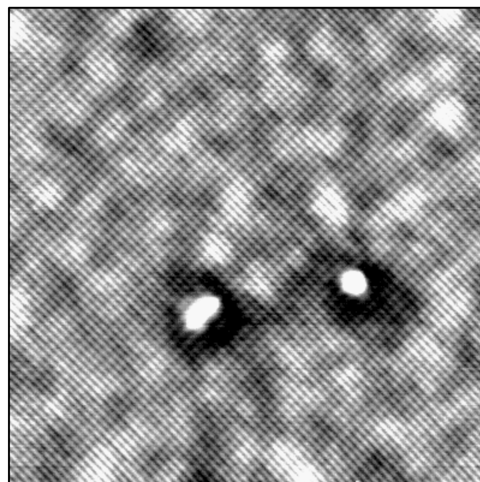

h: -1.730 V, 95 pA (8)

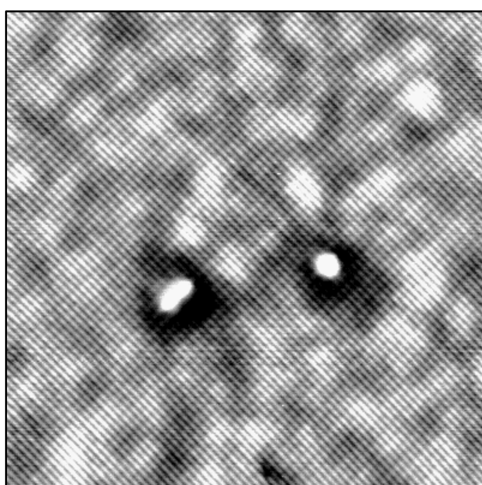

i: -1.667 V, 95 pA (9)

Fig. 6.2: *(both pages) Filled states STM-images of n-type $Al_{0.2}Ga_{0.8}As$. Frame size: 25 x 25 nm. The number in parenthesis indicates the order in time in which the images were aquired. In the last four images, adsorbates appear.*

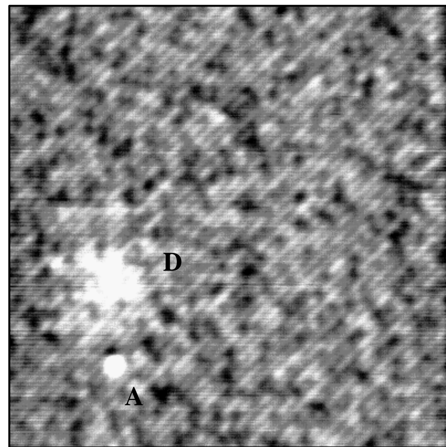

a: +1.467 V, 54 pA (1)

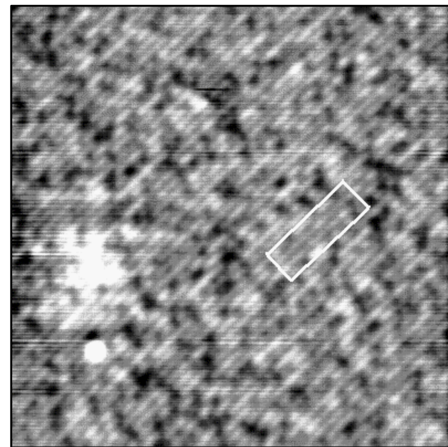

b: +1.268 V, 54 pA (2)

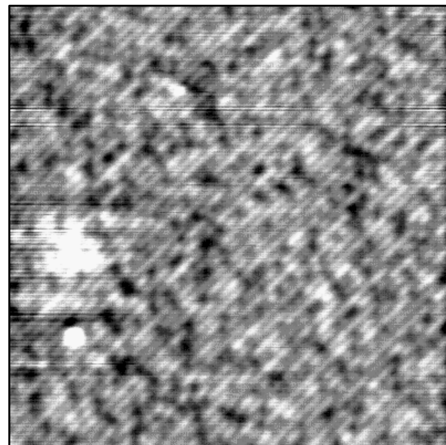

c: +1.222 V, 54 pA (3)

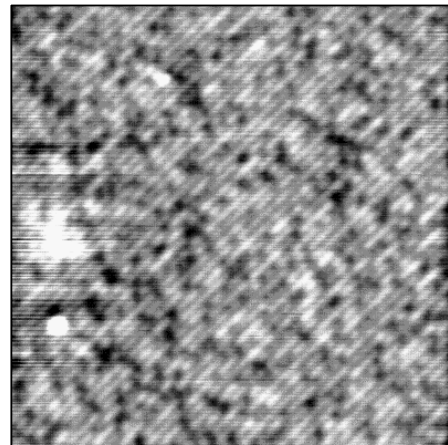

d: +1.178 V, 54 pA (4)

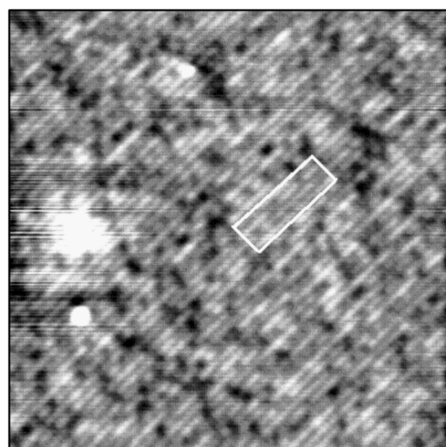

e: +0.981 V, 54 pA (5)

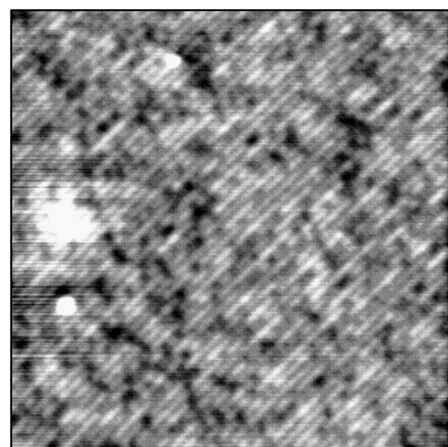

f: +0.946 V, 54 pA (6)

Fig. 6.3 : *Empty states STM-images of n-type $Al_{0.2}Ga_{0.8}As$. Frame size: 25 x 25 nm. The number in parenthesis indicates the order in time in which the images were aquired The small, sharp-bordered feature is interpreted as an adsorbate (A).*

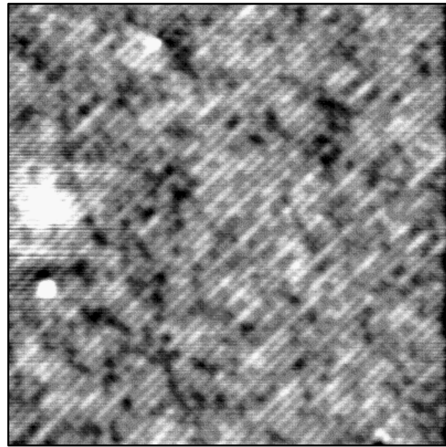

g: +0.879 V, 54 pA (7)

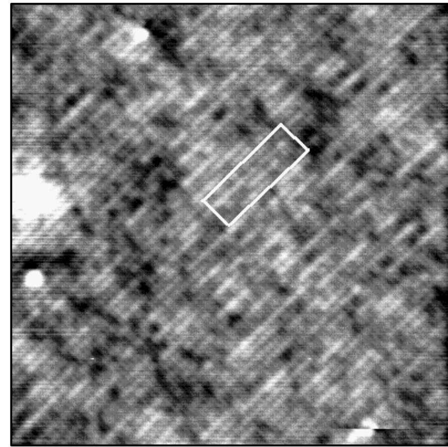

h: +0.803 V, 54 pA (8)

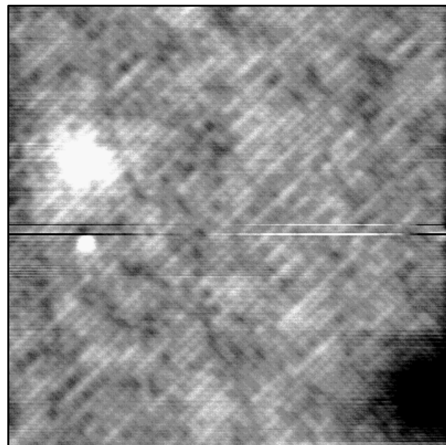

i: +0.774 V, 54 pA (12)

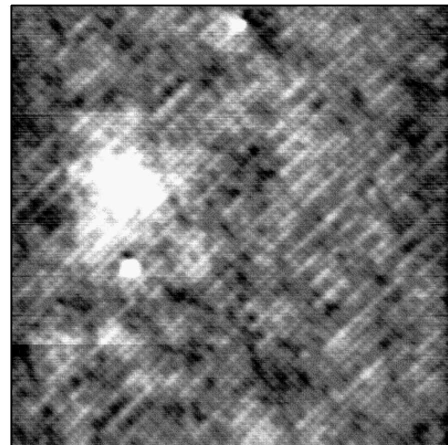

j: +0.746 V, 54 pA (9)

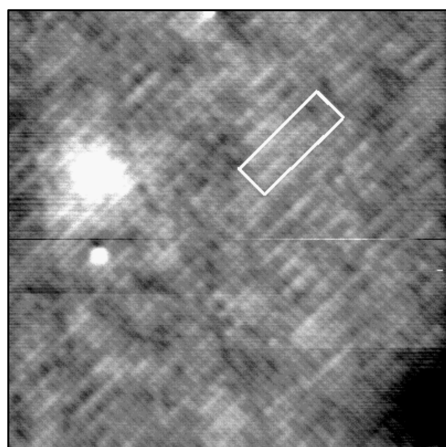

k: +0.719 V, 54 pA (11)

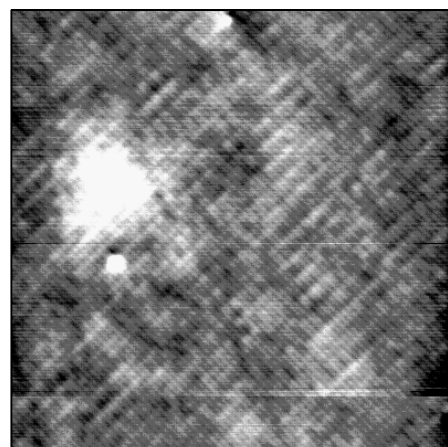

l: +0.693 V, 54 pA (10)

Fig. 6.3 *(continued)* **:**. *The large, fuzzy feature is probably a dopant (D). Notice that at small voltage, small ridges appear along the* **á***110***ñ** *direction. For very small voltage (see figure k) the ridges become longer (see rectangles).*

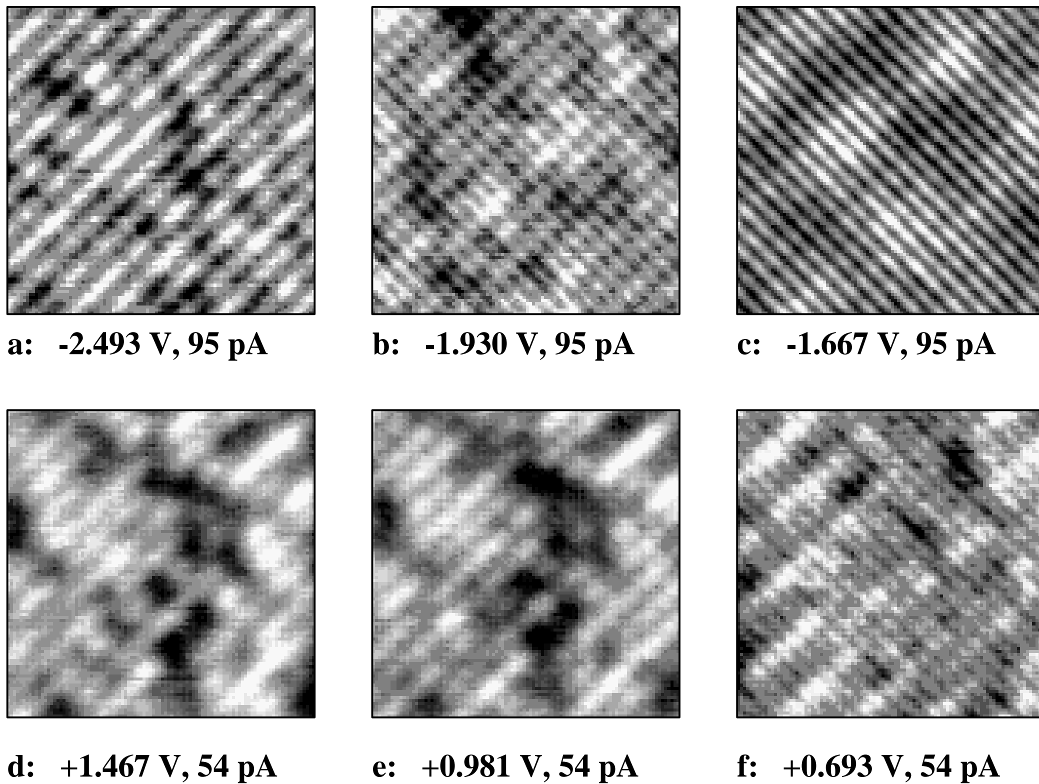

Fig. 6.4: *Selection of cut-outs from the frames shown in fig. 2 and 3, showing details of the atomic lattice for different voltages (6.25 x 6.25 nm).*

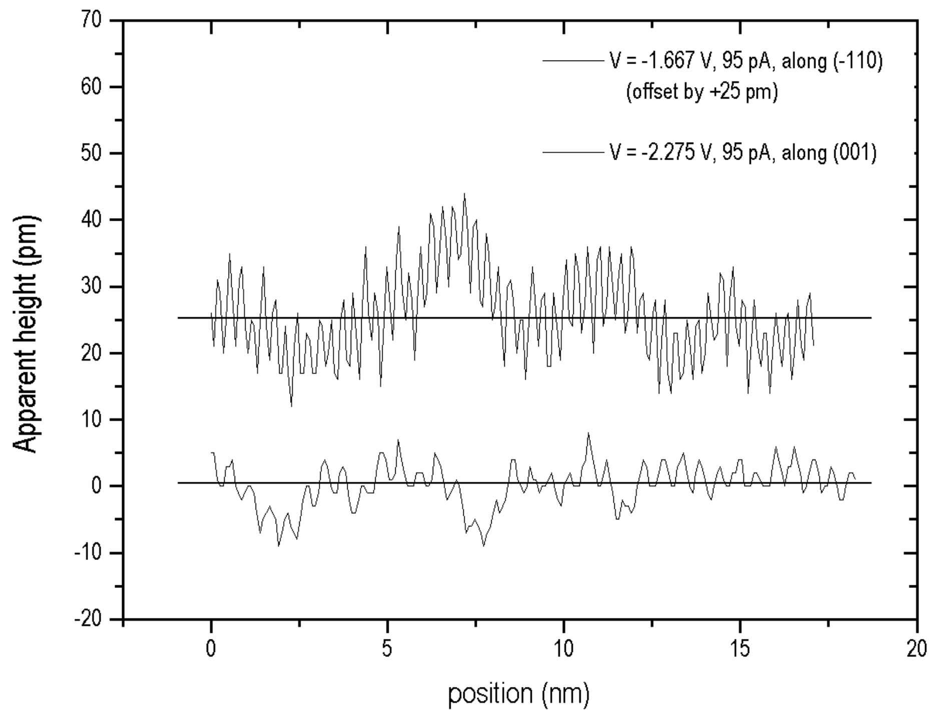

Fig. 6.5: *Height-profiles taken from two images in figure 1 (V = -1.667 V, V = -2.275 V). The height-differences in the image taken at higher voltage, commonly associated with alloy-fluctuations, are about 10 – 15 pm. Those associated with the bright areas observed at low voltage larger, up to 20 pm.*

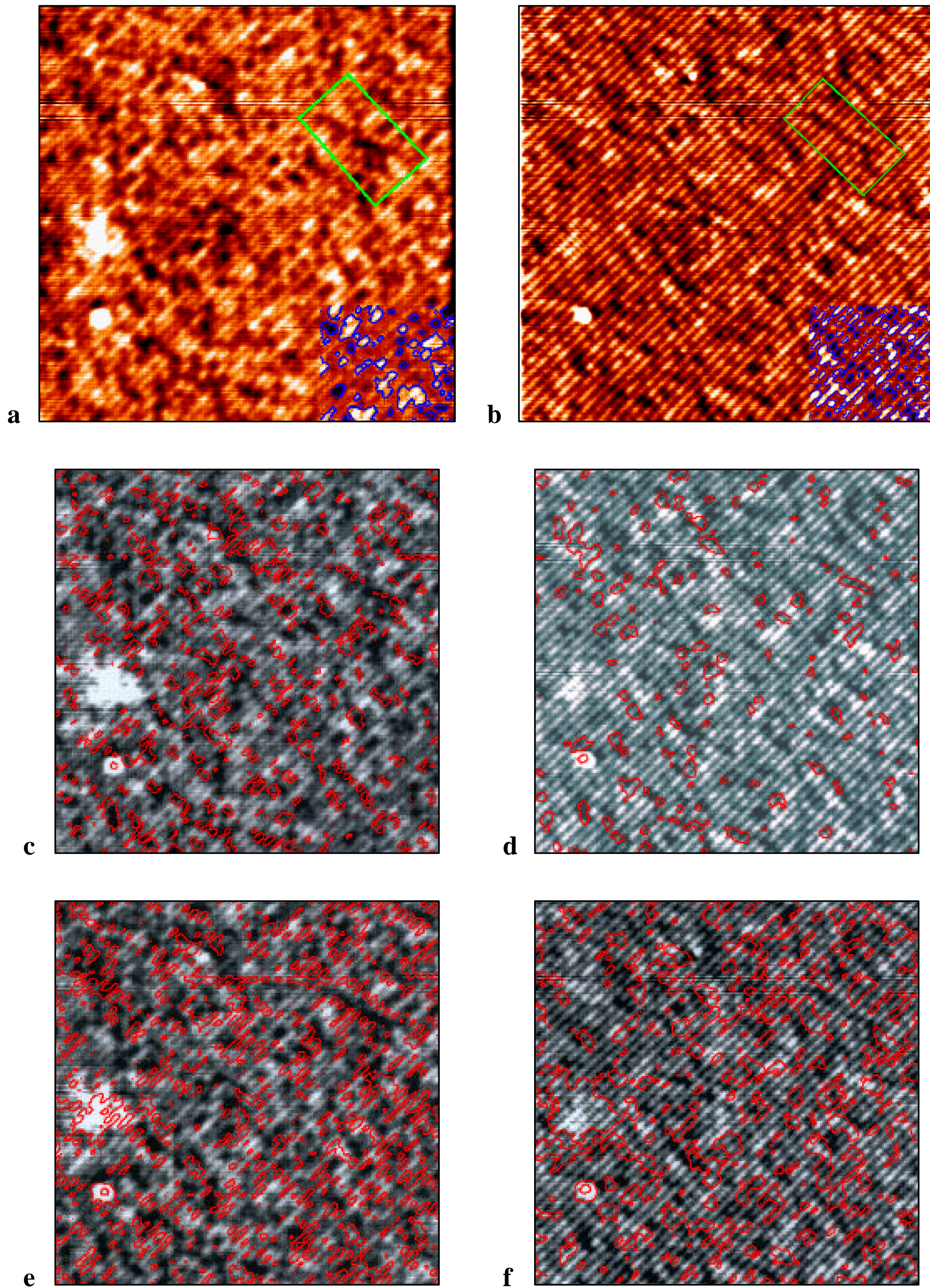
a
b
c
d
e
f

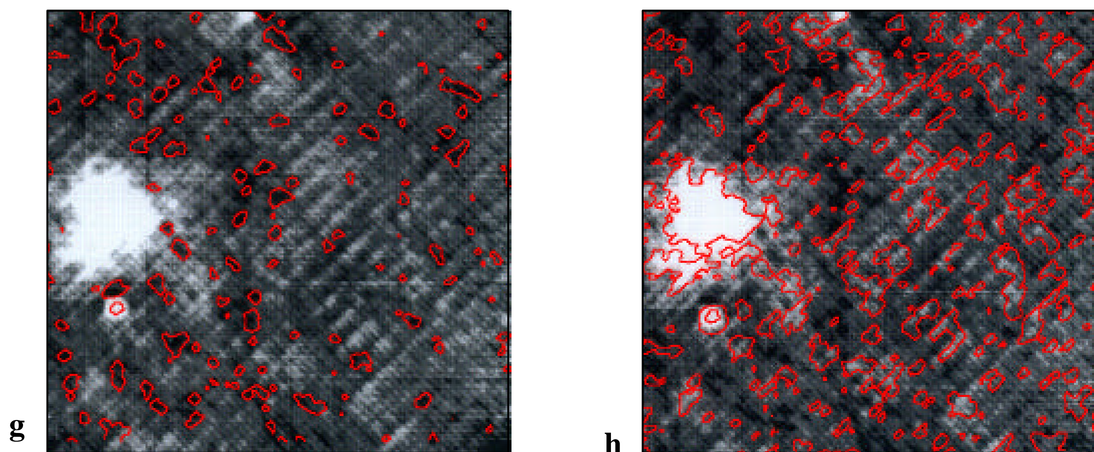

Fig. 6.6 *(both pages)* **a:** *Empty-states image of n-$Al_{0.2}Ga_{0.8}As$ (V = + 1.222 V, I = 54 pA). The contourlines z = 23 pm enclose all maxima and the contourlines z = 9 pm enclose all minima (see inset). Frames (a) and (b) are 25 x 25 nm. The other frames (20.5 x 20.5 nm) display the surface at the same scale.* **b:** *Filled-states image of the same area of AlGaAs (V = -2.193 V, I = 95 pA). The contourlines z = 18 pm enclose all maxima and the contourlines z = 8 pm enclose all minima.* **c:** *Empty-states image in which the contourlines enclosing the minima in the filled states image (b) have been projected. Figures 6.6 c –f show that the alloy-related minima appearing in figure 6.6a do not systematically coincide with the alloy-related minima in figure 6.6b. The same statement can be made for the alloy-related maxima. The contourline z = 75 pm indicates the position of the adsorbate and is used for alignment in figures c, d, e, f, g, h.* **d:** *Filled states image in which the contourlines enclosing the minima of the empty-states image have been projected.* **e:** *Empty-states image in which the contourlines enclosing the maxima in the filled states image are projected.* **f:** *Filled states image in which the contourlines enclosing the maxima in the empty-states image have been projected. The images show very clearly that the maxima and minima in the empty states images do not coincide. See further details in text.* **g:** *Low-voltage empty states image of n- $Al_{0.2}Ga_{0.8}As$ (V = +0.693, I = 54 pA) in which the contourlines enclosing the minima in the high-voltage empty-states image have been projected. It is seen that the ridges appearing at small, positive voltage do not coincide with the alloy-related minima that appear at large, positive voltage. Frame size: 20.5 x 19.2 nm.* **h:** *Low-voltage empty states image of n- $Al_{0.2}Ga_{0.8}As$ (V = +0.693, I = 54 pA) in which the contourlines enclosing the maxima in the high-voltage empty-states image have been projected. The ridges that appear at small, positive voltage more or less coincide with the alloy-related maxima that appear at large, positive voltage. Frame size: 20.5 x 19.2 nm.*

On the superlattice, the same changes in atomic corrugation are observed as on GaAs (110) and AlGaAs (110). For both polarities, the changes in corrugation occur on the AlGaAs-layers at higher absolute bias voltages than on the GaAs-layers. In figures 6.7 c,d,e, some instability of the tip manifests itself in the images. It can be seen that the changes are reversible and that they do not affect the general behaviour of the effects described in this section.

Besides a change in atomic corrugation, an inversion of contrast between the GaAs-layers and the AlGaAs-layers is observed: For large voltage, the AlGaAs-layers appear as dark, spotted bands. This is in fact the familiar look of a thin AlGaAs-layer in STM since AlGaAs-(110) is very often imaged at fairly large negative voltage (-2 V < V < -3V) [1,3,6]. For small voltage, the AlGaAs appears brighter than the GaAs. The effect occurs for both polarities, although it is strongest in the filled states images. In the empty-states images, the inversion of contrast appeerently occurs at small tip-sample distance, since the last image (V = 0.310 V, 35 pA) ended with a tip-crash.

In the empty states images at intermediate voltages, the GaAs-layers appear to become much broader than they really are. The height-profiles shown in figure 6.10 b also reflect this. Another feature that is apparent from the empty-states images, is that the the dark spots associated with the alloy-fluctuations disappear as the voltage slowly decreases. We come back to these points in sections 6.5 and 6.6.

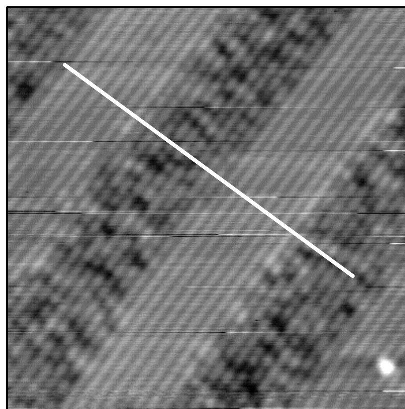

a: - 2.076 V, 75 pA

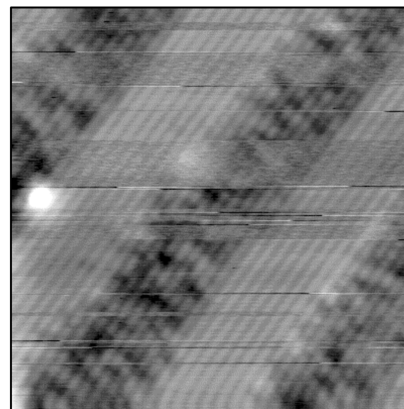

b: - 1.861 V, 75 pA

Fig. 6.7 a – g *(both pages)* **:** *Filled states images of an n-type GaAs/$Al_{0.33}Ga_{0.67}As$ superlattice. The GaAs and AlGaAs layers are both 5 nm wide. Frame size: 20 x 20 nm. The white line in (a) indicates the direction of the line-profiles shown in figure 6.9 a.* **h:** *Cut-out from figure 7-g (V = -1.364 V). Frame size: 13.4 x 6.7 nm. A box-reject fast Fourier transform filter (FFT) has been applied in order to remove noise which manifests itself as fine, horizontal lines in the image. The image shows details of the atomic lattice of the GaAs and AlGaAs-layers.*

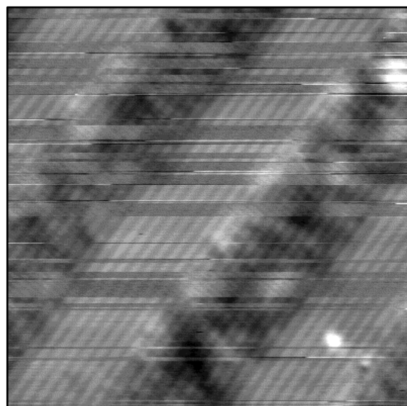

c: - 1.730 V, 75 pA

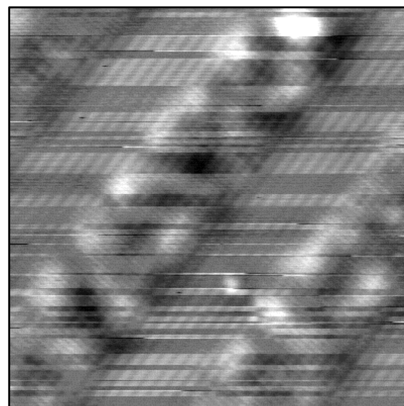

d: - 1.667 V, 69 pA

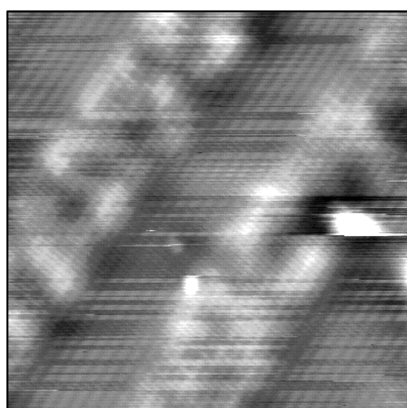

e: - 1.550 V, 69 pA

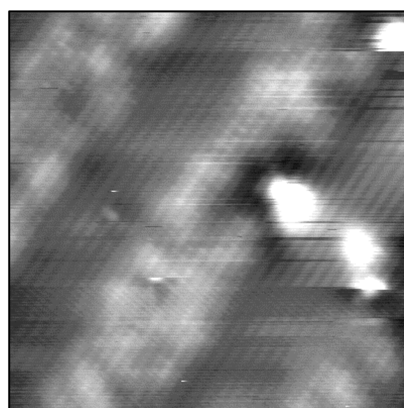

f: - 1.467 V, 69 pA

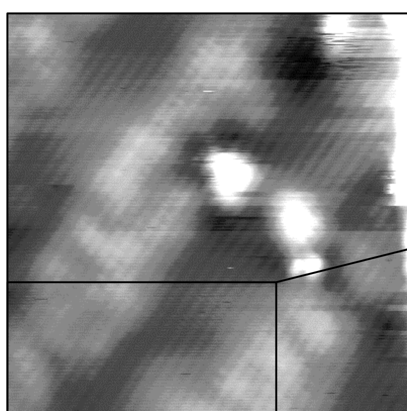

g: - 1.364 V, 69 pA

FFT

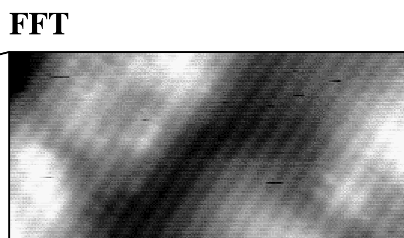

h

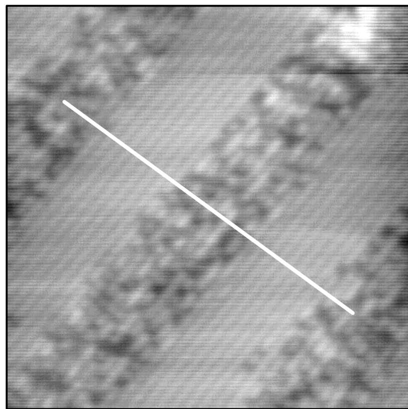

a: +1.136 V, 35 pA

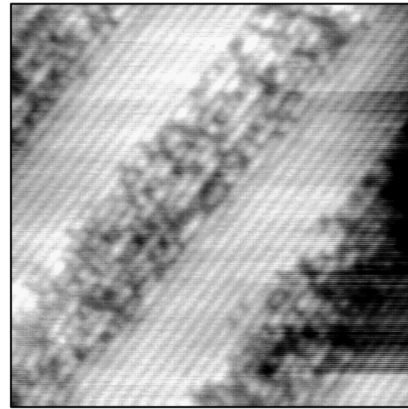

b: +0.964 V, 35 pA

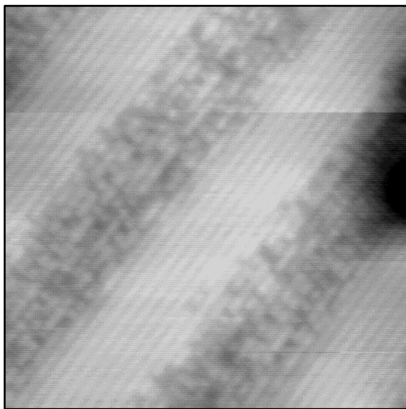

c: +0.876 V, 35 pA

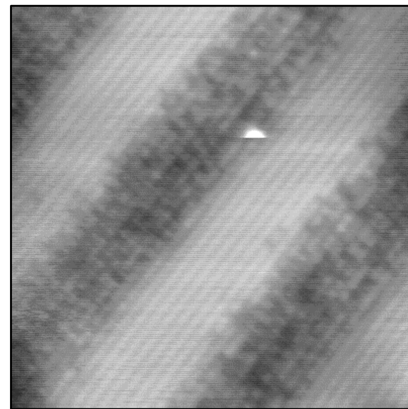

d: +0.803 V, 35 pA

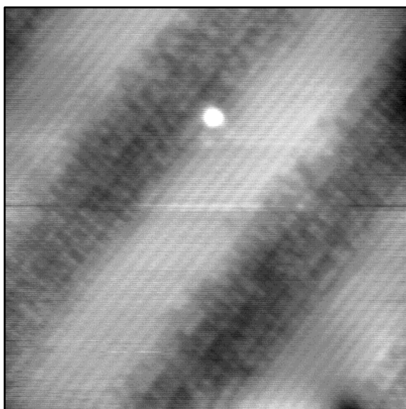

e: +0.760 V, 35 pA

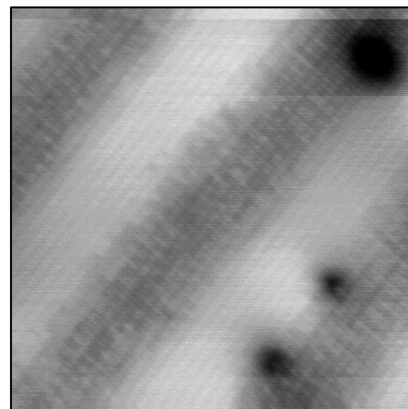

f: +0.706 V, 35 pA

Fig. 6.8 *(both pages)* **a-m:** *Empty states images of an n-type GaAs/$Al_{0.33}Ga_{0.67}As$ superlattice. The GaAs and AlGaAs layers are both 5 nm wide. Frame size: 20 x 20 nm. The last image ended with a tip-crash. The white line indicates the direction of the line-profiles shown in figure 6.9 b.*

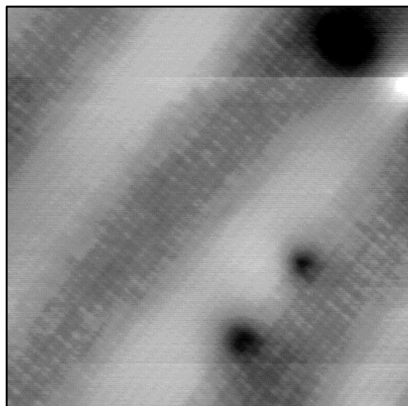

g: +0.645 V, 35 pA

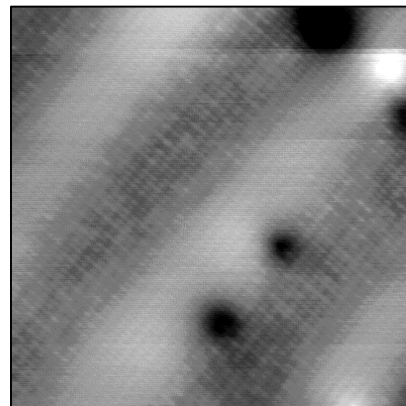

h: +0.588 V, 35 pA

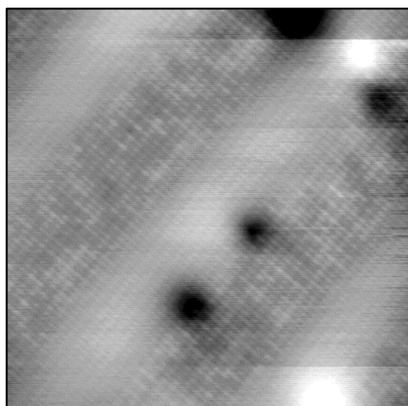

i: +0.499 V, 35 pA

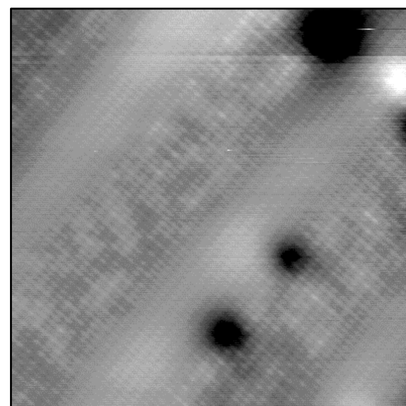

j: +0.447 V, 35 pA

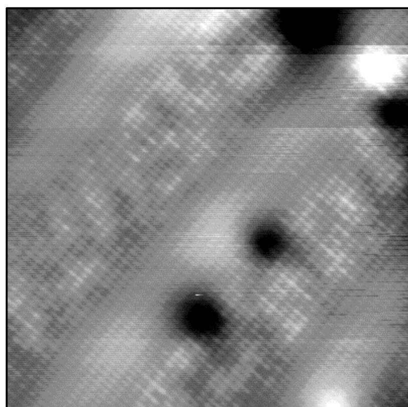

k: +0.408 V, 35 pA

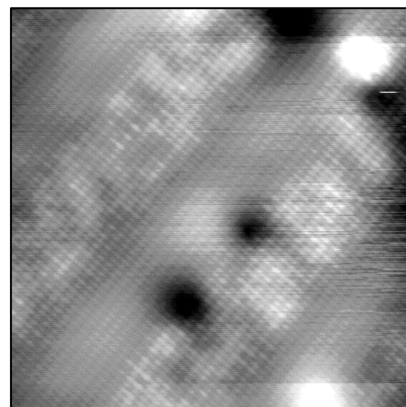

l: +0.359 V, 35 pA

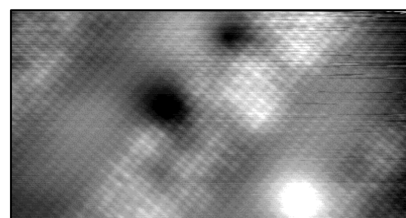

m: +0.310 V, 35 pA

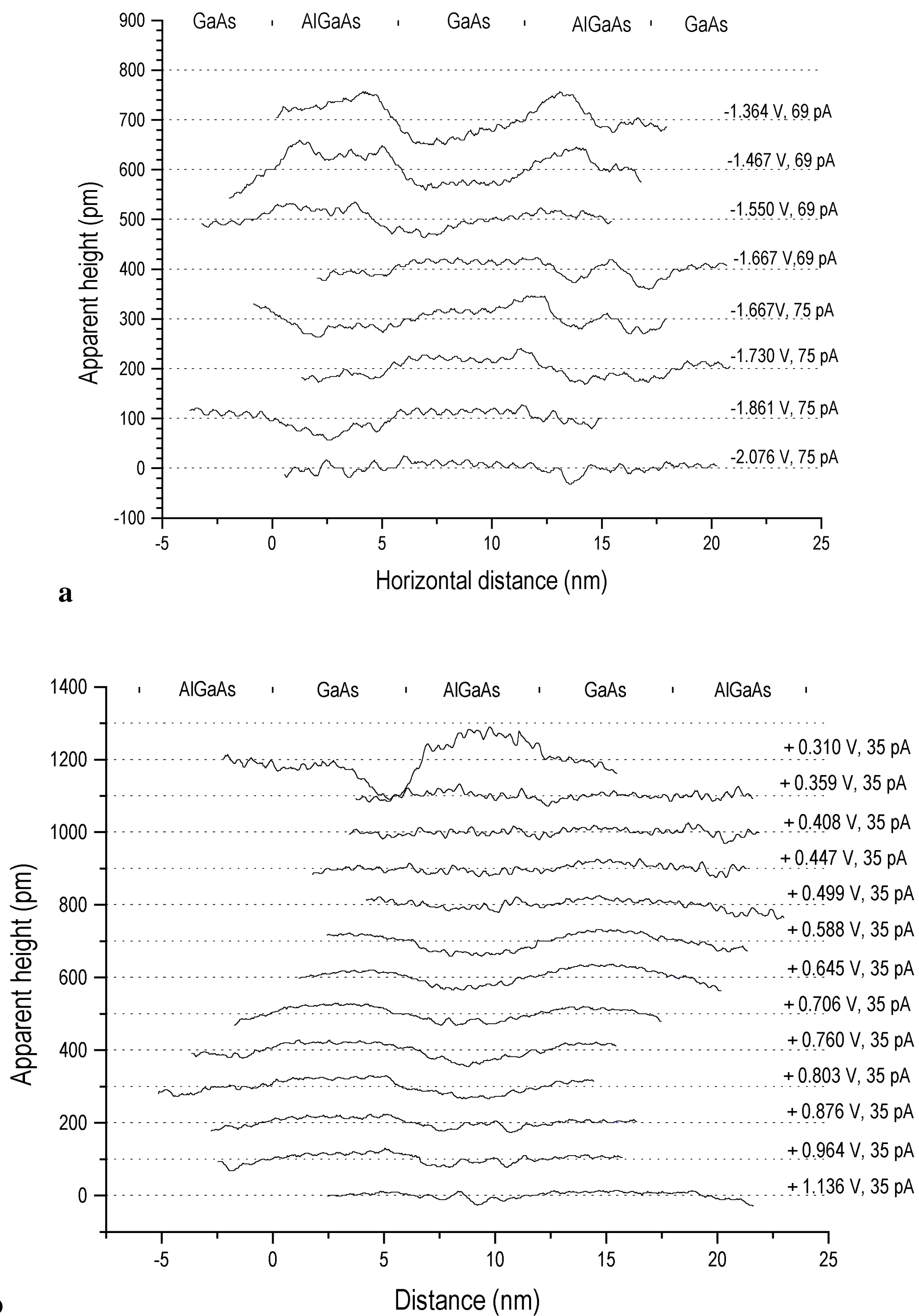

Fig. 6.9 a: *Apparent height-profiles the filled states images of the superlattice (figure 6.7), taken along* [001] *(perpendicular to the GaAs/AlGaAs layers). The profiles show the inverse of contrast between GaAs and AlGaAs.* **b:** *Apparent height-profiles of the empty states images (figure 6.8) taken along* [001], *showing the inverse of contrast between GaAs and AlGaAs and the broadening of the GaAs-layers at intermediate voltage.*

6.4 Expected tip-induced band bending

As is made clear in chapter 4, it is very important to take the effects of Tip-Induced Band Bending (TIBB) into account when interpreting voltage-dependent STM-images of a semiconductor surface. In order to do so, we have used the model described in section 4.2 to calculate the bandbending behaviour that we expect for the thick AlGaAs layer.

Determining the expected band bending behaviour for the GaAs/AlGaAs superlattice is slightly more complicated as the model described in section 4.2 lends itself only to calculations pertaining to a sample made up of a single material. It cannot deal with heterostructures. In subsection 6.4.2, therefore, we will first consider the electronic structure of a superlattice (figure 6.11). It will be shown that for an n-type superlattice surface, there are five screening mechanisms: 1) population of the conduction-bands of both the GaAs and AlGaAs layers by accumulation, 2) population of the conduction-band by accumulation of only the GaAs-layers and not the AlGaAs-layers, 3) population or depopulation of the Si dopants in both the GaAs and AlGaAs layers (depletion), 4) depopulation of the valence-band of only the GaAs-layers by inversion, and 5), depopulation of the valence-band of both the GaAs and AlGaAs layers by inversioin. We have to consider these various screening mechanisms, and assess their relative strengths by roughly estimating the density of free charge that each of these mechanisms must involve. From this, we can then construct a more or less qualitative description the band bending behaviour that we expect for a superlattice in general.

6.4.1 The thick AlGaAs layer

Figure 6.10 shows the behaviour of TIBB that we expect for the thick AlGaAs layer shown in figures 6.2, 6.3, 6.4 and 6.6. For $Al_{0.2}Ga_{0.8}As$ the following values are known for the bandgap and electron affinity [7]: $E_g = 1.67$ eV and $\chi = 3.85$ eV. For the tip work function, we have chosen $W_{TIP} = 4.125$ eV. This choice places the transition between type I depletion and type II depletion (see figure 6.10) near V = +0.75 V. At this volage, we observe in our experiments that the atomic corrugation is completely in the [-110] direction. The chosen value for the tip work function yields a TIBB-behaviour for n-AlGaAs that is in all respects similar what we have observed experimentally for n-GaAs [11]. The corrugation changes that one might expect from the expected TIBB-bahaviour are thus also similar to the corrugation-changes that we have observed for n-GaAs. This expectation is confirmed by our experimental results on n-AlGaAs. We have not recorded the voltage-dependent changes in the tip-sample distance during this measurement, and we are therefore unable to validate our choice for the tip work

function from the voltage-dependent changes in |dz/dV| like we have done in chapter 4. However, from the preceeding arguments the value of W_{TIP} = 4.125 eV seems a very justifiable choice.

From figure 6.10 we thus expect the following behaviour for the TIBB of the thick $Al_{0.2}Ga_{0.8}As$-layer: For large, negative voltage, the amount of TIBB levels off at about –0.3 eV, and the A5, A4, BVB and C3 states contribute to the tunneling current. We expect the contributions from the A5 and BVB states to dominate the tunneling current at these voltages, and therefore the corrugation should be in the [001]-direction (atomic rows along [-110]). In figure 6.10, the transition between type I accumulation and type II accumulation occurs for V = -2.0 V. For low voltage, we expect only a contribution from the C3 state, since the contributions from the other states gradually decrease as the voltage is decreased, whereas the contribution of the C3 state remains relatively constant. This causes the corrugation to be in the [-110] direction (atomic rows along [001]).

For large positive voltage, we expect mainly contributions from the C4 and C3 states. As the C3 state is a weak state in comparison to the C4 state, the C4 state determines the corrugation observed in the image at large positive voltage [8,10]. For V > 2.0 V, we expect type II inversion which involves a contribution from the A5 state as well. However, it is possible that the contribution from the A5 state is too weak in comparison with the contributions from the other states to manifest itself in the corrugation. The peak in the surface-DOS associated with the C4 state falls outside the energetically accessible window of states for most voltages of interest (V < +2.5 V), but we expect a significant influence on the corrugation from the low-energy shoulder of the C4 state at lower voltage, based on our previous results on n-GaAs [11]. The influence of the low energy shoulder is depicted in figure 6.7a by the dotted arrow. Furthermore, we expect a rather wide voltage-interval for which the surface is in type II depletion (+0.75 V < V < 2.0 V). In this region we expect the corrugation-change to occur due to a shifting balance between the competing contributions of the C3 and C4 states, in a fashion completely analogous to the behaviour that we have observed experimentally on n-GaAs [11].

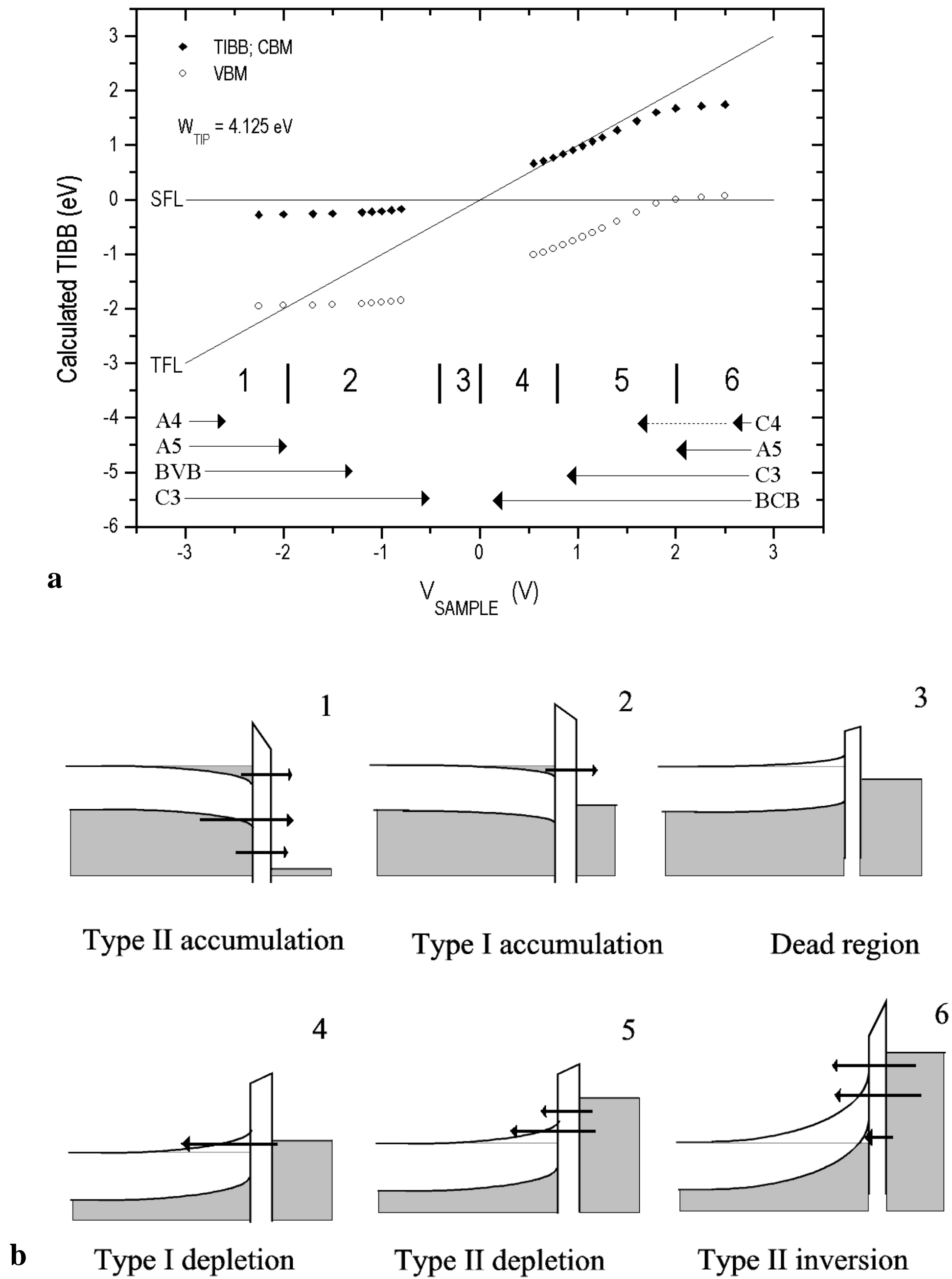

Fig. 6.10 a: *Calculated amount of tip-induced band bending (TIBB): W_{TIP} = 4.125 eV, $N_D = 5 * 10^{17}$ cm^{-3}. Filled states: I = 54 pA, empty states: I = 54 pA. All features of the surface-DOS that fall inside the two sharp triangles formed by the lines SFL and TFL are energetically accessible to the tunneling process.* **b:** *The different band bending configurations.*

6.4.2 The GaAs/AlGaAs superlattice

The calculated electronic structure of the GaAs/AlGaAs superlattice is displayed in figure 6.11. The nominal Al fraction in the $Al_xGa_{(1-x)}As$ layers is x=0.33. For $Al_{0.33}Ga_{0.67}As$, ref. 7 yields E_g = 1.836 eV for the bandgap and χ = 3.707 eV for the electron affinity. For the band offsets, it is generally accepted for a $GaAs/Al_xGa_{(1-x)}As$ heterojunction that the offset in the conduction-band equals $^2/_3$ of the difference in bandgap between the two materials, whereas the offset in the valence-band equals $^1/_3$ of the difference in bandgap. This means that in our superlattice, the conduction-band offset equals 0.247 eV and the valence-band offset equals 0.165 eV. The calculation-results displayed in figure 6.11 also reflect this. From the same calculation it is evident that a confined electron-level exists in the quantum wells formed by the GaAs-layers. It lies energetically at about $^1/_3$ of the conduction-band offset (0.08 eV) above the GaAs-CBM. The Fermi level of the structure lies slightly above the confined level (0.036 eV). Slightly below the GaAs-VBM, there is a confined hole-level.

In general, the band bending behaviour of a given surface depends on the screening mechanisms that are available, and on the difference between the tip work function and the electron-affinity of the sample material. For the superlattice, this means that we have to include the screening effects caused by population of the superlattice, and that we have to consider the fact that GaAs and AlGaAs have different electron-affinities. For the superlattice, we identify five different screening mechanisms. The first three involve depletion, inversion and accumulation of both the GaAs and AlGaAs layers of the superlattice. These screening mechanisms are similar to the ones that are also relevant for sample surfaces made up of a single material [11,23]. A fourth screening mechanism is provided by the population of the GaAs-quantum wells by accumulation, while at the same time the conduction-band of the AlGaAs-barriers remains unpopulated. The last screening mechanism occurs when the valence-band of the GaAs-layers becomes depopulated by inversion, whereas the valence-band of the AlGaAs-barriers remains populated. The relative strengths of these screening mechanisms may be estimated from the densities of states and doping concentrations of the materials making up the superlattice, since these quantities determine the charge-densities that are available for screening in the different band-bending regimes.

In the depletion regime, screening is provided by the ionized dopants. Since typical depletion-lengths are significantly longer than the period of the superlattice (10 nm), we can use the average of the doping-concentrations in the GaAs and AlGaAs, which is $8*10^{17}$ cm^{-3}. The charge-density available for screening when the surface is in accumulation can be estimated from the 3D-DOS of the conduction-band of GaAs and AlGaAs. For a parabolic dispersion-relation, the 3D-DOS is proportional to $E^{1/2}$ [25]. We have chosen to integrate the 3D-DOS for AlGaAs from E = 0 to E = 0.1 eV and the 3D-DOS for GaAs from E = 0.25 eV to E = 0.35 eV. This simulates the circumstance that the surface is populated by accumulation to up to 0.1 eV above the CBM of the AlGaAs barriers. Notice that for E < 0.25 eV, the electrons in the GaAs-layers are described by the DOS associated with the superlattice. The results indicate that for the GaAs-layers, the charge-density associated with accumulation should be around $1 * 10^{19}$ cm^{-3}. For the AlGaAs-layers, this density should be about $2 * 10^{20}$ cm^{-3}. The length

over which accumulation extends into the semiconductor is typically in the order of 20 nm in our calculations on band bending for the thick AlGaAs-layer, which justifies the assumption that the screening-behaviour is characterized by the averaged charge-densities in the GaAs- and AlGaAs-layers, which is 1 * 10^{20} cm^{-3}. The analogous calculation for the valence-band shows that the charge-density available for screening when the surface is in inversion, is around 2 * 10^{20} cm^{-3}.

The fourth screening mechanism becomes relevant when the downward band bending partly populates the superlattice but is insufficient to popolate the conduction-band of the AlGaAs-barriers. The charge-density involved with this screening mechanism may be estimated from the DOS of a two-dimensional electron-gas [25]. We have used the effective mass of a conduction-band electron in GaAs for the estimation [7]. The superlattice may be populated from the confined level in the quantum wells up to the CBM of the AlGaAs-barriers, which is an energy-range of 0.17 eV. This yields a total 2D-DOS which, when divided by the period of the superlattice, translates to a 3D-DOS of 5 * 10^{18} cm^{-3}. A similar calculation for the valence-band of the superlattice yields a 3D-DOS of 7 * 10^{19} cm^{-3}.

Although the above estimates are quite crude, they are adequate for giving a qualitative description of the band bending behaviour of the superlattice surface. We will first consider the case of negative sample voltage. At large, negative voltage, the conduction-bands of both the GaAs and AlGaAs layers are populated due to accumulation. In a similar way as is observed for a surface consisting of a single material, accumulation involves small amounts of band bending due to the large density of charge available for screening. We also expect the band bending behaviour to be relatively insensitive to the applied bias voltage and other parameters such as tip work function [11]. However, when at smaller negative voltage the screening properties of the surface are deterimined by the superlattice, we expect the amount of TIBB to become more sensitive to the applied bias voltage. For very small negative voltage, no tunneling is possible on n-type material.

For positive bias voltage, screening can be provided by ionized dopants (depletion), by depopulation of the valence-band of the GaAs quantum wells, or by depopulation of the valence-band of both the GaAs- and AlGaAs-layers (inversion).

The average concentration of dopants is very much lower than the charge density generated by the depopulation of the GaAs valence-band, or by the simultaneous depopulation of the valence-bands of the GaAs- and AlGaAs-layers. We may thus expect that in the regime of depletion, the amount of TIBB is quite sensitive to the applied bias voltage. From chapter 4 it is also clear that in the depletion regime in general, the amount of TIBB depends very sensitively on other parameters like the tip work function or doping concentration. We therefore expect that in this regime of band bending, the amout of TIBB fluctuates as the tip alternatingly faces a GaAs-layer and an AlGaAs-layer, since the two materials have different electron affinities. The same fluctuations might also occur in the other band bending regimes, but probably to a lesser extent due to the higher charge-densities that are involved in screening.

When depopulation of the GaAs valence-band occurs at larger positive voltage, the amount of TIBB is expected to level off. It is not certain if any voltage exists for which the valence-band to the AlGaAs-layers becomes depopulated as well. In figure 6.10 a, inversion depopulates the valence-band of the thick AlGaAs-layer only down to

70 meV below the VBM. In the superlattice, this would be insufficient to depopulate the AlGaAs valence band since it lies 0.165 eV below the VBM of the GaAs-layers.

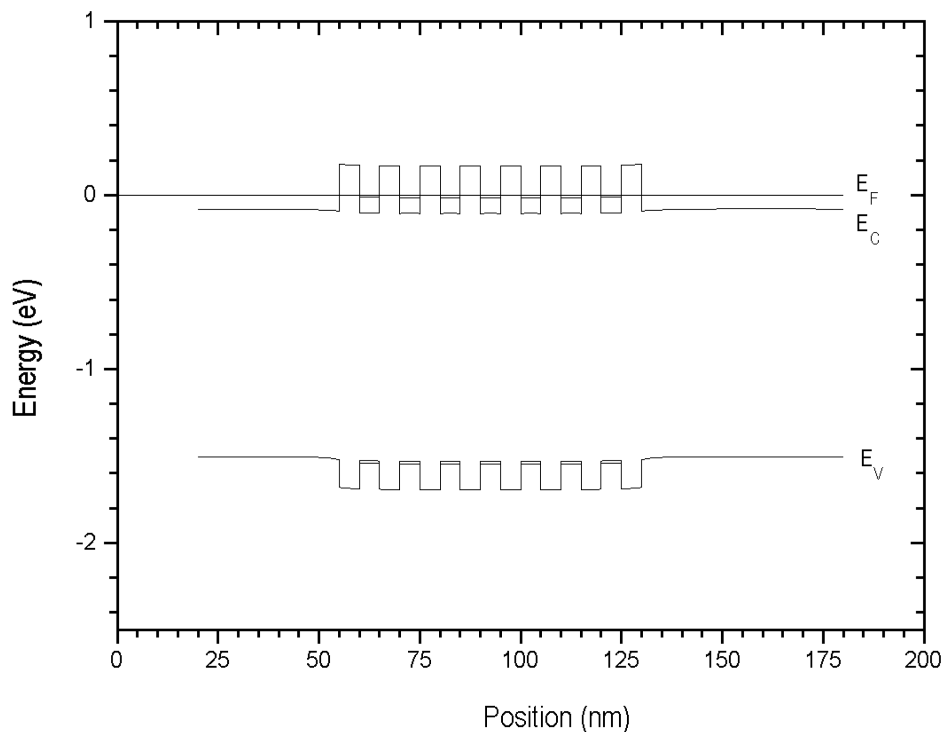

Fig. 6.11: *Calculated band offsets and position of the Fermi level of the GaAs/AlGaAs superlattice. The calculation represents the situation in the bulk of the crystal. The superlattice has been sandwitched between two layers of n-type GaAs (2 * 10^{18} cm^{-3}) to minimize band bending at the edges of the superlattice. This may affect the calculated position of the Fermi level, but this is uncritical since in the experiments, the Fermi level of the sample also shifts with respect to the sample band structure due to tip-induced band bending. The calculation shows the band-offsets between GaAs and $Al_{0.33}Ga_{0.67}As$ as well as the energetic location of the confined electron- and hole levels.*

6.5 Discussion on the thick AlGaAs layer

6.5.1 Filled-states images

The filled-states images (figure 6.2) show essentially two voltage-dependent changes: The first is a corrugation-change similar to the one that we have also reported for n-GaAs [11]. For large negative voltage, the atomic rows appear to run along [-110]. At small values the rows appear to run along [001]. The second change is that the atomic-scale fluctuations in the image, commonly associated with the presence of Al [1,3,4,22], gradually disappear. At low voltage, these alloy-related fluctuations are replaced by bright and dark areas several nm in diameter. The observed corrugation-changes are completely consistent with the behaviour that we expect based on the band bending arguments given in section 6.4. It is thus clear that for large voltage, we observe the spatial distribution of the valence-band related surface-DOS (mainly the A5-state). For low voltage, we image the C3-state which is populated due to the downward band bending of the surface.

The change in atomic corrugation is accompanied by the appearance of dark and bright areas for small negative voltage (figure 6.2 g,h,i). For these voltages (-1.667 V < V < -1.827 V), the tunneling current must orginate exclusively from the accumulation layer of electrons at the suface according to the band bending arguments given in section 6.4. This is confirmed by the appearance of the atomic corrugation which reflects the spatial distribution of the C3 state.

We interprete the appearance of these bright and dark areas as fluctuations of electron-density in this accumulation-layer: Due to small spatial variations in the local Al-content, the conduction-band electron-DOS near the surface varies as well. The electron-states in the conduction band near the surface are occupied due to the downward TIBB expected for negative voltage. The spatial distribution of the electrons in the accumulation layer is now influenced by two factors: The electron-DOS of the conduction-band near the surface, and by the interaction that exists between the electrons themselves. In general, the interaction between electrons making up an electron-gas consists of the repulsive Coulomb interaction and the exchange-correlation interaction. We postulate that the combined effect of the inhomogeneous surface-DOS and the (total) electron-electron interaction leads to the appearance of the bright and dark areas.

Let us consider the accumulation layer of electrons more closely: It consists of free electrons that occupy electron-states in a certain volume of crystal near the surface, due to the effects of TIBB. These electron-states are the solutions to a Schrödinger equation of which the potential is the sum of three terms: The atomic potential built by the crystal lattice at and near the surface; the interaction between the electrons themselves, and the rather wide potential well caused by TIBB itself. In this discussion (as well as throughout this thesis) we neglect the effects of the last term, although it can give rise to quantized levels in the accumulation layer [29]. In a quantum-mechanical system of free electrons, the electron-electron interaction contains the (conventional)

Coulomb-term as well as potential-terms arising from the exchange and correlation interactions [25 (p. 51,52), 27 (p. 184)]. Following the argument made in ref. 25 (p. 43) we will assume that the electron-electron interaction is dominated by the Coulomb-interaction, although that argument (the "Hartree approximation") relates to the energetic location of an electron-state rather than its spatial distribution. The Coulomb-term (and the exchange and correlation terms as well, for that matter [25 (p. 52), 27 (p. 184)]) contains the electron-density. If we were to evaluate the local density of electron-states in the accumulation layer, we would therefore have to solve the Schrödinger and the Poisson equations self-consistently [25 (p. 52), 27 (p. 184)]. The sum of the self-consistent solutions to these two equations (at an infinitesimal energetic interval) then equals a new near-surface DOS which includes the electron-electron interaction. The images shown in figure 6.2 g,h,i, thus reflect a "modified" conduction-band related surface-DOS for which the influence of the electron-electron interaction manifests itself in its spatial variation.

The significance of this becomes apparent when one compares the filled-states STM-images shown in figure 6.2 g,h,i, with the empty-states images shown in figure 6.3 j,k,l. Both sets of images show the lower part of the conduction-band related surface-DOS (the C3-state). However, the empty-states images (figure 6.3 j,k,l) show the surface-DOS in the absence of electron-electron interaction, as the electron-states are unoccupied while the image is aquired. The filled-states images (figure 6.2 g,h,i), on the other hand, reflect the same energetic part of the surface-DOS. However, in this case the electron-states are occupied by free electrons during the measurement. The difference in appearance between the images shown in figure 6.2 g,h,i and those shown in figure 6.3 j,k,l is thus a manifestation of the way in which the electron-electron interaction influences the distribution of free electrons near the surface of the AlGaAs-crystal.

We base this interpretation of the dark and bright areas on several aspects of our experimental observations: First of all, the effect is very clearly connected to the inhomogeneous nature of the AlGaAs surface. For the filled states results on n-GaAs (chapter 4), the bright and dark areas do not appear at all. At the same time, the band bending situation for small, negative voltage can be expected to be quite similar for both materials, as is confirmed by the similarity in the voltage-dependent changes in atomic corrugation observed for n-AlGaAs and n-GaAs.

The second aspect is that the dark and bright areas seem to have a characteristic size of a few nm. This length scale is about one order of magnitude larger than the atomic length scale on which the surface-DOS is observed to vary at other voltages. The length scale of a few nm agrees remarkably well with the (apparent) size of the two charged adsorbates that are present on the surface as well. The dark ring around the adsorbates is of a similar size as the bright areas, although the rings are slightly larger. Such a ring is characteristic for a negatively charged adsorbate on n-type GaAs imaged in filled states [11,14,21]. The dark ring is caused by the fact that the charged adsorbate creates a depletion zone around itself. The width of that depletion zone depends on the screening length of the material. If Coulomb-repulsion dominates the electron-electron interaction of the free electrons occupying the accumulation layer, the bright and dark areas should have a lateral extent that is similar to that of the depletion zone around a negetively charged adsorbate.

A very important argument is that the appearance of the bright and dark areas does not occur in the empty-states images, althought it remains possible that the effect occurs outside the range of voltages that we have applied in our experiment. This point is relevant because in general, an electron occupying a bound state of a potential well has a finite localization. The spatial extent of such a bound state is usually several nm or more, as is evident from the effective Bohr-radius of an electron bound to a donor impurity in a semiconductor [7 (p. 3, p. 11)]. If the imhomogenieties in the surface-DOS form small potential-wells in which the electrons in the accumulation layer can be bound, such bound states would probably also have a spatial extent of several nm. This effect could therefore in theory provide an alternative explanation for the appearance of the bright and dark areas. However, we reject this hypothesis on account of the fact that in this case, bright and dark areas of a similar length scale should also be observed in the empty states images. Besides, it remains to be seen whether the atomic-scale fluctuations in the atomic structure of an AlGaAs-surface can create potential-wells that are deep enough to give rise to bound electron-states. In the absence of bound electron-states, it seems plausible to assume that the interaction between the electrons themselves must cause the modification to the spatial distribution of the near-surface electron-states. Moreover, the characteristic length-scale of the bright and dark areas suggests that this interaction, at least for the circumstances at hand, is dominated by the Coulomb-interaction.

It is interesting to note that the accumulation layer is also present at large negative voltage, and that the contribution to the tunneling current from the C3 state should vary spatially in accordance with the bright and dark areas. However, at large voltage the contribution from the A5 and BVB-states apparently dominates the tunneling current, as is evident from the observed atomic corrugation.

We thus interprete the filled states results on the thick AlGaAs-layer in the following way: For large voltage, the image shows the surface-DOS of the sample associated with the valence-band (A5-state). At small voltage, only the C3-state is available to the tunneling process. The bright and dark areas are attributed to fluctuations of the local density of electrons in the accumulation layer near the surface. The variations in the density of electrons in the accumulation layer are determined by the combined effects of the inhomogeneous DOS of the AlGaAs-surface and the interaction between the electrons themselves.

6.5.2 Empty-states images

The empty-states images also show a change in atomic corrugation. For large voltage, the rows appear to run along [-110]. The behaviour is similar to the corrugation-changes seen in the empty-states images on n-GaAs that we have reported previously [11]. At low voltage, small, bright “ridges” along [-110] appear. It also seems that the alloy-related minima in the images are less pronounced with respect to the images taken at higher voltage.

Based on the band bending arguments given in section 6.4 we explain the corrugation-change as a result of a shifting balance between the competing contributions of the C3-state and the low-energy shoulder of the C4-state. That interpretation is completely analogous to the one we have proposed for the corrugation-change observed in the empty-states images of n-GaAs [11]. Therefore, at large positive voltage, the images should reflect the spatial distribution of the upper part of the conduction-band related surface-DOS (C4 state). At large voltage, the lower part of the conduction-band related surface-DOS (C3 state) also contributes to the total tunneling current, but since its contribution is relatively small, it should not influence the topography of the image [8,10]. For the lower voltages, the images show the lower part of the conduction-band related surface-DOS.

It is known for GaAs (110) that the C3 state has a low-energy shoulder which extends into the bandgap of the semiconductor. We have shown that electrons can tunnel resonantly through this shoulder, causing atomic corrugation in the STM-image of n-GaAs (110) when the surface is in type I depletion during imaging [11]. Since the C3 state is centered very near the CBM for AlAs (110) [17], it is reasonable to suspect that this mechanism also becomes relevant for the imaging of $Al_xGa_{(1-x)}As$ (110) when the appropriate bias voltage is chosen. Whether it has played a role in our experiments is unclear, since we cannot determine the voltage at which the transition from type I depletion to type II depletion occurred from the experiment (see section 6.4).

At low voltage, small ridges 5 - 10 surface unit cells in length appear along the [-110]-direction. They extend 1 surface unit cell in the [001]-direction. Some alloy-related minima are also visible. Many of the ridges coincide with the alloy-related maxima observed at higher voltage, although the correlation is not complete (figure 6.6 h). The depressions also roughly coincide with those obtained at higher voltage, but again, not completely (figure 6.6 g). The trend in the images as one goes from large positive voltage to small positive voltage, appears to be that the ridges along [-110] first appear and then become longer, and that the alloy-related depressions slowly disappear. It is interesting to compare the low-voltage morphology of the thick AlGaAs-layer to the low-voltage morphology of the AlGaAs-layers in the superlattice, since the AlGaAs-layers in the superlattice contain more Al. The AlGaAs-layers in the superlattice show no ridges along [-110] at low voltage. At the same time, the alloy-related depressions disappear completely. The appearance of the ridges, and the disappearance of the alloy-related minima, thus appear to be sensitive to the Al-content of the material.

The orientation and strong anisotropy of the ridges suggests that the electron-states that are involved have a finite $k_{//}$-vector in the [001]-direction, and a much smaller $k_{//}$-vector in the [-110]-direction. This means that the $k_{//}$-vectors of the states relevant for the appearance of the ridges must lie near the X'-point of the surface Brillouin zone [12]. In principle, the states that are involved can be either surface states or bulk states (see figure 6.1 a). In those parts of the surface-BZ where the dispersion-curve of a surface-state is overlaps with the projected bulk electronic structure, the surface state and bulk states combine into a surface resonance, making the distinction between bulk and surface states for that part of the surface-BZ irrelevant [31 (p. 91)].

From the surface band structure of GaAs (110) [12] it is clear that near the CBM of the material, the energetically lowest lying electron-states have $k_{//}$-vectors on the line

joining the Γ-point and the X'-point of the surface BZ. Notice that near the Γ-point of the surface-BZ, the C3-surface state is resonant with the projected bulk band structure. There are two more local minima in the projected band structure of the bulk conduction band which occur near the X-point and at the M-point, but these lie at slightly higher energies. Consequently, there is a small band of states just above the CBM that have a $k_{//}$-vector near the Γ-point, on the line joining the Γ-point and the X'-point. Immediately above it is a second band of states with a $k_{//}$-vector near the X'-point. Both bands of states have little or no localization in the [-110]-direction. Moreover, the second band of states has a peridicity in the [001]-direction of one surface unit cell, and thus corresponds to the two main features of the ridges that appear in the images at low voltage.

At higher energies, bulk states with $k_{//}$-vectors near the X- and M-points also become available to the tunneling process. This should cause the ridges to disappear, as electron-states with $k_{//}$-vectors in all parts of the surface-BZ now become available to the tunneling process. At the same time, the local minimum of the C3-state near the X-point of the surface-BZ lies at an energy that remains available to the tunneling process for all (positive) sample voltages, which manifests itself in the atomic corrugation in the [-110]-direction that is superimposed on the ridges.

Since the above arguments are based on the band structure GaAs (110), one might wonder why the ridges have been observed only on $Al_xGa_{(1-x)}As$ (110). We explain this from the fact that GaAs is a homogeneous material, whereas $Al_xGa_{(1-x)}As$ is not. If on GaAs (110) the individual electron-states contributing to the tunneling current all appear as identical features, none of them will show up with more contrast than its neighbors in order to appear as an individual ridge. Instead, the collective pattern might appear as atomic rows along [-110]. Combined with the corrugation in the [-110]-direction caused by the minimum in the dispersion curve of the C3 surface state near the X-point, the image as a whole would appear as an atomically resolved image of the surface lattice. On $Al_xGa_{(1-x)}As$, on the other hand, the structural inhomogeniety of the material makes it possible that at some spots, the low-lying bulk conduction band states have a slightly stronger contribution to the total tunneling current than the low-lying bulk conduction band states in the immediate vicinity. This way, one such state can stand out from its neighbors and appear as a single ridge.

If our interpretation of the ridges along [-110] is correct, then the effect should be highly sensitive to the Al-content of the material. For $x > 0.33$, the band structure of $Al_xGa_{(1-x)}As$ becomes indirect, and the lowest-lying bulk conduction band states have $k_{//}$-vectors near the X-point. For n-$Al_xGa_{(1-x)}As$ with a high content of Al, we thus expect the ridges to appear along the [001]-direction at low positive voltage. For $x = 0.33$, the lowest lying bulk conduction band states have $k_{//}$-vectors near the Γ-point and X-point, as for this concentration of Al, the Γ-minimum and the X-minimum in the bulk conduction-band structure lie at the same energy [15]. We therefore do not expect to see ridges in either the [001]-direction or the [-110]-direction for this value of the Al-concentration. Our images of the GaAs/AlGaAs superlattice are consistent with that prediction: In the images of the thin AlGaAs-layers taken at low positive voltage, we observe no ridges in the [-110]-direction. Instead, some small ridges along [001] are seen.

The appearance of the alloy-related depressions in the images also depends on the applied bias voltage. In the thick AlGaAs-layer, they become less pronounced for low voltage, although they have not disappeared completely for the lowest value of applied bias voltage (V = +0.693 V). On the GaAs/AlGaAs superlattice, some alloy-related depressions still appear for V = +0.706 V, but they disappear for lower values of the applied bias voltage. Given the fact that the alloy-related depressions tend to disappear for voltages at which the C3 state dominates the tunneling current, one might speculate that the local DOS associated with the C3 state is insensitive to local variations in Al-content. Since the lower conduction-band states are unoccupied for positive voltage, we cannot explain the disappearance of the alloy-related minima from electron-electron interaction effects like we have done for the filled states images. The precise mechanism for the disappearance of the alloy-related minima remains at present unclear to us.

Summarizing, the empty-states images of the thick AlGaAs-layer show the conduction-band related surface-DOS. For large voltage the images show the upper part of the surface-DOS (C4 state), and for small voltage the images show the lower part (C3 state). This interpretation is consistent with the observed changes in atomic corrugation. For small voltage, small ridges along [-110] appear in the image. We suspect that the ridges are associated with the bulk states near the bottom of the conduction band. We also suspect that the appearance of the ridges is sensitive to the Al-content of the material. Finally, we observe that the alloy-related minima which are seen in the image at large, positive voltage, tend to disappear for low voltage.

6.5.3 Comparison between filled- and empty-states images of AlGaAs

A common feature of STM-images of $Al_xGa_{(1-x)}As$ (110) obtained at relatively large bias voltage (2.0 V – 2.5 V of either polarity) is that for filled-states images, the alloy-related minima appear between the atomic rows, whereas for the empty-states images, they appear centered on the atomic rows [1,6,30]. In figures 6.2 a,b and 6.3 a,b, the same effect is seen, confirming that our experimental results are consistent with existing literature.

The general trend that the alloy-related minima appear between the atomic [-110]-rows for filled-states images and centered on the [-110]-rows for empty-states images, is by itself not surprizing: The Al atoms in AlGaAs occupy the cation-sites of the crystal lattice, and thus lie centered on the [-110]-rows for positive sample voltage, and between the [-110] rows when a negative sample voltage is applied. However, it is known for Al atoms that only have Ga atoms as next-nearest neighbors, that this trend does not apply [22. The position of the alloy-related minima in STM-images of AlGaAs may for this reason be a more complicated matter than it appears at first sight.

In figure 6.6, it is seen very clearly that the the alloy-related minima in the empty states image and those in the filled states image of the same area do not systematically coincide (figure 6.6 c and d). Instead, their distrubutions appear completely uncorrellated. The same observation is made for the alloy-related maxima in the two images (figure 6.6 e and f). It is also seen that in the filled-states image (figure 6.6 b), the alloy-related minima tend to be elongated and roughly orientated along [001]. Although some of the minima in the empty states image show signs of a similar ordering, the effect is much weaker in the empty states image (figure 6.6 a). It is thus clear that the alloy-related variations in the valence-band related surface-DOS are significantly different from the alloy-related variations in the conduction-band related surface-DOS.

One very interesting point is that some of the features in the filled and empty states images coincide in part: An example is seen in figures 6.6 a,b in the area enclosed by the rectangular box, where an elongated alloy-related minimum in the filled states image coincides in part with a smaller alloy-related minimum in the empty-states image. The area in the empty-states image that corresponds to the total area of the minimum in the filled states image, is seen to consist of a dark portion (lower right) and a portion that is darker than the average colour of the image, but lighter than the first portion (upper left). It is thus clear that the feature consists of two adjacent parts with a different atomic structure: The lower right part of the feature has an atomic structure that strongly suppresses both the valence-band related surface-DOS and the conduction-band related surface-DOS. The upper right part has a different atomic structure, which suppresses the valence-band related surface-DOS, but which suppresses the conduction-band related surface-DOS to a lesser extent, causing the upper left part of the feature to appear less dark in the empty-states image.

One of the main reasons to study a ternary material like $Al_xGa_{(1-x)}As$ is to learn about its atomic structure. For instance, the appearance of elongated dark features that tend to have a preferential orientation in the crystal in filled states images has been reported several times, and is usually attributed to clustering of Al during the epitaxial growth of the AlGaAs-layer [1,3,5,6]. Underlying this interpretation of such elongated features seems to be the assumption that dark patches in the image represent areas with a high local Al-content [3], although in ref. 6 the relation between the atomic structure of the material and the associated surface-DOS is considered in more detail. From ref. 22 it is clear that the presence of Al need not always cause a decrease in the local surface-DOS, even in the relatively simple case of dilute AlGaAs where one may assume that most of the Al-atoms in the top and bottom rows of the surface only have Ga as their next-nearest neighbors. In our own experiments which involve $Al_xGa_{(1-x)}As$ with Al-fractions of 0.20 and 0.33, several different bonding configurations are (about equally) likely to occur. This makes the relation between the atomic structure of the material and the resulting surface-DOS a very complicated one. Although the atomic structure uniquely defines the surface-DOS, the spatial distribution of the conduction-band related surface-DOS is different from the spatial distribution of the valence-band related surface-DOS as our results show. At this point, we have no reason to assume that one of the two types of images (filled or empty states) reflects the atomic structure of the material better than the other. In order to deduce the atomic structure of AlGaAs from a given STM-image, detailed knowledge of the relation between the atomic

structure of the material and the resulting spatial distribution of (the relevant part of) the surface-DOS is needed. Until this relation is known in full, statements about the atomic structure of AlGaAs cannot be made from STM-images without ambiguity.

On the other hand, the information about the (surface) DOS of the material that is shown directly by an STM-image may for many purposes be more useful than a detailed knowledge of the atomic structure itself. For example, the interest in atomic-scale roughness of hetero-structure interfaces originates from the concern that such roughness might influence the performance of semiconductor devices in which such interfaces are used. The physics and performance of such devices are directly related to the (atomic scale) DOS of the materials from which they are made. From this point of view, knowledge of the variations in the local DOS of the material at various energy-intervals seems more important than a precise knowledge of the atomic structure that underlies the observed DOS. To obtain information about the atomic-scale DOS, STM-images can be used directly.

6.6 Discussion on the GaAs/AlGaAs superlattice

In section 6.4, we have shown the electronic structure of a superlattice, and we have reflected on the kind of band bending behaviour that might, generally speaking, be expected for such a structure. Based on section 6.4, we will now discuss the voltage-dependent images of the superlattice that we show in figures 6.7 and 6.8.

6.6.1 Filled-states images

For the filled states images of the superlattice, we expect that the conduction-band states of both the GaAs and AlGaAs layers must have been populated due to accumulation during the entire measurement. The AlGaAs-CBM must have been below the SFL throughout the measurement, which can be seen from the fact that for the entire range of applied bias voltages, the GaAs-layers appear unbroadened. Had the downward band bending of the surface been such that the AlGaAs-CBM was above the SFL and the GaAs-CBM below it, then the electrons would have tunneled from the confined levels in the GaAs-layers. Since the energetic location of the confined levels effectively deterimines the SFL (see figure 6.11), the condition of downward band bending is sufficient to populate the confined levels. The sides of these levels extend into the AlGaAs-barriers. Consequently, if the contribution from the confined levels were to dominate the tunneling current, this would manifest itself as an apparent broadening of the GaAs-layers (see figure 6.8 f,g,h,i). Such broadening is not seen.

Besides, it is questionable whether the confined levels of the quantum-wells can be imaged at negative voltage. Population of only the GaAs conduction-band, if it occurs, is expected to happen only for relatively small negative voltage. In that regime no contribution from the A5-state or BVB-states is expected, so that no state other than the confined states of the quantum wells would contribute to the tunneling current. If the quantum wells are deep, the tails of the confined levels decay rapidly in the AlGaAs-barriers. Since no other state would then be available for the tunneling process, the tip would probably crash when it is over an AlGaAs-layer. If the quantum wells are sufficiently shallow for the superlattice-state to have significant localization in the AlGaAs-barriers as well, the state can be imaged at small negative voltage in filled states. However, this would necessarily involve a superlattice in which the electrons are not confined to two-dimensional motion inside the quantum wells.

At large negative voltage, the atomic rows are along [-110], indicating a strong contribution from the A5-state. The AlGaAs-layers show the same alloy-related features as those observed for the thick AlGaAs-layer, which confirms that the features are indeed associated with the presence of Al. The alloy-related minima appear between the rows, like they also do in the filled-states images of the thick AlGaAs-layer. For smaller voltage the rows are more and more along [001], although the changes in corrugation are difficult to observe due to the tip-instabilities that are apparent in the images. The corrugation-change is accompanied by the appearance of bright and dark areas in the AlGaAs-layers, similar to the bright and dark areas seen on the thick AlGaAs-layer.

The onset of the corrugation-change in the AlGaAs-layers and the appearance of the bright and dark areas lies at V = -1.730 V. Given the fact that the conduction-band states of the AlGaAs-layers must be populated, the VBM of the AlGaAs-layers must lie 1.836 eV or more below the SFL. Consequently, the A5-states of the AlGaAs-surface do not contribute to the tunneling current for V < -1.730 V. At V = -1.667 V and smaller (absolute) voltage, the contribution of the BVB-states of the AlGaAs-layers must have vanished as well since the TFL then lies energetically higher than the AlGaAs-VBM in the bulk. However, the contributions of the A5-state and BVB-states of the GaAs-layers are still available to the tunneling process at these voltages. These contributions manifest themselves in the apparent direction of the atomic rows in the GaAs-layers which is along [-110], and in an enhancement of the contrast in apparent height between the GaAs- and AlGaAs-layers.

At V = -1.550 V and smaller voltages, the inversion of contrast between the GaAs- and AlGaAs-layers sets in. The corrugation in the GaAs-layers also changes, although no complete change in corrugation is observed (figure 6.7h). Since the bulk-VBM of the GaAs-layers lies at 1.504 eV below the SFL, the tunneling current must originate completely from the populated conduction-band states for these small voltages. Given the fact that the GaAs-layers appear unbroadened, the amount of downward TIBB must exceed –0.17 eV, so that for V < -1.59 V, no contribution from the GaAs-A5 state is to be expected. We explain the inversion of contrast from the fact that the (bulk) conduction-band of $Al_xGa_{(1-x)}As$ has a higher 3D-DOS than the conduction-band of GaAs [7] (see also our discussion on the screening behaviour of the superlattice surface). In this regime where the tunneling current originates purely from the conduction-band of the GaAs- and AlGaAs-layers, this apparently causes the AlGaAs to appear brighter than the GaAs.

It appears quite odd that the change in apparent direction of the atomic rows in the GaAs-layers is not complete, even though we expect only the conduction-band related surface states to contribute at low voltage. It is interesting to notice that in the filled states images of n-GaAs (110) (chapter 4), some corrugation in the [001]-direction remains in the images at low voltage as well. This in spite of the fact that for the lowest voltage involved in that measurement, the TFL lies energetically higher than the VBM in the bulk, so that only a contribution from the conduction-band related surface-DOS is possible.

It is possible that the effect is related to the quality of the tunneling tip: It is seen in the other images that there are alternating horizontal bands in the images with two slightly different atomic morphologies. Apparently the tip had a bi-stable configuration during the measurement. We suspect, however, that the observed atomic morphology in the GaAs-layers is influenced by the low-energy shoulder of the C4-state. The C4-state influences the conduction-band related surface-DOS even for energies that lie below the peak position of the lower lying C3-state, as is made clear in chapter 4 (see also section 6.4). At the same time, the conduction-band of the GaAs-layers becomes populated by accumulation up to a higher energy than would be the case for a homogeneous GaAs-surface: The first 0.25 eV of the conduction-band related surface-DOS falls energetically within the superlattice, which does not screen as efficiently as the conduction-band of a homogeneous GaAs-surface.

It is in any case certain that at V = -1.364 V, no contribution from the A5-state of the GaAs-layers is to be expected. Since this voltage is less than the value of the bandgap in GaAs, a contribution from the A5-state to the filled states current at this voltage would require upward band bending. This would depopulate the C3-state, and the resulting dominance of the A5-state should lead to an atomic morphology that is similar to what is observed at high voltage. This is clearly not seen. Besides, a positive amount of TIBB at V = -1.364 V would require a tip work function of about 5.6 eV. For a tungsten STM-tip, such a high work function would be exceptional [11,14].

We thus summarize the interpretation of the filled states images of the GaAs/AlGaAs superlattice as follows: At large negative voltage, the image shows the valence-band related surface-DOS of both the GaAs- and AlGaAs-layers. At smaller negative voltage, we expect for both the GaAs- and AlGaAs-layers that the tunneling current is dominated by the contribution from the accumulated conduction bands. The fact that the GaAs-layers appear unbroadened means that throughout the measurement-series, the CBM of the AlGaAs-layers remained below the SFL. We explain the inversion of contrast between the GaAs- and AlGaAs-layers from the fact that the conduction-band has a larger 3D-DOS in AlGaAs than in GaAs.

6.6.2 Empty-states images

In the empty-states images of the superlattice, several changes occur: At large positive voltage the AlGaAs-layers appear as dark, spotted bands. The alloy-related minima appear centered on the [-110]-rows, in the same way as is observed for the thick AlGaAs-layer. For decreasing voltage, the apparent direction of the atomic rows changes for the AlGaAs-layers from [-110] to [001]. Then follows a regime in which the GaAs-layers appear broadened. The broadening disappears while the apparent direction of the atomic rows in the GaAs-layers changes as well. For very low voltage, the contrast between AlGaAs and GaAs inverts, although the effect is much weaker than it is for the filled states images. The black circles that appear for lower voltage are negatively charged adsorbates [21]. Another type of adsorbate appears in the image at V = +0.803 V, and remains in the two subsequent frames until for V = +0.645 V, it falls outside the frame. At V = + 1.136 V, the bright feature in one of the AlGaAs-layers is interpreted as a dopant. For V < +0.645 V, the bright features in the GaAs-layers are interpreted as dopants as well.

As explained in the discussion on the filled states images of the superlattice, the influence of the confined levels in the GaAs quantum-wells of the superlattice manifests itself as an apparent broadening of the GaAs-layers. The confined level defines the bottom of the lowest miniband of the superlattice. In the plane of the GaAs quantum-wells the electrons are free to move, whereas in the direction perpendicular to the layers, the spatial variation of the DOS is determined by the spatial variation of (the squared amplitude of) the confined level. The GaAs-layers appear broadened because the sides of the confined levels extend into the AlGaAs-barriers, so that inside the AlGaAs-barriers, a finite DOS associated with the superlattice-miniband remains. When the TFL rises energetically above the AlGaAs-CBM, the electron-states associated with a 3D-motion of electrons in the conduction bands of the GaAs- and AlGaAs-layers become available to the tunneling process. The density of these states is much larger than the DOS associated with the superlattice, as is seen in our discussion on the screening behaviour of the superlattice-surface. Therefore, when the TFL rises energetically above the AlGaAs-CBM, the broadening of the GaAs-layers should disappear since the confined levels are no longer the dominant feature in the accessible energetic range of the surface-DOS. This broadening can be seen in the empty-states images for +0.588 V < V < +0.706 V. We can use this effect to draw conclusions about the band bending behaviour of the superlattice-surface as it must have occurred during the measurement: The appearance and disappearance of the broadened GaAs-layers indicate that for +0.706 V < +0.876 V, the TFL passes the AlGaAs-CBM. For + 0.499 V < V < + 0.588, the TFL passes the confined level.

These two conclusions are consistent with the voltage-dependent changes in atomic corrugation on the GaAs- and AlGaAs-layers: The atomic corrugation in the GaAs-layers changes very gradually as the voltage decreases. The direction in which the atomic rows are most apparent changes from [-110] to [001] at around V = +0.588 V. This indicates that for that voltage, the TFL is about 0.15 eV above the GaAs-CBM [11]. The confined level in the GaAs-layers lies at about the same energy in the surface-DOS. It should therefore be expected that the lower end of the voltage-range for which the broadening of the GaAs-layers occurs, coincides with the voltage at which the (most)

apparent direction of the atomic rows in the GaAs-layers, changes from [-110] to [001]. In the range +0.706 V < V < +0.803 V, the upper limit of the voltage-range for which the broadening of the GaAs-layers occurs, indicates that the TFL is near the AlGaAs-CBM (when it faces a GaAs-layer). The TFL must thus be at around 0.25 eV above the GaAs-CBM. For V = +0.706 V, the atomic rows in the GaAs-layers are along [-110]. This is in accordance with the results presented in chapter 4.

A factor that complicates the interpretation is the fact that the GaAs- and AlGaAs-layers have different electron-affinities, which causes the amount of TIBB to fluctuate as the tip alternatingly faces a GaAs- and an AlGaAs-layer. Since the electron-affinity of GaAs is larger than that of AlGaAs [7], the amount of upward band bending is greater for AlGaAs than for GaAs at the same applied bias voltage. This has the following consequence: If the tip faces a GaAs-layer and the amount of TIBB is such that the TFL lies at or slightly above the AlGaAs-CBM, it may happen that the TFL lies below the AlGaAs-CBM when the tip faces the adjacent AlGaAs-layer, due to the difference in the electron-affinities of GaAs and AlGaAs. We thus expect that a voltage-interval exists in which for the GaAs-layers, the conduction-band related surface-DOS lying energetically slightly above the AlGaAs-CBM is imaged, whereas, due to the increased band bending, the tails of the confined levels are imaged when the tip faces an AlGaAs-layer.

In the range +0.760 V < V < +0.803 V, the GaAs-layers do not appear broadened, but the interfaces between GaAs and AlGaAs appear fuzzy. This may be due to the effect we just described. It may also simply be a feature that is associated with the surface-DOS at that energy. In any case, for V > +0.876 V, the interfaces between the GaAs- and AlGaAs-layers appear sharp, which suggests that the confined levels in the GaAs-layers no longer influence the topography of the images. This means that for these voltages, the TFL lies energetically above the CBM of the AlGaAs-layers, both when it faces a GaAs-layer and when it faces an AlGaAs-layer.

Notice that in the AlGaAs-layers, the change in corrugation appears to take place in the range +0.706 V < V < +0.876 V. We expect the corrugation-change to occur when the TFL lines up with the lower part of the conduction-band related surface-DOS, in analogy with our observations for n-GaAs (110) [11]. This is consistent with our expectation that at similar voltages (+0.706 < V < +0.803 V), the TFL passes the AlGaAs-CBM when the tip is over an AlGaAs-layer.

We thus expect the following band bending behaviour for the empty-states images of the GaAs/AlGaAs superlattice: For large voltage, the TFL lies energetically above the CBM of the GaAs- and AlGaAs-layers. At lower voltage, possibly in the range +0.760 V < V < +0.803 V, a voltage-interval may exist for which the TFL is above the AlGaAs-CBM when the tip faces a GaAs-layer and below it when it faces an AlGaAs-layer. When the voltage is decreased further (+0.588 V < V < +0.706 V), the tip lies between the GaAs-CBM and the AlGaAs-CBM for all locations on the surface, and the confined levels in the GaAs quantum-wells are imaged. For V < +0.499, we expect that the TFL lies energetically below the CBM of the GaAs- and AlGaAs-layers. The electrons then tunnel from the tip, through a surface depletion zone, into the bulk states near the bottom of the conduction-band (BCB-states) for both types of layers. This is analogous to what happens for a homogeneous surface in type I depletion [11].

Based on the preceeding arguments, it is clear that the inversion of contrast between GaAs and AlGaAs occurs when the electrons tunnel from the tip to the BCB-states for both the GaAs- and AlGaAs-layers. In this regime, we expect that the atomic corrugation is caused by electrons tunneling resonantly through the low-energy shoulder of the C3-state which extends into the bandgap [11,12,13]. Since the 3D-DOS of the AlGaAs conduction-band is larger than the 3D-DOS of the GaAs conduction-band [7], we suspect that this difference causes the inversion of contrast at low voltage between the GaAs- and AlGaAs-layers. From ref. 11 it is clear that when electrons tunnel into the BCB-states of an n-type surface in type I depletion, this involves a short tip-sample distance. We expect a similar band bending situation for the superlattice-surface in the voltage-range in which the inversion of contrast occurs. At the same time, the image that shows the inversion of contrast most clearly (V = 0.310 V), ended with a crash of the STM-tip. In view of the expected band bending situation and short tip-sample distance, this is no surprise.

A last point to make about the empty-states images of the superlattice is a comparison between the images taken at large voltage, and the ones showing the broadening of the GaAs-layers. Although the relation between the atomic structure of $Al_xGa_{(1-x)}As$ and the resulting surface-DOS is not fully clear, the presence or absence of Al can be recognized from the presence or absence of alloy-related variations in the surface-DOS at large voltage of either polarity. This local presence or absence of Al is also the factor that determines the local value of the bandgap of the surface. These variations in the local bandgap form the potential-landscape that is characteristic of a superlattice, and give rise to the confined levels in the GaAs-layers. At the same time, the images at a lower voltage reflect the spatial distribution of the confined levels themselves. In the images taken at intermediate voltage, the spatial distribution of the confined levels appears very smooth. This might suggest that the atomic-scale roughness of a GaAs/AlGaAs interface need not influence the spatial distribution or energetic location of the confined levels very strongly, provided that the roughness of the interface does not exceed one or two atomic layers. From a more educational point of view, the images taken at large voltage may be said to reflect the spatial variation of the potential, whereas the images showing the broadening of the GaAs-layers reflect the spatial variation of the corresponding solution of the Schrödinger equation.

6.6 Summary, conclusions, outlook

We have presented voltage-dependent images of a thick $Al_{0.2}Ga_{0.8}As$-layer and of a $GaAs/Al_{0.33}Ga_{0.67}As$ superlattice. These images show both the filled and empty states of the surfaces. The voltage-dependent images of the thick AlGaAs-layer show a change in atomic corrugation similar to the one that has been reported previously for n-GaAs [8,11]. At the same time, bright and dark areas appear at low negative voltage which we explain in terms of fluctuations in the electron-density of the surface-accumulation layer. In the empty states images, small ridges along [-110] appear at low voltage. From

the anisotropic band-structure near the bottom of the bulk conduction-band we speculate that the appearance of the ridges is connected with the bulk states lying at the CBM near the X'-point of the surface Brioullin zone. Furthermore, it is shown that the alloy-related features in a filled-states image and an empty-states image of the same patch of AlGaAs, do not coincide. This means that the relation between the atomic structure of the material and the resulting surface-DOS has to be understood in more detail than is now the case. Until this relation is understood in full, no unambiguous conclusions about the atomic structure of $Al_xGa_{(1-x)}As$ can be drawn from atomically resolved STM-images.

The voltage-dependent images of the superlattice show that for both polarities of the sample voltage, the change in atomic corrugation occurs at larger absolute bias voltage for AlgaAs than for GaAs. At the same time, an inversion of contrast between the GaAs- and AlGaAs-layers is observed at low voltage of either polarity, although the effect is strongest in the filled states images. For the empty-states imaging mode, the inversion of contrast apparently is accompanied by a small tip-sample distance. We attribute the inversion to the fact that the 3D-DOS of the (bulk) conduction band of AlGaAs is greater than that of GaAs. Finally, an apparent broadening of the GaAs-layers shows the spatial extent of the confined levels inside the GaAs-layers of the superlattice.

Looking ahead, it is clear that the relation between the atomic-scale structure of $Al_xGa_{(1-x)}As$ and the resulting surface-DOS has to be investigated further: Filled states images of $Al_xGa_{(1-x)}As$ usually suggest very strongly that clustering of Al takes place during the epitaxial growth of the material. However, the same is not so evident from the empty-states images. For a binary III-V semiconductor (110)-surface, the relation between the atomic structure and resulting surface-DOS is well understood. Since both reflect the same periodicity, the distinction between the two may even seem trivial at times. For $Al_xGa_{(1-x)}As$ (110), this is clearly not the case. The detailed investigation of the relation between the atomic structure of $Al_xGa_{(1-x)}As$ and the resulting surface-DOS of the (110)-surface represents an interesting basis for future work, mainly in the theoretical field.

At the same time, we are convinced that the images in this paper demonstrate very clearly the potential and usefulness of voltage-dependent imaging. A series of voltage-dependent images of the same area essentially combines spectroscopic information with atomic lateral resolution, and that is the main reason why voltage-dependent images are as informative as they are. In this way, a voltage-dependent series of images can characterize a given material or heterostructure in many more ways than a series of images taken at only a single voltage. Another point, although perhaps more educational than scientific, is that the voltage-dependent changes illustrate very beautifully the basic physical principle behind the STM.

REFERENCES

1: H.W.M. Salemink, M.B. Johnson, O. Albrektsen: *Cross-sectional scanning tunneling microscopy on heterostructures: Atomic resolution, composition fluctuations and doping*. Journ. of Vac. Sci. & Tech. B12, No. 1, pp. 362 – 368 (1994).

2: R.M. Feenstra, D.A. Collins, D.Z.Y. Ting, T.C. McGill: *Scanning Tunneling Microscopy of InAs/GaSb superlattices: Subbands, Interface roughness, and interface asymmetry*. Journ. of Vac. Sci. & Tech. B12, No. 4, pp. 2592 – 2597 (1994).

3: M.B. Johnson, U. Maier, H.W.M. Salemink: *Atomic-scale view of AlGaAs/GaAs heterostructures with cross-sectional scanning tunneling microscopy*. Appl. Phys. Lett, Vol. 63, No. 9, pp. 1273 – 1275 (1993).

4: A.R. Smith, K.J. Chao, C.K. Shih, Y.C. Shih, B.G. Streetman: *Cross-sectional scanning tunneling microscopy study of GaAs/AlAs short period superlattices: The influence of growth interrupt on interfacial structure*. Appl. Phys. Lett, Vol. 66, No. 4, pp. 478 – 480 (1995).

5: R.M. Feenstra: *Cross-sectional scanning tunneling microscopy of III-V semiconductor structures* (Review article). Semiconductor Sci. & Tech, Vol .9, pp. 2157 – 2168 (1994).

6: A.J. Heinrich: *Ordering in Ternary compound Semiconductors on the atomic scale*. Phd-thesis by A.J. Heinrich, Cuvillier Verlag, Göttingen, Germany (1998). See also: Appl. Phys. A, Vol. 66, pp. S959 – S962 (1998).

7: E.F. Schubert: *Doping in III-V semiconcductors*. Cambridge University Press, Cambridge, p. 542 (1993).

8: Ph. Ebert, B. Engels, P. Richard, K. Schroeder, S. Blügel, C. Domke, M. Heinrich, K. Urban: *Contribution of surface resonances to Scanning Tunneling Microscopy images: (110) surfaces of III-V semiconductors*. Phys. Rev. Lett, Vol. 77, No. 14, pp. 2997-3000 (1996).

9: C.S. Jiang,T. Nakayama, M. Aono: *Tip-induced occupation of an unoccupied surface state in Scanning Tunneling Microscopy imaging of a GaAs (110) surface with Ag clusters*. Japn. Journal of Appl. Phys, Vol. 36, pp. L1336-L1339 (1997).

10: B. Engels, P. Richard, K. Schroeder, S. Blügel, Ph. Ebert, K. Urban: *Comparison between ab initio theory and Scanning Tunneling Microscopy for (110)-surfaces of III-V semiconductors*. Phys. Rev. B, Vol. 58, No. 12, pp. 7799 – 7814 (1998).

11: G.J. de Raad, D.M. Bruls, P.M. Koenraad, J.H. Wolter: *Interplay between tip-induced band bending and voltage-dependent surface-corrugation on GaAs (110) surfaces* (to be published). See also chapter 4 of this thesis.

12: J.R. Chelikowski, M.L. Cohen: *Self-consistent pseudopotential calculation for the relaxed (110) surface of GaAs*. Phys. Rev. B, Vol. 20, pp. 4150-4159 (1979).

13: J.R. Chelikowski, S.G. Louie, M.L. Cohen: *Relaxation effects on the (110) surface of GaAs*. Phys. Rev. B, Vol. 14, No. 10, pp. 4724 - 4726 (1976).

14: G.J. de Raad, P.M. Koenraad, J.H. Wolter: *The use of the Schiller-decapitation process for the manufacture of high-quality tungsten STM-tips*. Journal of Vac. Sci. & Tech.-B, Vol. 17, No. 5, pp. 1946 – 1953 (1999).

15: M. Guzzi, J.L. Staehli: *Band structure of the GaAs/AlAs solid solutions,* in Physics of DX centres in GaAs Alloys, ed. J.C. Bourgoin, Sci-Tech pubications, Brookfield VT, USA and Vaduz, Lichtenstein (1990). See p. 29.

16: I.M. Tsidilkovski: *Band structure of semiconductors*. Pergamon Press, Oxford (1982). See p. 131.

17: R.E. Allen, H.P. Hjalmarson, J.D. Dow: *Surface electronic states in* $GaAs_{(1-x)}P_x$. Surf. Sci. Lett, Vol. 110, pp. L625 – L629 (1981).

18: D. Straub, M. Skibowski, F.J. Himpsel: *Unoccupied surface state and conduction band critical points of GaP (110): A high-resolution photoemission study*. Journ. of Vac. Sci. and Tech. – A, Vol. 3, pp. 1484 – 1486 (1985).

19: F. Manghi, C.M. Bertoni, C. Calandra, E. Molinari: *Theoretical study of the electronic structure of GaP (110)*. Phys. Rev. B, Vol. 24, No. 10, pp. 6029 – 6042 (1981).

20: C.M. Bertoni, O. Bisi, F. Manghi: *Surface bands in relaxed surface of GaP*. Journal of Vac. Sci. and Tech, Vol. 15, No. 4, pp. 1256 – 1261 (1978).

21: J.A. Stroscio, R.M. Feenstra, A.P. Fein: *Local state density and long-range screening of adsorbed oxygen atoms on the GaAs (110) surface.* Phys. Rev. Lett, Vol. 58, No. 16, pp. 1668 – 1671 (1987).

22: A.R. Smith, K.J. Chao, C.K. Shih: *Identification of first and second layer aluminum atoms in dilute AlGaAs using cross-sectional STM.* Appl. Phys. Lett, Vol. 69, No. 9, ppl 1214 – 1216 (1996).

23: R.M. Feenstra, J.A. Stroscio: *Tunneling Spectroscopy of the GaAs (110) surface.* JVST-B, Vol. 5, No. 4, page 923 (1987).

24: A.C.A.S. Grossi, J.L.A. Alves, A.C. Ferraz: *Band structure and surface geometry of AlAs (110)*, in Proceedings of the 5th Brazilian school of semiconductor physics, pp. 326 - 330. Ed: J.R. Leite *et al.* World Scientific, Singapore, 1992.

25: C. Weisbuch, B. Vinter: *Quantum semiconductor structures: Fundamentals and applications.* Academic Press, London, 1991. In this reference, the "Coulomb interaction" is named the "Hartree potential".

26: H. Eisele, O. Flebbe, T. Kalka, M. Dähne-Prietsch: *Cross-sectional STM-study of InAs quantum dots for layer devices.* Surface and Interface Analysis, Vol. 27, pp. 537 – 541 (1999). Also: D.M. Bruls, Technical Univ. of Eindhoven: To be published.

27: H.P. Myers: *Introductory Solid State Physics.* Taylor and Francis, London, 1990.

28: J.F. Zheng, X. Liu, E.R. Weber, D.F. Ogletree, M. Salmeron: *Si donors (Si_{Ga}) observed by Scanning Tunneling Microscopy.* Journal of Vac. Sci. and Tech. B, Vol. , pp. 2104 – 2106 (1994).

29: M.A. Rosentreter: *Rastertunnelmikroskopie auf der GaAs (110)-Oberfläche bei Temperaturen von 8 K – 300 K.* Phd-thesis by M.A Rosentreter, Cuvillier Verlag, Göttingen, Germany (1997).

30: O. Albrektsen, H.P. Meier, D.J. Ahrent, H.W.M. Salemink: *Terracing and step bunching in interfaces of molecular beam epitaxy-grown (Al)GaAs multilayers.* Appl. Phys. Lett, Vol. 62, Iss. 17, pp. 2105 – 2107 (1993).

31: C.J. Chen: *Introduction to Scanning Tunneling Microscopy.* Oxford University Press, New York, 1993.

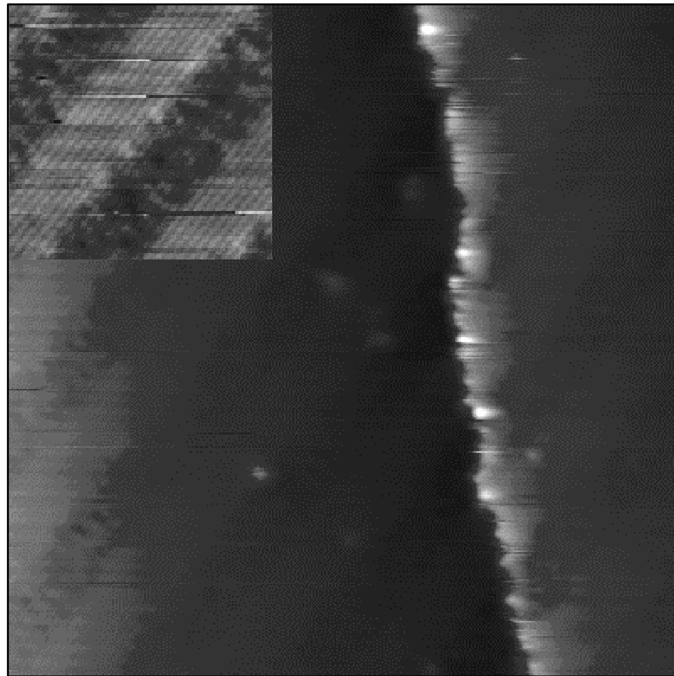

The GaAs / AlGaAs superlattice discussed in chapter 6 once more (filled states, frame size 50 x 50 nm). This image very clearly demonstrates the necessity of a smooth sample surface morphology. The difference in apparent height associated with the mono-atomic step is about 200 pm. The difference in apparent height between the GaAs and AlGaAs layers is in the order of 20 pm. The inset is a cut-out of the frame showing part of the lower terrace.

CHAPTER 7:

NANO-SCALE CHARACTERIZATION OF Si δ-DOPED LAYERS IN GaAs

7.1 Introduction

This last chapter deals with the spatial distribution of Si-dopants (n-type) making up delta-doped layers (δ-layers) in GaAs. Silicon atoms incorporate mainly on the Ga-sites of the GaAs-lattice, forming donors (Si_{Ga}) [1 (page 193)]. A small fraction of the Si atoms can also incorporate on an As-site, forming acceptors (Si_{As}) [1 (p. 193)]. Delta-doped layers are commonly prepared by interrupting the epitaxial growth of the host material. Then, the growth surface is exposed to a flux of dopant atoms for some time (typically tens of seconds), after which the epitaxial growth of the host material is resumed. When the growth temperature is chosen appropriately (T < 550 ^{o}C for Si in GaAs [2]), redistribution of impurities during the growth of the cap layer is minimal, and very narrow doping profiles (20 - 40 Å) can be achieved [2,27]. In the ideal δ-layer, all dopants lie in the same atomic plane (see figure 7.1).

Delta-doped layers can be used in a variety of electronic and optical semicondcutor devices, as is made clear in ref. 1. In a Field-Effect Transistor (FET), a δ-doped layer can serve as the conductive path between the source and drain (the "channel") which improves the electrical performance of such a FET with respect to a conventional FET with a homogeneously doped channel [1 (p. 467)]. Delta-doped layers can also be used to minimize the contact resistance in metal-semiconductor contacts [1 (p. 463)]. Finally, a structure of alternating p- and n-type δ-layers, or *doping superlattice*, has been used in the active region of Light-Emitting Diodes (LED) or LASERs [1 (p. 471)].

One remaining question about δ-layers in general is whether the dopants are distributed randomly within the dopant plane, or whether some type of ordering of dopants takes place. For Be δ-doped layers in GaAs, it has been shown by Johnson *et al.* [3] that considerable broadening of δ-layers can occur. The broadening is thought to be the result of drift of the impurities caused by the mutual Coulombic repulsion of the ionized dopants, after incorporation in the crystal. The spatial distribution of the dopants within the dopant plane was also deterimined in that article, using cross-sectional STM. These measurements suggest that inside the dopant plane, a minimum-distance between any two given Be atoms exists due to the mutual Coulombic repulsion between the ionized dopant atoms.

Similar broadening of δ-doped layers is also reported by Schubert *et al.* [17]. These results indicate that a maximum local concentration of Be in GaAs exists of about 10^{20} cm^{-3}. More recently, the diffusion-behaviour of Si atoms in a Si δ-doped layer in GaAs has been simulated by Averkiev *et al.* using Monte Carlo simulation [18]. In that paper it is shown that Coulombic repulsion between ionized dopants during growth can lead to a non-Gaussian dopant density profile when the surface-density of dopants

exceeds about 1.6 * 10^{13} cm^{-2}. It is thus clear from existing literature that Coulombic repulsion between dopants during growth of the cap layer can have a strong influence on the spatial distribution of dopants in a δ-doped layer. This influence can induce a short-range order in the (in-plane) distribution of dopant atoms in epitaxially grown δ-doped layers.

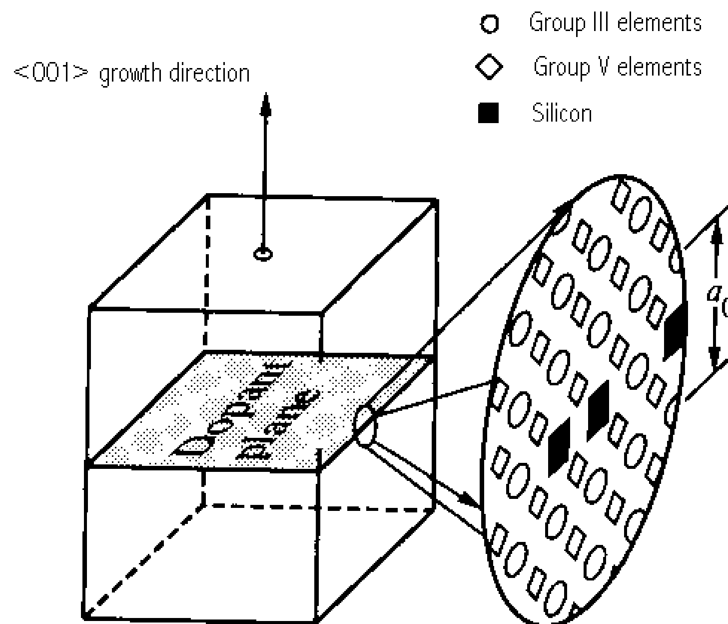

Fig. 7.1: *Schematic representation of a Si delta-doped layer (δ-doped layer) in a III-V semiconductor. In cross-sectional STM, the edge of the δ-doped layer is seen (see figure 7.3c). Taken from ref. 1, page 435.*

Delta-doped layers have interesting electronic properties: It has been shown that the 2D-mobility of electrons in an n-type δ-layer exceeds the 3D-mobility of electrons in a homogeneously doped n-type semiconductor [4]. This “mobility enhancement” is reported to occur at room temperature, and is also reported to increase with increasing carrier concentration. The mobility enhancement is attributed to three possible causes: The high degeneracy of the Fermi gas formed by the electrons; spatial donor-electron

separation in the odd-numbered subbands which have a node in the dopant plane; and screening of the impurity charges [4]. At low temperature (T < 100 K) the dominant mechanism that determines the electron-mobility in a δ-doped layer is ionized impurity scattering [13]. It has been shown by Levi *et al.* [14] that ionized impurity scattering is greatly reduced when the spatial distribution of the dopant atoms within a δ-doped layer is (partially) ordered. The same point is explained in detail by Headrick *et al.* [15]. Thus, an ordered in-plane distribution of dopants in a δ-layer is expected to enhance the mobility of electrons in that δ-layer, particularly at low temperature.

The focus of this chapter will be on the accurate determination of the spatial distribution of Si dopants in a δ-doped layer, using cross-sectional STM. All experimental results shown in this chapter involve n-type material. The emphasis in this thesis lies on the voltage-dependent effects described in chapters 4, 5 and 6. As a result, the scope and depth of the study presented in this chapter has been limited by the time available for it.

The outline of the rest of this chapter is as follows: In section 7.2 we discuss the identification of dopants from other nano-scale features in a given STM-image (see figure 7.3). This is a non-trivial matter, since Si donor atoms that lie in the surface layer of the crystal can have an appearance in STM that is similar to the morpology of certain other defects, like negatively charged adsorbates [5,6]. Subsurface Si donor atoms, on the other hand, can be identified in the images without ambiguity.

Section 7.3 describes the sample containing the δ-doped layers that we used in the experiments (see figure 7.4). In section 7.4, we will present high-resolution STM-images of Si-δ-doped layers in GaAs and discuss the kinds of features that are present in these layers (see figure 7.5). The identification of some of the features reported in section 7.4 is based on the discussion presented in section 7.2.

In section 7.5, the in-plane spatial distribution of Si dopant atoms in a δ-doped layer in GaAs is investigated (see figure 7.6). The analysis is analogous to the one used by Johnson *et al.* [3], and is based on the positions of the subsurface Si donor atoms in several large-scale images of the same δ-doped layer (see figure 7.4 c). It is shown that there is an apparent minimum distance of 2 nm between any two given dopants in the images. This may indicate that short-range ordering of dopants has occurred during the epitial growth of the δ-layers. The apparent minimum distance may, however, also be an artefact caused by the fact that two very closely separated dopant atoms cannot be resolved very clearly by STM (see figure 7.7). In section 7.6, the experimental results of section 7.5 are discussed.

7.2 Identification of dopants in filled-states STM-images of n-GaAs

As figures 7.2a and 7.3a show, a typical filled-states STM-image of Si-doped GaAs-(110) shows two types of features: Bright hillocks and bright features that are surrounded by a dark ring, to which we refer as “rosettes”. We identify the bright hillocks as subsurface Si_{Ga} donor atoms based on exisiting literature [6 (p. 226), 8, 10]. A rosette, on the other hand, can represent one of several defects. It can represent a surface-layer Si_{Ga} donor atom [5, 6 (p. 233)], or any type of negatively charged defect like a Si_{As} acceptor [26], an adsorbed oxygen atom [7], or a surface vacancy [6 (p. 163, p. 165)]. In this section, we will discuss the identification of Si-dopants in filled-states STM-images of n-type GaAs (110). The focus will be on how to distinguish rosettes representing a surface-layer Si_{Ga} donor atom from the other rosettes that represent other defects.

Dopants are reported to manifest themselves as bright hillocks of about 2 nm in diameter in the STM-image [5,6,8,9,10]. The bright contrast of dopants in STM-images has been explained from the fact that the presence of such a subsurface dopant locally increases the surface-DOS [10]. In an alternative model proposed by Zheng *et al.* the bright contrast of a dopant in an STM-image is explaned from the dopant’s influence on the local amount of Tip-Induced Band Bending (TIBB): A dopant has an electric charge associated with it [31], which locally changes the amount of TIBB. In ref. 8, the apparent height of a dopant in an STM-image can be up to 1 nm. In our experiments which involve smaller tunneling currents, the apparent height of a dopant can be up to about 100 pm with respect to the surrounding lattice. The dopant-height thus depends on the imaging-conditions, and also gradually decreases for dopants that lie deeper inside the crystal surface [8, 10]. From section 7.5, we expect to see dopants that lie up to 2 nm below the sample surface (see also ref. 10). The spatial extent of the feature that represents a dopant in STM varies with the spatial extent of the screened Coulomb potential that is associated with a dopant lying near the surface [6 (p. 230), 8, 25].

It has been shown recently that surface-layer Si-donors can have an oscillating contrast, consisting of a bright central part surrounded by a dark ring [5,6] (see figure 7.2 and 7.3 c). For n-type material, the oscillating contrast only occurs in the filled-states imaging mode: For the empty-states imaging mode, the dopant appears as a bright hillock without the surrounding depression. The depth of the dark ring which is seen in the filled states images is found to be highly dependent on the value of the applied bias voltage [5,6]. It is therefore expected to be highly dependent on the tip-DOS of the tunneling tip that is used during the experiment. The authors of ref. 6 also show that apart from the long-range signature (~ 1 nm or more) of a dopant, the “defect state” associated with a dopant can give rise to a feature in the STM-image that only extends over the nearest surface unit cells [6 (p. 203)] (see figures 7.2 b and 7.5 c, e). The exact morphology of such a defect-state depends critically on the location of the dopant (surface layer, the second subsurface layer, the third layer, etc). Si_{Ga} donor atoms that lie deeper below the surface show this oscillating contrast only very weakly or not at all. Those Si_{Ga} donors that do not show this oscillating contrast appear as bright hillocks instead [6 (p. 226)].

This oscillating contrast occurs at room temperature and is not to be confused with the Friedel oscillations around dopants that have been observed at low temperature [16]. Moreover, it is directly related to the charge-state of the defect: In simulations, the assumption that the defect has a positive (negative) charge-state is sufficient to reproduce the oscillating contrast for filled-states imaging of n-material and the enhancement (suppression) of the tunneling current the empty-states case [6 (p. 233)].

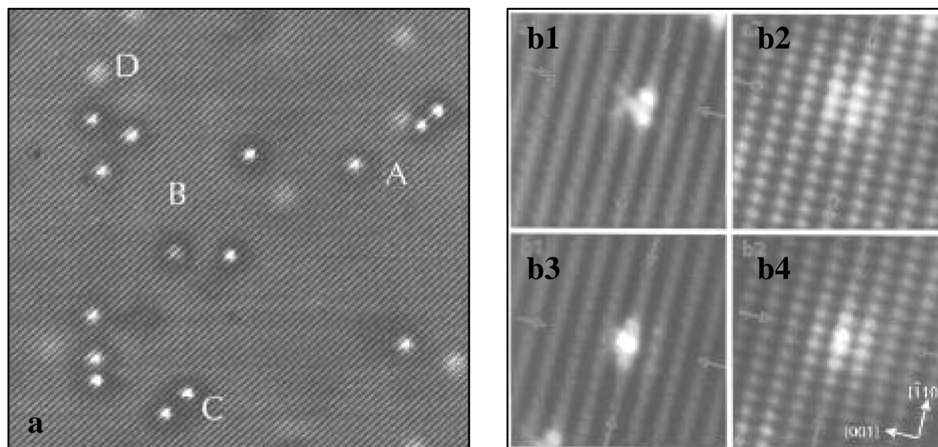

Fig. 7.2 a: *Filled-states STM-image of n-type GaAs (taken from ref. 6, page 226). The author of ref. 6 identifies the features marked A as surface-layer Si_{Ga} donors and the features marked D as subsurface layer donors. The features marked B and C are identified as Si_{As} acceptors and Ga vacancies, respectively. The image is obtained at V = -2.4 V.* **b:** *Si_{Ga} donor atom in the surface layer (b1 and b2) and in the first subsurface layer (b3 and b4). Frames b1 and b3 were obtained at sample voltage of –1.8 V, frames b2 and b4 at V = +1.6 V. Frames b1 and b3 clearly show the defect-state associated with a surface-layer Si_{Ga}-donor (b1) and a first subsurface layer Si_{Ga} donor (b3), respectively (taken from ref. 6, page 203).*

The fact that a surface-layer donor appears as a protrusion surrounded by a dark ring (a “rosette”) complicates the interpretation of STM-images showing Si dopants in GaAs, because apart from the surface-layer donor, there are several other defects that also appear as a rosette. Two such defects are the Si acceptor (Si_{As}) [6 (p. 228)] and the adsorbed oxygen atom [7]. It is shown in ref. 6 (p. 233) that the oscillating contrast associated with a rosette can be explaned from the charge-state of these defects and the resulting screening effects. This charge-state is positive for the surface-layer donor [31], and negative for the Si_{As} acceptor and the adsorbed oxygen atom [7].

In empty-states images, neither the (positively charged) surface layer Si_{Ga} donor nor the negatively charged defects appear as rosettes: Instead, the surface-layer Si_{Ga} donor appears as a bright hillock without a surrounding depression, whereas the

negatively charged defects (Si_{As} and adsorbed oxygen) appear as a depression [6,7]. The most straightforward way to discriminate between surface-layer dopants and negatively charged defects is therefore to image the structure in empty-states mode, or in "dual mode" (see chapter 2) with two voltages of opposite polarity: In the empty-states imaging mode, the Si_{Ga} donors are bright and the negatively charged defects like adsorbed oxygen atoms or Si_{As} acceptors, are dark.

The identification of surface-donors in existing STM-images, however, can be problematic if these have been aquired (only) in the filled-states mode. For many of the STM-images presented in this chapter, this is the case. Surface donor atoms and negatively charged defects both appear as rosettes in this imaging mode, making discriminating between surface-layer Si donors and negatively charged defects a non-trivial matter. As the rest of this section will show, it is possible to obtain information about a rosette in a given filled-states image, from its atomic-scale morphology. We will show that in filled-states images, there are two types of rosette: one type of rosette has a local change in atomic corrugation in the area that makes up the dark ring (see figure 4.11 b for an example), whereas the other type does not have such a local corrugation-change. We will also show that this difference can in principle be used to distinguish surface-layer Si_{Ga} donors from negatively charged defects. However, this identification-method is complicated by the fact that the atomic-scale morphology of a rosette also depends on the DOS of the tip used in the experiment. Based on figure 7.3, we will now discuss the possibilities and limitations of identifying rosettes from their atomic-scale morphology in the filled-states imaging-mode. Later in section 7.4, we will apply this identification method to the rosettes that are observed in the filled-states STM-images of a Si δ-doped layer in GaAs.

Figure 7.3 *(next page)* **a:** *Filled-states image of bulk doped n-GaAs (Si: 10^{18} cm^{-3}) at T=300 K. V = -1.861 V, I = 122 pA, frame size: 50 x 50 nm, grey scale: 0 – 50 pm.* **b:** *Same area as (a) imaged in empty-states. V = + 1.037 V, I = 85 pA, grey scale: 0 – 85 pm.* **c:** *Rosette and bright hillock. We interprete the rosette as a surface-layer donor. The hillock is identified as a subsurface donor. Frame size: 12.1 x 12.1 nm. grey scales: c1: 0 – 53 pm; c2: 0 – 43 pm.* **d:** *Rosette showing local corrugation-change. Frame size: 8.3 x 8.3 nm. Notice the change in tip-DOS in the upper part of the image. The slow scan direction is from bottom to top. Grey scales: d1: 0 – 41 pm; d2: 0 – 64 pm.* **e:** *Same area as in (d) after the tip-change. The bottom left rosette is also shown in (d). Notice that the local corrugation-change is now absent. Frame size: 14.0 x 12.0 nm. Grey scales: e1: 0 – 69 pm; e2: 0 – 79 pm. Frames c,d,e are cut-outs from 25 x 25 nm frames showing different types of features, obtained at V = -2.154 V, I = 122 pA (c1, d1, e1) and +1.037 V, 85 pA (c2, d2, e2).* **c3, d3, e3:** *As c1, d1, e1, after application of a high-pass fast Fourier transform filter (FFT) to show details of the atomic lattice in all areas of the frames.*

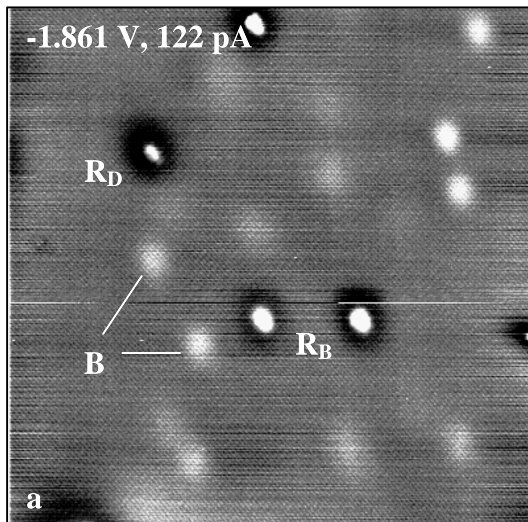
-1.861 V, 122 pA
R_D
B
R_B
a

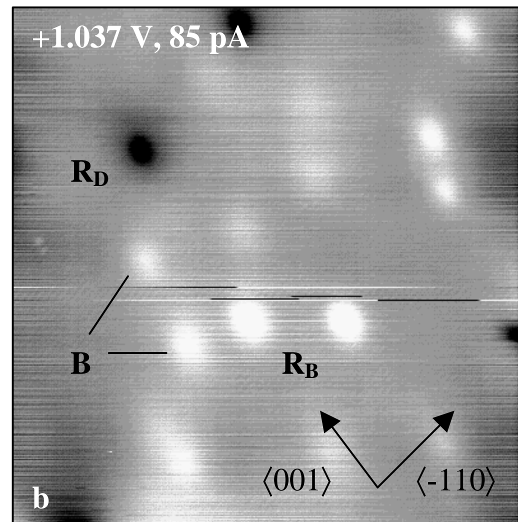
+1.037 V, 85 pA
R_D
B
R_B
⟨001⟩
⟨-110⟩
b

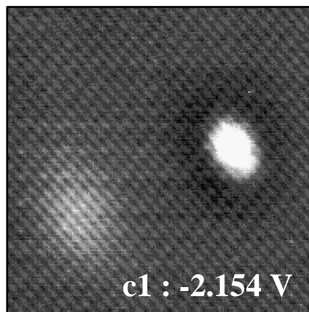
c1 : -2.154 V

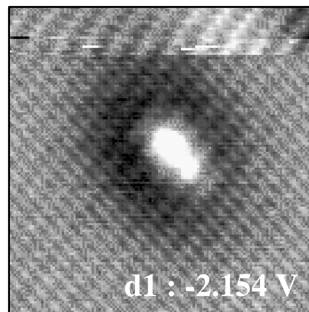
d1 : -2.154 V

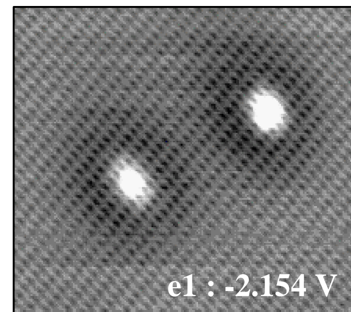
e1 : -2.154 V

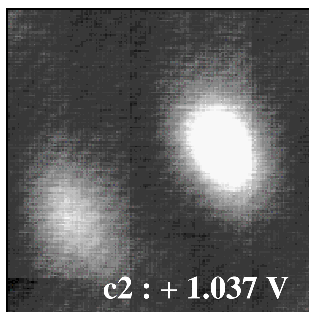
c2 : + 1.037 V

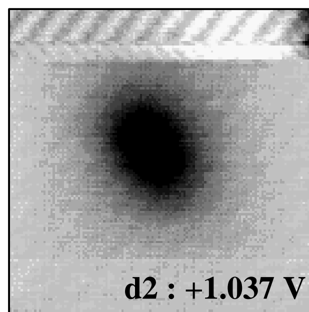
d2 : +1.037 V

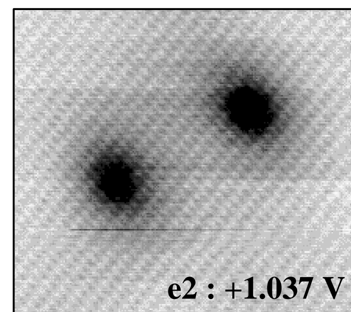
e2 : +1.037 V

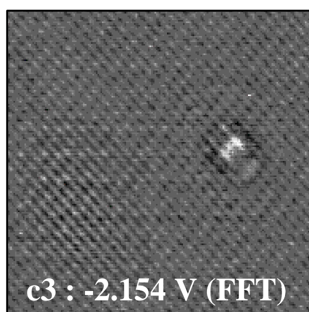
c3 : -2.154 V (FFT)

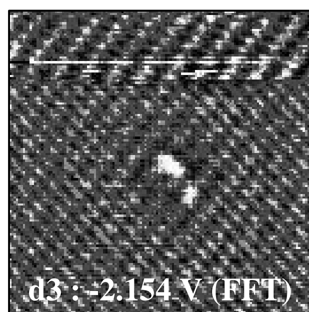
d3 : -2.154 V (FFT)

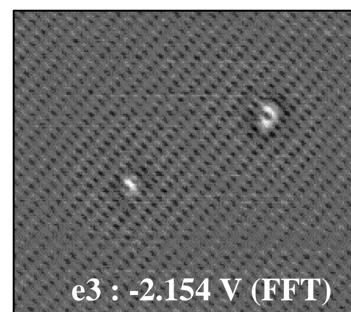
e3 : -2.154 V (FFT)

Figure 7.3 shows STM-images of a Si-doped GaAs-substrate of a nominal doping concentration of 10^{18} cm^{-3}. In the two large-scale images (figure 7.3 a and b) bright hillocks are seen (B). These hillocks appear as bright protrusions in the filled-states image (a), and are also bright in the empty-states image (b). According to refs. 5 and 6, this identifies the hillocks as subsurface Si_{Ga} donors [5, 6 (p. 226)]. Moreover, the subsurface Si_{Ga} donor is the only defect reported to manifest itself as a bright feature without oscillating contrast in both filled and empty states images [6 (p. 226)]. This is in contrast to the rosettes, where a given rosette can represent one of several defects [5,6,7]. In figure 7.3 a, we observe 12 bright hillocks on a sample area of 50 x 50 nm^2. If we assume that we can observe dopants that lie up to 2 nm below the sample surface (see section 7.5), this areal density of bright hillocks translates to a Si dopant density of 2.4 * 10^{18} cm^{-3}. This is consistent with the nominal doping concentration of the n-doped GaAs substrate used in this experiment. Furthermore, the Si δ-doped layers that are investigated in this chapter consist mainly of bright hillocks (see figure 7.4 c,d and figure 7.5). In Si δ-doped layers of a nominal areal density of less than 10^{13} cm^{-2}, Si incorporates mainly as a Si_{Ga} donor [1 (p. 459)]. Therefore, the occurrence of the bright hillocks must be related to the presence of Si_{Ga} donors in the GaAs host crystal

It should be kept in mind that the bright hillock which represents a subsurface layer Si_{Ga} donor is the signature of the screened Coulomb-potential that is associated with the dopant. Therefore, any subsurface defect that has a charge-state of +1 *e* (with *e* the elementary charge) will show up as a bright hillock which is in all aspects similar to the bright hillock that represents a subsurface Si_{Ga} donor. Fortunately, however, most types of defects that are commonly encountered on the (110)-surface of Si-doped GaAs do not have a positive charge-state: Ga surface vacancies (V_{Ga}) and As surface vacancies (V_{As}) are negatively charged [6 (p. 163, p. 165)], Si_{As} acceptors [5, 6 (p. 228), 26] and adsorbed oxygen atoms [7] are negatively charged as well, and Si_{Ga}-V_{Ga} complexes as well as Si clusters are neutral [28]. We therefore make the assumption that any defect with an apparently positive charge-state is in fact a Si_{Ga} donor atom.

Two types of rosette can be seen in figures 7.3 a and b: There are rosettes that become bright protrusions in the corresponding empty states image (R_B), and rosettes that turn into depressions (R_D). We identify the rosettes that remain bright in the empty states image (R_B) as surface-layer donors (Si_{Ga}) [6 (p. 227, p. 233), 31]: In ref. 6 (p. 229), only surface-layer Si_{Ga}-impurities are reported to manifest themselves as rosettes which remain bright in the corresponding empty-states image (R_B), although in principle, any type of positively charged defect might be expected to appear as an R_B-type rosette [6 (p. 233)]. We observe two R_B-rosettes in figure 7.3 a and b, which represents a sample area of 50 x 50 nm. When these rosettes are assumed to represent surface-layer Si_{Ga} impurities, this areal density of R_B rosettes would translate to a bulk Si-concentration in the crystal of 4 * 10^{18} cm^{-3}. That is roughly consistent with the nominal doping concentration of the crystal which is 1 * 10^{18} cm^{-3}.

Figures 7.3 c1 and 7.3 c3 show the atomic lattice of one such R_B rosette in detail. When comparing these images with figure 4.11 b, it is seen that this type of rosette does not have a local change in atomic corrugation in the area that makes up the dark ring of the rosette: In figure 4.11 b, the atomic rows in the area that makes up the dark ring of the rosette, appear to run in the [-110]-direction whereas in the rest of the image, the atomic lattice is clearly resolved in both the [-110] and the [001]-direction. Such local change in atomic corrugation is not seen in figures 7.3 c1 and 7.3 c3 (see also figure 7.5 c/d).

In figures 7.3 d1/d2/d3, a rosette is shown which appears as a depression in the corresponding empty-states image (R_D). According to ref. 6 (p. 233), a rosette that shows this pattern must have a negative charge. In existing literature, several defects have been reported to appear as a rosette in filled-states images, and as a depression in empty-states images of n-GaAs [5,6,7]. In ref. 7, these rosettes represent oxygen-atoms adsorbed onto the (110)-surface of an n-type GaAs crystal. An oxygen atom adsorbed onto the surface of an n-type crystal will aquire a net negative charge [7]. We can thus assume that the feature shown in figure 7.1 d has a negative charge-state.

At the same time, it is seen in figures 7.3 d1 and 7.3 d3 that inside the area which makes up the dark ring of the rosette, there is a local change in atomic corrugation, similar to the one seen in figure 4.11 b. Figures 7.3 d1/d2/d3 thus show that a rosette which represents a negatively charged defect, has a local change in atomic corrugation in the area making up the dark ring of the rosette. A similar local change in atomic corrugation is observed for the rosettes shown in figure 7.5 e/f, g/h and i/j. In section 4.6, the mechanism that underlies this local change in atomic corrugation is explained: The negative charge associated with the defect locally raises the electron-potential. It thereby decreases the (absolute value of the) local amount of TIBB. This in turn decreases the contribution of the C3-state to the total tunneling current, and increases the contribution of the A5-state to the total tunneling current. This leads to a local corrugation-change in the vicinity of the defect.

There is, however, an unfortunate complication: The local corrugation-change associated with a negatively charged defect, proves to be sensitive to the tip-DOS. Figures 7.3 d1/d2/d3 and 7.3 e1/e2/e3 show the same rosette before (d) and after (e) a spontaneous tip-change. In (e) the rosette in question is the lower left one. It can be seen clearly that before the tip-change, the rosette causes a local change in corrugation. After the tip-change, there is no local change in corrugation around the same rosette. The morphology of the bright centre of the rosette (figure 7.3 d3/e3) also appears to have changed.

This sensitivity of the local corrugation-change to the tip-DOS can be understood from the fact that corrugation-changes in general depend on the tip-DOS. As section 4.2 explains, a change in the tip-DOS "…causes a (slight) shift in the voltage at which the change in atomic corrugation occurs". The general trends in the observed corrugation-changes usually remain the same, even in the presence of changes in the tip-DOS (see section 4.2). A local change in TIBB has the analogous effect of a change in the applied bias voltage, since both events shift the energetic location of the surface states of the sample with respect to the tip Fermi Level. This means that for certain tip-states, the local change in TIBB induced by a negatively charged defect is sufficient to cause a significant change in the ratio in which the C3-state and the A5 state contribute to the total tunneling current, thereby changing the atomic corrugation. For other tip-

states, however, the same local change in TIBB may be insufficient to change the relative contributions of the C3- and A5 states to the total tunneling current very strongly, so that no local corrugation-change is observed [32].

This leads to a complication when identifying a given rosette from its atomic-scale morphology: When the rosette does not have a local corrugation-change in the area that makes up the dark ring, this can mean two things: It can mean that the rosette has a positive charge-state, but it can also mean for the applied bias voltage or the tip-DOS involved in the experiment, the change in the amount of TIBB is insufficient induce the expected corrugation-change. Therefore, the absence of a local corrugation-change in the dark ring of the rosette can only be interpreted as an indication that the rosette must represent a positively charged defect, when in the same measurement (for the same bias voltage and tip-DOS) *other* rosettes are observed that *do* show this local change in atomic corrugation.

Based on the foregoing, we will use the following method for identifying rosettes in STM-images of n-type GaAs (110) in the case that only filled states images are available: First, it should be established whether the images contain rosettes with a local corrugation-change as well as rosettes without a local corrugation change. When the images contain both types of rosette, it is certain that the chosen bias voltage and the tip-DOS are appropriate for the local corrugation-change to appear in a negatively charged rosette. A rosette with such a local corrugation-change can then be interpreted as a negatively charged defect. A rosette without a local corrugation-change must be charged positively, and is interpreted as a surface-layer dopant in accordance with ref. 6.

7.3 *Sample structure and STM-results*

The sample on which the images shown in figure 7.4 were obtained consists of an n-type GaAs substrate (Si 10^{18} cm^{-3}) on which a total 12 Si δ-doped layers was grown by Molecular Beam Epitaxy (MBE). The epitaxial structure on the sample consists of three identical stacks of four Si-δ-doped layers (figure 7.4 a). The layers have an increasing nominal areal density of Si ($3 * 10^{11}$ cm^{-2}, $1 * 10^{12}$ cm^{-3}, $3 * 10^{12}$ cm^{-2}, $1 * 10^{13}$ cm^{-2}). The stacks themselves are separated by $Al_{0.2}Ga_{0.8}As$ marker layers. Within a stack, the Si δ-doped layers are separated by 25 nm of non-intentionally doped GaAs. The separation between the first δ-layer of each stack and the nearest marker layer (on the substrate side) is 25 nm as well. The separation between the fourth δ-layer and the following marker (nearest marker on the epilayer side) is 35 nm. The markers themselves also have a finite spatial extent: M1: 2.5 nm; M2 and M3: 10 nm; M4: 17.5 nm. The entire structure has been grown at T = 480 ^{o}C. The δ-layer structure has been grown on top of an n-GaAs buffer layer (500 nm thickness, $5.4 * 10^{18}$ cm^{-3} Si), and has been buried under an n-GaAs cap layer (300 nm) with the same doping concentration.

Our description of the δ-layers is based on two sets of images: To identify the main features that make up the δ-layers we rely on atomically resolved images (25 x 25 nm) of individual features or small clusters (see figure 7.4 d). In order to characterize the distribution of dopants, we use overlapping large-scale images (figure 7.4 a,c,e: 150 x 150 nm): The positions of the δ-layers relative to the markers has (see table 7.1) has been measured from 4 overlapping large-scale images that cover a stripe running along the [001]-direction, extending over all three stacks of δ-layers (figure 7.4 e). The in-plane distribution of dopants has been measured from 6 overlapping large-scale images of the third stack of δ-doped layers (figure 7.4 a, c). The distances that occur between dopants have been measured for δ 3.4, resulting in the pair-distribution function presented in figure 7.6. The large frame-size (150 x 150 nm) has been chosen in order to maximize the number of dopants considered, which reduces the amount of expected statistical fluctuation in the pair-distribution function (the error-bars in figure 7.6).

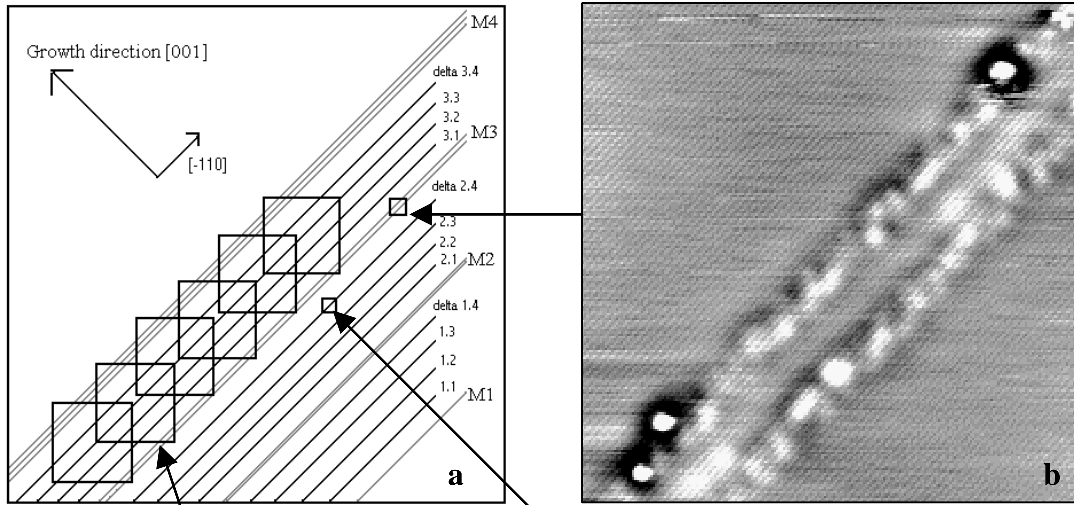

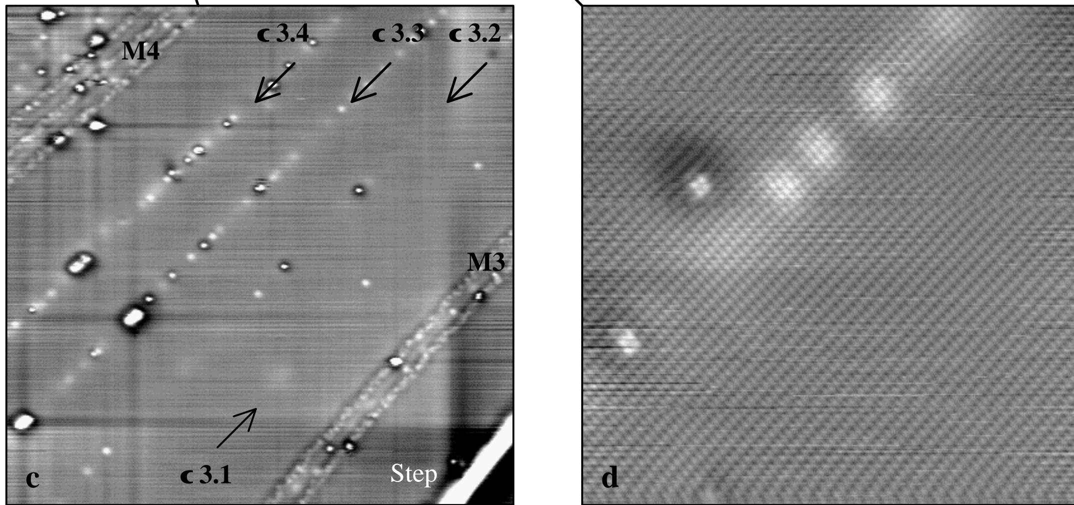

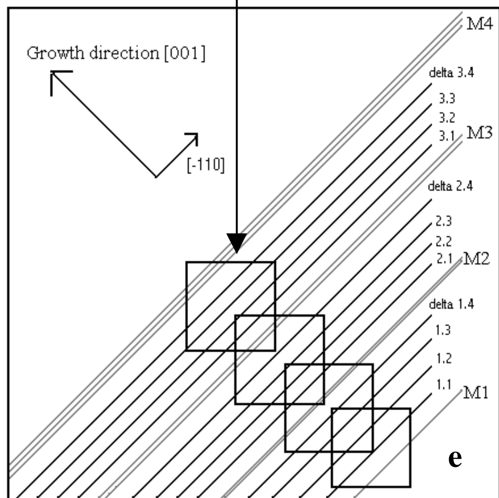

Layout large-scale images for table 7.1

M4		Surface
	δ 3.4	$1* 10^{13}$ cm^{-2} Si
	δ 3.3	$3 * 10^{12}$ cm^{-2} Si
	δ 3.2	$1 * 10^{12}$ cm^{-2} Si
	δ 3.1	$3 * 10^{11}$ cm^{-2} Si
M3		
	δ 2.4	$1* 10^{13}$ cm^{-2} Si
	δ 2.3	$3 * 10^{12}$ cm^{-2} Si
	δ 2.2	$1 * 10^{12}$ cm^{-2} Si
	δ 2.1	$3 * 10^{11}$ cm^{-2} Si
M2		
	δ 1.4	$1* 10^{13}$ cm^{-2} Si
	δ 1.3	$3 * 10^{12}$ cm^{-2} Si
	δ 1.2	$1 * 10^{12}$ cm^{-2} Si
	δ 1.1	$3 * 10^{11}$ cm^{-2} Si
M1		Substrate

f

Fig. 7.4 *(previous page)* **a:** *Lay-out of the epitaxial Si-δdoped layers and markers. The positions of figures (b), (c), and (d) are indicated by the boxes. See also text. The nominal surface concentrations of Si for each layer are given in (f).* **b:** *Details of the marker layer M3. The marker consists of two 2.5 nm $Al_{0.2}Ga_{0.8}As$-layers separated by 5 nm of GaAs. The AlGaAs marker layers appear as two bright bands due to the inversion of contrast occurring at low voltage. Frame size: 41.0 x 40.5 nm, V = -1.761 V, I = 88 pA.* **c:** *One of the 6 large-scale images of the third δlayer stack. Frame size: 150 x 150 nm; greyscale: 0 – 195 pm; V = -1.794 V; I = 88 pA. The delta-layers δ3.4, δ3.3, δ3.2 and δ3.1 are indicated in the image, as well as the marker layers M4 and M3. The white band near the bottom right corner represents a step.* **d:** *Detail of a Si δlayer (δ2.4) showing three subsurface Si dopants (bright hillocks) a second-layer Si_{As} acceptor, and a rosette which we identify as a surface-layer donor (see text) [5,6]. Frame size: 25 x 25 nm, greyscale: 0 – 238 pm, V = -1.930 V, I = 96 pA..* **e:** *Positions of the 4 large-scale images (similar to figure 7.4 b) from which table 7.1 is compiled.* **f:** *Table showing the nominal doping-concentrations of the δdoped layers.*

7.4 Individual features occurring in Si δdoped layers

The description of individual features occurring in the Si δ-layers is based on two sets of atomically resolved images. One set shows δ 2.4 (areal Si concentration: 10^{13} cm^{-2}, see figure 7.4 c, e) and extends over 200 ± 25 nm of δ-layer which contains a total of 29 atomic-size features and 4 larger features. The other set of images shows δ 2.3 (Si: 3 * 10^{12} cm^{-2}), covering a range of 140 ± 25 nm with 11 atomic-scale features. All images are acquired at V = -1.930 V, I = 96 pA. A selection of these images is shown in figure 7.5. For the atomic-scale characterization of the δ-layers, the most relevant features are the bright hillocks and several types of rosette.

The bright hillocks (figure 7.5 a) are the most numerous of all atomic-scale features, accounting for two thirds of all features observed. We identify the hillocks as subsurface donors (Si_{Ga}) based on section 7.2 [5,6 (p. 226)]. Moreover, it can be seen figure 7.5a that in the area that makes up the bright hillock, there is a slight, local change in atomic corrugation. Inside the hillock, the atomic rows appear to run more or less along the [001]-direction, which is not the case in the surrounding lattice. The effect can also be seen for the bright hillock shown in figure 7.5 b, or the one shown in figure 4.11 a. As is explained in section 4.6, this local change in atomic corrugation indicates that in the area which makes up the bright hillock, the contribution of the C3-state has increased with respect to the contribution of the A5-state. For n-GaAs imaged at negative sample voltage, this must mean that locally, the absolute amount of TIBB has increased, which is consistent with the assumption that the bright hillock represents a positively charged defect. For a Si_{Ga} donor atom, a positive charge-state is expected [31].

The rosettes account for about one third of the total number of features that is observed. In the images, we observe rosettes with a local corrugation-change in the area making up the dark ring of the rosette (figure 7.5 e/f, g/h, i/j), as well as rosettes that do not have this local corrugation-change (figure 7.5 c/d, see also figure 4.11 b and section 7.2). Given the fact that both types of rosette appear in the images, it is certain that the rosettes which do not show this local change in atomic corrugation in the dark ring must have a positive charge-state [31] (see section 7.2). Following the argument made in section 7.2 we identify these rosettes as surface-layer Si_{Ga} donor atoms. As is explained in section 7.2, the rosettes *with* a local change in corrugation (figure 7.5 e/f, g/h, i/j) must have a negative charge-state. Given this charge-state, they can represent several types of defects, like Si_{As}-acceptors [6 (p. 228)] or adsorbed oxygen atoms [7].

Having identified the rosette shown in figure 7.5 c/d as surface-layer Si_{Ga}-donor atom, we can compare its morphology with the morphology of a surface-layer Si_{Ga}-donor as it is reported in refs. 5 and 6 (see ref. 6, p. 226 and 227, or figure 7.2 b). This comparison shows that the morphology of the central bright part does not correspond to the spatial extent of what is called the “defect state” in refs. 5 and 6. The origin of this difference is at present unclear to us, but there are two factors which appear relevant.

First of all, we suspect that the appearance of the defect-state is voltage-dependent: Such voltage-dependency is reported for the morphology of the surface Ga-vacancy on GaP-(110) [6 (p. 173)]. If the appearance of the defect-state of the surface-layer Si_{Ga} donor is indeed voltage-dependent, it can also be expected to be sensitive to changes in the tip-DOS: Tungsten STM-tips that are optimized for high lateral resolution are expected to have a peaked tip-DOS [11]. A change in the tip-DOS can shift the energetic position(s) of the peak(s) in the tip-DOS [33]. This, in turn, will cause a change in the relative amounts in which the different sample surface states contribute to the total tunneling current, since the tunneling current consists of a convolution of the tip-DOS and sample-DOS (see equation 1.6). In this respect the effects of a change in the tip-DOS and the effects of a change in applied bias voltage are similar, so that if the morphology of a given feature depends on the applied bias voltage, it can also be expected to be sensitive to changes in the tip-DOS.

The second factor is that the experimental circumstances under which our images were acquired differ slightly from the ones that surround the images reported by

Ebert and Domke *et al.* [5,6]. The method of tip-preparation used by Domke *et al.* differs from the one we that use [26], which may result in a different tip-DOS. It should be noted that, although some of the images presented by Ebert and Domke *et al.* have been obtained at roughly the same voltage as the ones that we show in figure 7.5, there is a difference between our images and those presented in refs. 5 and 6 in the appearance of the atomic lattice that surrounds the dopants. Another difference is that Domke and Ebert *et al* [5,6] performed their measurements on bulk-doped n-GaAs, for which the authors report a maximum concentration of free carriers of $3.7 * 10^{18}$ cm^{-3} [5]. Our own images have been aquired on δ-doped layers, for which we estimate that the average free carrier concentration is around 10^{19} cm^{-3} [34]. For a homogeneous electron-gas, this difference in carrier concentration would raise the sample Fermi level by about 70 meV [35 (p. 21)]. A change in the sample Fermi level means that the sample-DOS shifts with respect to the tip Fermi Level, which is analogous to a change in applied bias voltage.

The rosettes shown in figure 7.5 e/f, g/h, i/j, all show a local change in atomic corrugation in the region that makes up the dark ring of the rosette. The corrugation-change indicates an increased contribution from the A5 state, which must involve a decrease in downward band bending. At V = -1.930 V, the surface is in (type II) accumulation (see section 4.4). The decrease in local downward band bending is indicative of the negative charge-state of the features. One of these types (e/f) can be identified as a second-layer Si_{As} atom from the four enhanced As-sites that make up the central, bright portion of the rosette [5, 6 (p. 228)]. The other two (g/h, i/j) have not been identified as a specific atomic structure. Given the large apparent height of the rosette shown in figure 7.5 k, we suspect that this rosette represents an adsorbed oxygen atom. The rosette shown in (i/j) looks similar to a second layer Si_{As} atom, although one of the As-sites is enhanced and slightly displaced with respect to the other three. We cannot identify this rosette, although it certainly cannot represent a surface-layer donor.

Summarizing, the Si δ-layers in GaAs that we have studied are mainly made up of bright hillocks and several types of rosette. The hillocks are identified as subsurface donors. One type of rosette (figure 7.5 c/d) is identified as surface layer donor. Another type of rosette (figure 7.5 e/f) is identified as second layer Si_{As}-acceptor, from its negative charge-state and the characteristic morphology of the defect state [6 (p. 228)]. The rosettes shown in figure 7.5 g/h and 7.5 i/j certainly represent a negatively charged defect. The former one is possibly an adsorbed oxygen atom.

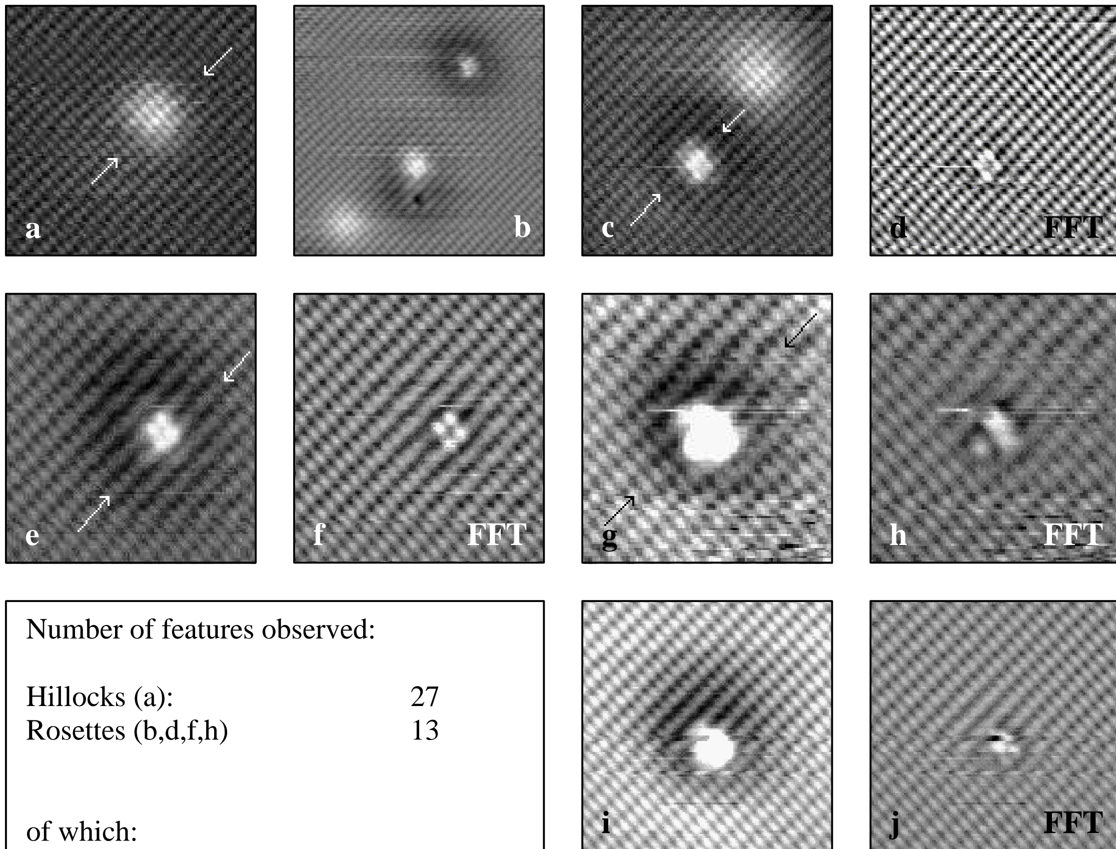

Number of features observed:

Hillocks (a):	27
Rosettes (b,d,f,h)	13
of which:	
Rosettes without corr. change (c):	3
2nd layer acc (e)	2
with corr. change (g,i):	8

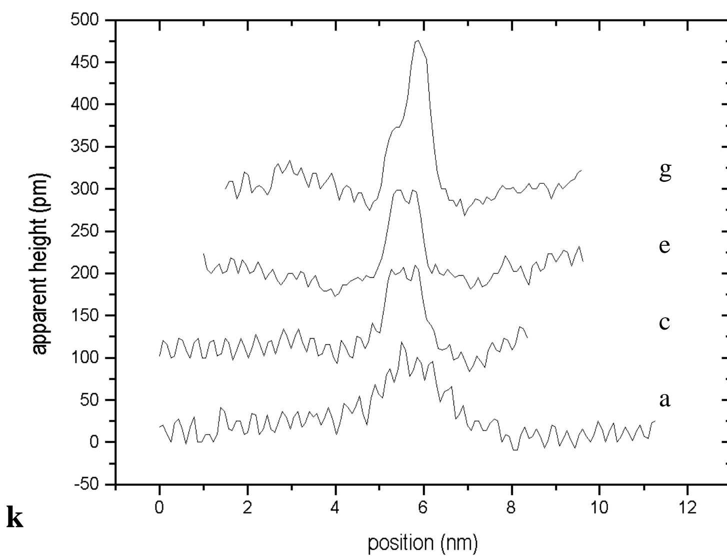

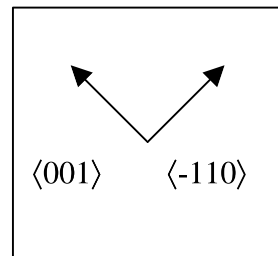

Fig. 7.5 *(preceeding page)* **a:** *Bright hillock: corresponds to subsurface donor (see section 7.2). Frame size: 9.8 x 9.9 nm, colour scale: 0 – 156 pm.* **b:** *Larger scale image (15.4 x 15.4 nm) showing several features. Bottom right: bright hillock; center: Surface vacancy and rosette without corrugation-change; upper right: Rosette with corrugation change. Colour scale: 0 – 229 pm.* **c:** *The central feature is a rosette without corrugation-change in the dark ring. The corrugation-change in the central part indicates that the feature is positively charged. We associate this type of rosette with a surface-layer donor. In the top right corner a subsurface donor is seen as well. Frame size: 10.1 x 10.3 nm, colour scale: 0 – 160 pm. (further details in sections 7.2 and 7.4)* **d:** *As c, after application of a high-pass fast Fourier transform (FFT) filter in order to show details of the lattice in all areas. Colour scale: 0 – 108 pm.* **e:** *Negatively charged rosette. From ref. 6 this type of rosette is identified as a Si_{As} atom in the second surface layer. Frame size: 7.2 x 7.6 nm, colour scale: 0 – 172 pm. (further details in section 7.2 and 7.4).* **f:** *As e, after application of a high-pass FFT-filter. Colour scale: 0 – 75 pm.* **g:** *Rosette showing a local corrugation-change in the dark ring, indicating that the feature is negatively charged. Frame size: 5.8 x 6.0 nm, colour scale: 0 – 87 pm. (further details in section 7.2 and 7.4)* **h:** *As g, after application of a high-pass FFT-filter. Colour scale: 0 – 108 pm.* **i,j:** *Other type of negatively charged rosette. This type is similar in appearance to the second-layer acceptor (e), although one As-dangling bond appears brighter than the other three. Frame size: 8.4 x 8.4 nm, colour scale 0 – 92 pm (h), resp. 0 – 110 pm (i). The peak of the rosette is 135 pm high with respect to the surrounding lattice.* **k:** *Height-profiles through the various features taken along the [-110] direction (see arrows). Curve a: bright hillock (figure 7.5 a); Curve c (offset by 100 pm): Positively charged rosette (figure 7.5 c); Curve e (offset by 200 pm): 2nd layer Si_{As} (figure 7.5 e); Curve g (offset by 300 pm): Negatively charged rosette (figure 7.5 g).*

7.5 Spatial distribution of Si-dopants within a δ-doped layer

The study of the spatial distribution of Si-dopants within the δ-doped layer is based on 6 partly overlapping large-scale images (150 x 150 nm) of δ 3.4, which have been aquired in the filled states imaging mode (see figure 7.4 a, c). The positions of the δ-layers relative to the marker layers have been measured from a second set of overlapping large-scale images (also 150 x 150 nm) that extends along [001], traversing all three stacks of δ-layers (figure 7.4 e). The large imaging-area has been chosen so that the radial distribution function of the dopants shown in figure 7.6 could be based on a large number of dopants (156). The consequence of the large imaging-area is that atomic resolution is lost as the area represented by one pixel becomes about as large as one surface unit cell (0.375 x 0.375 nm for an image of 400 x 400 pixels). We therefore cannot make a distinction between the various types of rosette on the basis of their atomic-scale morphology, and the adsorbates and acceptors (Si_{As}) cannot be distinguished from surface-layer donors (Si_{Ga}). We can, however, identify the bright hillocks as subsurface donors (see section 7.2). The study on the spatial distribution of the dopants within the δ-layer is thus based on the distribution of the bright hillocks, which represent subsurface donors, only. The statistical analysis underlying the radial distribution function shown in figure 7.6 has been carried out for δ 3.4.

The large-scale images show that none of the δ-layers has broadened significantly. Only the most heavily doped layer (δ 3.4) shows a small amount of layer-broadening: The δ-layer falls within a band of 7.5 nm wide. It is also clear that no significant segregation of dopants has taken place during growth, since the position of the δ-layers with respect to the AlGaAs marker layers matches the intended position of the δ-layers (see table 7.1). Segregation of dopants would have decreased the distance between the δ-layers with respect to the marker on the epilayer side (see also section 7.6). In table 7.1, we have expressed the distances between the δ-layers and the markers as a fraction of the distance between the two marker layers bordering the relevant stack of δ-layers, in order to eliminate scaling-effects caused by the calibration of the piezo-elements of the STM.

The absence of diffusion and segregation of the dopants during growth seems reasonably consistent with other experimental results found in the literature. According to refs. 1 (*e.g.* p. 346), 2, and 29 (p. 34), sharp doping profiles of Si in GaAs can be grown at temperatures below 500 ^{o}C – 550 ^{o}C. The δ-layers shown in figure 7.4 have been grown at 480 ^{o}C. The effect of growth temperature on the distribution of dopants in a Si δ-doped layer has also been investigated by Grandidier *et al.* [9]. In their paper, atomically resolved STM-images of two MBE-grown Si δ-doped layers in GaAs are shown: One layer has been grown at 480 ^{o}C, and the other at 580 ^{o}C. Nominal surface concentration of dopants is $1.9 * 10^{13}$ cm^{-2} for both layers. For both δ-layers, layer-broadening and a shift of the position towards the growth surface is observed, although the two effects are noticeably stronger for the δ-layer grown at 580 ^{o}C: From the STM-image in the paper, the δ-layer grown at 480 ^{o}C appears to be about 10 nm wide and appears to have been displaced by about 5 nm towards the growth surface. The δ-layer

grown at 580 °C appears about 20 nm wide, and appears to be shifted by about 10 nm. The fact that Grandidier *et al.* observe layer-broadening and a position-shift of the layer at a growth temperature as low as 480 °C appears to be at variance with our own experimental results. A possible explanation of this difference is the fact that the maximum concentration of Si used in our δ-doped layers is about half of the concentration used by Grandidier *et al.* [9, 37].

	Measured (± 0.02)	Nominal
	$\lvert M4 - M3 \rvert_{Measured} = 1$	$\lvert M4 - M3 \rvert_{Nominal} = 1$
$\lvert \delta 3.4 - M4 \rvert / \lvert M4 - M3 \rvert$	0.26	0.264
$\lvert \delta 3.3 - M4 \rvert / \lvert M4 - M3 \rvert$	0.44	0.445
$\lvert \delta 3.2 - M4 \rvert / \lvert M4 - M3 \rvert$	0.66	0.627
	$\lvert M3 - M2 \rvert_{Measured} = 1$	$\lvert M3 - M2 \rvert_{Nominal} = 1$
$\lvert \delta 2.3 - M3 \rvert / \lvert M3 - M2 \rvert$	0.45	0.445
$\lvert \delta 2.2 - M3 \rvert / \lvert M3 - M2 \rvert$	0.62	0.627
$\lvert \delta 1.4 - M2 \rvert / \lvert M3 - M2 \rvert$	0.26	0.264
$\lvert \delta 1.3 - M2 \rvert / \lvert M3 - M2 \rvert$	0.45	0.445
$\lvert \delta 1.2 - M2 \rvert / \lvert M3 - M2 \rvert$	0.65	0.627
M4 – M3 **	121 ± 2 nm	137.5 nm
	106 ± 2 nm	
M3 – M2	121 ± 2 nm	

** The numerical value of the distance between the two markers varies from one frame to the next due to temporal drift in the images.

Table 7.1: *Measured and nominal distances between the Glayers and the markers on the epilayer side. The distances are expressed as fractions of the distance between the markers in order to eliminate scaling-effects due to the calibration oj the piezo-actuators of the STM. The distances are measured within ±2 nm. The d layers d1.1, d2.1 and d3.1 are not considered since the layers are very dilute ana usually only a single dopant shows up in an image. M1 and d2.4 were invisible due to mono-atomic steps. The positions within the dlayer stack of the large-scale STM-images from which this table is compiled, are shown in figure 7.4 e.*

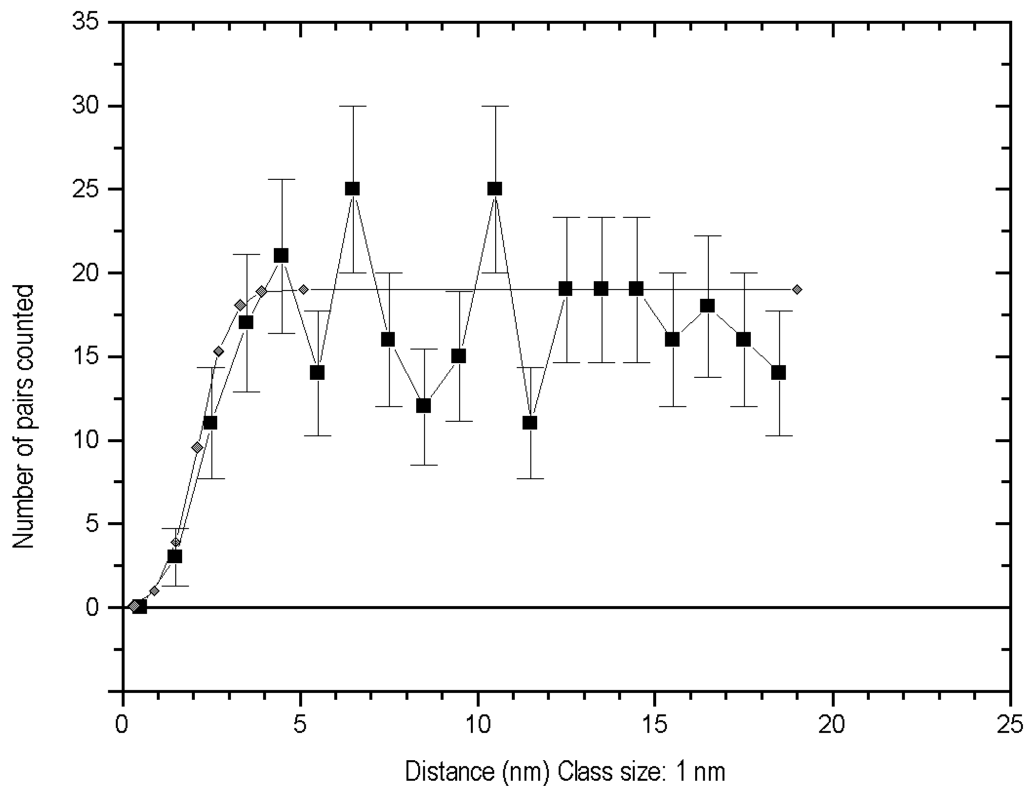

Fig. 7.6 *Pair distribution function associated with c3.4. The data-points are represented by squares, the lines are linear interpolations to guide the eye. The error-bars correspond to the square root of the number of distance-pairs counted. Diamonds: Theoretical pair distribution function based on the assumption that closely spaced hillocks cannot be imaged separately. The lines between the data-points are linear interpolations. See further details in text.*

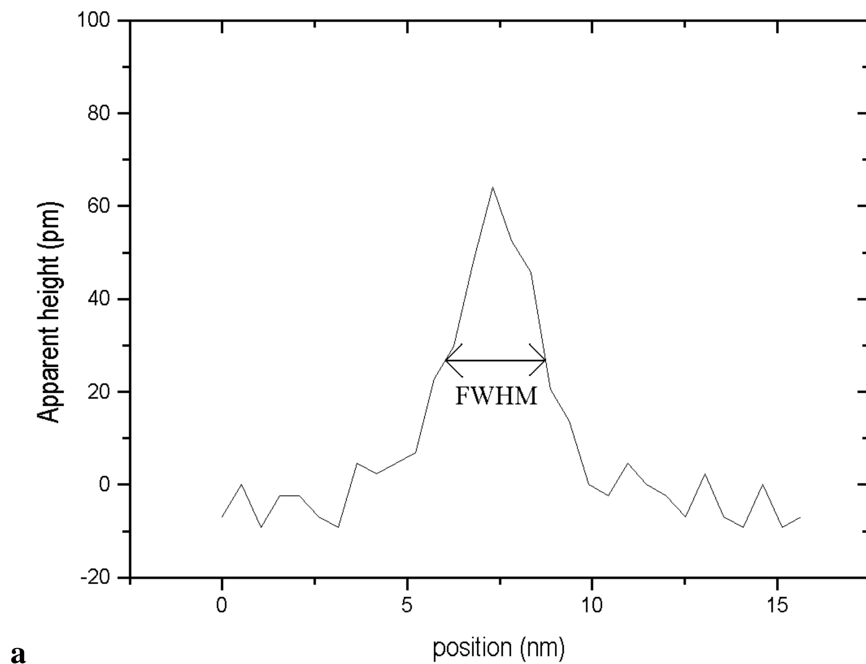

a

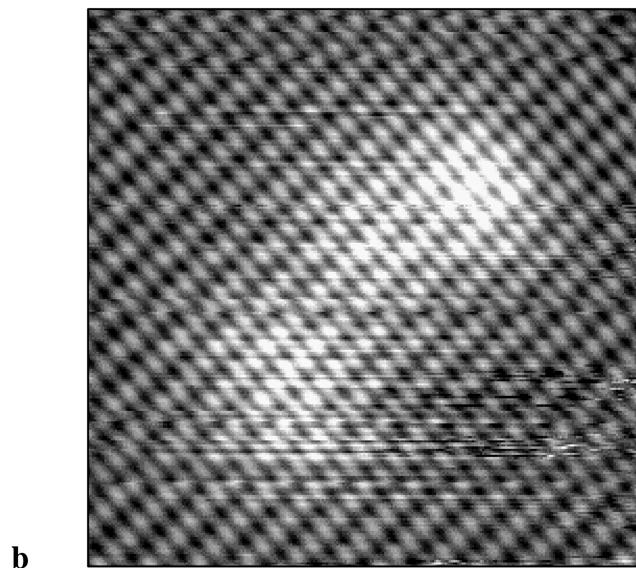

b

Fig. 7.7 a: *Typical height-profile of a hillock in a large-scale image (150 x 150 nm, see figure 7.4 c). The average FWHM of a hillock is 2.1 nm, standard deviation is 0.6 nm.* **b:** *Cluster of three closely spaced hillocks imaged at high resolution. Frame size: 10.0 x 10.0 nm, grey scale: 0 – 94 pm.*

Figure 7.6 shows the pair-distribution function evaluated for δ 3.4. The distribution function has been based on 156 subsurface donors (307 distance-pairs). The observed distances have been catagorized in classes of 1 nm (0 – 1 nm, 1 – 2 nm, 2 – 3 nm, etc.). In figure 7.6, the quatity plotted on the vertical scale is the number of dopant-pairs for which the distance between the two constituent dopants was observed to lie between 0 and 1 nm, 1 and 2 nm, 2 and 3 nm, and so on. We have ignored possible differences in the depth of the subsurface donor below the sample surface, so all distances between dopants are in fact projections of the actual distance onto the sample surface. The total length of δ-layer imaged is 680 nm. Given the nominal concentration of dopants, the total number of subsurface donors that is observed thus would indicate that dopants that lie up to 2 ± 0.3 nm below the sample surface still appear in the image. The square root of the number of events counted for a given distance-class is used as an estimate of the statistical error. The pair-distribution function strongly suggests that a projected distance between a given pair of dopant atoms of less than about 2 nm, is less likely to occur.

There is, however, a problem associated with the pair distribution function shown in figure 7.6: it is based on the distribution of the bright hillocks, which have a finite spatial extent themselves. As is evident from figure 7.7 b, it becomes difficult to image the bright hillocks individually when they are separated by only a small distance. If closely separated subsurface donors are preferentially interpreted as one single dopant due to the finite spatial extent of the hillocks themselves, this can cause an arteficial minimum distance to appear in the pair-distribution function. The spatial extent of the hillocks can be characterized by the full width-half maximum (FWHM) of the apparent height-profile. The average FWHM of the population of dopants used for the pair-distribution function shown in figure 7.6 is 2.1 ± 0.6 nm (see figure 7.7 a). The standard deviation of 0.6 nm reflects the differences in size of the hillocks that are caused by the fact that some subsurface donors lie deeper below the sample surface than others. We will now show that the measured pair-distribution function can be reproduced from a population of randomly distributed dopants, if one assumes that two dopants which are separated by a distance which is less than the average of the FWHM of the two hillock-profiles, cannot be imaged separately and are interpreted as one single dopant. This suggests that the minimum distance observed in figure 7.6 may well be an artefact caused by the fact that two closely separated subsurface donors cannot be imaged separately.

Consider a population of randomly distributed hillocks that are all equal in size (*i.e.* have equal FWHM). If one assumes that two hillocks can be seen separately only if the distance between them is larger than the FWHM of a single hillock, the measured pair-distribution function would be a step-function with the step located at r = FWHM (figure 7.8). The real pair-distribution function would of course equal 1 for all distances.

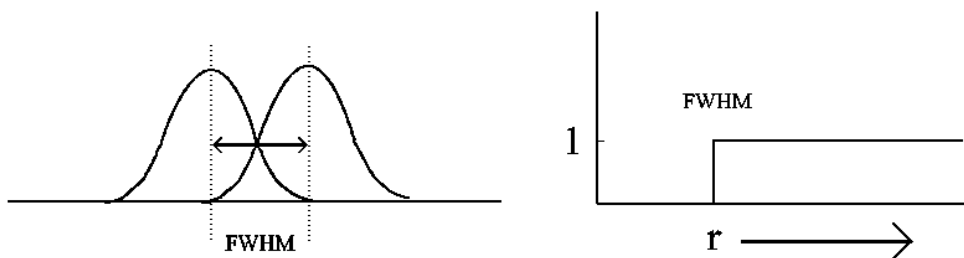

Fig. 7.8: *Relation between FWHM of the hillock-profiles and the resulting pair-distribution function (further details see text).*

If the hillocks are not of equal size, the step function in the pair-distribution function broadens into a curve which reflects the size distribution of the hillocks. Essentially, the pair-distribution function now represents a cumulative distribution plot of the dopant size. For an individual hillock, the probability that it has a neighbor at some distance r is assumed constant. However, the probability of observing that neighbor is proportional to:

$$P_i \sim \int_0^r f\left(r - FWHM_i\right) dr \qquad 7.1$$

with $f(r\text{-}FWHM_i)$ the size-distribution function of the hillocks centered on the FWHM of the ith hillock. Equation 7.1 defines the pair-distribution function that is associated with the ith hillock in the population. The pair-distribution function for the entire population is proportional to the sum of all individual pair-distribution functions P_i.

This summation can be approximated by integrating the size-distribution function of the hillocks centered around the mean value of the FWHM:

$$P_{total}(r) \sim \int_0^{\infty} f\left(r_0 - \overline{FWHM}\right) \left[\int_0^{r} f(r - r_0)dr\right] dr_0 \qquad 7.2$$

Since we have assumed that the variation in the FWHM of the hillocks can be described by a Gauss-curve, we can readily evaluate the integrals in equations 7.1 and 7.2 at whole intervals of the standard deviation (see table 7.2). The numerical values for P_{total} at whole intervals of the standard deviation correspond to the symbols in the theoretical line shown in figure 7.6. The lines between the symbols are a linear interpolation, and are meant only to guide the eye. From the agreement between the theoretical curve and the experimental one it is evident that it is very well possible to explain the observed minimum distance in the experimental pair-distribution function as an artefact caused by the fact that closely spaced hillocks cannot be imaged separately.

r (arb. units)	P_i (r)	r (nm)	(arb. units)	P_{total} (r)
$FWHM_i - 3\sigma$	0.000	0.3	avg. FWHM - 3σ	0.007
$FWHM_i - 2\sigma$	0.025	0.9	avg. FWHM - 2σ	0.050
$FWHM_i - \sigma$	0.170	1.5	avg. FWHM - σ	0.210
$FWHM_i$	0.500	2.1	avg. FWHM	0.500
$FWHM_i + \sigma$	0.850	2.7	avg. FWHM + σ	0.810
$FWHM_i + 2\sigma$	0.975	3.3	avg. FWHM + 2σ	0.950
$FWHM_i + 3\sigma$	1.000	3.9	avg. FWHM + 3σ	0.993
		4.5	avg. FWHM + 4σ	0.999

Table 7.2: *Tabulated values of equations 7.1 and 7.2. The numerical values for P_{total} (r) have been multiplied by 19 in figure 6.4 to fit the un-normalized experimental data.*

7.6 Discussion on the spatial distribution of Si-dopants within a δ-doped layer

This discussion will be limited to questions about the spatial distribution of the dopants that make up the δ-doped layers. Most of the features that we observe are bright hillocks, which can be identified as subsurface donors [5, 6 (p. 226)]. We have also recognized second-layer acceptors in the images shown in section 7.4, which indicates that some silicon-atoms have incorporated on As-sites [6 (p. 228)]. This is a known phenomenon for GaAs doped with Si at high concentration [1,30].

As for the spatial distribution of the dopants, it is plausible to assume that the initial distribution of the dopant atoms is random. During the growth interrupt that is part of the δ-doping process, the dopants arrive at the growth surface as a non-interacting Knudsen gas [36], much like hail-stones do when they reach the ground. From the literature, however, it is clear that significant redistribution of dopants takes place after deposition. This redistribution, which is highly sensitive to the growth parameters, determines the final distribution of the dopants. We will first discuss the reasons why one might suspect ordering of dopants to take place during the epitaxial growth of δ-doped layers. We already explained in the previous section that interpretation of figure 7.6 is severely complicated by the fact that dopants in STM-images have an apparent radius of several nm. In the second part of the discussion, we will therefore discuss possible improvements to the measurement method which might solve this problem.

7.6.1 Ordering effects during the epitaxial growth of delta-doped layers.

One very important mechanism by which redistribution of dopants can occur is by Coulomb-repulsion driven diffusion during the growth of the cap layer that covers the δ-doped layer. It has been shown by Schubert *et al.* that Be in GaAs incorporates only up to a local concentration of 10^{20} cm^{-3} [17]. They grew Be δ-doped layers of different nominal areal densities, ranging from $2 * 10^{13}$ cm^{-2} to $4 * 10^{14}$ cm^{-2}. These δ-doped layers were then analysed using Secondary Ion Mass Spectroscopy (SIMS). For areal densities of more than $1 * 10^{14}$ cm^{-2}, very significant broadening of the δ-doped layers occurred. The concentration-profiles of the δ-layers were either peaked or had a top-hat shape depending on the total areal density of dopants in the layer. The maximum local concentration of Be in the top-hat concentration profiles was about 10^{20} cm^{-3}. It was shown by numerical simulation that Coulomb-repulsion driven diffusion can account for such a maximum concentration, although their simulations also suggest that the concentration-profile is placed asymmetrically with respect to the intended position of the δ-layer. This latter point is at variance with Schubert's experimental results. The maximum local Be-concentration of 10^{20} cm^{-3} translates to a minimum average distance between the dopants of 2.68 nm.

Similar broadening of Be δ-doped layers has also been reported by Johnson *et al.* [3]. This paper shows radial distribution plots of 3 Be δ-doped layers as well. Like

the radial distribution shown in figure 7.6, the results of Johnson *et al.* suggest that an average maximum distance of about 2 nm exists between two given dopants within a single δ-layer. Johnson *et al.* explain the broadening of the layers as well as the minimum distance between the dopants by Coulomb-repulsion driven diffusion [3]. Finally, recent simulations by Averkiev *et al.* [18] show that a system of charged impurities that is allowed to diffuse under the influence of the self-consistent electrostatic potential generated by these impurities, will strive to minimize fluctuations in this self-consistent potential. These fluctuations are strongest when two dopants are located closely to each other. The simulation results indicate that the concentration-profile of the δ-layer becomes non-Gaussian. A minimum in-plane distance between the impurities is also expected by the authors of ref. 18.

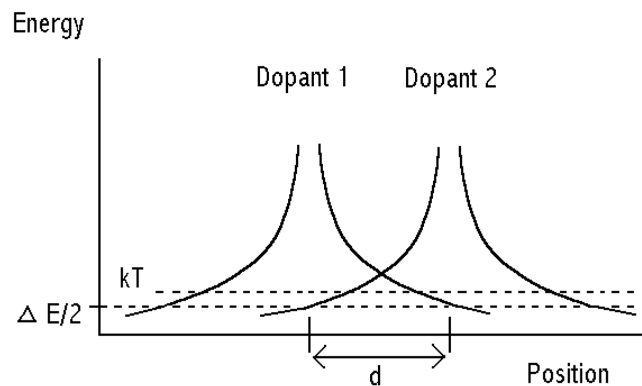

Fig. 7.9: *Schematic representation of the overlapping screened Coulomb potentials for two dopants located close to each other. Notice that the interaction between the dopants themselves is repulsive. Each dopant experiences the potential of the other dopant, which leads to an increase in potential energy* ΔE. *For d < 2 nm, this increase in potential energy exceeds the thermal energy associated with the growth temperature of the sample. See further details in text.*

When two dopants are at a short distance from each other, we can estimate the resulting increase of potential energy from the screened Coulomb potential that describes a dopant embedded in a semiconducting crystal. For a single dopant, this potential is given by $V(r) = [e / (4\pi\varepsilon_0\varepsilon_r r)]*\exp[r / r_s]$, with e the elementary charge, ε_r as the dielectric constant of GaAs, r_s as the screening length and r as the distance from the dopant [1 (p. 31)]. When two dopants are separated by a distance d (see figure 7.9), the resulting increase in the potential energy is given by $\Delta E = 2*[e^2 / (4\pi\varepsilon_0\varepsilon_r d)]*\exp[d / r_s]$. The factor 2 enters in the expression for ΔE because as the dopants approach each other, the potential energy of both dopants increases. We assume a screening length of $r_s = 45$

Å, which corresponds to a Si doping concentration of 2 * 10^{18} cm^{-3} [8]. For d = 20 Å, the resulting increase in potential energy would equal 70 meV. This exceeds the thermal energy kT at 480 ^{o}C (65 meV), which is the temperature at which our sample was grown. For this reason, we expect that if Coulomb-driven diffusion has led to short-range ordering of dopants in the δ-doped layers shown in figure 7.4, we should observe a minimum distance between the dopants of about 2 nm.

For the δ-doped layers shown in figure 7.4, one might wonder whether diffusion has played a significant role during growth of the sample, since the layers have not broadened very much. In fact, the growth parameters that are used for growing δ-doped structures are usually chosen in order to minimize diffusion of impurities, so as to avoid layer-broadening which is an unwanted effect. The absence of layer-broadening in the δ-doped layers shown in figure 7.4 suggests that little or no bulk-diffusion of dopants took place after incorporation. One might thus suspect that the in-plane distribution of dopants in these layers is simply a random one.

There is, however, an additional mechanism for in-plane ordering of dopants, caused by the fact that dopants deposited on the growth surface are mobile. The results of Däweritz *et al.* [19] indicate that Si atoms on vicinal GaAs-(001) surfaces can rearrange themselves along the steps of the surface during the growth interrupt. Upon subsequent growth of the cap layer, the dopants that have aligned themselves along the steps can form quantum-wires. The average terrace-length is 8 nm (2° miscut), and the growth interrupt lasted 180 s at T = 580 ^{o}C. Diffusion of Si atoms towards the steps of a vicinal growth surface during growth interrupt has also been reported by Wood *et al.* [20]. Later experiments by Däweritz *et al.* [21] show that it is possible for the dopants to form ordered arrangements on the growth surface. Growth temperature was 590 ^{o}C in these experiments in order to ensure sufficient mobility of the adsorbed Si atoms. The ordering of adatoms is concluded from changes in the RHEED-pattern (Reflection High-Energy Electron Diffraction) during and after deposition of Si. The Si-concentration profile as measured by Secondary Ion Mass Spectroscopy (SIMS) showed a peak concentration of Si at the intended position of the δ-layers, but also indicated that significant layer-broadening had taken place due to surface segregation. Ordering-effects of dopants on the growth surface have since then also been studied by *in plane*-STM [22,23,24]. The influence of the growth of the cap-layer to the distribution of dopants on the growth surface is not described by refs. 22 – 24. The benefit of cross-sectional STM is that it can characterize δ-doped layers after growth of the cap layer, *i.e.* in their final form.

From the foregoing, it is clear that Coulomb-repulsion driven diffusion during growth of the cap layer is an important mechanism for redistribution of the impurities that make up a δ-doped layer. The effect of such diffusion can be that a minimum distance between the two given dopants exists. During the growth interrupt that is part of the δ-doping process, the dopant atoms are adsorbed onto the growth surface. Depending on the growth-conditions, in-plane ordering of dopants can take place if an ordered arrangement of adsorbed dopants is thermodynamically favourable. Whether this ordered arrangement is preserved after growth of the cap-layer is at this point unclear to us. It is in any case very plausible to assume that the dopants making up an epitaxially grown δ-doped layer have a non-random spatial distribution.

7.6.2 Detecting short-range order in delta-doped layers using Cross-Sectional STM.

As seen in the figures 7.6 and 7.7, it becomes difficult to distinguish subsurface donors from each other when they partly overlap in a given STM-image. This can introduce an artificial minimum distance in a radial distribution plot derived from such STM-images. The apparent minimum distance equals the apparent diameter of the dopants in the STM-image, and thus depends on the spatial extent of the screened Coulomb-potential of a dopant near the surface [6 (p. 230), 8, 25] (see also section 7.2). At the same time, it is known that Coulomb-repulsion driven diffusion during growth of the cap-layer can introduce a real minimum distance between the dopants, which is also related to the spatial extent of the screened Coulomb potential of the dopants (see figure 7.9 and subsection 7.6.1). Therefore, the two effects, finite apparent diameter of a dopant in STM and Coulomb-repulsion driven diffusion, are expected to cause the same minimum distance to appear in a radial distribution plot. The minimum distance seen in figure 7.6 can thus be both real and arteficial.

We interprete the apparent oscillations in the radial distribution plot for $r > 5$ nm as statistical fluctuation since the oscillations are about as large as the expected statistical error. The interpretation of figure 7.6 as a whole is then as follows: Distances between dopants that are larger than about 5 nm occur equally frequent, suggesting an absence of long-range ordering between dopants. Smaller distances between dopants appear less and less likely to occur as the distance decreases. This can be either the result of a real short-range order that exists between dopants, or it can be an artefact caused by the finite apparent diameter of a dopant in STM. If any short-range order between the dopants in our δ-doped layer exists, the minimum distance is in any case shorter than about 2.5 ± 1 nm.

If the existence any short-range ordering of dopants is to be established by cross-sectional STM, the experiment must be carried out in such a way that two dopants lying close enough for their potential wells to overlap, are certainly resolved as two individual dopants. Only if one is certain that two very closely spaced dopants cannot be interpreted as one single dopant, can the absence of small distances between dopants in cross-sectional STM-images be accepted as experimental proof for short-range ordering of dopants. We will now reflect on how a sample containing δ-doped layers should be imaged by cross-sectional STM in order to fulfill this condition. We will also consider other aspects like identification of the various features and statistical accuracy.

At this point the most promising way to image dopants with adequate spatial resolution is to choose the tunneling parameters such that the defect-state associated with the dopant (see figure 7.2 b1, b3) manifests itself in the image as clearly as possible. The work of Domke *et al.* [26] shows that tunneling parameters that meet this requirement exist: Their STM-experiments are no different from our own except for a different tip preparation technique and the fact that Domke *et al.* use slightly higher tunneling currents than we do [26]. The defect-state associated with several configurations of Si in GaAs extends over only a few unit cells [6,26]. This is consistent

with our own results (see figures 7.3c and 7.5 b,c). Dopants lying about 1.5 nm or more apart should be resolved as separate dopants without problem if the tunneling parameters are chosen such that the defect-state shows up clearly in the image. Added benefits are that the morphology of the defect-state can help identify the feature, and that it becomes very straightforward to distinguish between dopants lying in the surface layer, the first subsurface layer, and so on (see figure 7.2 b).

A major concern when compiling a radial distribution plot from a set of cross-sectional STM-images is that the total number of dopants studied must be large enough in order to ensure a reasonable statistical accuracy in the number of dopant-pairs counted in each distance-class. In ref. 9, radial distribution plots are compiled from atomically resolved images of two δ-doped layers, but the significance of these plots is severely limited by the small number of dopants that is studied. In figure 7.6, statistical accuracy is quite reasonable but the spatial resolution is limited by the large scale of the images. Even if the large-scale images underlying figure 7.6 had been obtained at both polarities of the applied bias voltage, distinction between dopants in different layers near the surface on the basis of their defect-state would have been impossible due to the lack of atomic resolution.

Probably the best way to characterize a δ-doped layer is from a large collection of small-scale images, so that adequate spatial resolution is combined with statistical accuracy. In our experience, a frame size of 25 x 25 nm or 35 x 35 nm (400 x 400 pixels) is well-suited to show details of the atomic-scale morphology of defects. At the same time, these frame sizes are large enough to cover a reasonable total length of δ-layer within a reasonable amount of time. The images shown in figure 7.5 are cut-outs from overlapping 25 x 25 nm frames, which show a total of 340 ± 50 nm. These images were aquired in 70 minutes time. Covering a total length of 700 nm, which is the length of δ-layer imaged in the large-scale images underlying figure 7.6 would thus require roughly $2^1/_2$ hours of imaging-time. Experimentally, this is quite feasable.

It is reasonable to assume, however, that the defect-state of a dopant can only be imaged if the dopant lies near the surface. Of the deepest lying dopants, we expect to image only the Coulomb-field since this has a longer range. On the other extreme, it is clear from ref. 26 that of the dopants in the surface layer and first subsurface layer, the defect-state can be imaged. If only those dopants that lie in the surface layer and the first subsurface layer are used to compile the radial distribution plot, the expected minimum length of δ-layer to be imaged in order to obtain adequate statistical accuracy increases to 1250 nm. A practical consequence is that it becomes very important to understand and control the cleavage-process well enough to ensure a high success-rate in cleavage. The estimate of 1250 nm is made as follows: If the radial distribution plot is to be meaningful for the first 5 nm using a distance-class size of 1 nm, one would like to image at least 50 dopants (on average 10 for each distance-class). Given the areal density of 10^{13} cm^{-2}, one expects 4 dopants in the first two layers of the surface per 100 nm of δ-layer. To reach a total of 50, a strip of 1250 nm of δ-layer must be imaged.

Ideally, the sequence of measurements carried out to characterize δ-doped layers would then be the following. First, voltage-dependent images of dopants should be made in order to find the most suitable imaging-parameters. These parameters may differ from the ones used by Domke *et al.* [26], especially if a different tip-preparation technique is used. It goes without saying that all measurements of dopant-like features

should be carried out simultaneously in the filled- and empty-states imaging mode so that the features can be identified. These preparatory measurements can be carried out on bulk-doped material. Any problems regarding cleavage, if and when they occur, can also be addressed at this point (see chapter 2). Once the voltage-dependent morphology of individual dopants is known, the δ-doped layers can be characterized. In our opinion, the most useful measurement would be a set of small-scale images (25 x 25 nm) that covers a total length of δ-layer that is long enough to ensure adequate statistical accuracy.

7.7 Summary

In this chapter, a Si δ-doped layer in GaAs is characterized from cross-sectional STM-images. Identification of subsurface donors is straightforward since these show up as bright hillocks in filled-states STM-images. Surface layer donors as well as negatively charged adsorbates and Si_{As}-acceptors are known to show up as bright protrusions surrounded by a dark ring (a "rosette"). Identification of these rosettes is therefore difficult when only filled-states images are available. Some types of rosette can, however, be identified from details of their atomic-scale morphology. We have identified one type of rosette as Si_{As} in the first subsurface layer, confirming that some Si-atoms incorporate as acceptors rather than donors. Two other types of rosette are tentatively identified as surface layer donors and negatively charged adsorbate, respectively.

A radial distribution plot of the dopants in the layer is made from several large-scale images of a δ-layer of high concentration (Si: 10^{13} cm^{-2}). This radial distribution plot is based on the positions of the subsurface donors in the STM-images. In the radial distribution plot, an apparent minimum distance between dopants is seen of 2.5 ± 1 nm. However, this apparent minimum distance can very well be explained as an artefact caused by the finite apparent size of a subsurface donor in STM. In order to establish whether or not short-range ordering of dopants really takes place during the epitaxial growth of δ-doped layers, the δ-doped layers should be imaged using such parameters that the defect-state associated with a dopant shows clearly in the image. Statistical accuracy can be achieved by combining many small-scale images.

RERERENCES:

1: E.F. Schubert: *Doping in III-V semiconcductors.* Cambridge University Press, Cambridge, p. 542 (1993).

2: E.F. Schubert, J.B. Stark, B. Ullrich, J.E. Cunningham: *Spatial localization of impurities in δ-doped GaAs.* Appl. Phys. Lett, Vol. 52, No. 18, pp. 1508 – 1510 (1988).

3: M.B. Johnson, P.M. Koenraad, W.C. v.d. Vleuten, H.W.M. Salemink, J.H. Wolter: *Be delta-doped layers in GaAs imaged with atomic resolution using STM.* Phys. Rev. Lett, Vol. 75, No. 8, pp. 1606 – 1609 (1995).

4: E.F. Schubert, J.E. Cunningham, W.T. Tsang: *Electron-mobility enhancement and electron-concentration enhancement in δ-doped n-GaAs at T = 300 K.* Solid State Comm. Vol 63, No. 7, pp. 591 – 594 (1987).

5: C. Domke, M. Heinrich, Ph. Ebert, K. Urban: *Oscillating contrast in room-temperature STM-images of localized charges in III-V semiconductor compounds.* Journal of Vac. Sci. and Tech. B, Vol. 16, No. 5, pp. 2825 – 2832 (1998).

6: Ph. Ebert: *Nano-scale properties of defects in compound semiconductor surfaces.* Surface Science Reports, Vol. 33, pp. 121 – 303 (1999).

7: J.A. Stroscio, R.M. Feenstra, A.P. Fein: *Local state density and long-range screening of adsorbed oxygen atoms on the GaAs (110) surface.* Phys. Rev. Lett, Vol. 58, No. 16, pp. 1668 – 1671 (1987).

8: J.F. Zheng, X. Liu, N. Newman, E.R. Weber, D.F. Ogletree, M. Salmeron: *Scanning Tunneling Microscopy Studies of Si donors (Si_{Ga}) in GaAs.* Phys. Rev. Lett, Vol. 72, No. 10, pp. 1490 – 1493 (1994).

9: B. Grandidier, D. Stiévenard, J.P. Nys, X. Wallart: *Microscopic behaviour of silicon in delta-doped layer in GaAs.* Appl. Phys. Lett, Vol. 72, No. 19, pp. 2454 – 2456 (1998).

10: M.B. Johnson, O. Albrektsen, R. Feenstra, H.W.M. Salemink: *Direct imaging of dopants in GaAs with cross-sectional Scanning Tunneling Microscopy.* Appl. Phys. Lett, Vol. 63, No. 21, pp. 2923 – 2925 (1993).

11: S. Ohnishi, M. Tsukada: *Molecular orbital theory for Scanning Tunneling Microscopy.* Solid state comm. Vol. 71, No. 5, pp. 391 – 394 (1989).

12: S. Muto, S. Takeda, M. Hirata, K. Fuji, K. Ibe: *Structure of planar aggregates of Si in heavily Si-doped GaAs.* Phil. Mag. A, Vol. 66, No. 2, pp. 257 – 268 (1992).

13: P.M. Koenraad: *Electron mobility in d doped layers,* in: Delta-doping of semiconductors, ed. by E.F. Schubert, Cambridge Univ. Press, Cambridge, pp. 407 – 443 (1996).

14: A.F.J. Levi, S.L. Mc Call, P.M. Platzman: *Nonrandom doping and elastic scattering of carriers in semiconductors.* Appl. Phys. Lett, Vol. 54, No. 10, pp. 940 – 942 (1989).

15: R.L. Headrick, L.C. Feldman, B.E. Weir: *Ordered delta-doping,* in: Delta-doping of semiconductors, ed. by E.F. Schubert, Cambridge Univ. Press, Cambridge, pp. 461 - 484 (1996). The paper discusses ordered δ-doping in Si.

16: M.C.M.M. van der Wielen, A.J.A. van Roij, H. van Kempen: *Direct observation of Friedel oscillations around incorporated Si_{Ga} dopants in GaAs by low-temperature STM.* Phys. Rev. Lett, Vol. 76, No. 7, pp. 1075 – 1078 (1996). See also: *Study of imperfections near the cleaved GaAs (110) surface by low-temperature STM.* Phd-thesis by M.C.M.M. van der Wielen, Univ. of Nijmegen, the Netherlands (1998).

17: E.F. Schubert, G.H. Gilmer, R.F. Kopf, H.S. Luftman: *Maximum concentration of impurities in semiconductors.* Phys. Rev. B, Vol. 46, No. 23, pp. 15078 – 15084 (1992).

18: N.S. Averkiev, A.M. Monakhov, A. Shik, P.M. Koenraad, J.H. Wolter: *Random electric fields and impurity diffusion in d layers.* Phys. Rev. B, Vol. 61, No. 4, pp. 3033 – 3038 (2000)

19: L. Däweritz, K. Hagenstein, P. Schützendübe: *Self-organization during Si incorporation in MBE-grown vicinalGaAs (001) surfaces.* Journ. of Cryst. growth, Vol. 127, pp. 1051 – 1055 (1993).

20: C.E.C. Wood: *Dopant-surface migration and interactions from reflection high-energy electron diffraction dynamics.* Journ. of Appl. Phys, Vol. 71, No. 4, pp. 1760 – 1763 (1992).

21: L. Däweritz, P. Schützendübe, K. Stahrenberg, M. Maier, K. Ploog: *Real-time study of dopant incorporation and segregation during MBE growth of GaAs (001): Si.* Proceedings of IEEE: 24th International symposium on compound semiconductors (1995), pp. 51 – 56.

22: M. Wassermeier, S. Kellermann, J. Behrend, L. Däweritz, K.Ploog: *Submonolayer Si deposition at low temperatures on the GaAs (001)-(2x4) surface studied by STM.* Surface Science, Vol. 414, pp. 289 – 303 (1998).

23: H. Oigawa, M. Wassermeier, J. Behrend, L. Däweritz, K.H. Ploog: *Reconstruction of the GaAs (001) surface induced by submonolayer Be deposition.* Surface Science, Vol. 376, pp. 185 – 191 (1997).

24: H. Oigawa, M. Wassermeier, J. Behrend, L. Däweritz, K.H. Ploog: *Controlled anisotropic ordering of Be deposited on the GaAs (001) surface.* Surface Science, Vol. 399, pp. 39 – 48 (1998).

25: K. Kobayashi: *Scattering theory of subsurface impurities observed in STM.* Phys. Rev. B, Vol. 54, No. 23, pp. 17029 – 17038 (1996).

26: C. Domke, Ph. Ebert, K. Urban: *Atomic-scale properties of the amphoteric dopant Si in GaAs (110) surfaces.* Surface Science, Vol. 415, pp. 285 – 298 (1998). The tungsten tips used in this work are etched electro-chemically and then conditioned in vacuum by field emission. Tunneling currents range from 0.2 – 0.5 nA.

27: P.M. Koenraad, F.A.P. Blom, C.J.G. Langerak, M.R. Leys, J.A.A.J. Perenboom, J. Singleton, S.J.R.M. Spermon, W.C. van der Vleuten, A.P.J. Voncken, J.H. Wolter: *Observation of high mobility and cyclotron resonance in 20 Å silicon d doped GaAs grown by MBE at 480 ^{o}C.* Semiconductor Science and Technology, Vol. 5, ppl 861 – 866 (1990).

28: C. Domke, Ph. Ebert, M. Heinrich, K. Urban: *Microscopic identification of the compensation mechanisms in Si-doped GaAs.* Phys. Rev. B, Vol. 54, No. 15, pp. 10288 – 10291 (1996).

29: A.F.W. van der Stadt: *Magnetotransport in Si-ddoped GaAs/$Al_xGa_{(1-x)}As$ structures.* PhD-thesis by A.F.W.van der Stadt, University of Eindhoven, the Netherlands, 1998.

30: P.M. Koenraad, I. Bársony, J.C.M. Henning, J.A.A.J. Perenboom, J.H. Wolter: *Diffusion of Si in ddoped GaAs studied by magneto transport,* in Semiconductor Interfaces at the sub-nanometer scale, pp. 35 – 43. Ed. by H.W.M. Salemink and M.D. Pashley, Kluwer Academics Publishers, the Netherlands, 1993.

31: A donor impurity embedded in n-type material can either have a positive charge-state, or a neutral one, depending on whether it lies energetically above or below the Fermi level. When the surface of an n-type material is imaged in the filled-states imaging mode, the donor atoms lie below the sample Fermi level and therefore they are, as a whole, neutral. However, when the tip approaches the donor atom to within the effective Bohr-radius of the bound electron, the positive charge of the impurity atom is no longer screened completely by the bound electron, and the dopant atom manifests itstelf as a positively charged defect. The analogous argument applies to the un-ionized acceptor.

32: An apparent insensitivity of the observed atomic corrugation to local changes in the amount of TIBB is not as strange as it might appear: On n-type material, the rosettes appear for negative sample voltage, *i.e.* when the surface is in accumulation. For a surface in accumulation, the amount of TIBB can be relatively insensitive to changes in the applied bias voltage (see section 4.4). If a large, negative bias voltage is chosen (or the tip has a low work function), the negative charge associated with the defect may not cause a very large local change in TIBB. A second circumstance to consider is the presence of a peak in the tip-DOS which coincides energetically with the A5-state. In this case, the A5-state can remain the dominant contributor to the total tunneling current in spite of small changes in the amount of TIBB.

33: C.J. Chen: *In-situ characterization of tip electronic structure in Scanning Tunneling Microscopy.* Ultramicroscopy, Vol. 42 – 44, pp. 147 – 153 (1992).

34: The estimate for the free carrier concentration is made as follows: The deltalayers are grown in an epitaxial layer of 445 nm thickness, while the sum of the areal densities of Si of all layers equals $4.3 * 10^{13}$ cm^{-3}. If we make the rather crude assumption that all dopants are distributed homogeneously throughout this epitxial layer of 445 nm, then these figures translate to a bulk Si concentration of 10^{19} cm^{-3}. We can justify this assumption from the width of the V-shaped potential well associated with a δ-doped layer: According to ref. 1 (p. 442), this potential well of a Si δ-doped layer in GaAs of an areal concentration of $5 * 10^{12}$ cm^{-2} has a width of 40 nm, suggesting that in our structure, the potential wells of the adjacent δ-layers overlap. The concentration of free carriers may deviate from the nominal concentration of impurities due to autocompensation, but this effect only becomes significant for δ-layers with an areal concentration exceeding 10^{13} cm^{-2} (ref. 1, p. 277 and p. 459).

35: C. Weisbuch, B. Vinter: *Quantum Semiconductor Structures.* Academic Press, Boston (1991).

36: C. Kittel, H. Kroemer: *Thermal Physics.* W.H. Freeman and Company, New York, 2nd ed. (1980). p. 397.

37: Y.G. Chai, R. Chow, C.E.C. Wood: *The effect of growth conditions on Si incorporation in Molecular Beam Epitaxy GaAs.* Appl. Phys. Lett, Vol. 39, Iss. 10, pp. 800 – 802 (1981). In this paper it is shown that Si can form electrically inactive Si_{Ga}-Si_{As} pairs or precipitates when it is attempted to incorporate Si in an average concentration of more than $6 * 10^{18}$ cm^{-3} during MBE-growth.

Summary

The first chapter is meant to explain in qualitative terms some aspects of the theoretical background to tunneling between a metal tip and a semiconducting sample. The view of tunneling adopted in this thesis is expressed by equation 1.6. It is based on the Modified Bardeen Approach and the Tersoff-Hamann theory. In the thesis this view of tunneling is referred to as “regular tunneling”.

Semiconductor surfaces posess electronic surface-states which are imaged in STM and thus make it possible to obtain atomic resolution. The Tersoff-Hamann theory states that for an s-like tip-state, the tunneling matrix element is proportional to the local amplitude of the wavefunction representing the sample state involved in the tunneling process. However, most STM-tips have tip-states with a different symmetry. For a non-s tip state, the tunneling matrix element becomes proportional to a spatial derivative of the local amplitude of the relevant sample-state wavefunction. For a p_z- or d_z^2-like tip-state, the tunneling matrix element is proportional to spatial derivatives of the sample-state wavefunction with respect to z (*i.e.* perpendicular to the sample surface). Consequently, for the qualitative interpretation of topographic STM-data the Tersoff-Hamann theory remains applicable when the tip has a p_z- or d_z^2-like tip state.

It is assumed that the absolute tip-sample distance in STM on semiconductors is slightly less than 10 Å (7 – 10 Å). Therefore, even an STM-image is obtained under “normal” circumstances, the presence of a tip-sample interaction is to be expected. One of the most important consequences of the tip-sample interaction is that the spatial distribution of the electronic states involved in the tunneling process, is distorted. This results in a lowering of the tunneling barrier height, or in the formation of a chemical bond between the tip and one of the sample surface atoms if the tip and sample approach each other very closely (3 Å). Although a tip-sample interaction is usually present during STM on semiconductors under commonly used circumstances, topographic STM-data can often be interpreted without taking the influence of the tip-sample interaction into account.

Finally, the influence of Tip-Induced Band Bending (TIBB) is reviewed. TIBB arises due to the fact that the electric field present between the tip and sample penetrates into the semiconducting crystal. One of its effects is that it shifts the energetic position of surface states with respect to the sample Fermi level. In order to interprete voltage-dependent effects, it is indispensable to take TIBB into account.

Chapter 2 describes the experimental setup and sample preparation. We use a commercially available UHV-STM setup around which a dedicated vacuum-system has been built. The essence of cross-sectional STM is that one prepares a sample which is broken or cleaved inside the vacuum. The STM-experiment is then carried out on the freshly exposed fracture surface (figure 2.1). A remaining problem associated with the technique of sample preparation by cleavage is the presence of mono-atomic steps on the cleaved surface. We typically observe mono-atomic steps running parallel to the sample edge in the epilayer region of the sample surface (figure 2.6c). The absence of V-shaped steps suggests that in our samples the velocity with which the crack

propagates through the sample material is in the low-velocity (*i.e.* the non-oscillatory) regime.

We prepare our polycrystalline tungsten (W) STM-tips by electro-chemical etching (chapter 3). The tips are then heated, self-sputtered with Ne^{+}-ions, and subjected to an Ar^{+}-ion bombardment in UHV. When tungsten STM-tips are sharpened by self-sputtering, the Schiller-decapitation process can occur. It is shown that this process is accompanied by a very specific pattern in the sputter voltage as a function of time. This makes it possible to use the decapitation process for the manufacture of high-quality STM-tips. Secondly, we present a model which enables us to calculate the radius of curvature of the tip apex based on Fowler-Nordheim plots. Verification with Scanning Electron Microscopy (SEM) shows that our model is correct within 5 nm. A slight deviation of the experimental data from the theory suggests that our polycrystalline wire has a preferential crystal orientation. A potential problem with the use of the self-sputter treatment is the occurrence of vacuum-arcs, which can severely decrease the success-rate of this process. In order to prevent vacuum-arcs from occurring, the sputtering-gas must be kept clean (background pressure $< 2 * 10^{-9}$ torr) and adequate removal of the oxide layer present on the as-etched tips must be ensured.

In chapter 4 atomically resolved, voltage-dependent STM-images of GaAs (110) are compared to the results of a one-dimensional model used to calculate the amount of Tip-Induced Band Bending (TIBB) for a tunneling junction between a metal and a semiconductor. The voltage-dependent changes in the morphology of the atomic lattice are caused by the four surface states of the GaAs (110) surface contributing in varying relative amounts to the total tunneling current. Tip-induced band bending determines which of these states contributes to the total tunneling current at a given bias voltage, and thus has a profound influence on the voltage-dependent STM-images. In principle, this effect can be used to extract information about the amount of tip-induced band bending from the atomic morphology seen in the image. It is shown that certain voltage regions exist, for which none of the surface states present at the GaAs-(110) surface can contribute to the tunneling current. For these voltages, tunneling occurs between the tip and bulk states of the sample through a surface depletion layer several nm wide. Nevertheless, atomic, surface-like corrugation is observed for these circumstances. The effect may be caused by electrons tunneling resonantly through the low energy shoulder of the C3 state which extends into the bandgap of the semiconductor, or by the interaction between the electronic states of the tip and sample. We finally show three illustrative examples of a voltage-dependent change in atomic corrugation: The change in atomic morphology caused by a sudden transition from empty states imaging to filled states imaging, the local corrugation-change around dopants and adsorbates, and the difference in atomic corrugation on either side of a p-n junction.

Not all experimental results presented in this thesis can be interpreted without explicite consideration of tip-sample interaction effects: In chapter 5, we present an unusual image-form of the GaAs (110) surface observed in cross-sectional STM in UHV. It clearly shows the zig-zag row formed between the cations and anions in the top row of the GaAs (110) surface, as well as traces of the bottom row that lies between the top rows. It thereby closely resembles the true atomic lattice usually depicted by ball-and-stick models. We interprete the occurrence of this image-form in terms of a chemical bond that forms between the apex of the tip and the nearest Ga atom in the top

row of the sample surface. The formation of such a bond has recently been predicted theoretically. The results thus show that the tip-sample interaction, when it becomes significant, can give rise to entirely new and interesting image-forms.

The voltage-dependent effects observed on GaAs-{110} have also been observed for the {110}-surface of n-type $Al_{0.2}Ga_{0.8}As$ and for the {110}-surface of a crystal containing an n-type GaAs/$Al_{0.33}Ga_{0.67}$As-superlattice (chapter 6). The appearance of AlGaAs-(110) at large bias voltage is well known: At large negative sample voltage (V_{SAMPLE} ~ -3 V), the images show atomic rows along the [-110] direction, and the alloy-related minima appear between the atomic rows. At large positive sample voltage (V_{SAMPLE} ~ +2 V) the images also show atomic rows along the [-110] direction, but the alloy-related minima now appear to be centered on the atomic rows. This appearance changes radically when a small (absolute) value is chosen for the bias voltage. In the empty states imaging mode ($V_{SAMPLE} > 0$) the lower portion of the conduction-band related surface-DOS is imaged. Apart from a change in atomic corrugation that is similar to the one which we observed for n-GaAs {110}, small ridges that are oriented along the [-110]-direction appear in the image. The appearance of these ridges can be understood qualitatively from the electronic band structures of GaAs-{110} and AlAs-{110}. At small negative bias voltage, bright and dark areas that are several nm in lateral extent, appear in the image. We interprete these bright and dark areas in terms of fluctuations in the density of electrons that have accumulated at the sample surface due to TIBB.

An important conclusion can be drawn from two images that show the very same patch of AlGaAs-(110) surface in both the filled- and empty-states imaging modes: The shape and location of the alloy-related minima change as a function of the polarity of the applied bias voltage. This effect can be understood from the fact that a given Al atom in the sample surface can have several different bonding configurations.

The images of the GaAs/AlGaAs superlattice show similar effects. Apart from that, they also show that the contrast between GaAs and AlGaAs inverts for small bias voltage. The inversion of contrast occurs for both polarities of the bias voltage, althought the effect is stronger in the filled-states case (negetive sample voltage). Finally, the images of the superlattice obtained at intermediate positive sample voltage (+0.59 V < V < +0.71 V) show an apparent broadening of the GaAs-layers in the superlattice. For these voltages, we expect to be sensitive to the confined electron-levels that are present in the GaAs-layers of the superlattice. Since the spatial distribution of these levels extends into the AlGaAs barriers, we think that the observed broadening of the GaAs-layers indicates that for these voltages, the confined electron level in the GaAs quantum-well of the superlattice is imaged directly.

From the literature, it is known that during the epitaxial growth of Si δ-doped layers in GaAs, Coulomb-repulsion between dopants can have a significant influence on the spatial distribution of the dopants making up the δ-doped layer (chapter 7). For this reason it is suspected that a minimum distance may exist between any two given dopants within a δ-doped layer. This partial ordering is expected to enhance the mobility of electrons occupying the potential-well formed by the δ-doped layer. It is also known from existing literature that subsurface donors (Si_{Ga}) atoms appear as bright hillocks several nm in diameter in STM-images. Surface-layer donors (Si_{Ga}) appear as protrusions surrounded by a dark ring (a “rosette”) in filled-states images and as a bright

hillock in empty-states images. Acceptors (Si_{As}) and negatively charged adsorbates appear as rosettes in filled-states images and as depressions in empty-states images. Furthermore, surface-layer donors and acceptors have a "defect state" associated with them which can appear in the image as well. In chapter 4 of this thesis it is shown that the polarity of the charge-state of a rosette can be determined from the local change in atomic corrugation around it.

In chapter 7 of this thesis, STM-images of Si δ-doped layers in GaAs are presented. It is evident that some of the Si atoms have incorporated on As-sites rather than Ga-sites. In order to investigate the spatial distribution of the dopants making up the δ-layers, a pair-distribution function has been determined for one of the δ-doped layers (figure 7.4). The pair-distribution function shows that a distance between any two given dopants of less than 2 nm is less likely to occur. This result, however, cannot be accepted as experimental proof for the existence of an ordered arrangement of dopants in δ-doped layers. In STM-images dopants show up as features that are several nm in diameter. It thus becomes difficult to image two very closely spaced dopant atoms individually (figure 7.5). If two closely spaced dopants are interpreted as one single dopant lying close to the sample surface, a minimum distance between dopants would appear in the pair-distribution function as an artefact.

A real minimum distance between the dopants due to Coulomb-repulsion is expected to depend on the spatial extent of the screened Coulomb-potential associated with a Si-dopant in GaAs. An artificial minimum distance caused by the finite feature-size of Si dopants in STM also depends on the spatial extent of the screened Coulomb-potential associated with a dopant, since this quantity determines the feature-size of a dopant in STM. Therefore, the apparent minimum distance between two dopants of 2 nm found in figure 7.6 can be both real and artificial. A way to resolve this problem may be to image the dopants under such circumstances that the defect-states of the dopants manifest themselves clearly in the image.

Nederlandse samenvatting

Het eerste hoofdstuk is bedoeld om in kwalitatieve termen enkele aspecten van de theoretische achtergrond van het tunnelproces tussen een metalen tip en een halfgeleidend preparaat uit te leggen. Het mentale beeld van het tunnelproces dat in dit proefschrift wordt gebruikt is uitgedrukt in vergelijking 1.6. Het is gebaseerd op de *Modified Bardeen Approach* en de Tersoff-Hamann theorie. In dit proefschrift wordt dit beeld van het tunnelproces aangeduid als "regulier tunnelen".

Halfgeleideroppervlakken bezitten oppervlakte-electronentoestanden die met de STM worden afgebeeld, en het zo mogelijk maken om atomaire resolutie te verkrijgen. De Tersoff-Hamann theorie stelt dat, als de tipelectronentoestand een s-achtig karakter heeft, het tunnelmatrixelement recht evenredig is met de locale amplitude van de golffunctie die de bij het tunnelproces betrokken electronentoestand vertegenwoordigt. Echter, de meeste STM-tips hebben tiptoestanden met een andere symmetrie. Voor een niet-s tip-toestand wordt het tunnelmatrixelement evenredig met een ruimtelijke afgeleide van de locale amplitude van de relevante preparaat-toestandsgolffunctie. Voor een p_z- of $d_z{}^2$- achtige tiptoestand is het tunnelmatrixelement evenredig met ruimtelijke afgeleiden van de preparaat-toestandsgolffunctie naar de z-richting (d.w.z. loodrecht op het preparaatoppervlak). Dientengevolge blijft voor de kwalitatieve interpretatie van topografische STM-data de Tersoff-Hamann theorie toepasbaar als de tip een p_z- of $d_z{}^2$-achtige tiptoestand heeft.

Het wordt aangenomen dat de absolute tip-preparaat afstand in STM iets minder is dan 10 Å (7 Å – 10 Å). Daarom is, zelfs als een STM-beeld onder "normale" omstandigheden werd gemaakt, de aanwezigheid van een interactie tussen de tip en het preparaat te verwachten. Eén van de belangrijkste gevolgen van die tip-preparaat interactie is dat de ruimtelijke verdeling van de electronentoestanden die betrokken zijn bij het tunnelproces, wordt verstoord. Dit resulteert in een verlaging van de tunnelbarrièrehoogte, of in de vorming van een chemische binding tussen de tip en één van de oppervlakteatomen in het preparaat, als de tip en het preparaat elkaar zeer dicht naderen (3Å). Hoewel een tip-preparaat interactie meestal aanwezig is tijdens STM op halfgeleiders onder gewoonlijk gebruikte omstandigheden, kan topografische STM-data vaak worden geïnterpreteerd zonder rekening te hoeven houden met de tip-preparaat interactie.

Tenslotte wordt de invloed van tip-geinduceerde bandverbuiging (Tip-Induced Band Bending: TIBB) bekeken. TIBB ontstaat doordat het electrisch veld, dat aanwezig is tussen de tip en het preparaat, doordringt in het halfgeleidend kristal. Eén van de effecten daarvan is dat de energetische ligging van de oppervlaktetoestanden verschuift ten opzichte van het Ferminiveau van het preparaat. Om spanningsafhankelijke effecten te kunnen interpreteren, is het zonder meer noodzakelijk om TIBB in rekening te brengen.

Hoofdstuk 2 beschrijft de experimentele opstelling en de wijze waarop het preparaat gemaakt wordt. We gebruiken een commercieel beschikbaar UHV-STM systeem waaromheen een speciaal ontworpen vacuumsysteem is gebouwd. De essentie van cross-sectionele STM is dat men een preparaat maakt dat in het vacuum gebroken of gekliefd wordt. Het STM-experiment wordt dan uitgevoerd op het verse breukvlak (figuur 2.1). Een blijvend probleem dat hoort bij de aanmaak van preparaten door middel van klieven is de aanwezigheid van mono-atomaire stappen op het gekliefde oppervlak. Typisch zien we dat mono-atomaire stappen parallel langs het epilaag-gebied van het preparaatoppervlak lopen (figuur 2.6 c). De afwezigheid van V-vormige stappen suggerreert dat in onze preparaten de snelheid waarmee de breuk zich voortplant in het lage-snelheidsgebied (d.w.z. het niet-oscillerende regime) ligt.

We maken onze polykristallijne wolfraam (W) STM-tips d.m.v. een electrochemische ets (hoofdstuk 3). Daarna worden de tips in UHV verhit, en ondergaan ze een zelf-sputter proces met Ne^{+}-ionen en een Ar^{+}-ionen bombardement. Wanneer een wolfraam STM-tip aangescherpt wordt door middel van zelfsputteren, kan het *Schiller-decapitatieproces* optreden. We laten zien dat dit proces vergezeld gaat van een specifiek patroon in de sputterspanning als functie van de tijd. Dit maakt het mogelijk om het decapitatieproces te gebruiken voor de aanmaak van STM-tips van hoge kwaliteit. Verder presenteren we een model dat ons in staat stelt de kromtestraal van de punt van de tip te berekenen uit een Fowler-Nordheim plot. Verificatie met Scanning Electronen Microscopie (SEM) toont aan dat het model binnen 5 nm correct is. Een kleine afwijking tussen de experimentele data en de theorie suggerreert dat ons polykristallijn draad een preferentiele kristalorientatie heeft. Een potentieel probleem met het gebruik van het zelfsputterproces is het voorkomen van vacuum-bogen, hetgeen de succes-ratio (aantal goede tips/totaal aantal tips) van het proces ernstig kan verlagen. Om het optreden van vacuum-bogen te voorkomen moet het sputtergas schoon gehouden worden (achtergronddruk $< 2 * 10^{-9}$ torr) en moet de oxidelaag die altijd op een net-geëtste tip anwezig is, op adequate wijze verwijderd worden.

In hoofdstuk 4 worden atomair opgeloste, spannings-afhankelijke STM-beelden van GaAs vergeleken met de resultaten van een één-dimensionaal model dat de hoeveelheid tip-geinduceerde bandverbuiging (TIBB) berekent voor een tunnelcontact tussen een metaal en een halfgeleider. De spannings-afhankelijke veranderingen in de morfologie van het atomaire rooster worden veroorzaakt door de vier relevante oppervlakte toestanden van GaAs-(110) die in verschillende verhoudingen bijdragen aan de totale tunnelstroom. Tip-geinduceerde bandverbuiging bepaalt welke van deze toestanden bijdraagt aan de totale tunnelstroom bij een gegeven spanning, en heeft op die manier een grote invloed op spanningsafhankelijke STM-beelden. In principe kan dit effect gebruikt worden om informatie te verkrijgen over de hoeveelheid tip-geinduceerde bandverbuiging op basis van de atomaire morfologie die te zien is in het STM-beeld. We laten zien dat er bepaalde spanningsgebieden bestaan waarvoor geen van de oppervlaktetoestanden van het GaAs-(110) oppervlak aan de tunnelstroom kan bijdragen. Voor deze spanningen vindt tunneling plaats tussen de tip en de bulk-toestanden van het preparaat, door een oppervlaktedepletielaag van enkele nm dikte heen. Toch wordt er onder die omstandigheden een atomaire, oppervlakte-achtige corrugatie waargenomen. Het effect kan veroorzaakt worden door electronen die resonant door de laag-energetische schouder van de C3-toestand tunnelen, welke in de

bandgap van de halfgeleider doorloopt, of door een interactie tussen de electron-toestanden van de tip en het preparaat. Tenslotte laten we drie illustratieve voorbeelden zien van een spannings-afhankelijke verandering van de atomaire corrugatie: De verandering in atomaire morfologie veroorzaakt door een plotselinge overgang van het afbeelden lege toestanden naar het afbeelden van gevulde toestanden, de locale corrugatie-verandering rondom doteringen en adsorbaten, en het verschil in atomaire corrugatie aan beide zijden van een p-n junctie.

Niet alle experimentele resultaten die in dit proefschrift worden gepresenteerd kunnen worden geinterpreteerd zonder expliciete beschouwing van de tip-preparaat interactie: In hoofdstuk 5 presenteren we een ongebruikelijk STM-beeld van GaAs (110), waargenomen in cross-sectionele STM in UHV. Het laat duidelijk de zig-zag rijen zien die de anionen en cationen in de bovenste rij van het GaAs-(110) oppervlak vormen, evenals sporen van de onderste rij die tussen de bovenste rijen in ligt. Daarmee lijkt het beeld sterk op het werkelijke atomaire rooster dat gewoonlijk wordt afgebeeld d.m.v. de “ball-and-stick” modellen. We interpreteren het voorkomen van deze beeldvorm in termen van een chemische binding die zich kan vormen tussen de apex van de tip en het dichtstbijzijnde Ga-atoom in de bovenste rij van het preparaatoppervlak. De vorming van zo’n binding is onlangs theoretisch voorspeld. De resultaten laten zien dat de tip-preparaat interactie, als ze belangrijk wordt, aanleiding kan geven tot hele nieuwe en interessante beeldvormen.

De spannings-afhankelijke effecten die zijn waargenomen op GaAs-(110), zijn ook gezien voor het (110)-oppervlak van n-type $Al_{0.2}Ga_{0.8}As$, en voor het (110)-oppervlak van een kristal dat een n-type $GaAs/Al_{0.33}Ga_{0.67}As$-superrooster bevat (hoofdstuk 6). Het uiterlijk van AlGaAs-(110) bij hoge tunnelspanning is zeer bekend: Bij een grote, negatieve preparaatspanning ($V_{SAMPLE} \sim -3$ V), laten de beelden atomaire rijen langs de [-110]-richting zien, waarbij de legeringsgerelateerde minima (*alloy-related minima*) tussen de atomaire rijen in lijken te liggen. Bij grote, positieve preparaatspanning ($V_{SAMPLE} \sim +2$ V) laten de beelden ook atomaire rijen langs de [-110]-richting zien, maar nu lijken de legeringsgerelateerde minima gecentreerd te liggen op de atomaire rijen. Dit uiterlijk verandert radicaal wanneer een kleine (absolute) waarde voor de tunnelspanning wordt gekozen. In de lege-toestanden afbeeldingsmodus ($V_{SAMPLE} > 0$) het lagere deel van de geleidingsband-gerelateerde oppervlaktetoestandsdichtheid wordt afgebeeld. Behalve een verandering in de atomaire corrugatie die lijkt op de verandering die we voor GaAs-(110) hebben waargenomen, verschijnen er ook kleine richeltjes in het beeld, die geörienteerd zijn langs de [-110]-richting. Het verschijnen van deze richeltjes kan kwalitatief worden begrepen vanuit de electronsiche bandstructuur van GaAs-{110} en AlAs-{110}. Bij kleine, negatieve preparaatspanning verschijnen er in het beeld kleine lichte en donkere gebiedjes die zich enkele nm uitstrekken. We interpreteren deze lichte en donkere gebiedjes in termen van fluctuaties in de dichtheid van de electronen die geaccumuleerd zijn aan het preparaatoppervlak ten gevolge van TIBB.

Een belangrijke conclusie kan getrokken worden uit twee STM-beelden die precies hetzelfde stukje AlGaAs-(110) oppervlak laten zien in zowel de gevulde- als de lege-toestanden afbeeldingsmodus: De vorm en plaats van de legeringsgerelateerde minima verandert als functie van de polariteit van de aangelegde tunnelspanning. Dit

effect kan begrepen worden vanuit het feit dat een gegeven aluminium atoom in het preparaatoppervlak meerdere verschillende bindingsconfiguraties kan hebben.

De beelden van het GaAs/AlGaAs superrooster laten soortgelijke effecten zien. Bovendien laten ze ook nog zien dat het contrast tussen GaAs en AlGaAs inverteert voor een lage tunnelspanning. De contrastinversie vindt plaats voor beide polariteiten van de aangelegde tunnelspanning, al is het effect sterker voor het geval dat de gevulde toestanden worden afgebeeld (negatieve preparaatspanning). Tenslotte laten de beelden van het superrooster bij intermediaire positieve preparaatspanning ($+0.59$ V $<$ V $<$ $+0.71$ V) een schijnbare verbreding van de GaAs-lagen in het superrooster zien. Voor deze spanningen verwachten we dat de STM gevoelig is voor de opgesloten electronentoestanden die aanwezig zijn in de GaAs-lagen van het superrooster. Omdat de ruimtelijke verdeling van deze toestanden in de AlGaAs-lagen doordringt, denken we dat de waargenomen verbreding van de GaAs-lagen aangeeft dat we voor deze spanningen de opgesloten electronentoestand in de GaAs-kwantumput van het superrooster afbeelden.

Vanuit de literatuur is het bekend dat tijdens de epitaxiale groei van Si δ-gedoteerde lagen in GaAs, Coulomb-repulsie tussen de doteringen onderling een sterke invloed kan hebben op de ruimtelijke verdeling van de doteringen die samen de δ-laag vormen (hoofdstuk 7). Om die reden wordt vermoed dat er een minimum afstand kan bestaan tussen twee willekeurige doteringen in een δ-laag. Van deze gedeeltelijke ordening wordt verwacht dat ze een gunstige invloed heeft op de mobiliteit van electronen die de potentiaalput bevolken die gevormd wordt door de δ-laag. Het is vanuit bestaande literatuur ook bekend dat donoren onder het oppervlak (Si_{Ga}) als lichte heuveltjes van enkele nm in doorsnee verschijnen in het STM-beeld. Donoren in de oppervlaktelaag (Si_{ga}) verschijnen als uitstulpingen, omgeven door een donkere ring (een “rozet”) in de gevulde-toestandsbeelden in als een licht heuveltje in lege-toestandsbeelden. Acceptoren (Si_{As}) en negatief geladen adsorbaten verschijnen als rozetten in gevulde-toestandsbeelden en als kuiltjes in lege-toestandsbeelden. Bovendien hebben oppervlaktelaag-donoren en acceptoren een *defect toestand* die ook in het beeld kan verschijnen. In hoofdstuk 4 van dit proefschrift wordt getoond dat de polariteit van de ladingstoestand van een rozet kan worden vastgesteld op basis van de locale verandering in de atomaire corrugatie er omheen.

In hoofdstuk 7 van dit proefschrift worden STM-beelden van Si δ-gedoteerde lagen in GaAs gepresenteerd. Het is duidelijk dat sommige van de Si-atomen op As-roosterplaatsen zijn ingebouwd in plaats van op Ga-roosterplaatsen. Om de ruimtelijke verdeling te onderzoeken van de doteringen die de δ-lagen vormen, is een paar-distributiefunctie vastgesteld voor één van de δ-gedoteerde lagen (figuur 7.4). De paar-distributiefunctie laat zien dat een afstand tussen twee willekeurige doteringen van minder dan 2 nm minder vaak voorkomt. Dit resultaat, echter, kan niet worden aanvaard als experimenteel bewijs voor het bestaan van een geordende verdeling van doteringen in δ-gedoteerde lagen. In STM-beelden zien doteringen eruit als objecten met een diameter van enkele nm. Het wordt dus moeilijk om twee heel dicht bij elkaar gelegen doteringen gescheiden af te beelden (zie figuur 7.5). Als twee vlak bij elkaar gelegen doteringen worden geinterpreteerd als één enkele dotering die dicht onder het oppervlak ligt, dan zou in de paardistributiefunctie een minimum afstand tussen doteringen kunnen verschijnen als een artefact.

Voor een echte minimum afstand tussen de doteringen tengevolge van Coulomb-repulsie is het te verwachten dat deze afhangt van de effectieve reikwijdte van de afgeschermde Coulomb-potentiaal die bij een Si-dotering in GaAs hoort. Een kunstmatige minimum afstand veroorzaakt door de eindige afmeting van een Si-dotering in STM hangt ook af van de effectieve reikwijdte van de afgeschermde Coulomb-potentiaal horende bij een dotering af, want van deze grootheid hangt de schijnbare grootte van een dotering in STM af. Daarom kan de in figuur 7.6 gevonden schijnbare minimum afstand tussen twee gegeven doteringen van ongeveer 2 nm zowel echt als kunstmatig zijn. Dit probleem is mogelijk op te lossen door de doteringen onder zodanig omstandigheden af te beelden, dat de defect-toestand duidelijk in het STM-beeld naar voren komt.

Voor niet-natuurkundigen…

In dit gedeelte staat een beknopte uitleg van het onderzoek waarvan de bedoeling is, dat ze toegankelijk is voor diegenen die onbekend zijn met de specifieke vaktaal van de experimentele natuurkunde. Deze uitleg is in twee stukken ingedeeld: Het eerste stuk legt uit wat een STM is en wat er nou precies in een STM-beeld te zien valt. Het tweede deel gaat over het onderzoek van het proefschrift zelf. Soms ontkom ik er niet aan om toch een vakterm te gebruiken, of moet ik iets eerst zeggen om het pas daarna te kunnen verduidelijken. Wie iets tegenkomt wat op het eerste gezicht onduidelijk lijkt, kan om die reden het beste aandachtig verder lezen, in veel gevallen volgt de uitleg vanzelf.

Wat is een STM?

De Scanning Tunneling Microscoop (STM) is uitgevonden door de heren Binnig en Rohrer in 1981, in het onderzoekslaboratorium van IBM te Zürich. Net als iedere microscoop dient een STM om dingen zichbaar te maken die te klein zijn om met het blote oog te zien. De vergroting gaat bij een STM echter verder dan bij de meeste andere typen microscopen die vandaag de dag bekend zijn: Een “normale” optische microscoop vergroot zo’n 400 maal, en kan b.v. de cellen waaruit levend weefsel is opgebouwd zichtbaar maken. Een electronenmicroscoop kan 100.000 tot 1.000.000 maal vergroten, afhankelijk van het type electronenmicroscoop waarom het gaat. Met een electronenmicroscoop kunnen onderdelen van cellen worden afgebeeld. Electronenmicroscopen worden ook gebruikt om bijvoorbeeld roosterfouten in metalen te bestuderen. Met een speciaal type electronenmicroscoop, de Hoge-Resolutie Transmissie-electronenmicroscoop (HR-TEM), kan ook het atomaire rooster van een kristallijne[1] stof worden afgebeeld.

Met een STM kan een vergroting van ongeveer 3.000.000 maal of meer worden bereikt (zie figuur 3.3a). Net als de HR-TEM kan een STM het preparaatoppervlak op atomaire schaal zichtbaar maken. Een belangrijke voorwaarde daarbij is dat het materiaal waaruit het preparaat bestaat, electrisch geleidend is. Daarmee is een STM dus geschikt om metalen en halfgeleiders af te beelden, maar kunnen er b.v. geen keramische materialen of plastics mee worden afgebeeld. Een andere beperking is dat het oppervlak van het preparaat dat moet worden afgebeeld, niet te ruw mag zijn. Om een object of materiaal met een dermate hoge vergroting af te beelden moet het echter vaak wel een speciale voorbehandeling ondergaan, en vaak is die voorbehandeling destructief. Als het af te beelden object of materiaal d.m.v. die voorbehandeling geschikt gemaakt is om te worden afgebeeld, heet het een “preparaat” of “sample”.

[1] In een kristallijne stof zitten de atomen waaruit de stof is opgebouwd netjes gerangschikt in rijen. Zoiets wordt het “kristalrooster” genoemd (zie figuur 4.1 a). Heel veel stoffen hebben die eigenschap. Enkele voorbeelden: Keukenzout en suiker zijn kristallijne stoffen, en de meeste metalen en halfgeleiders ook. Het verschil tussen gewoon glas en kwarts is dat kwarts uit kristallijn silicium-oxide bestaat, terwijl in gewoon glas datzelfde silicium-oxide niet kristallijn is.

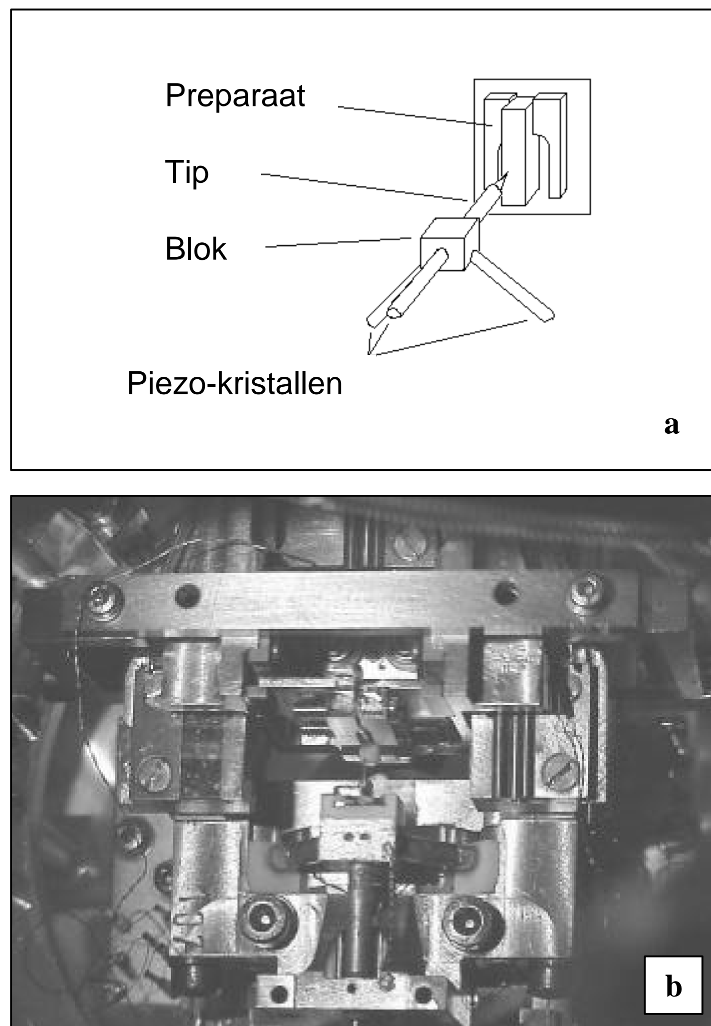

Figuur 1a: *Schematische weergave van het "hart" van een STM: de tip en sample. Het piezo-kristal (of "piezo-buis") dat in het verlengde van de tip ligt regelt de afstand tussen de tip en het preparaat (zie tekst).* **b:** *Dezelfde onderdelen in het echt (zie ook figuur 2.2 van dit proefschrift). In de foto zijn het preparaat, het blok waarin de tip rust en de drie piezo-kristallen goed te zien. De tip is in de foto vanwege zijn kleine afmeting wat moeilijker te herkennen. In dit proefschrift is het preparaat altijd een stukje halfgeleidermateriaal. Overigens is in de foto de STM wat gekanteld afgebeeld ten opzichte van de schets.*

De STM die in dit onderzoek is gebruikt staat afgebeeld in figuur 2.2 van dit proefschrift. Het “hart” van de STM staat afgebeeld op de foto in figuur 2.2b en ook in de bovenstaande figuur (figuur 1). Om de STM heen is een vacuum-opstelling gebouwd, zodat het afbeelden van de preparaten in het luchtledige plaats kan vinden. De opstelling die ik gebruikt heb is namelijk speciek bedoeld om halfgeleiders te bestuderen. Halfgeleiders vormen in lucht altijd een dun laagje oxide aan het oppervlak, en dit maakt het afbeelden van het halfgeleideroppervlak met STM onmogelijk. Om over een schoon halfgeleideroppervlak te beschikken, breken we in het vacuum van de opstelling het te onderzoeken halfgeleiderkristal in tweeën en bestuderen dan het breukvlak (zie figuur 2.1). Dit breken of “klieven” moet zo kort mogelijk voor de meting gebeuren. Ter indicatie van de schaal: De gehele opstelling rust op een tafel van ongeveer 1 x 2 meter (zie figuur 2.2c). Het gebied dat in figuur 1b te zien is, beslaat ongeveer 10 cm.

Een STM bestaat uit een metaaldraadje waaraan een zeer scherpe punt is gemaakt: De tip. Die tip is op een houder gelast of geklemd, en de tip-houder zit op zijn beurt in een blok geschoven (zie figuur 1)[2]. Het blok rust op drie piezo-electrische kristallen, of “piezo-buizen”. Een piezo-electrisch kristal heeft een bijzondere eigenschap: Als je de beide uiteinden van het kristal electrisch verbindt met een (gelijk)spanningsbron, dan zal het kristalletje iets langer of korter worden.[3] In figuur 1 is te zien hoe het blok op drie van zulke piezo-electrische kristallen rust. Door over elk van die kristallen de juiste spanning te zetten kan ik de positie van het blok, en daarmee uiteindelijk de positie van de tip, heel nauwkeurig sturen.

Het afbeeldingsproces van een STM werkt nu als volgt: De tip wordt met behulp van de piezo-kristallen tot vlak bij het oppervlak van het preparaat of “sample” gebracht. “Vlak bij” is in dit geval tussen de 0.7 en 1.0 nm, dat is 3 tot 4 maal de afstand tussen twee naburige atomen in de meeste metalen en halfgeleiders, of 7 tot 10 maal de afstand tussen het zuurstofatoom en één van de twee waterstofatomen in het watermolecuul. In alle vaste stoffen zijn electronen aanwezig, en in geleidende vaste stoffen zijn die electronen vrij om door het hele stuk materiaal te bewegen. Als de punt van de tip het oppervlak tot op die afstand genaderd is, kunnen electronen vanuit de tip “overspringen” naar het preparaat, ondanks dat de tip en het preparaat elkaar nog niet echt raken en dus in de klassieke zin des woords nog geen electrisch contact maken. Dit proces heet “tunnelen” en hiernaar is de scanning tunneling microscoop genoemd.

Als de tip nu alleen maar dicht bij het preparaat wordt gebracht en verder wordt er niets gedaan, dan zullen er per seconde evenveel electronen van de tip naar het sample springen als omgekeerd. Aangezien het overspringen van de electronen op zichzelf niet is waar te nemen, gebeurt er dan ogenschijnlijk niets. Echter, als over de tip en het sample een electrische spanning wordt aangelegd zal er een heel klein electrisch stroompje lopen. De grootte van deze “tunnelstroom” is zeer gevoelig voor de afstand

[2] Doordat de tiphouder los in het blok geschoven is kan de tip gemakkelijk worden vervangen door een nieuwe. Voor elke meting wordt een nieuwe tip gebruikt, en soms wordt een tip tijdens de meting vervangen. De tips maken we zelf.

[3] Het omgekeerde werkt ook: Als je kracht uitoefent op een piezo-kristal, zal het iets worden ingedrukt of uitgerekt. Daardoor ontstaat een electrische spanning op de uiteinden van het kristal. Bepaalde typen aanstekers voor gasfornuizen maken gebruik van dit effect.

tussen de tip en het preparaat. De STM wordt door electronica bestuurd, en die electronica is zo ingesteld dat de tunnelstroom ten allen tijden op een vooraf ingestelde waarde gehouden wordt: Is de stroom wat te laag, dan zal de electronica de spanning op één van de piezo-buizen wat bijregelen zodat de tip iets dichter bij het preparaatoppervlak komt (zie figuur 1). Is de stroom wat te hoog, dan zal de electronica de tip wat terugtrekken. Op die manier kunnen we dus de tip op een constante, zeer kleine afstand van het preparaatoppervlak brengen en houden. Tegelijk kan de electronica de beide piezo-buizen die loodrecht op de tip staan zodanig aansturen dat de tip een zijdelingse, heen-en-weergaande beweging zal maken, zodanig dat hij uiteindelijk een heel gebiedje bestreken heeft. Dat heet “scannen”. Zo kan een klein gebiedje van het preparaatoppervlak worden afgetast.

De spanning op de piezo buizen die nodig was om de tip op constante afstand van het preparaat te houden tijdens de scanbeweging wordt bijgehouden door een computer die met de electronica is verbonden. Die spanning vormt het meetsignaal: Een STM-beeld bestaat (bij ons apparaat) uit een matrix van 400 bij 400 punten, en van elk punt is bekend welke spanning op de z-piezo buis gezet moest worden om de tunnelstroom constant te houden. Hieruit kan dus voor elk punt in het STM-beeld bepaald worden over welke afstand de tip verplaatst moest worden om de tip-preparaat afstand constant te houden. Een STM-beeld is dus eigenlijk een “hoogtekaart” van het preparaatoppervlak, precies als de aardrijkskundige hoogtekaarten in een atlas (zie b.v. figuur 2 a,b). Alleen is bij een STM-beeld de schaal vele malen kleiner. Bij die hoogtekaartjes betekent een lichte kleur dat iets “hoog” is, en een donkere kleur dat iets “laag” is.

Hiermee is duidelijk wat een STM is: Het is een zeer scherpe naald die vlak boven het oppervlak van een preparaat kan worden gehouden, en waarmee je op hele kleine schaal het oppervlak van dat preparaat kunt aftasten. Het STM-beeld is in feite een soort “hoogtekaart” van het preparaatoppervlak.

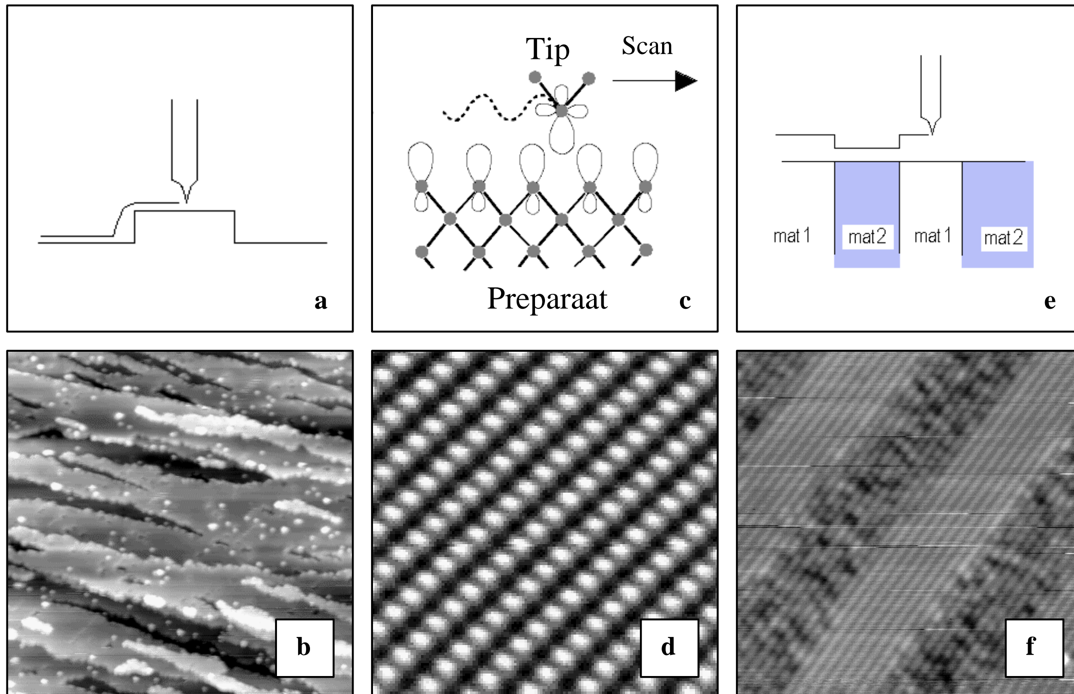

Figuur 2a: *De STM zal de (fysische) hoogteverschillen op het preparaatoppervlak volgen.* **b:** *Voorbeeld: Stapranden op een galliumarseen (GaAs) oppervlak (vergroting: 450.000 maal).* **c:** *In veel kristaloppervlakken zitten de elektronen op de atomen in het oppervlak (al zijn bij deze opmerkingen heel wat kanttekeningen te plaatsen). Omdat de STM gevoelig is voor de locale hoeveelheid electronen in het oppervlak, kan men daarom met een STM de atomen van het preparaatoppervlak afbeelden.* **d:** *Voorbeeld: Het oppervlak van GaAs. Elke lichte vlek is één arseen atoom. De gallium atomen zitten min of meer tussen de As-atomen, maar ze zijn bij de parameters die voor deze meting zijn gekozen niet in het beeld te zien (vergroting: 11 miljoen maal).* **e:** *Electronisch contrast tussen twee verschillende materialen: Hoewel het oppervlak fysisch gezien glad is, lijkt één van de materialen dieper te liggen in het STM-beeld.* **f:** *Voorbeeld: Electronisch contrast tussen galliumarseen (licht) en aluminiumgalliumarseen (donker/gespikkeld). In het AlGaAs zitten minder electronen en daarom lijkt het dieper te liggen (vergroting: 2,2 miljoen maal).*

Wat kunnen we in een STM-beeld zien?

De “hoogtekaartjes” die een STM maakt zijn echter geen gewone hoogtekaartjes van het preparaatoppervlak. De STM is namelijk niet alleen gevoelig voor hoogteverschillen in het oppervlak, hij maakt ook zichtbaar of ergens in het preparaatoppervlak veel of weinig electronen aanwezig zijn.[4] En daardoor kan een STM de atomen in een oppervlak “zien”, want in het oppervlak van een metaal- of halfgeleiderkristal zitten de electronen vaak op de atomen zelf[5] (zie figuur 2 c,d). Ook kun je daardoor in een STM-beeld van halfgeleideroppervlakken sommige typen onzuiverheden zien zitten, omdat die een extra electron bij zich hebben. Veel halfgeleiders worden via een soort “opdamptechniek” gemaakt, waarbij het mogelijk is om verschillende soorten materiaal op elkaar te stapelen.[6] Dit laatste is van groot technologisch belang: Apparaatjes als b.v. halfgeleiderlasers zoals we die in onze CD-spelers vinden, worden nooit van één enkel halfgeleidermateriaal gemaakt. Ze bevatten altijd meerdere laagjes van verschillende typen halfgeleidend materiaal die op elkaar gestapeld zijn, en ontlenen juist aan de verschillen tussen die laagjes hun eigenschappen. De overgangen tussen de verschillende materialen in zo’n stapel zijn met een STM ook goed te zien (zie figuur 2 e,f).

We moeten onze beschrijving van de STM dus een beetje aanpassen: Het is een zeer scherpe naald waarmee je op hele kleine schaal het preparaatoppervlak kunt aftasten. Het STM-beeld is daarbij in feite een soort hoogtekaart van het preparaatoppervlak, maar wel een heel speciaal soort hoogtekaart: Locale verschillen in de hoeveelheid

---

[4] Dit geldt alleen voor het geval dat de electronen vanuit het preparaatoppervlak naar de tip tunnelen. In de vaktaal wordt dan gezegd dat de “gevulde electronentoestanden” worden afgebeeld (filled states images). Tunnelen de electronen vanuit de tip naar het preparaat, dan laat de STM zien waar de electronen het liefst in het oppervlak *gaan* zitten als er nieuwe electronen aan het oppervlak worden toegevoegd. In vaktaal zeggen we dan dat de “lege electronentoestanden” worden afgebeeld (empty states images). Voor deze uitleg is dit verschil echter niet van groot belang, omdat een gevulde electronentoestand niet wezenlijk verschilt van een lege. Bovendien kan een gegeven electronentoestand onder sommige experimentele omstandigheden gevuld zijn, maar onder andere juist leeg. Als de aangelegde spanning tussen de tip en het preparaat een positieve waarde heeft, dan tunnelen de electronen van de tip naar het preparaat en worden de “lege electronentoestanden” afgebeeld. Heeft de aangelegde spanning tussen de tip en het preparaat een negatieve waarde, dan tunnelen de electronen van het preparaat naar de tip en zien we in het STM-beeld de “gevulde electronentoestanden”.

[5] Dit is een vrij grove vereenvoudiging van de werkelijkheid. Vaak zitten de electronen op de atomen in het oppervlak, maar waar ze precies zitten hangt heel sterk van het oppervlak af. Wat b.v. bij sommige halfgeleideroppervlakken wel eens voorkomt, is dat de electronen niet op alle atomen zitten, maar b.v. alternerend wel op het ene atoom en niet op het volgende. Dan zie je in je STM-beeld ook maar de helft van het werkelijke aantal oppervlakteatomen. Wat ook een groot verschil maakt, is of de electronen vanuit het oppervlak ver “naar buiten” steken, of juist meer in het oppervlak liggen.

[6] Dit zijn de zogenaamde “epitaxiale groeitechnieken”. Het zou te ver voeren die technieken hier uit te leggen. De vervaardiging van halfgeleidermaterialen en halfgeleiderstructuren d.m.v. epitaxiale groei is echter een zeer groot en belangrijk wetenschapsveld. De epitaxiale groei van kwalitatief goede halfgeleidermaterialen en halfgeleiderstructuren is alles behalve triviaal, in tegenstelling tot hetgeen de wat simpele benaming “opdamptechniek” misschien doet vermoeden.

electronen aan het oppervlak zullen zich in dat hoogtekaartje laten zien als schijnbare verhoginkjes of verlaginkjes in het preparaatoppervlak. Als ergens veel electronen zijn, dan lijkt het oppervlak van het preparaat hoger te liggen, en als ergens weinig electronen zijn, dan lijkt het preparaatoppervlak lager te liggen.

Waarover gaat dit proefschrift?

In dit onderzoek is (met name) gekeken naar het oppervlak[7] van galliumarseen (GaAs) en aluminiumgalliumarseen (AlGaAs). In GaAs zitten gallium (Ga) en arseen (As) atomen om en om in het kristal, en samen vormen de gallium en arseen atomen hetzelfde soort kristalrooster als waaruit bijvoorbeeld ook Silicium en diamant bestaan. In het AlGaAs-kristal is een deel van de gallium atomen vervangen door aluminium atomen.

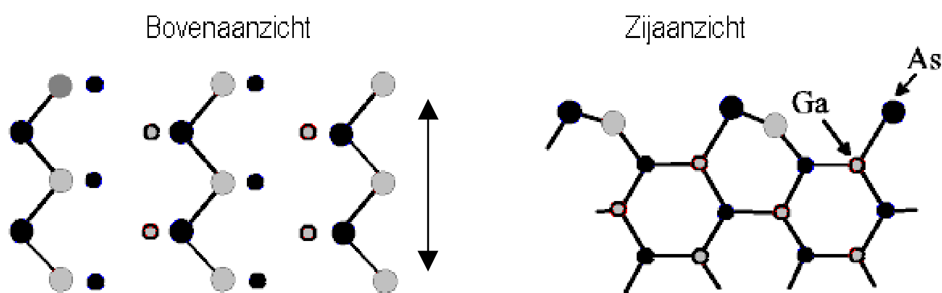

Figuur 3a: *Bovenaanzicht van het GaAs oppervlak. De atomen in de bovenste rij zijn groot getekend. Als de electronen van het preparaat naar de tip tunnelen, zijn alleen de As-atomen in de bovenste rij te zien (zie figuur 2). Tunnelen de electronen van de tip naar het preparaat, dan zijn alleen de Ga-atomen in de bovenste rij te zien. De atomen in de onderste rij zijn doorgaans niet te zien. De dubbele pijl geeeft de richting van de zig-zag rijen aan.* **b:** *Zijaanzicht van het GaAs oppervlak. Het oppervlak van AlGaAs ziet er net zo uit, alleen zijn dan sommige van de Ga-atomen vervangen door Al-atomen.*

[7] Elk kristal heeft verschillende facetten, en vaak hebben die facetten een verschillende structuur en eigenchappen. "Het oppervlak" van GaAs betekent hier in alle gevallen het zgn.{110}-oppervlak van GaAs. Dit is het natuurlijk kliefvlak van GaAs en AlGaAs. Voor onze metingen "maken" we een schoon preparaatoppervlak door een GaAs-kristal in het vacuum van de opstelling vlak voor de meting in tweeën te breken, en dat lukt alleen goed als het vlak waarlangs je wilt breken een natuurlijk kliefvlak is (net als bij het splijten van hout). In principe kun je andere kristalfacetten ook met STM afbeelden, maar dan moet je het kristal buiten de opstelling langs het gewenste vlak doorzagen en binnen in de opstelling schoonmaken. De opstelling die ik heb gebruikt leent zich daar niet voor.

Deze materialen vallen onder de zogenaamde “III-V halfgeleiders”. Deze klasse van halfgeleiders wordt veel gebruikt om licht-emitterende diodes (LED’s) te maken, of halfgeleiderlasers. LED’s vinden we op onze stereos als lampjes. Halfgeleiderlasers worden onder andere toegepast in CD-spelers, laser-pointers en in de glasvezelnetwerken waarover het telefoonverkeer over lange afstanden wordt geleid. Een nieuwe ontwikkeling in de glasvezel-optica is het onderzoek naar optische schakelaars, die ook gemaakt worden van III-V halfgeleiders.

Het oppervlak van GaAs bestaat uit evenwijdige zig-zag rijen van Ga en As atomen die om en om zitten. Bovendien zijn er rijen die hoog in het oppervlak liggen, en daartussen rijen die wat lager liggen (figuur 3a). Als we de electronen vanuit het oppervlak in de tip laten tunnelen, zien we in het STM-beeld alleen de As-atomen in de bovenste rij, omdat daar veel electronen in het oppervlak zitten. In de onderste rij zitten ook electronen, maar die liggen dieper in het oppervlak en zijn om die reden in het STM-beeld niet zichtbaar. Laten we de electronen vanuit de tip in het preparaatoppervlak lopen, dan zien we in het STM-beeld de Ga-atomen in de bovenste rij. Normaal gesproken zitten er op de Ga-atomen in het oppervlak geen electronen. Echter, als we nog meer electronen aan het oppervlak zouden toevoegen, dan zouden ze het liefst op die Ga atomen gaan zitten. Daarom zien we die Ga-atomen in het STM-beeld als de electronen vanuit de tip naar het preparaatoppervlak laten lopen.[8] Overigens is de richting waarin de electronen tunnelen (vanuit het preparaat naar de tip of omgekeerd) eenvoudig te kiezen met behulp van de spanning tussen het preparaat en de tip: Als het preparaat electrisch negatief is ten opzichte van de tip, dan tunnelen de electronen van het preparaat naar de tip. In dit proefschrift is dat aangegeven met een negatieve waarde van de tunnelspanning. Is het preparaat positief ten opzichte van de tip, dan tunnelen de electronen de andere kant uit.

Nu is er met de plaats van de electronen in het oppervlak iets vreemds aan de hand: Sommige electronen zitten voornamelijk langs de zig-zag rijen in het kristaloppervlak. Andere electronen zitten ook in rijen, maar die rijen staan loodrecht op de zig-zag rijen van het oppervlak[9]. En door de spanning tussen de tip en het preparaat te varieren kunnen we kiezen welke van de twee groepen electronen we in het STM-beeld zien (figuur 4). Uit de literatuur is bekend waar de electronen in het GaAs-oppervlak zouden moeten (gaan) zitten, en dus wat voor soort rijen we zouden moeten zien. Uit het optreden van dit soort effecten, en vooral uit de spanning waarbij dat gebeurt, valt heel veel te leren over het tunnelproces tussen een metalen tip en een halfgeleidend preparaat

[8] Figuur 4.10 van dit proefschrift laat daarvan een voorbeeld zien: Tijdens die meting is de spanning omgeschakeld van een positive naar een negatieve waarde, waardoor in het onderste deel van het plaatje de Ga-atomen te zien zijn en in het bovenste deel de As-atomen.

[9] De electronen in het oppervlak van een kristal kunnen verschillende energieen hebben. De oppervlakken van GaAs en AlGaAs hebben de eigenschap dat de electronen, afhankelijk van hun energie, óf in rijen langs de zig-zag rijen liggen, óf juist in rijen loodrecht erop. De energie van een electron in een kristaloppervlak is een beetje te vergelijken met de toon die een pianosnaar voortbrengt: Hoe hoger de toon, hoe sneller de snaar trilt en hoe meer energie er in de beweging van de snaar ligt opgeslagen.

zoals dat in een STM plaatsvindt. Zo blijkt onder andere het volgende: De manier waarop men aankijkt tegen het feit dat de STM atomen kan zien is op zichzelf juist, maar onder sommige experimentele omstandigheden kan die theorie niet opgaan. Toch zien we onder die omstandigheden wel degelijk atomen. Onder die experimentele omstandigheden moet er dus een ander mechanisme opgaan dat er ook toe leidt dat de STM atomen af kan beelden. Dit is één van de hoofdonderwerpen van dit proefschrift (hoofdstuk 4).

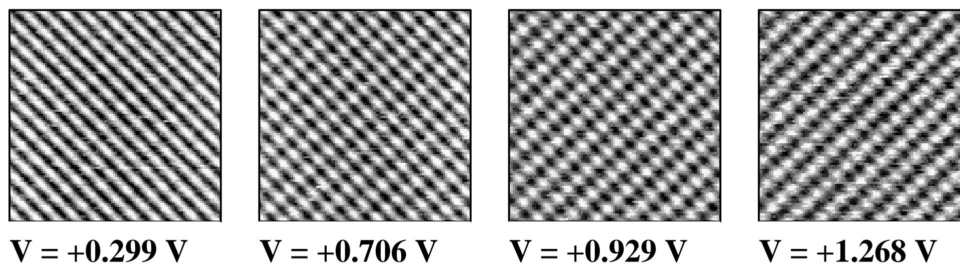

Figuur 4: *In het GaAs-oppervlak zitten sommige electronen langs de zig-zag rijen in het oppervlak, terwijl andere electronen in rijen zitten die loodrecht op die zig-zag rijen staan (zie figuur 3). Welke groep electronen wordt afgebeeld door de STM hangt af van de spanning die aangelegd is tussen de tip en het preparaat. Overigens zijn deze plaatjes ten opzichte van figuur 3 gedraaid: De zig-zag rijen lopen van linksonder in het STM beeld naar rechtsboven. Bij de spanningen tussen preparaat en tip die bij het maken van deze beelden zijn gekozen, tunnelen de electronen van de tip naar het preparaat, en dus vallen de verbredingen in de atomaire rijen samen met de galliumatomen. (Vergroting: 5 miljoen maal).*

Dit soort effecten zijn niet alleen voor galliumarseen te zien, maar ook voor aluminiumgalliumarseen (AlGaAs) (zie hoofdstuk 6). Zoals net ook al gezegd is in AlGaAs een deel van de gallium atomen vervangen voor aluminium atomen. Dit zorgt ervoor dat het AlGaAs net iets andere eigenschappen heeft dan GaAs. In heel veel halfgeleider-apparaatjes (b.v. lasers) worden laagjes van deze twee materialen op elkaar gestapeld (zie voetnoot 5). De electronen in zo'n stapel hebben de neiging om in het GaAs te gaan zitten en het AlGaAs te mijden. Uit alle veranderingen die in de STM-beelden optreden als functie van de aangelegde spanning tussen het preparaat en de tip, is heel veel te leren over waar nou de electronen in een materiaal als AlGaAs zitten (figuur 6.2, 6.3). Ook een stapel van afwisselend dunne laagjes GaAs en AlGaAs (een zgn "superrooster" of "superlattice") is op die manier te onderzoeken (figuur 6.8, 6.9).

Eén van de resultaten is te zien in figuur 6.6 a en 6.6 b: Dit figuur laat precies hetzelfde stukje AlGaAs-oppervlak zien, één keer voor het geval dat de electronen vanuit de tip het preparaat in tunnelen, en één keer voor het geval dat de electronen precies de andere kant uit tunnelen. Wie de beide figuren goed met elkaar vergelijkt, zal zien dat de zwarte vlekjes in die twee figuren niet met elkaar samenvallen. Vaak wordt

beweerd dat zulke donkere vlekjes in het STM-beeld van AlGaAs betekenen dat op die plaats veel aluminium zit[10]. Voor mensen die zich bezig houden met de vervaardiging van “gemengde” halfgeleiders zoals AlGaAs is de precieze verdeling van het aluminium interessant, want een vraag die op dit moment leeft, is of het aluminium in AlGaAs de neiging heeft om clusters (“klontjes”) te vormen of juist niet. De bewering “een zwart vlekje in het STM-beeld vertegenwoordigt een hoge locale concentratie aluminium” gaat dus niet zonder meer op, want in dat geval zou de vorm en plaats van die zwarte vlekjes nooit kunnen afhangen van de omstandigheden waaronder het AlGaAs wordt afgebeeld.

Een ander belangrijk onderwerp van dit proefschrift is het volgende: Als de spanning tussen de tip en het preparaat wordt gevarieerd terwijl de ingestelde waarde voor de tunnelstroom gelijk blijft, dan zal de afstand tussen het preparaat en de tip veranderen. Zo kan het gebeuren dat bij een kleine waarde van de spanning tussen de tip en het preparaat de afstand tussen het preparaat en de tip erg klein wordt. Daarbij kan het gebeuren dat de electronen die in het oppervlak zitten, gaan overlappen met het electron dat op de punt van de tip zit.[11] Dit verstoort de electronen aan het preparaatoppervlak en het electron op de punt van de tip. Als de verstoring groot genoeg is, kan een chemische binding ontstaan tussen de tip en het preparaat. Je zou dan kunnen verwachten dat de tip aan het preparaatoppervlak vast blijft plakken, maar dat gebeurt niet: Tijdens het scannen van de tip kan de chemische binding tussen de tip en één van de atomen in het preparaatoppervlak overspringen naar een naburig atoom in het preparaatoppervlak[12]. Hoe dit hele proces precies in zijn werk gaat is uitgerekend door enkele theoretici die daarover in de vakliteratuur hebben gepubliceerd.

Heel af en toe zien we, als we GaAs afbeelden met de STM, een heel vreemd beeld (zie figuur 5). Hierin is heel duidelijk de zig-zag structuur van het GaAs-oppervlak te herkennen. Vanuit de literatuur is al bekend dat, als de afstand tussen de tip en het preparaat erg klein wordt, die zig-zag rij in het STM-beeld gezien kan worden en dat je dan ook inderdaad zowel de gallium als de arseen atomen in de bovenste rij ziet. In dit beeld, en daarom is het zo bijzonder, is ook de structuur te herkennen van de tweede zig-zag rij die wat dieper in het oppervlak ligt (zie figuur 3). Voor zover we

---

[10] Uit bestaande literatuur was eigenlijk al duidelijk dat er uitzonderingen op deze “vuistregel” zijn. Toch wordt ze nog vaak toegepast, al is het maar als eerste benadering. Figuur 6.6 laat zien dat je ook daarmee uit moet kijken.

[11] Een electron dat in een kristaloppervlak zit, steekt altijd een eindje naar buiten. Dat is de reden dat het fenomeen “tunnelen” überhaupt bestaat. Uit het oppervlak van de tip steken ook electronen. Bij een goede, scherpe tip is er daarvan maar ééntje betrokken bij het tunnelproces. Alle andere electronen in het oppervlak van de tip zitten te ver weg van het preparaatoppervlak om deel te kunnen nemen aan het tunnelproces.

[12] Het is niet zo dat de chemische binding tijdens het scannen continu gevormd en weer verbroken wordt: Als de tip niet precies boven één atoom in het preparaatoppervlak hangt, maar meer tussen twee atomen in, zijn de electronen in het oppervlak en op de tip nog steeds verstoord. Die verstoring heeft dan niet precies het karakter van een chemische binding, maar zorgt nog steeds voor een aatrekkende kracht tussen de tip en het preparaat. Als de tip wél precies boven een oppervlakte atoom hangt, dan is de aantrekkende kracht tussen de tip en het preparaat uiteraard het sterkst (dat is namelijk het wezen van een chemische binding).

weten is dat nog niet eerder gezien. Doordat ook die tweede zig-zag rij te zien is, lijkt het beeld in alle opzichten op het “werkelijke” atomaire rooster van GaAs zoals dat meestal alleen in een boek valt te zien (zie figuur 3). Heel waarschijnlijk ontstaat zo’n soort beeld van GaAs als er tussen de tip en het preparaat een chemische binding, zoals net beschreven werd, ontstaat. We begrijpen nog lang niet alles van dit type beeld, en we slagen er lang niet altijd in om GaAs op deze manier af te beelden als we dat proberen. Maar ondanks dat laat dit resultaat wel zien dat onder bijzondere omstandigheden het GaAs-oppervlak er heel anders uit kan zien dan normaal, en dat het ook mogelijk is om de “werkelijke” atomaire structuur van het GaAs-oppervlak zichtbaar te maken met de STM.

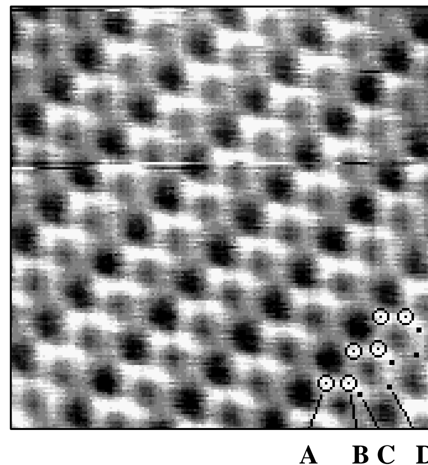

Figuur 5: *Ongebruikelijk atomair STM-beeld van GaAs. Waarschijnlijk wordt dit beeld veroorzaakt door het ontstaan van een chemische binding tussen de tip en het preparaat als deze twee elkaar dicht naderen. We identificeren de B-punten als de Ga-atomen in de bovenste rij (zie figuur 5.3). Dan geldt voor de andere punten: Punt A: As in de bovenste rij; B: Ga in de bovenste rij; C: As in de onderste rij; D: Ga in de onderste rij.*

Hiermee kom ik aan het eind van deze uitleg. Heel kort samengevat heb ik de afgelopen vier jaar het volgende gedaan, dankzij mede uw belastinggeld: Ik heb met een Scanning Tunneling Microscoop de oppervlakken van twee technologisch belangrijke halfgeleiders, galliumarseen en aluminiumgalliumarseen, bestudeerd. Daarbij heb ik de electrische spanning tussen de tip en het preparaat gevarieerd. Uit de veranderingen die dan in het beeld te zien zijn, is heel veel te leren over het tunnelproces zelf, en ook over hoe de electronen die in het oppervlak van die halfgeleiders zitten, zich gedragen.

2-D; 3-D	Two-dimensional; Three-dimensional
AFM	Atomic Force Microscopy
BCB	Bulk Conduction Band (states)
BEEM	Ballistic Electron Emission Microscopy
BVB	Bulk Valence Band (states)
BZ	Brillouin Zone
CBE	Chemical Beam Epitaxy
CBM	Conduction Band Minimum
CN	Corrugation Number
DC	Direct Current
DOS	Density Of States
FFT	Fast Fourier Transform
FWHM	Full Width Half Maximum
HF	Hydrogen Fluoride
HOMO	Highest Occupied Molecular Orbital
KOH	Potassium Hydroxide
LDOS	Local Density of States
MBE	Molecular Beam Epitaxy
PL	Photo-Luminescence
PLE	Photo-Luminescence Exitation
SEM	Scanning Electron Microscopy
RHEED	Reflection High Energy Electron Diffraction
SFL	Sample Fermi Level
SIMS	Secondary Ion Mass Spectroscopy
STM	Scanning Tunneling Microscope
TEM	Transmission Electron Microscopy
TIBB	Tip-Induced Band Bending
TILS	Tip-Induced Localized States
TFL	Tip Fermi Level
TLRC	True Lattice Resemblant Corrugation
X-STM	Cross-sectional Scanning Tunneling Microscopy
UHV	Ultra-High Vacuum
VBM	Valence Band Maximum

Experimenteel onderzoek doe je nooit alleen. Dat mag als een cliché klinken, want vrijwel elk proefschrift in de experimentele natuurkunde wijst hierop, maar het is daarom niet minder waar. Daarom zou ook dit proefschrift niet compleet zijn zonder een uiting van mijn oprechte dank aan iedereen die me op enig moment tijdens mijn onderzoek geholpen heeft.

Als eerste wil ik mijn directe begeleider, Paul Koenraad, bedanken. Hoewel je me af en toe behoorlijk nerveus kon maken met je ongebreidelde optimisme en vooral met de korte termijn waarbinnen je meestal denkt dat één en ander wel te realiseren is, heb ik met heel veel plezier met je samengewerkt. In een goede relatie hoef je het lang niet altijd eens te zijn, maar kun je de meningsverschillen die er bestaan goed bespreken. Dat hebben we vanaf het begin gehad, en ik heb dat altijd ontzettend in je gewaardeerd.

Ook mijn promotor, Professor Wolter, wil ik graag bedanken voor de gelegenheid om in zijn groep te promoveren. Als groepsleider bent U eindverantwoordelijke geweest voor een werkomgeving waarin ik goed heb kunnen gedijen en ook groeien. Dank U daarvoor. Verder wil ik de commissieleden, Prof. Salemink, Prof. van Kempen en Prof. Frenken oprecht bedanken voor het kritisch doorlezen van mijn proefschrift. Prof. Salemink ben ik bovendien dank verschuldigd voor zijn opmerkinen over het sputteren van STM-tips, waar ik veel aan gehad heb.

Dominique Bruls ben ik heel veel dank verschuldigd voor een goede werksfeer, levendige koffietafelconversaties, fluitconcerten, maar vooral ook voor de vele hand- en spandiensten die hij voor me deed. Zo waren er de “dagelijkse” STM-klusjes als het maken van tips en samples, of het bestellen van een voeding dat van een dermate buitenaards type bleek dat geen hond het ding nog in voorraad had. Ook nog bedankt voor al je hulp met mijn soms weerbarstige PC en voor het “babysitten” tijdens de nachtelijke metingen, een taak die grotendeels op jouw en op Paul is neergekomen. Het is mooi om te zien hoe jij, nu ik zelf de vakgroep verlaten heb, op zo’n naadloze manier het STM-onderzoek in onze vakgroep hebt overgenomen.

Ook Emile Martens zal een groot stuk van zijn afstudeerwerk in dit proefschrift terugvinden, in hoofdstuk drie waar het model beschreven staat dat de veldemissiekarakterisatie theoretisch onderbouwt. Verder wil ik graag Rob Dekkers en Niall Phelan bedanken voor hun werk aan resp. het etsen van Platina tips en het kliefgedrag van GaAs. Martijn Kemerink gebruikt nu die platina-tips (of heeft dat in elk geval een lange tijd gedaan) en Niall’s werk heeft ons begrip van het kliefproces weer wat verder gebracht.

Geen experimenteel onderzoek zonder technische ondersteuning, en dat brengt me bij Jos van Ruyven die de vacuum-opstelling in elkaar gesleuteld heeft en Marius Bogers en zijn groep die een groot aantal “STM-accesoires” heeft gemaakt. Ook Frans van Setten wil ik bij deze nogmaals hartelijk danken voor het onderbrekingskastje dat we bij het etsen van tips gebruiken. Verder wil ik Maarten Leys bedanken voor het geduldig antwoorden van al mijn vragen over groei en halfgeleideroppervlakken, en Peter Nouwens voor (onder andere) het bereidwillig en min of meer permanent afstaan van een stuk van zijn zuurkast. Ook Willem van der Vleuten, die het delta-laag sample

en het sample uit hoofdstuk 6 heeft gegroeid, ben ik dank verschuldigd. Jammer dat je er niet bent om de resultaten van je werk te zien.

In de loop van de tijd heb ik verschillende kamergenoten gehad: Martijn Kemerink, altijd goed voor een originele screen-saver tekst, Arnout van der Stadt, waarvan ik me soms afvroeg of hij zich na de lange werkdagen die hij maakte de weg naar huis nog wel zou weten te herinneren, en (alweer) Dominique, wiens bijdrage aan de sfeer in de werkkamer en aan de koffietafel een (overigens positief) verhaal apart is. Verder wil ik alle andere HF-ers bedanken voor alle gezelligheid en antwoorden op fysische en andere vragen.

Buiten mijn eigen groep wil ik graag de groep “Electronische Bouwstenen” van de faculteit electrotechniek bedanken voor het gebruik van hun SEM, en daarbij Professor Kaufmann, Erik-Jan Geluk en Ben van Roy in het bijzonder. Und auch möchte ich Martin Wenderoth, Kathi Sauthoff, Klaus Engel und Berhart Spichter danken für den sehr angenehmen und lehrreichen Besuch in Göttingen. En “last, but by far not least”: Hans Dalderop, voor zijn enthousiaste uitleg over allerlei scheikundige zaken en voor het feit dat ik de meest gekke chemische stofjes meestal zo van hem kon lenen.

In mijn vriendenkring heeft Marcel Davids een bijzondere bijdrage geleverd door één van zijn PC’s zo lang aan me uit te lenen. Verder wil ik vooral Jolanda bedanken, eigenlijk in hoofdzaak voor het simpele feit dat ze er is. En ook voor haar begrip als ik voor de zoveelste keer niet vanachter de PC weg te slepen was, niet meehielp met de afwas, of als ik weer eens vond dat een verjaardag in haar familie ook best zonder mijn aanwezigheid kon worden gevierd. Datzelfde geldt voor mijn zus Machteld, mijn vader, Netty, Arjan, Olivie, Mark, Inna, Jan en Anne-Marijke. En voor tante Cock. Jij, tante Cock, neemt hierin een heel bijzondere plaats in: In de drie jaar dat ik bij je in huis woonde, heb je me heel veel belangrijke lessen meegegeven. Daarom draag ik dit proefschrift graag aan jou op.

Gijs de Raad, november 2000

G.J. de Raad, P.M. Koenraad, J.H. Wolter: *Use of the Schiller-decapitation process for the manufacture of high-quality Tungsten STM-tips.* Journal of Vac. Sci. and Tech.-B, Vol. 17, No. 5, pp. 1946 - 1953 (1999). See also chapter 3 of this thesis.

G.J. de Raad, D.M. Bruls, P.M. Koenraad, J.H. Wolter: *Interplay between tip-induced band bending and voltage-depending surface-corrugation on GaAs-(110) surfaces.* Submitted for publication in Phys. Rev. B. See also chapter 4 of this thesis.

G.J. de Raad, D.M. Bruls, P.M. Koenraad, J.H. Wolter: *Observation of a new image-form of GaAs-(110) showing the top- and bottom zig-zag rows of the surface.* Submitted for publication in Phys. Rev. B. See also chapter 5 of this thesis.

G.J. de Raad, D.M. Bruls, P.M. Koenraad, J.H. Wolter: *Voltage-dependent changes in the filled- and empty-states images of* $Al_xGa_{(1-x)}As$ *(110) and of GaAs /* $Al_xGa_{(1-x)}As$ *thin layers.* Submitted for publication in Phys. Rev. B. See also chapter 6 of this thesis.

Naam: Gijs Jan de Raad

Geboren: 26 oktober 1969

Middelbaar onderwijs: VWO-B, doorlopen op de Rijks scholengemeenschap "Professor Zeeman" te Zierikzee en de Katholieke Scholengemeenschap "Veluws College" te Apeldoorn (1982 - 1988).

Uitwisselingsjaar: Senior year aan de "Lakeville High School" te Lakeville, Minnesota, Verenigde Staten (1988 - 1989).

Studie: Technische Natuurkunde, doorlopen aan de Rijksuniversiteit Groningen (1989 - 1995).

Industriële stage: *The Prickstick: Testing a capacitive soil moisture measurement probe for tropical conditions.* Uitgevoerd bij het *International Centre for Research in Agro-Forestry* (ICRAF) te Machakos/Nairobi, Kenya.

Afstudeeronderzoek: *Scratching the surface: The study of irradiated and unirradiated NaCl using Atomic Force Microscopy.* Uitgevoerd aan de Rijksuniversiteit Groningen, vakgroep Materiaalkunde (Prof.dr. J. de Hosson).

Promotieonderzoek: *Voltage-dependent Scanning Tunneling Microscopy on the {110}-surfaces of GaAs, AlGaAs and their heterostructures.* Uitgevoerd aan de Technische Universiteit Eindhoven, vakgroep Halfgeleiderfysica. Eerste promotor: Prof.dr. J.H. Wolter, copromotor: dr. P.M. Koenraad. (1996 - 2000).

Per 1 maart 2000 in dienst getreden als proces integratie ingenieur bij Philips Halfgeleiders te Nijmegen.

Stellingen

behorende bij het proefschrift

Voltage-dependent Scanning Tunneling Microscopy on the {110}-surfaces of GaAs, AlGaAs and their heterostructures

1) Bij het zelfsputterproces van wolfraam STM-tips treedt het Schiller-decapitatieproces op, wat te herkennen is aan een specifiek gedrag van de signaal-ruisverhouding van de sputterspanning als functie van de tijd. *(dit proefschrift, hoofdstuk 3).*

2) Atomaire oplossing in STM-beelden van halfgeleideroppervlakken hoeft niet altijd veroorzaakt te worden door het tunnelen van electronen in- of vanuit oppervlaktetoestanden. Onder bepaalde omstandigheden zijn andere mechanismen voor atomaire oplossing ook mogelijk. *(dit proefschrift, hoofdstuk 4 en 5; N. Horiguchi et al., Jap. Journ. of Appl. Phys, Vol. 37, part I, p. 3782; F. Fukumizu et al., Jap. Journ. of Appl. Phys, Vol. 37, part I, p. 3785).*

3) De vaak kwalitatieve behandeling van tip-geinduceerde bandverbuiging in de literatuur doet onterecht vermoeden dat dit fenomeen weinig méér tot gevolg heeft dan een verschuiving van de tip-sample spanning waarbij een bepaalde oppervlaktetoestand in het STM-beeld te zien is. De invloed van tip-geinduceerde bandverbuiging kan namelijk veel verder gaan. *(dit proefschrift, hoofdstuk 4).*

4) De atomaire morfologie van AlGaAs-{110} en van GaAs/AlGaAs heterostructuren in STM is zeer sterk afhankelijk van de aangelegde tunnelspanning. Deze omstandigheid biedt veel nieuwe mogelijkheden om informatie over de electronische structuur van dit soort oppervlakken te verkrijgen. *(dit proefschrift, hoofdstuk 6).*

5) Bij de interpretatie van STM-beelden van AlGaAs wordt wel eens de vuistregel “een lage schijnbare hoogte vertegenwoordigt een hoge locale concentratie aan aluminium” toegepast. Aan de geldigheid van deze vuistregel moet, zelfs wanneer men die slechts in eerste benadering toepast, worden getwijfeld. *(dit proefschrif, hoofdstuk 6).*

6) De atoomkern kan, net als de electronenwolk van een atoom, met behulp van een zgn. “schillenmodel” worden beschreven *(Fundamentals of Nuclear Physics, door N.A. Jelley, Cambr. Univ. Press).* Gezien de educatieve waarde van dit feit voor studenten zou het wenselijk zijn om dit gegeven een prominentere plaats in het studieprogramma te geven *(eigen ervaring bij het tweedejaarspracticum).*

7) Met de wichelroede als oudste vertegenwoordiger waren de Scanning Probe Technieken al in de Middeleeuwen bekend.

8) Gezien de soms hoge verkoopprijs van moderne, abstracte schilderkunst zou de STM-gemeenschap een belangrijk deel van haar activiteiten moeten kunnen financieren door de verkoop van experimentele resultaten als kunst.

9) Een planning is zinloos zonder goede afspraken.

10) Een ideaal is te vergelijken met een ster: het ideaal zelf is onbereikbaar, maar je kunt je er wel op orienteren.

Eindhoven, 22 januari 2001 Gijs de Raad